FeNi metal condensation and evolution in the Early Solar System : a study of germanium isotopes and siderophile elements in Ordinary and Bencubbinite primitive chondrites

Guillaume Florin

Thèse de doctorat

présentée et soutenue publiquement pour l'obtention du grade de

Docteur de l'Université de Lorraine en Géosciences

FeNi metal condensation and evolution in the Early Solar System: a study of germanium isotopes and siderophile elements in Ordinary and Bencubbinite primitive chondrites.

Condensation et évolution du métal Fe-Ni dans le Système Solaire jeune : systématiques des isotopes du germanium et des éléments sidérophiles dans les chondrites primitives (Chondrites Ordinaires et Bencubbinites).

Par

Guillaume Florin

Soutenance publique le 30 juin 2020

Membres du Jury de thèse

Mickaël TOPLIS	Directeur de Recherche CNRS, OMP, Toulouse	Rapporteur
Vinciane DEBAILLE	Maître de Recherche FNRS, ULB, Bruxelles, Belgique	Rapportrice
Ali BOUHIFD	Directeur de Recherche CNRS, LMV, Clermont-Ferrand	Examinateur
Frank WOMBACHER	Professeur, Université de Cologne, Allemagne	Examinateur
Laurie REISBERG	Directrice de Recherche CNRS, CRPG, Nancy	Examinatrice
Béatrice LUAIS	Chargée de Recherche CNRS – HDR, CRPG, Nancy	Directrice de thèse
Tracy RUSHMER	Professeur associé, Université de Macquarie, Sydney, Australie	Directrice de thèse
Olivier ALARD	Directeur de recherche CNRS – HDR, Géoscience Montpellier	Co–Directeur de thèse
Jérémy GUIGNARD	Post-Doc, IRAP, Nantes	Invité

Centre de Recherches Pétrographiques et Géochimiques

15 Rue Notre-Dame des Pauvres, 54501 Vandoeuvre-Lès-Nancy, France

"There is nothing like looking, if you want to find something. You certainly usually find something, if you look, but it is not always quite the something you were after."

J. R. R. Tolkien

A mon père,

Avant-propos

Cette thèse a été réalisée sous la direction d'encadrants français (Béatrice Luais, Olivier Alard) et australien (Tracy Rushmer) et est le résultat d'une collaboration entre l'Université de Lorraine, Nancy, France, et l'Université de Macquarie, Sydney, Australie. De plus le jury de thèse est composé de membres internationaux. De ce fait, et conformément à l'accord de cotutelle signé entre les deux Universités, le manuscrit est intégralement rédigé en anglais. Un résumé étendu en français des travaux de thèse est inclus au début du manuscrit.

Foreword

This thesis was conducted under the direction of French supervisors (Béatrice Luais, Olivier Alard) and Australian supervisor (Tracy Rushmer) and is the result of a collaboration between the University of Lorraine (Nancy, France) and Macquarie University (Sydney, Australia). In addition, the jury is composed of an international member. As a result, and in accordance with the cotutelle agreement signed between the two Universities, the manuscript is entirely written in English. An extensive French summary of the work done is included at the beginning of the manuscript.

Remerciements / Acknowledgements

Écrire de la science n'est pas chose aisée, mais lors d'une thèse, une partie significative du temps y est consacrée. Malheureusement ce n'est pas le cas des remerciements, qui peuvent en apparence être faciles à écrire alors qu'il n'en est rien. Ce sont ici les derniers mots que je couche sur le papier (enfin sur mon clavier) pour cette thèse, ils seront en français et en anglais.

First of all, I would like to gratefully thank the members of the jury who agreed to read and examine this manuscript. Thanks to Mike T., Vinciane D., Frank W., Ali B., Jérémy G., Laurie R. for their interest in my work and their presence today. Also, thanks to Jesse D. for his careful corrections of the article.

Arriver dans un nouvel environnement de travail n'est jamais facile et je souhaiterais remercier Raphaël pour m'avoir accueilli au CRPG. Je souhaite aussi remercier toute l'équipe administrative du CRPG, Aurélie, Cathy, Isabelle, Corinne, Joëlle pour leur efficacité à tous les niveaux, ainsi que leur patience. Les choses seraient beaucoup trop compliquées sans vous toutes. Merci aussi à Larry sans qui le CRPG serait bien démuni niveau informatique.

Durant ces trois ans, j'ai à de nombreuses reprises sollicité les compétences analytiques du SARM dont l'équipe de choc a toujours été très conciliante, même avec mes demandes les plus complexes. Je les remercie toutes et tous pour leur aide et leurs apports à cette thèse. Je remercie en particulier Delphine Y. pour toutes les analyses que tu as faites et je m'excuse pour tes béchers en platine qui, il semblerait, n'aiment pas trop les Chondrites Ordinaires. Merci à toi Christophe pour m'avoir éclairé de tes lumières, en science et d'un point de vue humain, ainsi que pour les quelques chasses aux Pokémons ! Merci aussi à Pierre–Yves, les indicateurs colorés c'est quand même super fun à faire. Enfin à Camille de m'avoir aiguillé lorsque je m'égarais dans les laboratoires du SARM.

J'aimerais remercier tout particulièrement Damien, sans qui il m'aurait été impossible de mener à bien toutes ces analyses. Je suis arrivé avec des connaissances rudimentaires du fonctionnement d'un spectromètre de masse et de la chimie, grâce à toi je peux me targuer de savoir utiliser un Neptune et de faire la chimie du meilleur élément au MONDE (sans un échec au compteur… pour le moment du moins). Merci aussi de m'avoir supporté toutes ces heures lorsque je venais te poser mes multiples questions. Tant que l'on est dans ce bureau, je souhaite remercier Aimeryc pour tes conseils, ta gentillesse et participation à l'épuisement des réserves de bière du CRPG 😉. Merci aussi à Catherine pour ton aide, et pour m'avoir laissé trifouiller le défunt IsoProbe, j'ai un super souvenir sur une étagère. Merci, Christiane, même si tu nous voles régulièrement de l'eau MQ, ta bonne humeur est indispensable de bon matin en salle blanche. Also, a special thanks to Stepan for all his advice in chemistry and more.

Lorsque l'on explore le CRPG, l'on peut avoir à descendre dans ses entrailles, où par 30°C toute l'année il fait très bon vivre. Vous pourrez y rencontrer François, que je remercie pour les discussions enrichissantes que l'on a eues, Tix et Delphine merci à eux pour leur aide.

Je remercie aussi David J. de m'avoir permis de faire un peu de terrain, car en cosmo cela est un peu compliqué. Merci à toi aussi Karine de m'avoir permis d'encadrer des étudiants sur le terrain et de m'avoir fait découvrir ce délicieux breuvage qu'est la mauresque.

Je remercie Yves d'avoir éclairé ma lanterne en cosmo, d'avoir bien voulu partager un logement au Japon, de m'avoir supporté au lendemain de la MetSoc alors que je faisais mes emplettes, et bien sûr, pour ce mémorable Boombastic de Shaggy interprété à la perfection. Merci aussi à Johan, grâce à toi j'ai découvert le mochi, et c'est définitivement trop bon. Merci à Laurette pour tes conseils au Japon et les discussions que l'on a pu avoir. Merci à Bernard pour ton aide pour l'Australie et tes anecdotes croustillantes sur les anciens de la cosmo. Merci à Camille C., je garderai un souvenir indéfectible de ta danse avec Mister Wood, la même à la MetSoc cette année ? PH et Julien, merci d'avoir participé activement au renouvellement (et à la consommation) des victuailles du bureau. Merci aussi à Lydéric et à tous ceux que j'aurai pu oublier, merci pour ces quelques années riches en émotion.

S'il y a quelque chose de fort au CRPG c'est la cohésion, le soutien et l'esprit de camaraderie entre doctorants. Je ne sais pas ce qu'aurait été cette thèse sans le bureau magique qu'était le mien et je tiens à remercier tout particulièrement Apolline, Marine et David. Merci Apo de t'être laissé corrompre de si nombreuses fois pour « juste boire une bière vite fait à la maison », merci pour ta richesse de conversations et d'avoir décomplexe tout le monde sur les horaires d'arrivé le matin. Marine, merci pour tous ces cafés le matin, ces fous rires, tes numéros d'équilibriste ta bonne humeur, ainsi que pour ton aide quand on en a eu besoin, ne change pas tes la meilleure. David, que dire, tu es le boss du game et une des meilleures personnes que j'ai rencontrées, j'admire ta capacité à être multi tache, merci pour tout, et sur tout ne change pas. Je regrette de ne pas avoir été là pour vos soutenances… Merci Michael, cette année en kilt à la MetSoc ? Je souhaite aussi remercier le bureau d'en face, merci à Valentin et Julien. Julien merci de m'avoir fait découvrir tous ces magnifiques vins durant ces soirées ou nous faisions un peu plus que déguster. Merci aussi à Seb pour son aide lors du déménagement, ces parties de Pokémon, et de sa confiance. Cécile et Maxime merci pour ces moments inoubliables au Japon, Maxime un onsen quand tu veux. Finalement Merci à toute la nouvelle génération de doctorants, Marion, Antoine, Delphine, Mathis, Julien, Arbia, Mathieu, sans vous le CRPG serait différent. Et bien sûr, merci à tous pour votre aide pour le déménagement.

Je tiens aussi à remercier l'ancienne génération, et en particulier Gaëlle, Rémi et Papache, tant de bons moments passés ensemble, de lutte contre le système (surtout Papache), j'ai hâte de venir voir votre nouvelle maison, le chat et les poules, et peut-être de s'envoyer quelques hydromels cet été ? Merci à Lionel pour ces soirées jeux, la richesse de nos conversations, cette visite de la Mère Patrie. J'en profite aussi pour remercier Julie et vous féliciter pour votre mariage, j'espère que ça se passe bien pour vous deux aux USA. Merci à Léa, Fred et Loïc pour ces incroyables parties de jeu de rôle et le temps passé à rendre l'univers meilleur. Merci à Paul et Christelle pour votre amitié et convivialité. Merci à Yumi, toujours de bonne humeur. Finalement merci à Nina, toi et ton humour aurez fait passer le temps en salle blanche bien plus vite.

I also want to thank all the people at Macquarie University, and especially, Marina, Rosa (I love your cakes), Sinan, Tusita, Kui, Lou, thank you all for welcoming me at MQ. Thanks to Lauren for all those advices and all those conversations, your capacity to analyse and translate

my English and to have shared Olivier. I hope we will meet again in France and I'm sure you will speak a perfect French. Fran, thanks for everything, and in particular for your cakes continue like that, you are the next! See you at the MetSoc! Also, thanks to Antony, you helped me a lot, those capsules worked perfectly!

Merci aussi aux copains, Martin, Kevin, Stéphane, Manon, Marion, qui, malgré la distance, nous ont aidés (un peu sous la menace 😉) à déménager et qui sont venus régulièrement dans le froid de Nancy. Votre absence cette dernière année s'est faite sentir. Je vous aime les ami · e · s.

Also, I want to thank all my mates in Australia, Ricky, Dawid, Rhys, Pat, Robert, Rick from the North, Masha, Louis, Hugo, Charlotte that was an amazing year with all of you, and you are all welcome home in France.

Je souhaiterais remercier chaleureusement Béatrice, sans qui cette aventure n'aurait pas été possible. Béatrice, tu es une personne merveilleuse et je suis fier de pouvoir dire que tu as supervisé ma thèse. Merci de m'avoir donné ma chance, de m'avoir transmis ton savoir, et merci pour ta patience. S'il y a bien une chose que je redoutais avant de te rencontrer c'était les relations doctorant-chercheur, mais je peux dire que je prends un vrai plaisir à échanger avec toi, et je pense que nos conversations ont été très fructueuses. J'ai hâte de continuer à collaborer.

Merci aussi à Olivier, qui m'a ouvert les portes du laser, merci d'avoir pris du temps pour moi et de m'avoir soutenu pendant cette année à Macquarie. J'espère t'avoir redonné goût aux petits cailloux venus de l'espace.

I would like to warmly thank Tracy who supported me during that PhD. For her work at Macquarie that has made possible this cotutelle. Thank you for allowing me to come, I really appreciated our collaboration. I hope to be able to come back to continue working with you.

Finalement, je souhaite remercier ma Maman et mon Papa qui toutes ces années ont cru en moi (et ce n'était pas gagné). Merci de m'avoir laissé libre de mes choix, grâce à ça j'ai pu trouver ma voie. Je dédicace ce manuscrit à Papa qui, je suis certain, serait très fier. Merci Maman, d'avoir bravé ta peur du kangourou ! Merci au frérot qui s'occupe de repeupler la terre avec sa charmante femme Aline et leur famille 😉, alors que je m'intéresse à ces petits fragments de roche. Merci aussi à Française et Saïd, je vous aime fort. Merci à mes deux petites sœurs, Estelle et Iris (un classement par âge pour ne pas faire de jalouse 😋) que j'aime par-dessus tout et pour qui je ferais n'importe quoi (enfin presque hein, moi je ne mange pas de fleur).

Mes derniers mots sont pour mon amour, ma confidente, meilleure amie, et bien plus, Aurélie. Merci d'avoir supporté ton Guigui pendant toute cette thèse, pendant les hauts et les bas. Merci de m'avoir suivi à Nancy, et même jusqu'en Australie (ça valait le coup pour le kangourou non ?). Je ne sais pas ce que j'aurais fait sans toi, tu es la meilleure ! Et cette thèse est un peu la tienne. Tu me demandes où serons-nous l'année prochaine ? Qu'en sais-je ?... Ensemble et c'est tout ce qui compte.

Merci à tous ! / Thanks to all

Table of Contents

List of Figures

Résumé des travaux

Chapter 1

Chapter 2

Chapter 3

Chapter 4

Chapter 5

Chapter 6

List of Table

Résumé des travaux

I. Introduction

1 Contexte de la thèse

La cosmochimie est une branche de la géochimie qui s'intéresse spécifiquement à la composition chimique de l'Univers et du système solaire. Le but principal de cette science est de comprendre la formation des systèmes planétaires, et plus spécifiquement des objets du Système Solaire tels que les planètes et leurs satellites, les astéroïdes et les comètes. Dans ce but, le cosmochimiste utilise une combinaison d'instruments tels que les télescopes, des sondes spatiales, mais aussi des expériences en laboratoire afin de caractériser les compositions élémentaires et isotopiques d'objets naturels (e.g. météorites) ou synthétiques. Ces études visent à extraire les informations chimiques enregistrées par les objets durant leur formation afin de mettre en lumière les processus se déroulant à la création du système solaire ainsi que la chronologie de ces évènements. Les échantillons à disposition du cosmochimiste sont variés et comprennent les météorites, primitives ou différenciées, ainsi que les échantillons récoltés lors de missions spatiales (e.g. *Apollo* et *Luna missions*, ou encore *Star Dust*), ou encore les assemblages expérimentaux créés en laboratoire.

Le but de cette thèse est d'étudier les premiers instants de la formation du métal ainsi que son évolution sous l'action de processus nébulaire et planétaire. Pour ce faire, j'ai concentré mes efforts sur l'étude des chondrites (météorites primitives), car elles offrent une fenêtre ouverte sur les premiers processus d'évolutions du disque protoplanétaire.

2 Les météorites

Les météorites sont des fragments de planétésimaux, de planètes, de lunes ou d'astéroïdes formés durant l'histoire du système solaire. Toutes ces roches ont été éjectées de leur corps parent lors de gigantesques impacts à leur surface. Certaines de ces météorites échantillonnent des objets toujours présents dans le Système Solaire, par exemple les météorites lunaires ou martiennes d'autres sont les témoins de planétésimaux ayant été détruits (par exemple les météorites de fer). Dans les collections actuelles de météorites, la grande majorité des échantillons proviennent de collisions au sein de la ceinture d'astéroïdes, située entre Mars et Jupiter.

Les premières classifications de météorites ont été établies durant la fin du 19$^{\text{ème}}$ siècle, et sont majoritairement basées sur les caractéristiques minéralogiques et texturales des météorites. L'unification de ces premières classifications est appelée la classification de Rose-Tschermak-Brezina (Rose, 1863 ; Tschermak, 1883 ; Brezina, 1904). Le siècle dernier, l'avancée des technologies de quantification élémentaire et isotopique a permis le développement d'une

classification plus précise basée sur les caractéristiques chimiques de ces objets (e.g. Mason, 1967, Kallemeyn and Wasson, 1981 Kallemeyn *et al.*, 1989, 1991, 1994 etc.).

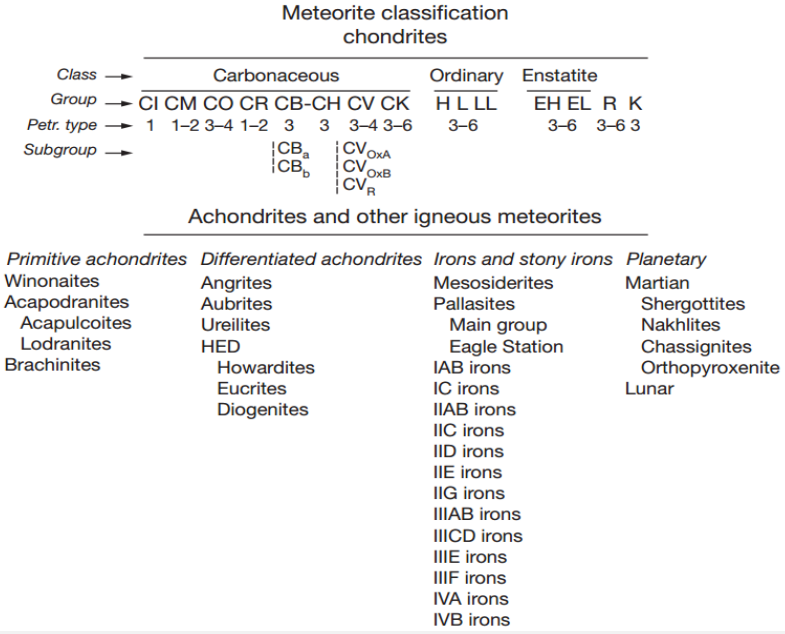

Figure 1 : Classification des météorites d'après Krot et al. (2014).

Deux groupes de météorites peuvent être différenciées, celles dites non–chondritiques et celles dites chondritiques (Fig. 1). Les chondrites sont des agglomérats hétérogènes, non différenciés (i.e. les phases métal et silicates n'ont pas été ségréguées) de métal, sulfure, silicate (les chondres), et d'inclusions réfractaires, cimentées ensemble par une matrice à grains fins. Deux grandes catégories de chondrites existent, celles carbonées (e.g. CB, CI, CH etc.) et celles non carbonées (e.g. H, L, LL, EH etc.). Parmi ces groupes, certaines contiennent de grandes quantités de métal quand d'autres en sont dépourvues (Fig. 2).

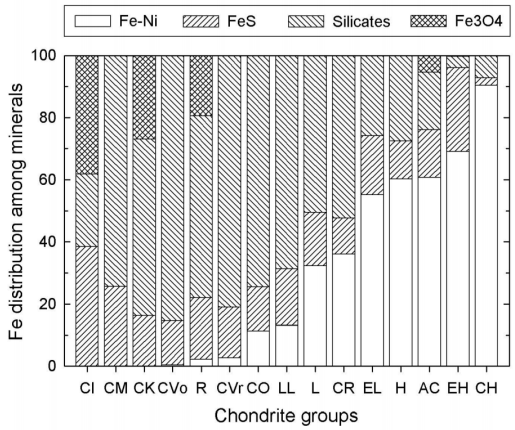

Figure 2 : Répartition du Fer dans les phases majeures au sein de différents groupes de chondrites. D'après Campbell et al. (2005) et Koblitz (2010).

Les chondrites peuvent aussi être subdivisées en classes en fonction de leur composition élémentaire, isotopique, minéralogique et pétrologique (Van Schmus et al., 1967). On leur attribue donc un numéro, e.g. H3 ou H6, qui définit leur degré d'oxydation ou de métamorphisme (Fig. 3). L'oxydation augmente de 3 à 1 et le métamorphisme de 3 à 6, de sorte que le groupe 3 représente les météorites les plus primitives.

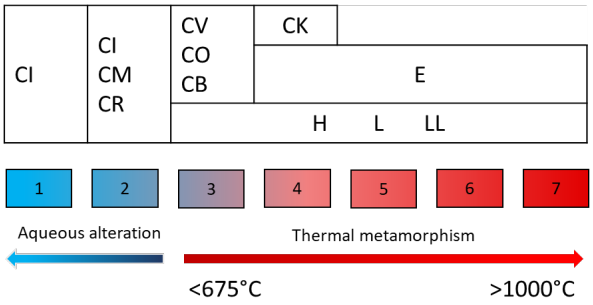

Figure 3: Classification pétrographique d'après Van Schmus et al. (1967) et Tait et al. (2014).

Le groupe non-chondritique est beaucoup plus diversifié, et se caractérise par l'absence de chondres. Ces météorites sont à différents stades de différenciation. Les achondrites primitives contiennent du métal et de grands cristaux de silicate. Elles représentent un stade très avancé – mais incomplet – de différenciation métal-silicate (e.g. Winonaïtes : Benedix et coll., 2000 ; Wasson et Kallemeyn, 2002 ; Brachinite : Warren et Kallemeyn, 1989 ; Acapodranite : Krot et coll., 2014). Les achondrites et les météorites de fer sont donc les témoins du dernier stade de différenciation planétaire et représentent respectivement le manteau et le noyau des planétésimaux (Prinz et al., 1983 ; Scott et Wasson, 1975).

La relation entre les chondrites et les météorites différenciées a été théorisée depuis le début de la cosmochimie (Urey, 1955). Le modèle le plus communément accepté propose que les météorites différenciées (achondrites et météorites de fer) soient le résultat de la ségrégation du métal et des silicates dû à l'augmentation de la température sur des corps parents chondritiques (Fig. 4). Cette augmentation de température peut-être le résultat de processus radioactif par décroissance du ^{26}Al et ^{60}Fe (e.g. Elkins–Tanton, 2017) ou d'impact (Tomkins et al., 2013).

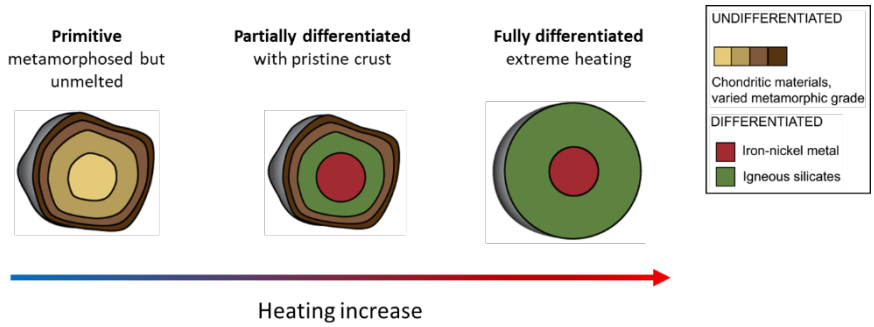

Figure 4 : Schéma de la différenciation d'un planétésimal suite la à l'augmentation de sa température. Figure modifiée d'après Elkins–Tanton (2017).

Le métal est une phase ubiquiste dans le système solaire jeune et par conséquent son étude est d'une importance capitale afin de comprendre la formation et l'évolution des premiers planétésimaux. Les études chimiques de la phase métal dans les météorites ont été menées, dans un premier temps, sur les météorites de fer au travers d'une série de 12 papiers scientifiques intitulées « *The Chemical Classification of Iron Meteorites* » par Wasson et collaborateurs. Via la quantification des éléments sidérophiles (e.g. Ir, Ni, Au, Ge, Ga) de ces météorites, elles ont été classifiées en quatre catégories, I, II, III, IV et sous catégories (A, B, C, D, E, F, G), elles-mêmes s-distinguées en deux grands groupes : les météorites de fer magmatiques et non-magmatiques. Pour les météorites de fer magmatiques, les variations chimiques du métal peuvent être modélisées par cristallisation fractionnée d'un liquide métallique, en utilisant des modèles expérimentaux de répartition des éléments chimiques entre le métal liquide et le métal solide (Chabot and Jones, 2003 ; Chabot and Haack, 2006). La formation de ces météorites de fer a donc été attribuée à la cristallisation d'un noyau métallique au cœur de planétésimaux (Haack and McCoy, 2004). Les compositions chimiques des météorites de fer non- magmatiques ne peuvent pas être modélisées de la sorte, leurs formations sont donc attribuées à d'autres processus. Par exemple, l'utilisation conjointe des isotopes du germanium ainsi que des compositions élémentaires du Ir, Au et Ni a montré que les météorites de fer de type IIE se sont probablement formées par des impacts successifs sur un planétésimal non solidifié résultant en une évaporation partielle des éléments sidérophiles volatils (Wasson et al. 1986, Wasson, 2017 ; Luais, 2007). Ces études sur les compositions élémentaires et isotopiques des météorites de fer nous montrent que les éléments sidérophiles réfractaires tels que Ir, Os, Re, Pt et modérément volatils tels que Ge et Ga, sont de très bons traceurs pour étudier la formation et l'évolution de la phase métal lors des processus prenant place dans les premiers stades d'évolution du Système Solaire.

Le but de cette thèse est de contraindre les processus de formation et d'évolution du métal dans les météorites primitives. Pour cela, nous avons sélectionné deux types de météorites, les chondrites ordinaires (OC) et les chondrites carbonées de type Bencubbin (CB). Les premières présentent une évolution métamorphique (Van Schmus et al., 1967 ; Tait et al., 2014) nous permettant d'étudier la phase métallique depuis des stades très précoces durant lesquels elle n'a presque pas été modifiée par l'élévation en température sur le planétésimal (~200-300 °C, Huss et al., 2006). La phase métal conserve donc ces caractéristiques nébulaires, jusqu'à des stades relativement évolués durant lesquels le métal a subi des augmentations de températures jusqu'à 1000 °C (Tait et al., 2014). Les CB quant à elles se sont formées par condensation d'un gaz de composition similaire à celle du disque protoplanétaire (Newsom and Drake, 1979). Leur étude a donc permis de comprendre la réponse isotopique des éléments modérément volatils lors de la condensation du métal.

L'étude présentée dans ce manuscrit est divisée en trois grandes parties : (1) la formation du métal par condensation dans le Système Solaire (2) les effets sur le métal de l'oxydation et

des processus de chauffe dans le disque d'accrétion (3) l'évolution du métal avec le métamorphisme et sa migration dans les planétésimaux non différenciés.

II. Méthodes analytiques

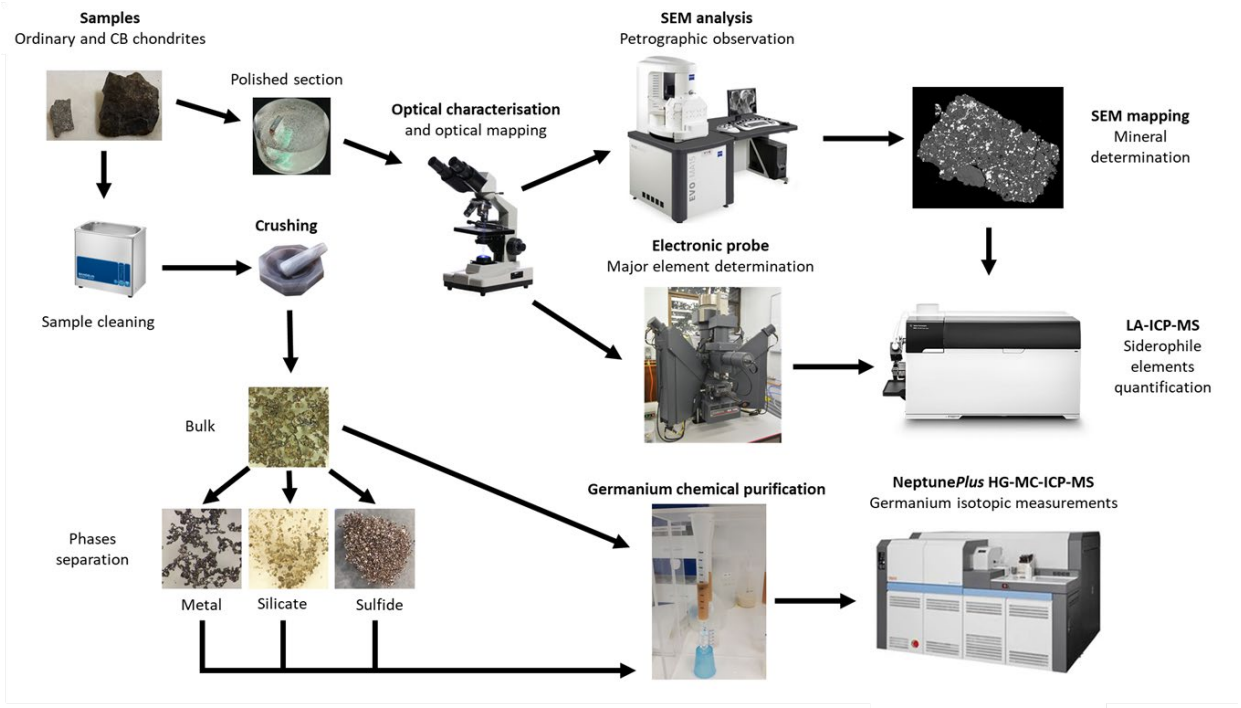

Figure 5 : Représentation schématique des différentes étapes d'analyses faites durant cette thèse.

Le protocole analytique présenté dans ces travaux est résumé dans la figure 5, il consiste en deux études respectives :

1) L'étude *in situ* des éléments sidérophiles réfractaires et volatiles dans les phases métal et sulfure des chondrites H et CB par spectrométrie de masse à plasma induit couplée à l'ablation laser (LA–ICP–MS)
2) L'étude du fractionnement isotopique du germanium dans les phases métal, sulfure, silicate ainsi que dans le bulk de chondrites ordinaires H, L et LL, par spectrométrie de masse à multi-collection (MC–ICP–MS)

Dans le cadre des mesures par LA–ICP–MS, les échantillons sélectionnés ont été montés en section polie afin de mener une étude pétrologique et minéralogique au microscope optique. Cela nous a permis de définir les proportions de métal, de sulfure et de silicate présentes dans les différents échantillons de météorites étudiées, mais aussi de choisir les grains de métal et de sulfure à analyser. Ensuite, des cartes élémentaires ont été produites par microscopie électronique à balayage (MEB) afin de préciser l'identification des différents minéraux. L'analyse *in situ* des

éléments chimiques majeurs et mineurs dans les grains de métal et de sulfure a été faite par microsonde électronique et par Spectrométrie de masse à plasma induit couplée à l'ablation laser (LA-ICP-MS).

Pour les analyses isotopiques du germanium, les échantillons ont été nettoyés par *leaching* dans des bains d'acide dilué, puis ensuite rincée à l'eau distillée et à l'acétone. Ils ont ensuite été réduits en poudre précautionneusement. Une partie des poudres obtenues a été utilisée pour en séparer les différentes phases minérales. Le métal a été séparé des silicates avec un aimant, et les sulfures ont été séparés à la main sous une loupe binoculaire. Chaque phase fut par la suite dissoute, et a suivi un protocole chimique de purification du germanium sur résine échangeuses d'ions, ce protocole est spécifique à chaque type de matrices et décrit en détail par Luais (2012). La mesure des compositions isotopiques en germanium des solutions obtenues après chimie a été faite par spectrométrie de masse à multi-collection.

III. Résultats

1 Processus de formation du métal par condensation

Une première étude sur la condensation du métal a été menée sur les chondrites carbonées de types Bencubbin (CB). Ce projet combine des analyses élémentaires *in situ* par LA–ICP–MS et des mesures de la composition isotopique en germanium des billes de métal de ces météorites. Les résultats de cette étude sont présentés dans le chapitre 3 et font l'objet d'un article scientifique intitulé « The formation of CB chondrites : inferences from germanium isotopes and highly siderophile element abundances » soumis à *Meteoritical & Planetary Sciences*.

Les chondrites CB sont divisées en deux groupes, les CB_a et les CB_b. Ces météorites sont caractérisées par un pourcentage élevé de grains de métal (~60 à 80 vol%) ainsi que par une absence de matrice. Ces grains de métal sont particulièrement intéressants, car ils n'ont pas été métamorphisés et présentent des compositions élémentaires caractéristiques d'une formation par condensation (Anders and Grevesse, 1989 ; Weisberg et al., 1990, 1995). Cependant, des études récentes ont montré que leurs compositions élémentaires ne correspondaient pas à une formation à partir du gaz composant le disque protoplanétaire bien que sa composition en soit très proche (Campbell et al., 2002). Ces grains de métal présentent aussi un appauvrissement atypique en élément volatil (e.g. Ge, Ga, Campbell et al., 2002). De plus l'âge de formation de ces objets suggère qu'ils se sont formés après la dissipation du gaz présent dans le disque d'accrétion (~ 4.2 Ma after CAIs, Bollard et al. 2015 ; Krot et al. 2005 ; Marty et al. 2010 ; Zhu et al. 2019). Le modèle actuel suggère que ces météorites se sont formées à la suite d'un impact entre deux corps parents (Kallemyn et al., 2001 ; Weyrauch et al., 2019). Cependant les modélisations numériques

ne permettent pas d'expliquer les compositions élémentaires et isotopiques de tous les constituants des CB (Fedkin et al., 2015). Par ailleurs, ce modèle de formation a été défini sur la base d'éléments réfractaires (e.g. Re, Os, Ir etc.) ou de volatilité intermédiaire (e.g. Fe, Ni), et peu d'attention a été portée aux éléments modérément volatils. Dans le chapitre 3 nous examinons les compositions isotopiques du germanium, élément modérément sidérophile et volatil, ainsi que les variations élémentaires dans les grains de métal des CB.

Les objectifs de cette étude sont triples. Dans un premier temps, il s'agit d'évaluer l'effet de la condensation sur le fractionnement isotopique du germanium, dans un second temps de contraindre la condensation du métal à température intermédiaire (~900 – 800 K) dans des conditions proches de celles du disque protoplanétaire, et enfin d'identifier les processus successifs et dynamiques de formation des CB.

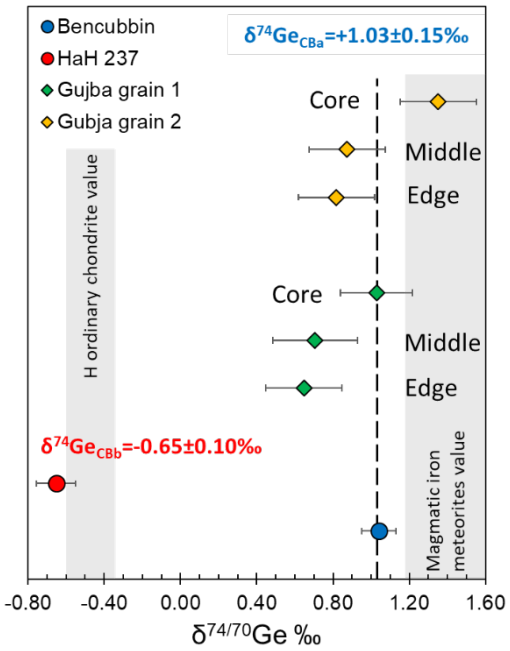

Figure 6: Variations des compositions isotopiques du germanium ($\delta^{74/70}$Ge) des CB.

Dans la première partie de cette étude, nous avons caractérisé les compositions isotopiques en germanium ($\delta^{74/70}$Ge) dans le métal des CB_a (Chondrites Carbonées Bencubbinite de type a) et des CB_b (Chondrites Carbonées Bencubbinite de type a). Nous montrons que les deux groupes, CB_a ($\delta^{74/70}Ge_{moyenne}$ = +0.97 ± 0.2‰, 2σ SD) et CB_b ($\delta^{74/70}$Ge = -0.65 ± 0.1‰, 2σ SD) peuvent être distingués par leurs compositions isotopiques en germanium, et que cette variabilité est liée à des différences de taux de refroidissement (Fig. 4). Nous proposons donc que la formation des CB_a se fait à des taux de refroidissement plus faibles que pour les CB_b. Les études précédentes montrent que les CB se forment potentiellement dans un panache ou « plume » de gaz formé par évaporation lors d'impact (Weyrauch et al., 2019). Si tel est le cas, nos observations impliquent que ce « plume » doit être zoné thermiquement. Par conséquent, nous proposons que

les CB_a se forment dans la zone la plus chaude (intérieur du « plume ») et les CB_b dans la zone la plus extérieure où la température diminue rapidement.

Dans la deuxième partie, nous avons dissous séquentiellement deux grains de métal parfaitement sphériques séparés de la météorite Gujba (CB_a). Les résultats montrent une diminution de la composition isotopique en Ge depuis le cœur des grains jusqu'à leurs bordures (e.g. $\delta^{74/70}Ge = 1.03 \pm 0.19‰$; $0.71 \pm 0.22‰$; $0.65 \pm 0.20‰$, 2σ SD). Ces variations sont positivement corrélées avec la diminution de la concentration en germanium depuis leurs cœurs jusqu'à leurs bordures (Fig. 5). Nous proposons que ces variations soient le résultat de processus d'évaporation et de recondensation durant la formation de ces grains de métal. Le scénario suivant est suggéré pour expliquer la formation des larges grains de métal dans les CB_a :

1) Le cœur des grains de métal se forme par condensation à l'équilibre.
2) Ces cœurs migrent dans une zone plus chaude ou ils subissent une évaporation partielle du germanium, ce qui augmente leurs compositions isotopiques et diminue celle du gaz environnant.
3) À cause de la pression de gaz importante ainsi que de la présence de grains de métal déjà formés, les cœurs vont agir comme des nucléus, sur lesquels vont se recondenser du métal, inhibant l'évaporation totale du Ge.
4) Cette couche extérieure va par la suite enregistrer la composition isotopique plus faible du gaz, expliquant la diminution du $\delta^{74/70}Ge$ du cœur aux bordures.

Cette étude démontre la capacité des isotopes du germanium à enregistrer les étapes ultimes de la condensation du métal, ce que les éléments avec des températures de condensation plus élevées (Ex. Fe, Ni) ne permettent pas.

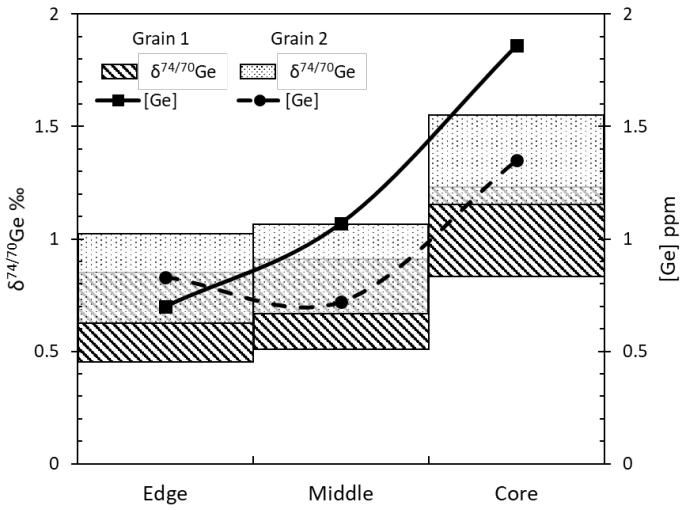

Figure 7 : Représentation de l'évolution de [Ge] et $\delta^{74/70}Ge$ dans les deux grains analysés. Les pourcentages correspondants aux différentes fractions dissoutes sont donnés en table 3.2.

2 Processus de chauffe avant et après accrétion

Cette seconde étude s'intéresse à la diversité de composition du métal et des sulfures dans les chondrites ordinaires de types H. Lors de ce projet, des analyses élémentaires *in situ* par LA–ICP–MS dans des grains de métal et de sulfure dans des chondrites de types H, à tous les stades du métamorphisme, ont été étudiées. Les résultats sont présentés dans le chapitre 4 sous la forme d'une version d'un manuscript à soumettre, et intitulé « Siderophile element composition of the metallic phases in H ordinary chondrites, formation and evolution ».

Les chondrites ordinaires de type H sont des objets non différenciés composés de métal, sulfure et de silicate. Elles sont subdivisées en groupes pétrologiques de H3.0 à H3.9 (les plus primitives, dites non équilibrées) puis de H4 à H6, le groupe 6 représentant les plus métamorphisés, Tait et al, 2014). La provenance du métal dans ces météorites est sujette à débat, et aucun consensus clair n'existe. Il a été proposé que le métal peut se former par réduction de FeO présent dans des silicates (Kong and Ebihara, 1997), par le mélange de deux types de métal formés séparément dans le disque protoplanétaire (Horan et al., 2009), durant des évènements de chauffe dans le disque (Campbell and Humayun, 2003 ; Okayabashi et al., 2019), ou par désulfurisation de sulfures (troïlite FeS) (Hewins et al., 19997). Le but de cette étude est de combiner éléments volatils et réfractaires, afin de décrire la formation et l'évolution du métal dans les chondrites ordinaires de type H.

Nous montrons qu'il existe dans ces météorites des variations de concentration importantes en éléments volatils et réfractaires d'un grain de métal à l'autre, en accord avec les études précédentes (Campbell and Humayun, 2003). Par ailleurs, dans les chondrites H non–équilibrées, les concentrations en éléments réfractaires des grains de métal sont corrélées avec le rapport Ge/Ir. Ces corrélations s'atténuent avec l'augmentation du métamorphisme, ce qui signifie qu'elles sont le résultat de processus pré-accrétionnaires. Elles peuvent être modélisées par la fusion partielle de précurseurs métalliques enrichis en carbone à hauteur de 5.2 %. Cependant ce modèle ne nous permet pas d'expliquer les compositions très variables de W, Mo et Ga dans les H3. Nous proposons donc que les variations de W, Mo et Ga reflètent une variation de l'état d'oxydation à l'échelle du grain. Une possibilité pour produire ces changements d'état d'oxydation locale est l'évaporation de particules riches en composés oxydants (e.g. phyllosilicates), répartis de manière hétérogène au sein des précurseurs du métal et des silicates dans le disque. De ce fait, pendant un évènement de chauffe dans le disque l'évaporation, des fractions variables d'agents oxydants vont produire une variation locale (de grain à grain) de l'état d'oxydation, indépendant de celui du disque (Fegley and Palme, 1985). Dans ces conditions, plus une zone sera riche en agents oxydants, plus W, Mo et Ga seront incorporés dans les silicates par rapport au métal. Cette hypothèse permet par ailleurs d'expliquer les larges gammes de variation de %Fa dans les météorites très primitives (<H3.4) comparé aux équilibrées (de H4 à H6).

Les compositions très similaires en élément sidérophiles réfractaires et modérément volatiles entre les groupes de chondrites ordinaires (Fig. 8) suggèrent que cette composition n'a pas évolué après la formation du métal dans le disque. Cela implique que la différence de pourcentage de métal contenu dans les H, L et LL n'est pas le résultat de processus chimique dans le disque, mais résulte plutôt d'une répartition mécanique après la formation du métal. Cela suggère que les précurseurs du métal étaient similaires entre les trois groupes.

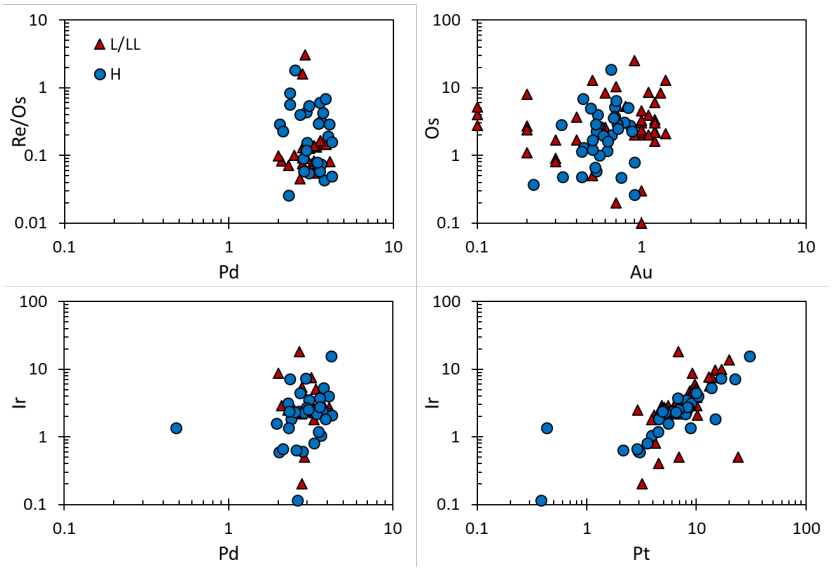

Figure 8 : Composition en éléments sidérophiles dans les chondrites H (cercle bleu) et L–LL (triangle rouge). Les valeurs de concentrations sont en ppm, Données de L et LL d'après Okabayashi et al. (2019).

3 Rôle des processus oxydants sur l'évolution du métal

Le rôle et les conséquences des processus d'oxydation sur le métal ont été explorés en analysant les compositions isotopiques du germanium dans les phases métal, sulfure et silicate des chondrites ordinaires H, L et LL par MC-ICP-MS (Neptune*Plus*, CRPG-Nancy, France). Ces travaux ont fait l'objet d'une publication : G. Florin, B. Luais, T. Rushmer, O. Alard (2020). Influence of redox processes on the germanium isotopic composition of ordinary chondrites. *Geochimica et Cosmochimica Acta* **269**:270–291.

Dans cette étude, nous montrons que les différents groupes de chondrites ordinaires peuvent être distinguées par la composition isotopique en germanium de la phase métal qui augmente du groupe H à L puis LL ($\delta^{74/70}Ge_{metal}$ = –0.51 ± 0.09‰ ; –0.31 ± 0.06‰ ; –0.26 ± 0.09‰, 2σ SD, respectivement). Les valeurs du $\delta^{74/70}Ge$ du métal et de l'échantillon bulk sont corrélées avec l'augmentation du $\delta^{18}O$, $\Delta^{17}O$ et %Fa des groupes H, à L et LL (Fig. 9). Nous proposons que ces corrélations soient le résultat de l'accrétion d'un agent oxydant ayant des compositions en $\delta^{74/70}Ge$, $\delta^{18}O$, et $\Delta^{17}O$ élevées. Pendant le métamorphisme sur les différents corps parents, le germanium ainsi que l'oxygène vont être libérés par le composé oxydant. Le fluide résultant va alors oxyder le métal et augmenter la composition isotopique du Ge dans le

métal. L'oxydation du métal va donc provoquer la formation d'oxyde de fer avec une composition isotopique en oxygène élevée, et l'incorporation de FeO dans les silicates. Le fait que le composé oxydant contienne des proportions significatives de Ge implique qu'il ne peut pas s'agir d'eau ou de glace, mais plutôt d'un minéral hydraté tel que des phyllosilicates. Cette étude a aussi permis de mettre en avant un fractionnement isotopique métal-silicate de Ge ($\Delta^{74/70}Ge_{métal\text{-}silicate}$) positif. Finalement, nous montrons que l'utilisation combinée des traceurs isotopiques $\delta^{74/70}Ge_{métal}$ et $\Delta^{17}O_{silicates}$ permet d'établir des liens génétiques forts entre les chondrites ordinaires et les météorites de fer IIE.

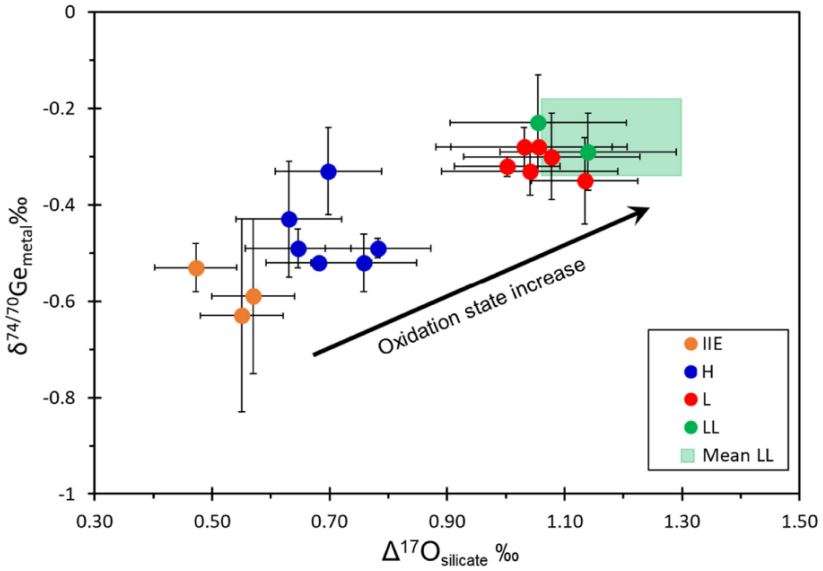

Figure 9 : Composition isotopique en germanium *vs* l'anomalie en oxygène pour le « old group » des météorites de Fer IIE, et les chondrites ordinaires H, L et LL. Le rectangle vert représente la composition moyenne des LL. La corrélation positive mise en évidence depuis les météorites de Fer IIE vers les chondrites ordinaires LL démontre que les IIE se seraient formés sur un corps parent distinct et plus réduit que celui des chondrites H.

Chapter 1

Introduction

Table of contents

I. Cosmochemistry, What? Why? How?

1 Introduction

In the present state of our knowledge, the Universe can be divided into visible matter and invisible matter, the dark matter. The visible matter is composed of particles named atoms that are classified in elements denpending on their characteristics: mass, number of neutrons, protons and electrons. In Earth and Planetary Sciences, the study of these elements, their properties, their assemblages (molecules) and their interaction is called chemistry or geochemistry. This science aims at highlighting elemental and isotopic behaviour during geological processes.

Cosmochemistry is a branch of the geochemistry focused on the chemical composition of the Universe and the Solar System. The main goal of this science is to understand how planetary systems, as well as the Solar System itself, with its star, planets, satellites, asteroids, comets and meteorites, have been formed. In order to do that, the cosmochemist uses telescopes, space probes, experiments and elemental and isotopic measurements in the laboratory to examine natural objects from the Solar System. These methods aim at extracting the chemical information recorded by these objects during their formation in order to reveal the processes that occurred in the Solar System and thus to determine the chronology of these events.

Samples that we have at our disposal consist in primitive and differentiated meteorites, samples returned from space missions (e.g. *Apollo* and *Luna missions*, or *Star Dust*), material created by impacts on Earth likes tektites and experimental assemblages produced in laboratory.

The scope of this PhD is to study the early stage of metal formation and its evolution. We have focused our efforts on chondrites (primitive meteorites) as they offer an open window on the first processes occurring in the protoplanetary disk.

2 Meteorite diversity

Meteorites are pieces of planetesimals, and planets formed during the course of our Solar System history. They can be falls on Earth, other planets, satellites, and more broadly on the surface of any object in our solar system and can be evidenced from observable craters. Various mechanisms of meteorite formation are possible. Some may have been formed by a giant and disruptive collision between asteroids, originating from the asteroid belt between Mars and Jupiter. Other meteorites appear to come from planets (e.g. Mars), or moons (Earth's Moon), and are ejected during major impacts on the surface of these objects.

Rose, (1863), Tschermak (1883) and Brezina (1904) have established the first mineralogy and textural-based meteorite classification called the "Rose-Tschermak-Brezina classification". A few decades later, a chemistry-based classification was established (Farrington, 1907; Prior, 1916, 1920; Mason, 1967). Since 1950, many scientific papers have been published on meteorite classification (e.g. Kallemeyn and Wasson, 1981; Kallemeyn *et al.,* 1989, 1991, 1994 etc.). The current classification is based on petrologic evidence as well as the elemental and isotopic compositions of bulk materials and minerals.

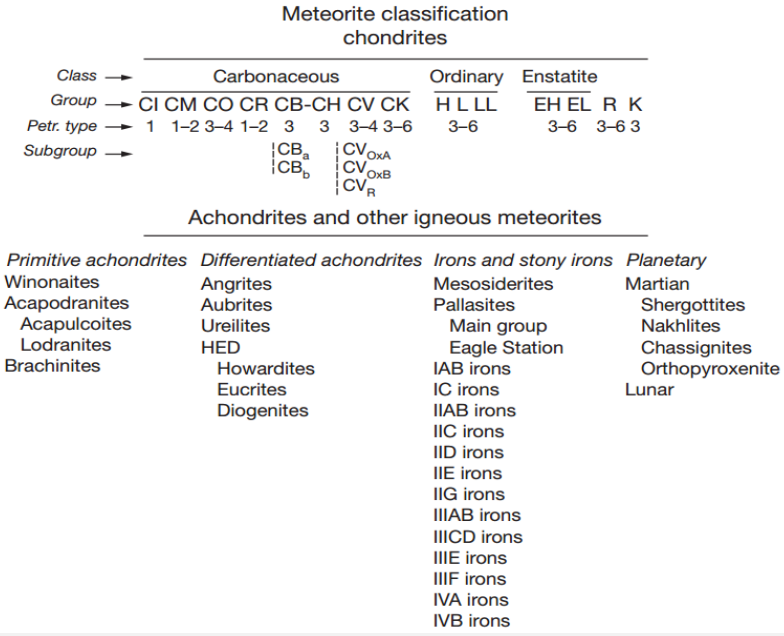

Figure 1.1:Meteorites classification after Krot et al. (2014).

Meteorites are classified into two groups the chondrites and the non-chondritic meteorites (Fig. 1.1). These two groups are subdivided into different classes based on their chemical compositions, oxygen isotopes, mineralogy and petrography (Van Schmus et al., 1967).

2.1. Overview of chondrites characteristics

Chondrites are an agglomerate of particles heterogeneously repatriated and cemented by a fine-grained matrix enriched in light elements. The chondrites are named after one type of these particles called chondrules, small droplets of silicates mostly composed of olivine, pyroxene and some metal. The chondrites also contain various proportions of metal and sulfide nodules, high condensate phases, the refractory inclusion (CAIs or AOAs) and presolar phases (SiC). Their compositions highly suggest that they did not undergo metal–silicate segregation during heating events and consequently can be defined as undifferentiated objects. The repartition of these components and their compositions determine how chondrites are classified into different groups such as CB, H, L, LL etc. (Table 1.1).

Table 1.1: principal petrographic characteristics of chondrites groups

Chondrite clan	Meteorite groups	Metal (Vol%)	Chondrule (vol%)	Matrice (vol%)	Refracory incl.
Carbonaceous	CI	<0.01	<5	95	<1
	CK	<0.01	15	75	4
	CM	0.1	20	70	5
	CV	0-5	45	40	10
	CO	1-5	40	30	13
	CR	5-8	50-60	30-50	0.5
	CH	20	~70	5	0.1
	CB	60-70	30-40	<5	<0.1
Ordinary	LL	1.5	60-80	10-15	<0.1
	L	3	60-80	10-15	<0.1
	H	8	60-80	10-15	<0.1
Enstatite	EH	8	60-80	<0.1-10	<0.1
	EL	15	60-80	<0.1-10	<0.1
Others	R	<0.1	>40	35	<0.1
	K	6-9	20-30	70	<0.1

Data from Scott and Krot (2014) and Jarosewich (1990)

2.2. Non-chondritic groups and relations with chondritic ones

The non–chondritic group is much more diverse but is mostly characterised by the absence of chondrules within meteorites, with the exception of some relics chondrules in non-magmatic iron meteorite groups (e.g. IIE, IAB, IIICD, Van Roosbroek et al., 2015). These objects are at different stages of differentiation. The Primitive achondrites contain metal and large silicate crystals, they represent a very advanced – but incomplete – stage of differentiation triggered to radiogenic melting[1] or impact (e.g. Winonaïtes: Benedix et al., 2000; Wasson and Kallemeyn, 2002; Brachite: Warren and Kallemeyn; 1989; Acapodranite: Krot et al., 2014). On the other hand, the achondrites and iron meteorites are the witness of the last stage of planetesimal differentiation and represent respectively the mantle and the core of planetesimals. (Prinz et al., 1983; Scott and Wasson, 1975).

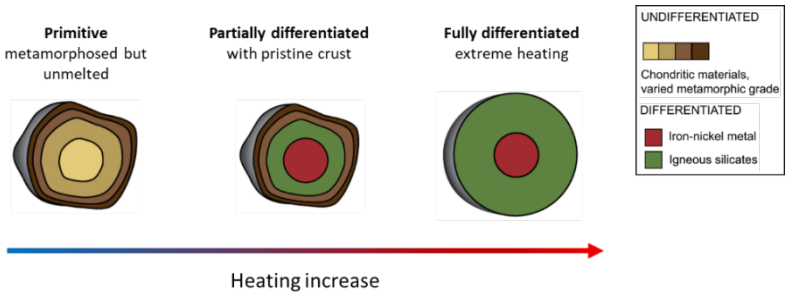

Figure 1.2: Example of the differentiation of a planetesimal with temperature increase. Figure modified after Elkins–Tanton, 2017.

The relationship between chondritic and non–chondritic objects has been theorised since the beginning of cosmochemistry (Urey, 1955). The most commonly accepted theory suggests that after the accretion of chondrites, and under the influence of radiogenic heating (^{26}Al and ^{60}Fe decay, Elkins–Tanton, 2017 and reference therein; Monnereau et al., 2013, see part 1.2), or

[1] Radiogenic melting is the result of the increase of temperature on planetesimals after their accretions due to the radiogenic decay of ^{26}Al and ^{60}Fe isotopes (Urey, 1955).

impact (Tomkins et al., 2013, see part 1.3), the metal and the silicates contained in primitive objects (*i.e.* Chondrites) have been segregated to form a silicate mantle and a metallic core (Fig. 1.2). Through the migration of metal within the planetesimal that leads to core formation, the structure and the composition of planetesimals drastically changed. These changes need to be assessed to constrain the formation of planets in the Solar System.

Therefore, to fully describe how planetesimals and planets formed, it is necessary to understand the formation and the evolution of metal grains in the Solar System.

In the following parts of this introduction, focus is placed on previous studies on metal to demonstrate the importance of: (1) its formation (developed in **Chapter 3**); (2) its evolution in the solar nebula (developed in **Chapter 4**); (3) the effect of oxidation that modified its composition (developed in **Chapter 5**); (4) and finally the effect of oxidation on metal migration in parent bodies (developed in **Chapters 4 and 5**).

II. The study of metal in cosmochemistry

Iron is one of the major components of our Solar System. When oxidised, it occurs in sulfide (FeS) or silicate (Fe_xO_y) and in the form of FeNiCo alloy when reduced (note *FeNi* or *metal* in the rest of the chapter). Three types of FeNi minerals have been described relative to the Ni% in the alloy, kamacite and taenite (Ni < 10% and Ni > 10%, Roming and Goldstein, 1980) and tetrataenite (57% > Ni > 48%, Clarke et Scott, 1980). Many different types of meteorites contain metal, that is, after silicates the most abundant mineral phase in the Solar System. In most chondrite groups iron concentrates up to 95% of chondritic metal (e.g. CH chondrites). When metal is not the main phase, Fe is mainly in silicate phase and for CI is distributed between FeS, silicate phases and Fe3O4 for the other carbonaceous groups (Fig. 1.3, Campbell et al., 2005). This suggest that the relationship between the percentage of oxidised iron (Fe_{oxides} + FeS) vs metallic iron is one of the major characteristics of the classification of the chondrite groups (Urey and Craig, 1953).

Processes leading to a variation in the metal percentage is mainly iron oxidation or reduction. It can result from – but is not restricted to – metal oxidation, sulfurization or silicate reduction in the solar nebula or on meteorite parent bodies (Campbell et al. 2005). The level and nature of these processes vary between groups of chondrites and are highly characteristic of their environment of formation. For example, due to its lower temperatures and higher water content, the outer solar system is more oxidised than its inner part and objects that formed close to the sun are supposed to have a higher FeNi content compared to those formed farther from the star

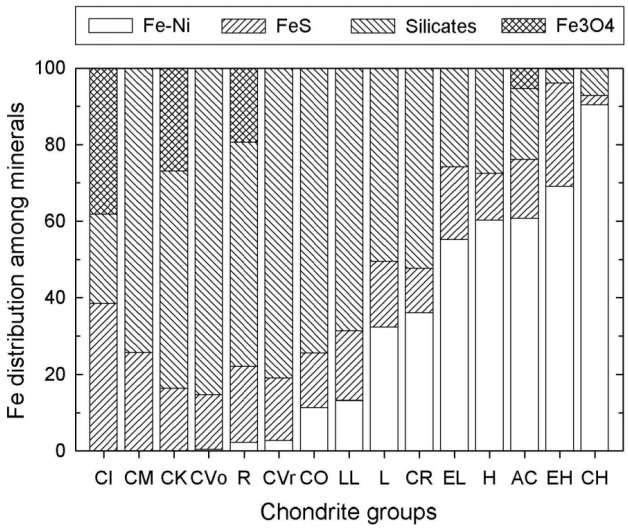

Figure 1.3: Major phases in some chondrite groups and acapulcoite (AC) and the repartition of iron within them, after Campbell et al. (2005) and Koblitz (2010).

Regarding the large proportion of metal in chondritic groups (Fig. 1.3), it is likely that the metal phase has played a major role in the chemical fractionation of the siderophile elements

from lithophile or chalcophile[2] ones. Thus, the study of the metal phases is of major interest to understand how it influences the formation and the evolution of the different objects in the Solar System. At first glance, the iron seems to be the best element to study metal evolution through time. However, its multiple species are such that it is very difficult to de-convolute its repartition between the different mineral phases. Therefore, to understand and track specific processes that affect the metal and to reveal its history, other elements are needed.

It raises the question of the elements that should be used to study the metal phase. To study metal geochemistry we can first focus on iron meteorites as they represent the majority of metal occurrence in the early Solar System.

1 Elemental composition of iron meteorites

The iron meteorites are composed of a FeNi alloy containing between 5 and 60% of Ni and minor amount of Co (0.4 to 0.8 wt%), as well as sulphur, phosphure and carbon in the form of troilite (FeS), schreibersite ($(Fe,Ni)_3P$) and Fe–Ni carbides (e.g. cohenite $(Fe,Ni)_3C$), respectively (Scott and Wasson, 1975). Through a series of 12 scientific papers entitled *"The Chemical Classification of Iron Meteorites"* Wasson and collaborators have used volatile and refractory siderophile elements to classify and describe the processes that lead to the formation of iron meteorites.

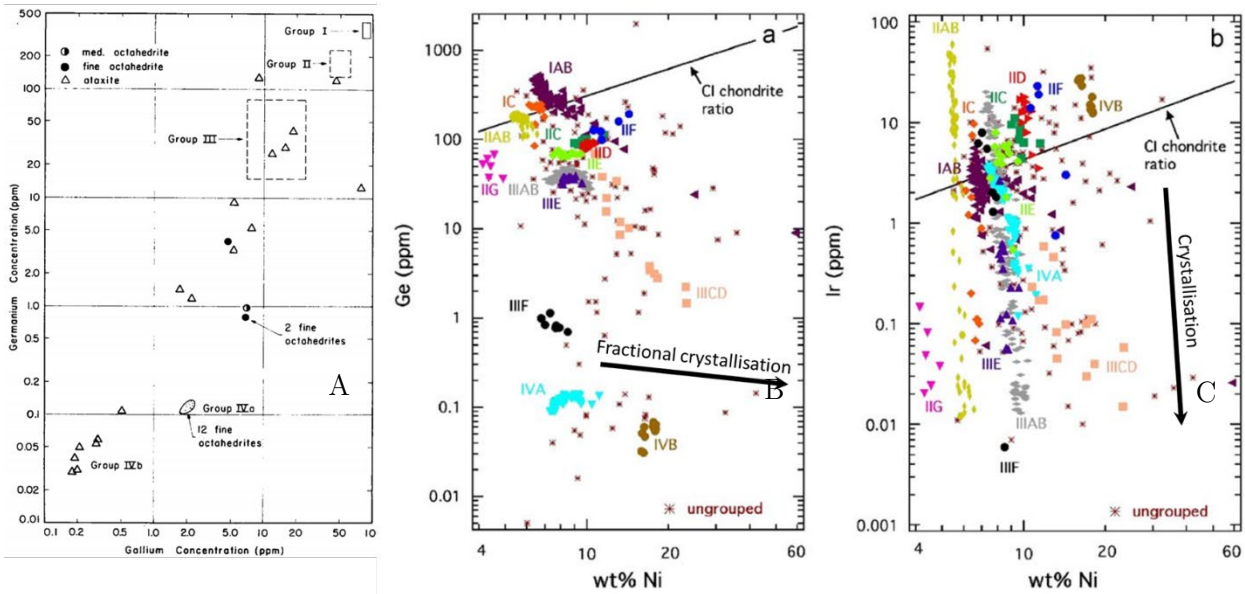

Figure 1.4: Classification of iron meteorites based on siderophile elements (Ge, Ir and Ni) (Wasson, 1967; Goldstein et al., 2009) after J.T. Wasson data collected from 1967 to 1998.

[2] Siderophile elements have affinity with iron; Lithophile with silicon; Chalcophile with sulfide.

Based on refractory Ni and volatile Ge – Ga elements, iron meteorites were first classified into four groups from high to low Ge – Ga content: I, II, III, IV, respectively (Lovering et al., 1957; Wasson 1967). As Germanium and Ga are siderophile elements they are very useful for the study of the metal. Then, they are highly partitioned during metal-silicate segregation (core formation) and not significantly fractionated between solid and liquid metald during core solidification. As a result, Ge and Ga concentrations define a very narrow range within iron meteorite groups (of a factor ~2.5 log units) whereas their concentrations vary on ~4 log units between the entire iron groups (1.4 A). New data has shown a very large range of siderophile concentrations between and within iron meteorite groups (Fig. 1.4 B, C). Thus, the four groups I, II, III, IV, have been latterly subdivided into 14 clusters mostly according to their Ga, Ge and their Ir, Au and Sb contents.

This classification (*i.e.* I-IV) has led to the recognition of two different types of iron meteorites, the magmatic and the non –magmatic groups (Wasson, 1985). The magmatic one regroups the IIAB, IID, IIIAB, IVA, IVB groups and possibly the IC and IIIF groups. Magmatic iron meteorites have chemical composition trends that can be modelled through fractional crystallisation laws using experimental solid/liquid partitional coefficients (Chabot and Jones, 2003, Chabot and Haack, 2006). This suggests that a process of chemical fractionation is taking place during cooling and the crystallisation of metal melt in depth (FeNi ± S, C, P). These magmatic iron meteorties are therefore considered to be proxies for the metallic core of planets (Haack and McCoy, 2004). Additionally, the elemental behaviour of siderophile elements changes according to the proportion in light elements (i.e. S, C, P) in the metal (Chabot et al. 2017), thus, it is possible to infer the composition of the starting material of these metallic phases. On the other hand, the non – magmatic (iron meteorite included) the IAB, IIICD and IIE groups. In these groups, silicates are much more abundant, and siderophile trends cannot be model fractional crystallisation (Chabot and Jones, 2003). The formation of the non–magmatic groups is much more complex. Wasson and Kalemeyn (2002) proposed that impact processes on subsurface of chondritic porous parent bodies (chondritic or partially differentiated) induce partial melting and the segregation of pools of liquid metal (Choi et al, 1995; Wasson and Kallemeyn, 2002). In the case of the IIE group, the variations in Ge, W, Ir and Niindicate that it was formed by an impact on non–solidified parent bodies resulting in the formation of metal melt pools and partial evaporation of metal (Luais, 2007, Wasson, 2017).

The decades of studies on siderophile element in iron meteorites have highlighted their use in describing the formation and the evolution of metallic phases. From an elemental point of view, it appears that Ge, Ga, Au and refractory elements (e.g. Ir, Os, Re, Pt) are the best tracers to understand the formation and evolution of metal. In addition to elemental compositions, isotopic compositions also bring important information on the processes that affect the metal in the early ages of the Solar System.

2 Germanium and its isotopic fractionation in iron meteorites

The term isotope refers to two or more forms of a same element that share the same number of protons – characteristic of that element – but a different number of neutrons in their nucleus, such that their masses are different. Isotopes can be classified into radiogenic isotopes or stable isotopes. The latter are not produced by any radioactif decay (e.g. ^{74}Ge) and have a half–life that is too short to produce significant fractionation >10^9yrs (e.g. ^{76}Ge) (Johnson et al. 2004). Stable isotopes are historically classified between *traditional* and *non–traditional isotopes*. The former refers to "light elements" (H, C, N, O and S) that were first studied as they can be conveniently converted into gas form for analysis, and their large natural isotopic fractionation have been possible to be detected at the beginning of the stable isotope geochemistry instrumentation (Weiderhold, 2015). The term *non–traditional* stable isotopes refers to heavier elements corresponding to metal (e.g. Fe, Ni, W, Mo), metalloids (e.g. Ge, Si) or transition metals (e.g. Ga). The first analytical techniques were not able to resolve their small fractionation in natural samples, they were thought to be too heavy to fractionate significantly (Johnson et al. 2004). However, the last two decades of analytical developments, using the multi-collector inductively couple plasma mass spectrometer (MC-ICP-MS) has enhanced *non–traditional* stable isotope analysis to most of the periodic table, allowing discoveries of prime importance in cosmochemistry.

2.1. Theory of mass dependent isotopic fractionation

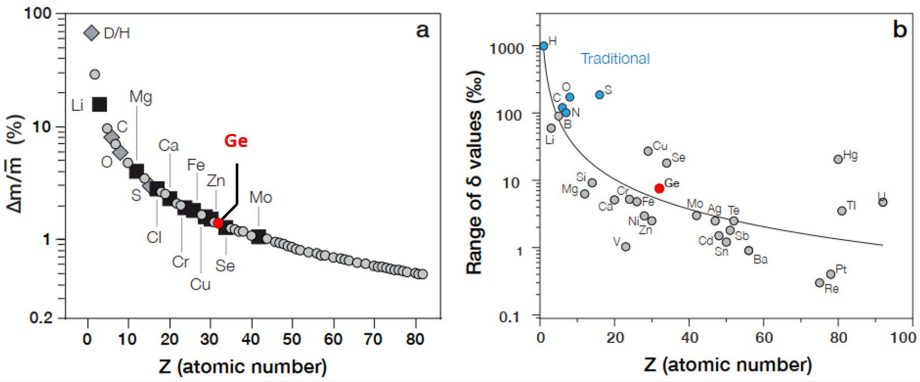

Figure 1.5: A) Difference in mass for elements that have two or more isotopes in function of the atomic number. Δm is the unit mass difference and m̄ the average mass of all the isotopes of a considered element (Johnson et al. 2004). B) range of delta value compared to the mass fractionation trend (from Belissont, 2016, after Weiderhold, 2015). Germanium, the element of interest in this thesis, is highlighted in red.

Mass dependent fractionation of stable isotopes describes the range of isotopic compositions for an element as a function of the mass difference between two considered isotopes (Fig. 1.5 a). The large relative difference in mass of light elements (e.g. H vs D, the difference is close to 100%) is expected to produce large mass fractionation, whereas the small relative difference in mass for heavy ones produces smaller isotopic fractionation (Fig. 1.5 b). Stable isotope fractionation is influenced by different parameters: (1) the nature and the length of the

atomic bonds, which are the most important parameter; (2) the crystal structure; (3) the redox state of the elements, heavy isotopic composition correlates with high oxidation state (e.g. Schauble, 2004); (4) relative changes in temperature (Richter, 2004). It should be noted that mass independent fractionation also exists and has been highlighted for the first time in meteorites and Ozone (Clayton et al., 1973; Thiemens and Heidenreich, 1983), but is out of the scope of this thesis.

The respective difference (i.e. isotopic fractionation) between two isotopes in a sample is usually noted in delta unit (δ ‰) and is expressed in function of a reference standard (Equation 1.1).

$$\delta^{x/y}E_{Standard} = \delta\ {}^{x}E/{}^{y}E = \left(\frac{({}^{x}E/{}^{y}E)_{Sample}}{({}^{x}E/{}^{y}E)_{Standard}} - 1\right) * 1000 \qquad \text{Eq. 1.1}$$

With E the element of interest, x and y two different masses of this element. The δ value therefore reports the relative variation of the isotopic ratio of the sample with respect to the standard, such that negative δ values are found for a sample enriched in light isotopes compared to the standard, and positive δ values for an enrichment in heavy isotopes. This method allows isotopic ratios to be compared between laboratories. The use of a specific standard for a given element usually results from a consensus in the scientific community. NIST 3120a standard is the recommended standard for Ge (Luais, 2012; Escoube et al., 2012).

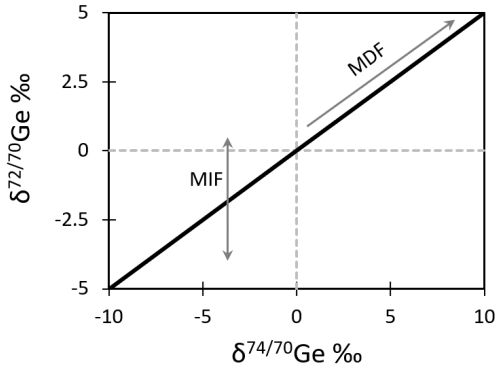

Figure 1.6: Example of mass dependant fractionation (MDF) for $\delta^{72/70}$Ge vs $\delta^{74/70}$Ge, symbolised by the black line. MIF: mass independent fractionation, shown as an example.

Due to mass fractionation, two isotopic ratios of the same element fall on a line (Fig 1.6) described by the equation 1.2, where E is the element of interest, x, y and z mass of the different isotopes with x<y<z:

$$\delta^{y/x}E \approx \left(\frac{y-x}{z-x}\right) * \delta^{z/x}E \qquad \text{Eq. 1.2}$$

The relative fractionation between two minerals at equilibrium is mostly a function of the crystalline nature of these two components (Rouxel and Luais, 2017), and can be approximated by *ab–initio* quantum chemistry calculations (see Li et al., 2009, for Ge). They suggest that the enrichment in light or heavy isotopes is inversely proportional to the atomic bond lengths. . For example, theoretically, in a metal–silicate assemblage at equilibrium, the silicate would be enriched in heavy germanium isotopes (Ge–Si ~1.760 Å) while the metal would be enriched in light ones (Ge–Fe ~2.494 Å, Cavell et al., 2004; Rouxel and Luais, 2017). The

fractionation of an isotopic ratio $R^{i/j}$ between two phases A and B can be expressed as the fractionation factor α (Equation 1.3):

$$\alpha_{A/B} = \frac{R_A^{i/j}}{R_B^{i/j}} \qquad \text{Eq. 1.3}$$

It can be expressed as a function of the delta value in the following way (Equation 1.4 and 1.5):

$$\alpha_{A/B} = \frac{1000 + \delta^{i/j}E_A}{1000 + \delta^{i/j}E_B} \qquad \text{Eq. 1.4}$$

$$1000 \ln \alpha_{A-B} = \delta^{i/j}E_A - \delta^{i/j}E_B \equiv \Delta_{A-B} \qquad \text{Eq. 1.5}$$

Isotopic fractionation can be divided into kinetic and equilibrium fractionation. At equilibrium, experimental studies describe the fractionation between two phases as two linear curves inversely proportional to the square of the temperature (Fig. 1.7 A), with A and B two experimental parameters (Equation 1.6):

$$1000 \ln \alpha_{A-B} = \frac{A}{T^2} + B \quad \text{Eq. 1.6}$$

A change in reaction rate (e.g. a quick increase or decrease in temperature) affects the isotopic composition of the two phases, leading to a partial and unidirectional repartition of the isotopes. Kinetic effect on isotopic fractionation between two reservoirs is commonly described using the Rayleigh distillation law, expressed as (Equation 1.7):

$$R = R_0 f^{\alpha-1} \qquad \text{Eq. 1.7}$$

with R the isotopic ratio of interest, R_0 its initial isotopic composition, f the remaining fraction of the substance in the source and α the kinetic fractionation factor between the two phases A, B defined as (Equation 1.8):

$$\alpha_{A-B} = \frac{D_i}{D_j} = \left(\frac{mass\ i}{mass\ j}\right)^{\beta} \quad \text{Eq. 1.8}$$

where i, j are two isotopes of a given element with $m_i < m_j$, β an empirical parameter (Bearman and Jolly, 1981) equal to 0.5 in a pure Rayleigh fractionation and defined as the slope in a diagram of $\log(D_i/D_j)$ vs $\log(m_i/m_j)$ with D_i and D_j the diffusion coefficient of *i* and *j*. The equivalent δ isotopic fractionation for Ge, for example, can then be calculated using the equation 1.9:

$$\delta^{74}Ge_f = \left[\left(1000 + \delta^{74}Ge_0\right) * f^{(\alpha-1)}\right] - 1000 \quad \text{Eq. 1.9}$$

where $\delta^{74}Ge_f$ is the final isotopic composition and $\delta^{74}Ge_0$ the initial isotopic composition. The difference between a closed system at equilibrium and Rayleigh fractionation is shown in Figure 1.7 A. An example of pure theoretical Rayleigh fractionation that occurs during Germanium evaporation from different minerals (metal, silicate, and sulfide) or liquid is given in Figure 1.7 B.

During the mixing of n different reservoirs, the isotopic composition of the $\delta^{x/y}E_{mix}$ mix can be calculated as the composition of each reservoir weighted by their respective proportions x (Equation 1.10):

$$\delta^{x/y}E_{mix} = \sum_n x_n * \delta^{x/y}E_n \quad \text{Eq. 1.10}$$

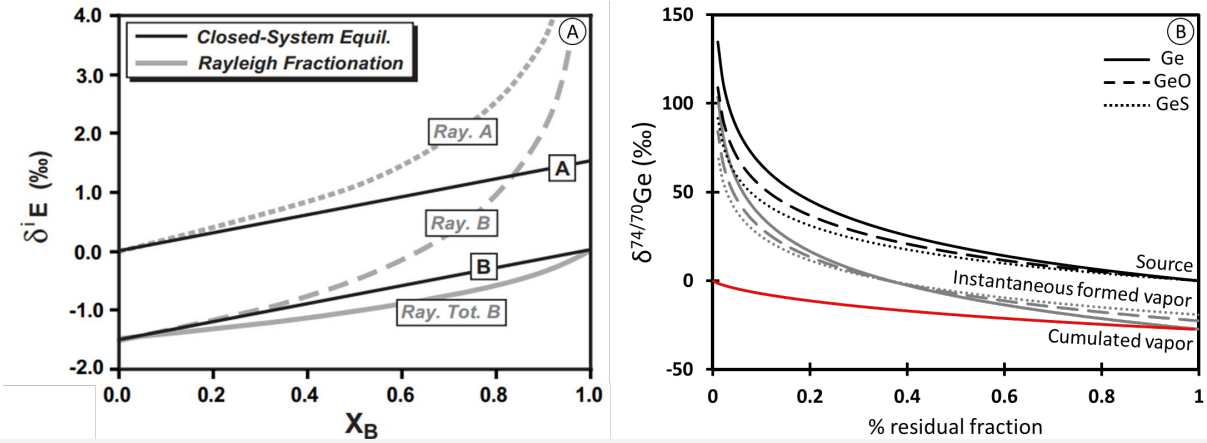

Figure 1.7: A) Difference in the isotopic fractionation occurring between two phases A and B during closed–system equilibrium (Grey line) and Rayleigh fraction (black line). The full grey line represents the evolution of the cumulated isotopic composition of the product (B), the dashed line the instantaneous isotopic composition of material removed from the source (A) and the dotted line the evolution of the source; adapted Johnson et al., 2004. B) Example of Rayleigh isotopic evolution during Ge evaporation from a condensed source reservoir. We can observe the effect of the presence different types of Ge (Ge, GeO, GeS). The α(Ge) = 0.97259; α(GeO) = 0.97752; α(GeS) = 0.98096, for a β=0.5.

2.2. Germanium isotopes and their behaviour

2.2.1. Overview of germanium characteristics

Germanium (Ge) has the electronic configuration $[Ar]3d^{10}4s^24p^2$. The similarity between the external electronic layers of Si and Ge (Si: [Ne] $3s^23p^2$) leads to very similar behaviours and the isomorphous substitution of Ge^{4+} (39 ρm ionic, 121 ρm) covalent with Si^{4+} (26 ρm ionic, 116 ρm, Bélisson, 2016) in silicates.

Germanium is a moderately siderophile element because its metal–silicate partitional coefficient is comprised between 10 and 10^4 (by comparison, a slightly siderophile coefficient is comprise between >1 to <10, and a highly siderophile coefficient ≥10^4, Walter et al., 2000). It can also have lithophile, chalcophile and organophilic behaviour. Five stable isotopes have been identified for germanium : ^{70}Ge (20.38 %), ^{72}Ge (27.31 %), ^{73}Ge (7.76 %), ^{74}Ge (36.72 %), ^{76}Ge (7.83 %). Ge has three oxidation states: 0, when it occurs in its metallic form, and 2+ or 4+ when oxidised. In the silicate, it mainly occurs as GeO_2species, but GeO species have been identified under specific redox conditions (Mare et al., 2018). Germanium is also a moderately volatile element (i.e. $T_{50\%\ condenation}$ =883 K, between 664 and 1324 K, Lodders et al., 2009). GeO and GeS are the most important volatile species in the solar nebula (Wai and Wasson, 1979). Germanium's multiple behaviour make it a highly valuable element for cosmochemistry, especially in studies of metal –silicate fractionation, metal condensation-evaporation and metal oxidation.

The concentration of Ge on Earth is usually low, varying from 0.8 to 3.5 µg/g (ppm) with a mean of 1.17 ppm for the bulk of silicate in Earth (El Korh et al., 2017, Luais et al., 2012). Its lithophile behaviour is highlighted by its relative enrichment in the BSE compared to the primitive earth (~1.1 ppm, Dasch, 1996). This lithophile characteristic leads to a concentration of up to 6 ppm in some evolved igneous rocks (e.g. pegmatites, skarn). Silicate reservoirs in the Solar System usually either have a composition close to that of Earth (e.g. Mars, 0.8-2ppm), or a very low concentration < 0,1ppm (e.g. Moon, Vesta) (Luais, 2015).

The chalcophile behaviour of Ge has been demonstrated by Belissont et al. (2014), who report high Ge concentrations in sphalerite (up to 2000 ppm). This high concentration is triggered by a high sulfide (high fS_2) environment and the affinity of Ge for Pb–Zn sulfides. Yet, in the troilite (FeS, sulfide in meteorites), the concentration of Ge is very low because of its higher affinity with the metallic phase (*i.e.* in the form of Ge^0) compared to the sulfide phase in a FeNiS environment where Ge occurs as Ge^{4+} or Ge^{2+} (Chabot et al., 2003, Florin et al., 2020, Belisson et al., 2016; Bonnet et al., 2017).

Ge siderophile characteristics are evidenced throughout the incorporation of Ge in metal during the condensation of the solar nebula gas ($T_{50\%}$ = 883 K; Lodders et la., 2009; Wood et al., 2019), through the relative enrichment of metal phases in Ge compared to their lower enrichment in silicates and sulfides in chondrites (Chou et al., 1973; Chou and Cohen, 1973) and through the enrichment of Ge in most of the different iron meteorites (Scott and Wasson, 1975, Table 1.2).

Table 1.2: Germanium content in metal, sulfide and silicate of meteorites (data in ppm)

Meteorites groups	Metal	Sulfide	Silicates	Meteorite groups	Metal	Sulfide	Silicates
Ordinary chondrites				**Pallasite**			
H	64	0.002	0.32	Main-group	45-65		0.04-0.07
L	115		0.4	Eagle Station	63		0.135
LL	236		0.5	**Differentiated body**			
Iron meteorites				Mars-Shergottite			~1
IA	190-520			Mars-Nackite			2.58
IB	25-190			Mars-Chassigny			~1.5
IC	212-247			Vesta-Eucrite			0.05
IIA	170-185			Vesta-Howardite			0.05
IIB	107-183			Vesta-Diogenite			0.126
IIC	88-114			**Moon**			
IID	82-98			Basalt			0.14
IIE	62-75			Metallic Spherule Apollo 16	37.8		
IIIA	32-47			Highland rock			0.25
IIIB	27-46						
IIIC	8-70						
IIID	1.4-4						
IIIE	34-37						
IIIF	0.7-1.1						
IVA	0.09-0.14						
IVB	0.03-0.07						

Data from Chou et al. (1973); Chou and Cohen (1973); Florin et al. (2020); Scott and Wasson (1975), Humayun et al (2016), Luais et al. (2017)

2.2.2. Germanium isotopic composition in iron meteorites

The studie of siderophile elements have attributed the formation of magmatic iron meteorites to planetesimal differentiation and core crystallisation. However, the large variations in siderophile elements high diversity of siderophile elements, including Ge, and the occurrence of silicate clasts within the metal of non–magmatic meteorites are less understood, making the formation of these meteorites a topic for discussion. The recent developments in Ge isotopic measurements have confirmed previous hypotheses on magmatic groups and brought new clues to explain the formation of non–magmatic groups.

Luais (2007, 2012) describes the Ge isotopic composition of iron meteorites, bothmagmatic and non–magmatic. The author shows that all magmatic groups (i.e. IIA–IIB, IIIAB, IIC) have a similar Ge isotopic composition of 1.41 ± 0.22‰ (Fig. 1.8), for varying Ge/Ni ratios. Autors demonstrate that these groups, including the super-chondritic Ge/Ni of IIA group, have had a high condensated metal content before their differentiation (Ge/Ni increase with increasing condensation). It also shows that the high $\delta^{74/70}$Ge compared to the bulk silicate earth (BSE, 0.53 ± 0.16‰). This disagrees with theoretical hypothesis of isotopic fractionation based on bond length differences between metal and silicate. Luais (2007) suggests that the $\delta^{74/70}$Ge ratio in silicates represented by the BSE composition does not reflect the composition of silicates that segregate from metal during the formation of the core. Recently, the positive metal-silicate fractionation ($\Delta^{74/70}Ge_{iron\text{-}BSE}$ = 0.88 ‰) has been experimentally reproduced by metal–silicate melting in an open system (Luais et al. 2009, 2019). The results have demonstrated that at the iron–wüstite buffer (IW–0), and because of evaporation the $\delta^{74/70}$Ge of the metal increases up to +3 ‰ after 60 hours of heating , and increases quicker that the $\delta^{74/70}$Ge in the silicate. It suggests that the small range of $\delta^{74/70}$Ge variation of iron meteorites results from very fast processes of metal-silicate segregation and melting.

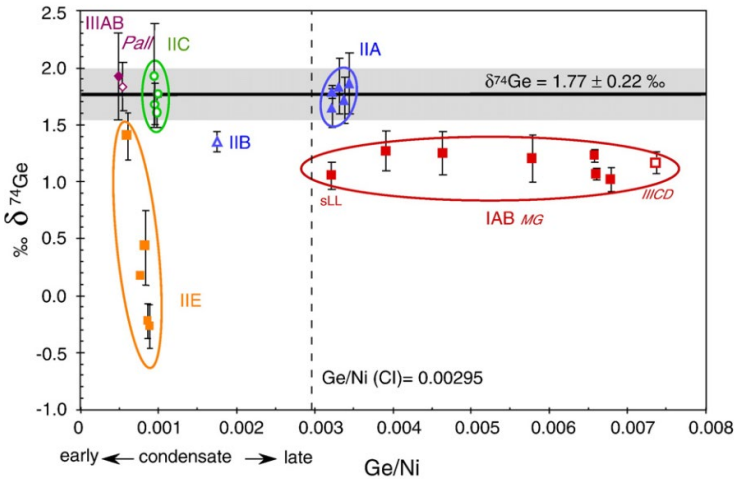

Figure 1.8: $\delta^{74/70}$Ge for iron meteorites, data are reported with respect to the JMC standard. $\delta^{74/70}Ge\ NIST_{3120a}$= $\delta^{74/70}$Ge JMC–0.36‰ (Luais, 2007)

Recent measurements of $\delta^{74/70}$Ge in the newly defined IIG magmatic group are similar to those of the IIB group, and thus support the view that IIG has been formed on the same parent body as the IIAB group. What is more, the very high isotopic fractionation between metal and schreibersite in IIG suggests that this group derives from a final metallic product from the IIAB core (Luais et al., 2014).

Finally, the quantification of Ge isotopic variations in IIE and IAB non-magmatic iron meteorites (Luais, 2007) demonstrates that they formed through volatilisation processes. While the processes leading to IAB formation remain unclear, we can track the processes leading to young IIE groups. The latter contain more $\delta^{74/70}$Ge and simultaneously less Ge content than old IIE groups. , showing that they formed through evaporation and successive impacts on the IIE parent (Fig. 1.9). The data also demonstrate the capacity of Ge to track volatilisation processes of the metal phase.

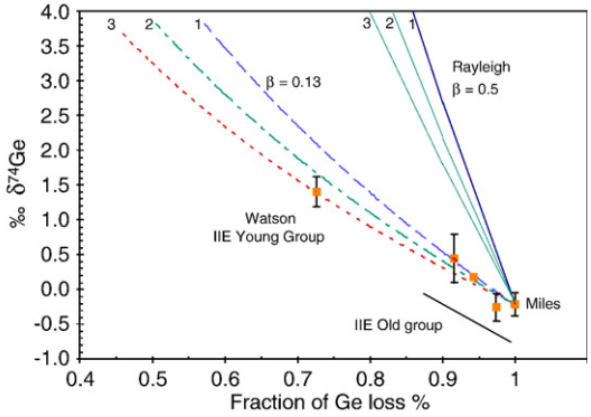

Figure 1.9: $\delta^{74/70}$Ge vs Ge content for IIE meteorites. A Rayleigh distillation is shown for β=0.13, α(Ge) = 0.99079; α(GeO) = 0.99410; α(GeS) = 0.99501, curves 1, 2, 3 respectively (Luais, 2007). Where α is the isotopic fractionation factor ($\alpha=(m_{70}/m_{74})^{\beta}$) and β a parameter experimentally defined.

2.2.3. Comparison of $\delta^{74/70}$Ge between FeNi-metal and other phases

Compared to metallic reservoirs, the $\delta^{74/70}$Ge of silicate reservoirs are suggested to be cogenetic and always enriched in light isotopes (Fig. 1.10 A). This has been first shown for magmatic iron meteorites which are thought to be the core of destroyed planetesimals and earth silicate (Luais, 2007, 2012). The same observation has been made between metal and silicate from pallasites (Luais et al., 2017) and from ordinary chondrites (Florin et al., 2020). The lower positive $\Delta^{74/70}Ge_{metal\text{-}silicate}$ has been described as the result of high temperature processes. However, this isotopic fractionation disagrees with the theoretical isotopic calculation based on bound lengths that predict a lower $\delta^{74/70}$Ge for metal than for the silicate while they are cogenetic. This issue will be discussed using ordinary chondrites in **Chapters 4 and 5**. Low tempeture processes can produce large isotopic fractionation with light delta values, especially in Zn-sulfides due to the chalcophile behaviour of Ge (Belisson et al., 2014; Escoube et al., 2014, Fig. 1.10 B). The relationship between metal and sulfide in primitive chondrites at an isotopic scale will be developed in **Chapter 5**.

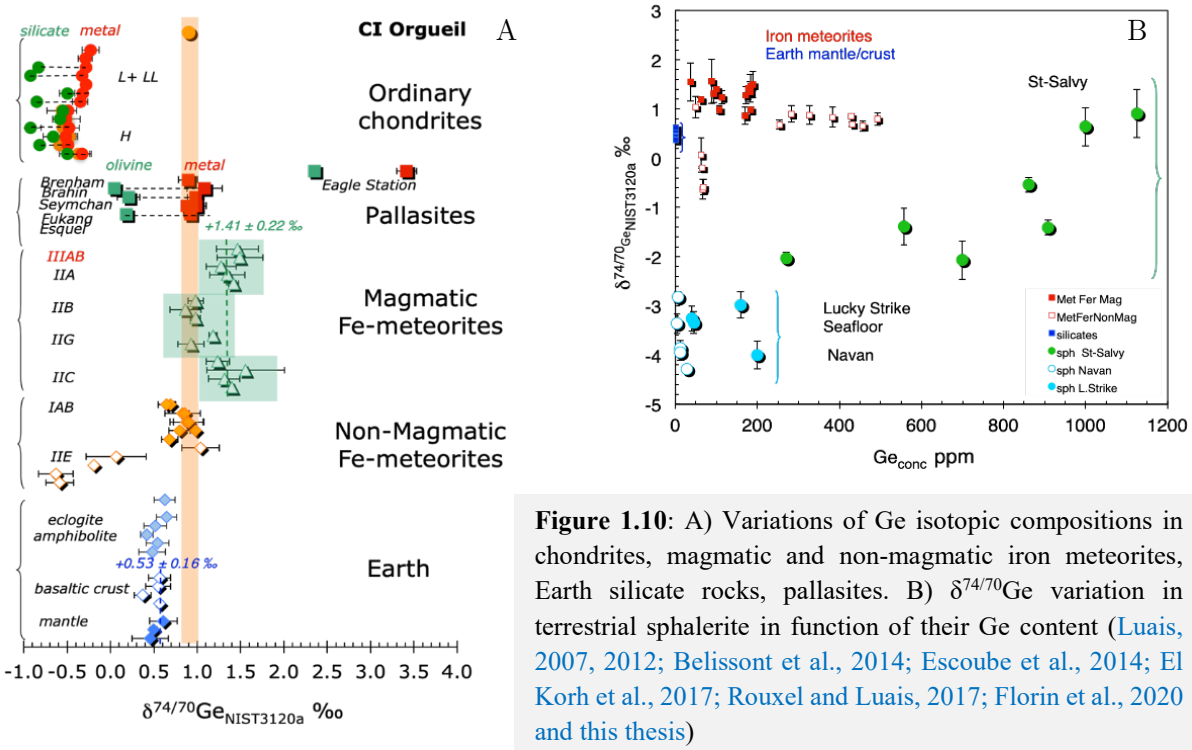

Figure 1.10: A) Variations of Ge isotopic compositions in chondrites, magmatic and non-magmatic iron meteorites, Earth silicate rocks, pallasites. B) $\delta^{74/70}$Ge variation in terrestrial sphalerite in function of their Ge content (Luais, 2007, 2012; Belissont et al., 2014; Escoube et al., 2014; El Korh et al., 2017; Rouxel and Luais, 2017; Florin et al., 2020 and this thesis)

These results emphasise the potentiality of germanium isotopes to: (1) track magmatic processes; (2) define genetic links between parent bodies; (3) recognise volatilisation processes.

3 The ages of iron meteorites

It is of prime importance in cosmochemistry to be able todate the formation of objects in the Solar System and the processes engaged in their formation. The relative ages of these events bring useful constraints to validate or invalidate processes active during the evolution of the Solar System. Ages can be directly obtained from measurements of the amount of isotopes produced by the decay of long-lived radionuclides (e.g. U–Th–Pb, $t_{1/2}(^{138}U \rightarrow ^{206}Pb) = 4.47*10^9$ yrs; ^{40}K–^{40}Ar, $t_{1/2}$[3]$(^{40}K \rightarrow ^{40}Ar) = 1.27*10^9$ yrs). Under these circumstances, they are *absolute ages*. The use of extinct radionuclides (e.g. ^{26}Al–^{26}Mg, $t_{1/2}(^{26}Al \rightarrow ^{26}Mg) = 7.3*10^5$ yrs) assumes that their repartition was homogeneous in the solar nebula. Comparing the proportion of stables isotopes produced by radiogenic decay in two different objects gives us the age of their formation processes relative to one another. By using these two approaches it is possible to define a timeline of processes occurring in the Solar System. To address questions of homogeneity and because relative ages need a starting event, ages of objects and processes are reported as "time after calcium–aluminium–rich inclusions (CAIs) formation" (CAIs ≈ 4567.94±0.31 Ma, Pb–Pb technic,

[3] $t_{1/2}$ is the time needed for the quantity of parent radionuclides to be divided by 2 through radiogenic decay. First values werefound by Steiger and Jäger (1977) and later improved upon by other studies.

Bouvier et al. 2011). CAIs are the oldest known object of the Solar System and considered to be the first condensates from the solar nebula.

The age of meteorites has been described by numerous studies over the past decades. One of the most important studies, which is also a topic of controversy, is the discovery in iron meteorites of the possible very young W isotope ages compared to chondrites and other differentiated objects (between 0 and 2 Myrs after CAIs, Kleine et al., 2005; Qin et al., 2008). This suggests that they predate the accretion of chondrites (Fig. 1.11) and has revived the debate about their formation and may rule out the common view of their origin by differentiation of the chondrite parent body.

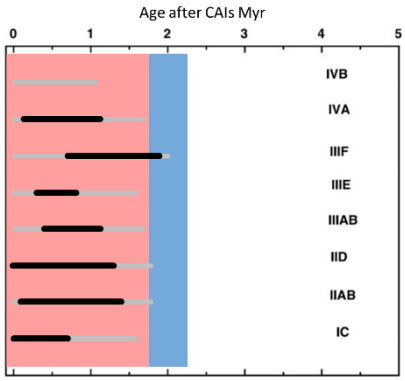

Figure 1.11: Accretion ages for different iron magmatic groups relative to CAIs. The black line represents preferred ages and the grey line conservative ages. The pink zone is the time for chondrules formation and the blue zone the interval of ordinary chondrites accretion. Figure modified after Qin et al. (2008), data for chondrules and ordinary chondrites are from Elkins–Tanton et al. (2011) and Desch et al. (2018) compilations.

If iron meteorites formed so early in the Solar System, it means that the metal present in chondrites not only derives from a condensation process directly from the solar nebula but also from the disruption of previously formed planetesimals. Chondritic metal formation needs to be assessed to better understand the evolution of objects: the first steps of iron meteorite formation and the processes that lead to core formation. Thus, the careful analysis of metal in chondrites is needed.

4 Carbonaceous, non–carbonaceous dichotomy

The newly highlighted anomalies in ^{50}Ti, ^{54}Cr, ^{62}Ni, $^{95,\ 94}$Mo and $^{182,\ 183}$W identified in meteorites divide meteorites into two groups (Fig. 1.12), the *non–carbonaceous* (NC) and the *carbonaceous* (CC), they both including chondrites and iron meteorites. (Kruijer et al., 2017; Trinquier et al., 2007, 2008; Warren et al., 2011). Therefore, it has been suggested that meteorites come from two different reservoirs and a new hypotheis proposes that the Solar System has been divided into two parts, the inner and the outer Solar System (Brasser and Mojzsis, 2020). Currently, it is suggested that Jupiter (or some pressure bumps in the disk) is the root of this dichotomy. However, the clear processes that lead to these stable isotopic anomalies within the protoplanetary disk are still under investigation. However, this agrees with the formation of carbonaceous chondrites in the outer Solar System and enstatites, ordinary chondrites in the inner Solar System. Additionally, this dichotomy agrees with the relationship between ordinary

chondrites and IIE iron meteorites (Wasson, 2017; Florin et al., 2020) and suggests that at least ordinary chondrites and iron meteorites can be genetically linked.

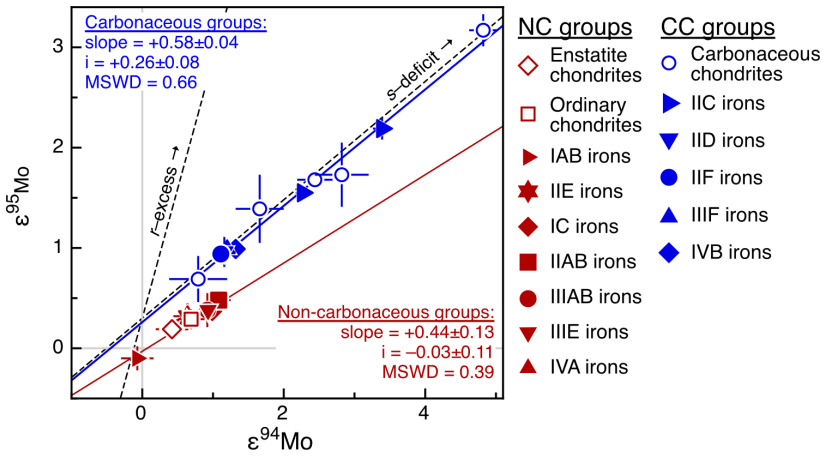

Figure 1.12:^{95}Mo vs ^{94}Mo anomaly data for chondrites and irons meteorites that define two trend, the non–carbonaceous (NC in red) and the carbonaceous (CC, in blue) ones. Those two trends correspond to the two reservoirs separated by Jupiter, after Kruijer et al. (2017).

Moreover, the fact that ordinary and enstatite chondrites do not form inthe same parts of the disk as carbonaceous chondrites is supported by the difference in oxidation state and in the proportion of metal in these different groups. This difference has been explained by the lack of significant migration of oxidising components in the inner solar system during the snow line migration (Morbidelli et al., 2016). A possibility suggested by Morbidelli et al. (2016) is that the ice and silicate flux associated with the snow line migration was mostly blocked by the formation of the proto–Jupiter at 3AU[4], depleting the inner Solar System in oxidising components. This effect may explain the very low percentage of metal, at similar bulk iron content, between the carbonaceous and other chondrites (Table 1.1).

*From recent studies, it appears that chondrites are younger than iron meteorites, implying that they cannot be the precursor of early formed planetesimals and then of iron meteorites,. This leads to the question: "where does metal come from and how does it evolve in pristine chondrites?". The study of metal in the chondrites is therefore of primary importance in order to understand: (1) the formation of metal in the Solar System; (2) the effect of oxidation state and heating events on metal in the solar nebula or in planetesimals; (3) the difference in metal content between chondrite groups; (4) metal migration in undifferentiated parent bodies. Answering these questions will enhance our knowledge of the building blocks of asteroids and planets in our solar system. In our thesis we address these questions are addressed by the use of Germanium isotopes (**Chapter 3 and 5**) and highly and moderately siderophile elements measurements on solar system sample material (meteorites) (**Chapter 3 and 4**). In the next*

[4] AU : Astronomical Unit, 1 AU corresponds to the Earth–Sun distance, i.e. 150'000'000 km.

section, we present a comprehensive description of ordinary chondrites and Bencubbin carbonaceous chondrites groups studied in this thesis along with their use to understand metal formation and evolution

III. Metal phase condensation

Metal formation and condensation processes have been explored by theoretical thermodynamic calculations. The results of these calculations are now used to understand the thermodynamic conditions as well as the processes occurring in the environment of metal formation. To address these conditions, cosmochemists study the elemental and isotopic composition of the metal phase. In this section, we discuss the state-of-the-art of metal condensation models and then apply them to Bencubbin Carbonaceous (CB) chondrites as well as to other earlier studies.

1 Overview of metal condensation

The condensation sequence of the elements has been described by thermodynamic calculations (e.g; Kelly and Larimer, 1977). The temperature of condensation is expressed at 50% of nebular condensation, which describes the temperature at which 50% of an element in the gas is condensed (temperature of 50% condensation are summarised in Table 1.3, Grossman and Larimer, 1974; Lodders et al., 2009). Following this calculation, elements are classified into refractory elements which have a temperature of condensation ~>1400 K (e.g. Re, Os, Ru), moderately volatile elements that condense between 1324 and 664 K (e.g. Ga, Ge, S) and the volatile elements condensing at lower temperatures (e.g. Cd, Hg; Lodders et al., 2009).

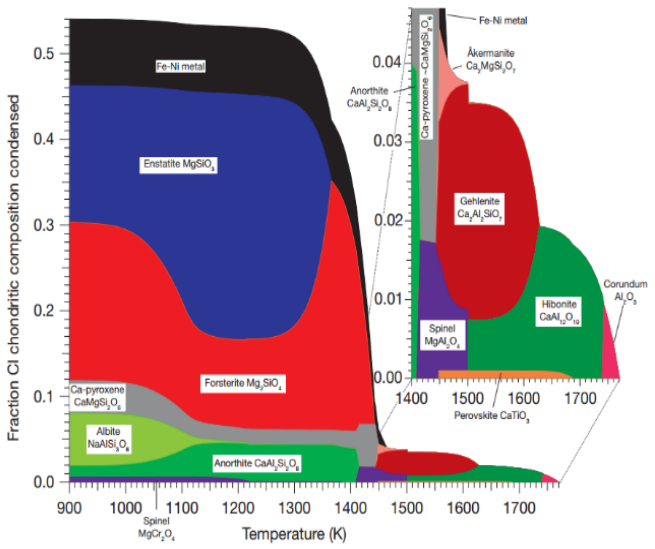

Figure 1.13: Condensation sequence from Davis & Richter (2014), based on Anders & Grevesse (1989) data.

Table 1.3: Temperature of 50% of condensation.

Element	Wasson (1985)	Lodders (2003)	Wood et al. (2019)		Element	Wasson (1985)	Lodders (2003)	Wood et al. (2019)	
	T_{50} (K)	T_{50} (K)	T_{50} (K)	Host phase		T_{50} (K)	T_{50} (K)	T_{50} (K)	Host phase
	Refractory elements					Moderately volatile elements			
Os	1804	1812	1806	Os metal	Pd	1334	1324	1330	Fe alloy
W	1802	1789	1736	W-Re alloy	Cr	1277	1296	1291	Fe alloy
Re	1819	1821	1736	W-Re alloy	P	1151	1229	1287	Scb
Zr	~1780	1741	1722	ZrO_2	As	1157	1065	1235	Fe alloy
Hf	1652	1684	1720	HfO_2	Mn	1190	1158	1123	Fo + En
Al	1650	1653	1652	Crn	Na	970	958	1035	Pl
Nd	1510	1602	1630	Hbn	Cu	1037	1037	1034	Fe alloy
Gd	1545	1659	1630	Hbn	Ga	918	968	1010	Fe alloy
Tb	1560	1659	1630	Hbn	K	1000	1006	993	Pl
Dy	1571	1659	1630	Hbn	Au	1225	1060	967	Fe alloy
Ho	1568	1659	1630	Hbn	Sb	912	979	890	Fe alloy
Er	1590	1659	1630	Hbn	Ge	825	883	830	Fe alloy
Tm	1545	1659	1630	Hbn	Rb	~1080	800	752	Sa
Lu	1597	1659	1630	Hbn	B		908	740	Pl
Th	1545	1659	1630	Hbn	Zn	660	726	704	Tro
La	1520	1578	1615	Hbn	Se	684	697	701	Tro
U	1420	1610	1609	Hbn	Ag	952	996	699	Tro
Ir	1610	1603	1566	Os-Ir alloy	F	736	734	674	F-Ap
Ti	1549	1582	1565	Prv	S	648	664	672	Tro
Nb	~1550	1559	1561	Prv	Te	680	709	665	Tro
Be		1452	1551	Mll		Highly volatile elements			
Y	1592	1659	1551	Mll + Prv	Sn	720	704	604	Fe alloy
Pr	1532	1582	1550	Hbn + Prv	Cs		799	593	Sa
Sr		1464	1548	Prv	Cd	430	652	502	Tro
Ta	~1550	1573	1546	Prv	Pb	496	727	495	PbS
Sm	1515	1590	1545	Hbn + Prv	In	456	536	492	Tro
Sc	1644	1659	1541	Prv + Mll	Bi	451	746	480	Bi metal
Ca	1518	1517	1535	Mll	Cl	863	948	472	Cl-Ap
Ru	1573	1551	1533	Os-Ir-Ru alloy	Br	~690	546	420	Syl
Yb	1455	1487	1528	Mll + Prv	I		535	390	Kl
Mo	1608	1590	1520	Mo metal	Tl	428	532	365	Tl_2S, Tl
Eu	1450	1356	1491	Mll + Prv	Hg		252	240	Tro
Ce	1500	1478	1454	Mll+ Prv		Ice and gases			
Ba		1455	1423	Prv	O		180	183	Rock + Water ice
V	1450	1429	1370	Fe alloy+Prv	C		40		
Rh	1391	1392	1370	Fe alloy	N		123		
Pt	1411	1408	1370	Fe alloy	Ne		9.1		
	Major elements				Ar		47		
Ni	1354	1353	1363	Fe alloy	Kr		52		
Co	1351	1352	1354	Fe alloy	Xe		68		
Mg	1340	1336	1343	Fo + Cpx					
Fe	1336	1334	1338	Fe alloy					
Si	1311	1310	1314	Fo + Cpx					

Siderophile elements are in blue. En = enstatite; Fo = forsterite; Cpx = clinopyroxene; Mll = melilite; Pl = plagioclase; Fsp = feldspar; Ap = apatite; Crn = corundum; Hbn = hibonite; Scb =schreibersite; Tro = troilite; Sdl = sodalite; Prv = perovskite; Syl = sylvite; Sa = sanidine.

When the temperature of a gas reaches 1363 – 1314 K, 50% of the major elements have condensed, in the form of FeNi alloys and fayalite (Table 1.3 and Fig. 1.13; Wood et al. 2019). Then with afurther decrease in temperature, the moderately volatile elements are incorporated in the condensed phases by reaction with the condensed mineral as a function of their chemical behaviour and of the environmental parameters (oxidation rates, cooling rates etc.; Fegley and Palme, 1985).

The oxidation state of the solar nebula is very reduced with $\log(fO_2) = -16.67$ (i.e. IW-6.5 at 1600 K and 10^{-4} bar; Cartier and Wood, 2019). In this environment, iron and nickel are expected to condense from pristine nebular gases into their metal forms During this condensation step, the first metal condensates are enriched in refractory elements and in nickel, whereas later metal phases will be progressively enriched in moderately volatile and siderophile elements and depleted in refractory elements and nickel (Fig. 1.14, 1.15 A, B). This forms zonations in the metallic grains with cores having higher refractory compositions but lower volatile contentthan

the edges of the grains. The relative ratio of these elements is acquired by equilibrium condensation and can be measured to track condensation processes, as they cannot be recreated by other processes. For example, the Co/Ni ratio is defined at 0.045 (at P_{tot}[5] = 10^{-4} bar Grossman and Olsen, 1974) as Co condenses simultaneously with Ni but in different proportions (also true for Pb). This ratio is similar to CI[6] and it is possible to calculate the E/Ni for each element by referring to the CI group. However, it should be noted that this ratio may change for a gas of non–solar composition. Thus, we can deduce that in the first steps of the formation of the Solar System, elements experienced two fractionation processes: an an initial fractionation between silicate and metal as well as within the metal.

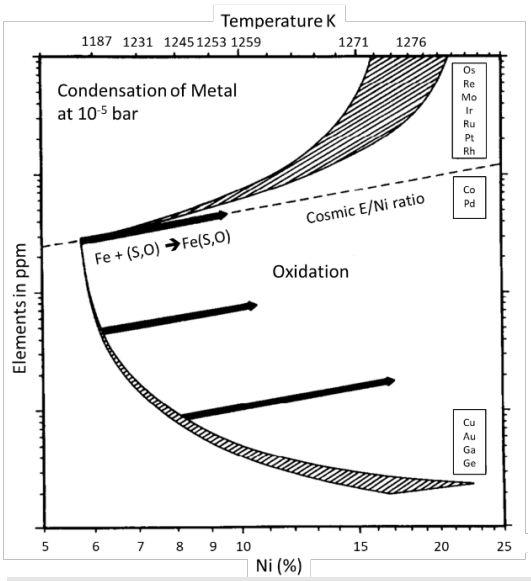

Figure 1.14: composition of the metal phase during condensation at 10^{-5} bar. Black arrows are parallel to the cosmic ratio and represent the effect of Fe oxidation on the composition. The dashed line represent the solar ratio. After Kelly and Larimer (1977).

2 Bencubbin carbonaceous chondrites

2.1. Benccubin formation

Bencubbin carbonaceous chondrites or CB chondrites are composed of 60 to 70 vol% of metal and 30 to 40 vol% of silicates (Fig. 1.15A). These meteorites do not show any aqueous or metamorphism alteration and thus are very pristine. They have been latterly subdivided into two groups, CB_a and CB_b based on their petrological texture, elemental and isotopic compositions (Weisberg et al., 2001). This is described in more details in Chapter 3. The two CB groups are related to the CR and the CH chondrite groups (Fig. 1.15B through their oxygen isotopic compositions, thus defining a large CB-CR-CH chondrite clan. In an oxygen isotopic diagram, the oxygen isotopic composition $\delta^{17/16}O$ is represented against $\delta^{17/16}O$. The TFL, representing the Terrestrial Fractionation Line on which all terrestrial rocks fall, corresponds to the mass dependent fractionation line. Therefore, the variation from that line is represented by a positive or negative oxygen anomaly ($\Delta^{17}O$). Apart from terrestrial samples, only the EH and EL meteorites fall on the TFL.

[5] P_{tot} is the total pressure of the gas in the solar nebula.

[6] CI bulk composition is trusted to represent the composition of the solar nebula.

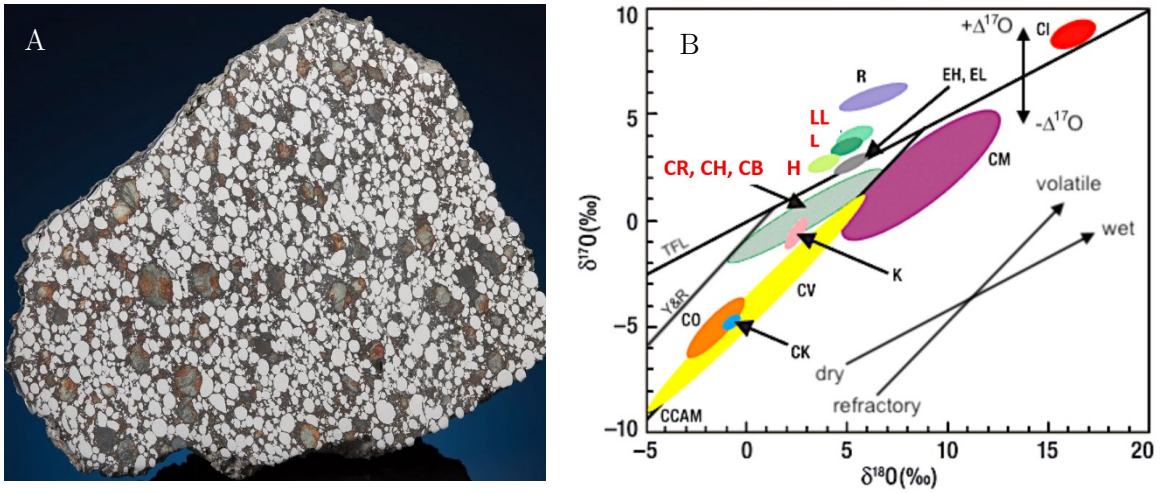

Figure 1.15:A) Picture of Gujba (CBa, picture from the Maine Mineral & Gem Museum). B) Range of oxygen isotopic composition of the different chondrite groups. After Grady (2009). TFL: Terrestrial Fractionation Line.

The first studies of Bencubbin have shown that CB groups have solar Co/Ni and P/Ni ratios which agree with the theory of metal condensation from the solar nebula (Newsom and Drake, 1979). Furthermore, the depletion of Ge and Ga in the metal grains also agrees with the theory of condensation in a high temperature environment. The occurrence of Si in the metal indicates that condensation occurs at equilibrium for some grains of Bencubbin (Newsom and Drake, 1979). However, the chromium content in iron is in excess of that predicted by condensation from the solar nebula (Grossman and Olsen, 1974). Also, whereas Co/Ni, P/Ni ratios and Si contents agree with the theory of condensation from the solar nebula, different pressures are needed to create the two ratios and the Si enrichment in the metal, namely 10^{-3}, 10^{-4}, 1 bar, respectively. Additionally, CB ages, ~ 4.2 Ma after CAIs, support a formation after the disappearance of the solar nebula (Krot et al., 2005; Marty et al., 2010). *How it is possible to reconcile these observations?*

Recent in–situ measurements of highly and moderately volatile siderophile elements (HSE: Os, Re, Ir, W, Ru, Mo, Rh, Pt; MSE: Pd, Fe, Ni, Co, Au, Ga, Ge, respectively) have shown that their elemental contents in this CB meteorite group contradict the theory of condensation under solar nebula conditions. What is more, the high *in–situ* measured Ni/Co and Pd/Fe ratios imply a condensation in an environment where siderophile elements are 10^7 times more enriched compared to a 10^{-4} bar solar gas (Campbell et al., 2002). Thus, authors have suggested that instead of a gas of solar composition, condensation in an impact plume in more likely (Campbell et al., 2005; Kallemeyn et al., 2001; Krot et al., 2005; Rubin et al., 2003). Therefore, CB chondrites seems to be formed by condensation, yet, all these studies are based on elemental composition, which leads to the question:

" *What is the response of isotopes to condensation?".*

2.2. Gas–condensate interactions and isotopic fractionation in Bencubbin chondrites

2.2.1. Theory of isotopic fractionation during condensation and evaporation

Condensation and evaporation are two processes that can produce large isotopic fractionation. However, it is difficult to evaluate to which extent and in which direction isotopic fractionation occurs between a metal condensate and its vapour source especially in low gravity context. It mostly depends on the system dynamics, namely on whether it evolves at equilibrium or not (which is a function of the cooling rate), on the partial pressure of the gas, and on whether the system is closed or open. In the case of homogeneous phases in a closed system, Richter (2004) describes equilibrium and kinetic limits of both processes (e.g. condensation and evaporation) as a function of their characteristic time scales (τ_{cond}, τ_{evap}) versus timescale of temperature change (τ_T) and a corollary of the ratio of the partial pressure of a considered volatile element (P_i) to its saturation vapour pressure ($P_{i,sat}$). In the case of slow temperature changes compared to the ideal time scale for equilibrium condensation or evaporation, the system would reach the equilibrium limit with $P_i \approx P_{i,sat}$, thus there will be no, or limited, isotopic fractionation between solid and gas. On the other hand, disequilibrium processes are characterised by fast temperature changes and thus $P_i \neq P_{i,sat}$. In case of high-cooling rates ($\tau_{cond} / \tau_T > 0.001$) where the condensation is not complete, condensation becomes function of the kinetic energy average of each isotope defined as $K_e = 1/2*m*v^2$ where m is the mass and v the velocity of a selected isotopes (Hirth and Pound, 1963; Humayun and Clayton, 1995). Under these conditions, the light isotopes have a higher kinetic energy than the heavy isotopes, resulting in higher interaction (i.e. collision) between the vapour and the condensing phase. Therefore, the light isotopes are more easily incorporated in the condensing phase than the heavy isotopes, thus leading to the condensed phase to be enriched in light isotopes as opposed to the gas (Humayun and Clayton, 1995; Richter, 2004).

2.2.2. Iron and Nickel isotopic composition in CB

Metal grains in Bencubbin chondrites can be elementally and isotopically zoned or not. Zoned grains are manly found in CB_b chondrites while unzoned ones are predominantly found in CB_a groups. Zoned grains have their core enriched in Fe–Ni light isotopes compared to their rims (Fig. 1.16). The difference in isotopic composition between the two types of grains is suggested to be the result of kinetic versus equilibrium condensation as described by Richter (2004). It has led authors to argue in favour of metal grains formations in two different types of environments, one with high cooling rate and another one with low cooling rate (Krot et al., 2004; Richter et al., 2014; Weyrauch et al., 2019). Therefore, it has been suggested that CB chondrites may formed in an impact plume, if so, this structure has been thermodynamically zoned with the exterior having high cooling rate and low gas pressure, and the inner part defined by low cooling

rates and high gas pressures. However, this hypothesis only partly agrees with models of metal condensation (Fedkin et al., 2015) as it is not possible to reproduce the composition of associated silicates. Moreover, some grains are characterised by the occurrence of plessite in their core, which is not explained and may be indicative for low temperature processes (Meibom et al. 2005).

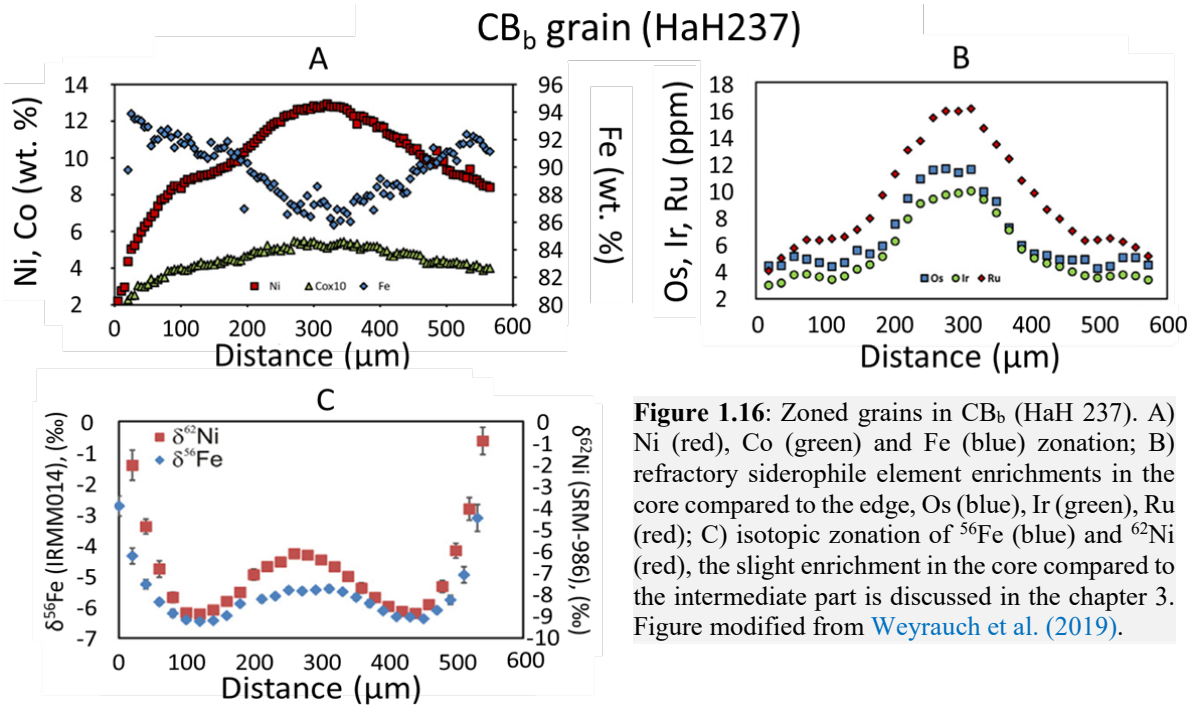

Figure 1.16: Zoned grains in CB$_b$ (HaH 237). A) Ni (red), Co (green) and Fe (blue) zonation; B) refractory siderophile element enrichments in the core compared to the edge, Os (blue), Ir (green), Ru (red); C) isotopic zonation of ^{56}Fe (blue) and ^{62}Ni (red), the slight enrichment in the core compared to the intermediate part is discussed in the chapter 3. Figure modified from Weyrauch et al. (2019).

We have seen that, CB chondrites are the perfect objects to study the effect of metal condensation under kinetic and equilibrium conditions. Previous studies have pinned down the temperature of condensation of metal and shown that it needs to be at a temperature higher than the temperature for Fe, Ni condensation (i.e. $t_{50\%}$(Fe) = 1338 K, Wood et al., 2019). Condensation seems to be well constrained by major elements and refractory siderophile elements. However, the processes that occur at temperature below $T_{50\%}$(Fe) are not well known. We are going to explore them in ***Chapter 3*** *through the quantification of germanium isotopes and moderately siderophile–volatile elements.*

In the next section, we present the formation and the evolution of metal phase in ordinary chondrites caused by heating and oxidising events.

IV. Oxidation and heating processes

After its formation, metal can undergo multiple processes (such as redox processes) that can be linked or not to heating events either in the solar nebular or on parent bodies. The metal being very sensitive to these processes, their studies are of primary importance in the understanding of metal evolution. In this section, we present ordinary chondrites groups showing both, on their respective parent bodies, a sequence of oxidation from H to L to LL and a sequence of metamorphism due to heating events.

1 Ordinary chondrites sequence

Ordinary chondrites are primitive meteorites composed of metal (FeNi alloy), silicates (chondrules), sulfides (troilite), with other minor minerals (e.g. phosphates, oxides, etc.), cemented by a fine grain matrix. (Fig. 1.17). Some rare refractory inclusions can also be found in these types of chondrites.

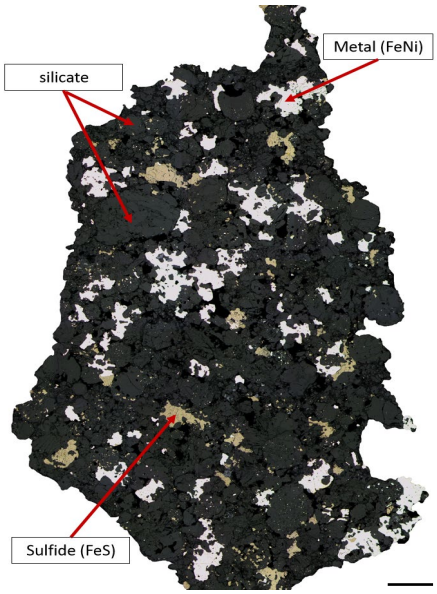

Figure 1.17: Example of an ordinary chondrite (Kernouvé, H6).

The ordinary chondrites are divided into three groups, H (High total Fe), L (Low total Fe), and LL (Low total Fe, Low metallic Fe, Table 1.1). These three groups have been first recognised by Urey and Craig (1953) due to the evolution of Fe_{metal} vs {FeS + Fe_xO_y} across the sequence (Fig. 1.18). The decrease of metallic iron and the increase of oxidised iron from H to LL suggests that a part of the iron has been transferred from metal to silicate during oxidation. This effect of oxidation is well illustrated by the increase of the percentage of fayalite (%Fa) from H to L to LL which correspond to the percentage of oxidised iron in olivine. Whereas the three groups are clearly defined in the most metamorphosed ordinary chondrites (see next section for metamorphism description), in very pristine ones it is not possible to differentiate the three groups with their %Fa (Rubin, 1990). Moreover, this process is incomplete, and it is not possible to transition from one group to another by the mixing of metallic and non–metallics components, or by oxidation (Urey and Craig, 1953). Therefore, some metal appears to have been lost. Some authors have suggested that the decrease of the total iron from H to LL may be the result of volatilisation during ordinary chondrite formation in the solar nebula (Campbell et al., 2005, and references therein).

At this time, it is difficult to confirm the cause of the decrease in metal. This will be approached in the ***Chapters 4 and 5****.*

The difference between the three groups of ordinary chondrites is also highlighted by their bulk and metal siderophile element content (Chou et al., 1973; Chou and Cohen, 1973). For example, the L and the LL groups are enriched in volatile elements and depleted in refractory ones compared to H groups (Wasson, 2017). This difference in element content suggests that the three groups correspond at least to three different planetesimals (Kallemeyn et al., 1989). Moreover, oxygen isotopic measurements (Clayton et al., 1991; Clayton and Mayeda, 1996), show that the three groups are distinguishable in the analytical error (Fig. 1.15) and that they come from different planetesimals that correspond to different –but related– environments in the protoplanetary disk. These observations have been recently confirmed by the identification of two different asteroids associated with two OC groups (8–Flora for LL and 6–Hebe for H) in the asteroid belt.

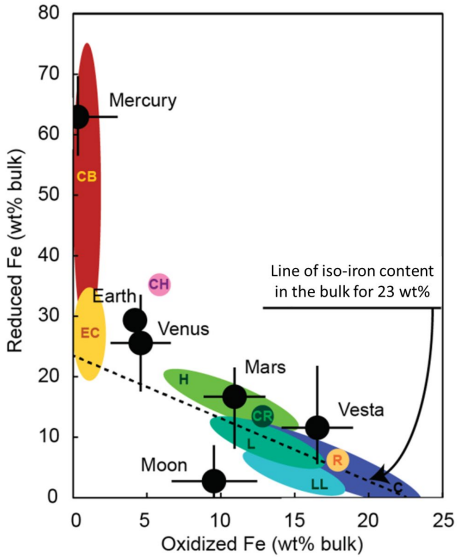

Figure 1.18: Distribution of the different meteorites groups in function of their Fe_{metal} vs $\{FeS + Fe_xO_y\}$. When oxidation occurred, point evolved on a line parallel to the dashed one. After Urey and Craig type diagram Cartier and Wood (2019).

Recent studies have highlighted some similarities between the IIE iron group (non–magmatic) and the ordinary chondrite sequence, such that the IIE seems to correspond to a more reduced HH group (Clayton and Mayeda, 1996; Wasson, 2017). However, this relation is not fully explained and can be the result of the disruption of a HH parent body by impact or impact on a parent body closely related to the H group.

The formation of metal in the ordinary chondrites group is also a subject of debate. The non-chondritic Co/Ni of the metal phase suggests that these groups cannot be formed by direct condensation (Kong and Ebihara, 1996, 1997). It was suggested that the metal can result from the reduction of an oxidised precursor (Kong and Ebihara, 1996, 1997). However, this is not in line with the content of highly refractory siderophile in the metal phase, as well as the enrichment of small metallic grains in refractory elements compared to larger ones (Horan, 2009). *In–situ* elemental analyses have shown that the metal and the chondrules may have been formed during the same event (Campbell and Humayun, 2003), which agrees with the elevated Ir/Ni ratio in the non–magnetic fraction (Chou et al., 1973; Rambaldi et al., 1978). More recently, the finding of carbon associated with metal in OCs (Mostefaoui et al., 2000) has led these authors to suggest that the diversity of metal composition in L and LL groups may result from fractionation due to metallic precursors melting that have contained 3% of carbon (Okabayashi et al., 2019). Another hypothesis is that the metal was desulfurized during heating events (Hewins et al., 1997).

However, it is still unclear if H chondrites also experience this melting and hence, how H metal phase is related to L and LL metal phases.

Ordinary chondrites have many interesting characteristics that make them perfect objects to characterise the effect of oxidation state and heating processes in the solar nebula on the metal formation and its evolution:

1) *The evolution of metal content from H to L to LL.*
2) *The increase in oxidation state through the ordinary chondrite sequence.*
3) *The very close relationship between the three groups, and their sampling of different parent bodies.*
4) *The recognition of a probable iron meteorite groups related to the ordinary chondrite sequence.*
5) *The possible formation of the metal by melting processes occurring in the solar nebula.*

The subjects of the formation of metal, as well as the mineralogical, elemental and redox evolution though the ordinary chondrite sequence and the consequences for metal evolution are examined in the ***Chapters 4 and 5****.*

2 Heating processes and differentiation

2.1. Impact of metamorphism on metal evolution and migration

2.1.1. The petrographic groups

In addition to the classification of meteorites, petrographic and textural analysis have resulted in the subdivision of meteorites groups in petrologic groups that quantify the intensity of the metamorphism and the aqueous alteration (Fig. 1.19, Van Schmus et al., 1967). This classification has been improved by adding elemental constraints (e.g. bulk carbon content, percentage of Ni in sulfides, CaO in orthopyroxene etc. Tait et al., 2014). Associated with its groups, each chondrite has a number that describes its petrographic group (e.g. H6), these numbers vary from 1 to 7 (Tait et al., 2014). The first two groups (1 and 2) define the aqueous alteration that increases from 2 to 1. The groups 4 to 7 describe the increase of temperature (from <675°C for the type 4 to >1000°C for type 7, Tait et al., 2014) associated with a progressive dehydration of the parent body and an increase of the metamorphism. These meteorites are named "equilibrated". Types 3 corresponds to pristine meteorites such as CB chondrites or some ordinary chondrites. Types 3 is subdivided in categories (from 3.00 the more pristine ones to 3.9 the more equilibrated ones) corresponding to an increase of the temperature from <260°C for 3.00 (Alexander et al., 1989), to 300–350°C for L3.15 (Rambaldi and Wasson, 1981), to 350–

400°C for 3.4 to 3.6 (Brearley, 1990), to 500–700°C for 3.5 to 3.8 (Huss et al., 2006, and references therein).

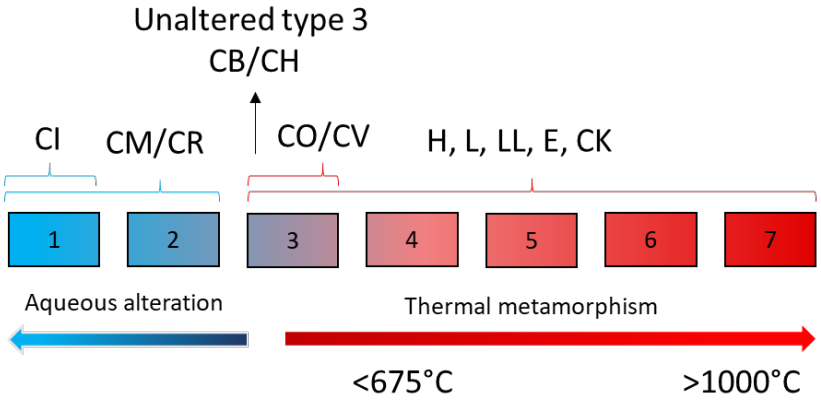

Figure 1.19: The different petrographic types and their associated chondrite groups. After Van Schmus et al. (1967) and Tait et al. (2014).

2.1.2. Temperature and depth associated to petrographic groups

According to recent studies, the inner temperature of early formed planetesimals is mostly results of ^{26}Al ($t_{1/2}$ = 7.3 * 10^5 yrs) and ^{60}Fe (1.5 Myrs) radiogenic decay, which may lead to its differentiation (e.g. Baker et al., 2005). The repartition of the produced heat in the planetesimal has been described by thermal models. In principle, if the distribution of short life radionuclides is homogeneous in the planetesimal the heat distribution is controlled by the loss of heat due to diffusion from the inside to the outside of the planetesimal. Hence, the thermal conductivity of planetesimal components as well as the size of the planetesimal is the limiting factor for the maximum temperature that can be reached in its centre. Therefore, the heat experienced by mineralogical assemblages in the planetesimal is going to increase from the outside to the inside of the planetesimal (Fig. 1.20, Monnereau et al., 2013). Another important parameter concerning the heat that a planetesimal can accumulate is its time of accretion. As ^{26}Al and ^{60}Fe have very short lifetime, an early accretion event leads to a higher temperature in the centre of the planetesimal than a later accretion event. Also, for a planetesimal that has accreted more than 5 Myrs after CAIs formation the remaining quantity of ^{26}Al and ^{60}Fe will be too low to provide an efficient heat source, leading to an undifferentiated, unequilibrated planetesimal. Recently, closure time of different minerals has been used to quantify the cooling rates of the different petrographic groups (e.g. Göpel et al., 1994; Trieloff et al., 2003; Kleine et al., 2008). If all the samples from a given meteorite group come from the same parent body, the correlation obtained for the H group means that a layered distribution of petrographic groups is expected. If so, a chondrite with a high petrographic grade (e.g. type 6) is expected to originate from deeper than a low petrographic grade one (e.g. type 3), this model is called onion shell (e.g. Minster and Allègre, 1979; Fig. 1.20). Therefore, textural modification (Guignard and Toplis, 2015) as well as chemical equilibration (e.g. Dodd, 1981) are expected with increasing depth. Also, if the temperature is sufficiently high, a metal–silicate fractionation is expected in the planetesimal.

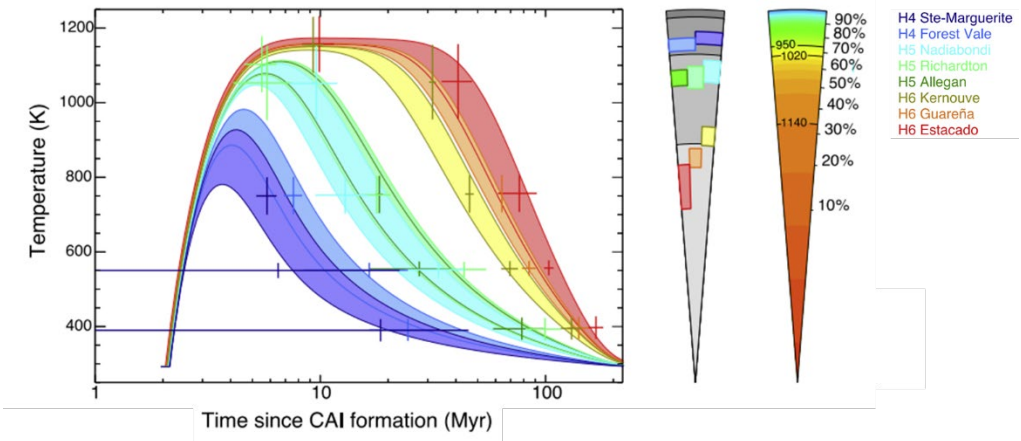

Figure 1.20: Thermal model for an accretion during 0.2Myrs and starting 2Myrs after CAIs formation. On the left side, the thermal evolution of the planetesimal in function of the time is represented. In the middle part is the best fitting radii for each meteorite. On the right–hand side is the radial distribution of temperature peaks in the planetesimal. The percentages indicate the volume of the body. Figure after Monnereau et al. (2013).

The large effect of metamorphism on ordinary chondrites and the potential link with core formation make them very interesting objects for the study of metal evolution after accretion. This aspect is going to be explored using germanium isotopes in ***Chapter 5****.*

2.2. Differentiation triggered by impact

Collision between planetesimals or asteroids were likely very common during the first steps of Solar System formation. Some authors have suggested that this can be a suitable heat source for planetesimal differentiation. The force of the impacts is classified from S1 (unshocked) to S6 (very strongly shocked), in which the whole rock is melted (Stöffler et al., 1991). Stöffler *et al.* (1991) have shown that the petrologic groups of ordinary chondrites correlate with shock stages, such that the Group 3 do not show S4 to S6-type shock stages while they are more common from 4 to 6. Moreover, to create an interconnected network of metal within silicates, the high dihedral angle of 60° is needed to be overcome (<60° is required for metal segregation within silicates). Either a high shock stage, or large degrees of partial melting, or both are required (Rushmer et al., 2000). This implies that the metallic liquid would not contain a large amount of sulfide as this lowers the degree of connection by sealing pores in the rocks (Néri et al, 2019). Moreover, impact leading to large scale melting is unlikely on small planetesimals (~100 km) as a large impactor would be needed to efficiently heat the planetesimal, which is likely to destroy the planetesimal instead of heating it (Davison et al., 2013).

Tomkins et al. (2013) have studied the fabric and the relationship between different types of metallic phases found in H chondrites. They conclude that, after an impact, the three stages of the process of metal migration can be described (Fig. 1.21):

1) Stoffler et al. (1991) show that impact-related shockwaves induce heating by compression/decompression. The heat induced can thus be located at the interface between

minerals with large differences in density. In this first phase, shockwaves produce friction between minerals which brings about the emulsion of metal and silicate (Tomkins et al., 2013).

2) Droplets of metal and sulfide will then migrate through the rock containing the silicate melt. Differences in viscosity between the metal and the silicate, and a higher speed of melting in the centre of veins than in the boundaries make isolated droplets of metal migrate to the margins of the veins. These droplets then form veins of connected metal and sulfide, independently from silicates. Moreover, the network of fractures created by the impact-deformation increases the permeability and allows metal-sulfide melts to migrate through it (Rushmer and Petford, 2011). Forinstance, in an H parent body with 10 vol.% metal content, it is possible to produce 1 m3 of pure metal in 2 minutes by extracting 50% of the Fe–metal contained in the rock. This process requires both a differential pressure of 1.44 bar (2.89 bar to extract metal in 1 min and 17.32 bar for 10 s) and a fault of 20 m^2 (Tomkins et al., 2013).

3) Sulfide-metal segregation starts when sulfides become dominant in the melt. This occurs at Fe-Ni-S eutectic during cooling. The remaining Fe-S melt wets the surface of silicates. Then porosity in the silicate matrix will act as capillary tubes for FeS, which drives the FeNi liquid away by differential pressure (Tomkins *et al.*, 2013).

After this last phase, metal migrates to form veins, then dykes. Contrasts in density and gravity will force the migration of the metallic liquid deeply into the planetesimal until those liquids form a planetesimal core.

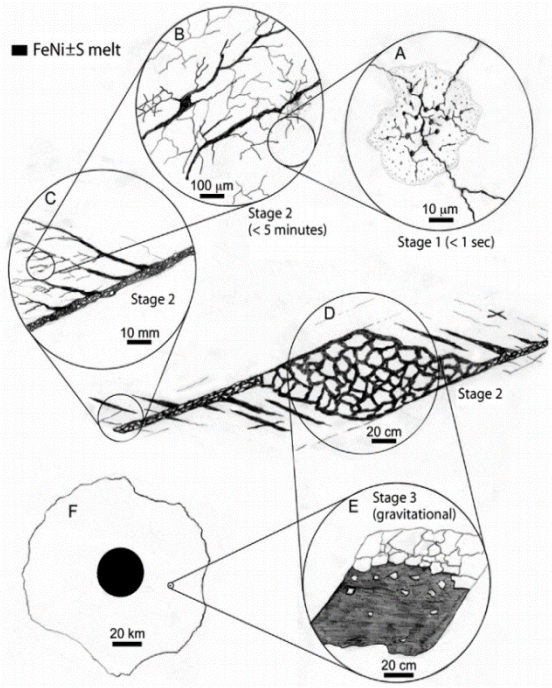

Figure 1.21: Schematic representation of the possible migration of metal triggered by an impact on a planetesimal. After Tomkins et al. (2013).

Regarding the effect of impacts on parent bodies as well as the possible migration of metal linked with it, the same evolution of germanium isotopic composition as for IIE iron meteorites is expected to occur . The consequences of an impact on metal migration are discussed in ***Chapter 5****.*

Chapter 2

Sample preparation and analytical techniques

Table of contents

I. Studied samples and protocols

This thesis aims to explore the formation and the evolution of metal phases from the early stages of Solar System formation to the accretion of first objects and their differentiation. We have chosen two different types of meteorites that are rich in Fe-Ni metal: the carbonaceous Bencubbin chondrites with 60 to 80 wt. % metal (CB, Chapter 3) to study condensation processes, the ordinary chondrites with 2 to 8 wt. % metal (H, L, LL groups; Chapter 4 and 5) to investigate redox processes in the solar nebula and the metamorphic processes on parent bodies body

This analytical chapter is organised into three sections: the petrologic characterisation of these meteorites, the elemental characterisation of metal and sulfide phases (chapter 3 and 4) and the germanium isotopes of bulk samples, and metal, sulfide and silicate phases (chapter 3 and 5). Two main points were followed during the analytical work:

1- Possible metal oxidation during sample preparation before analyses has to be avoided as it would have considerable effect on the elemental and isotopic composition. Thus, in all steps such as sample cutting, polishing, or cleaning, water is avoided and replaced by ethanol. When it was not possible, we have taken care to minimize the contact time between sample and water, and the sample was immediately rinsed with pure acetone and dried under a laminar hood.

2- Considering the rarity of some studied meteorites, a particular attention was given to the right quantity of sample necessary for a given technique in order to save samples for following studies. Finally, the volatile feature of germanium also requires a monitoring of the temperature and acids used during all chemical purification steps to avoid any loss. Then, the different protocols described below required a high degree of precision and skills.

This chapter describes the principles of the different analytical methods used during this thesis from sample preparation to in situ elemental analysis and then to germanium isotopic measurements. The figure 2.1 summarizes the different steps that have been carried out in the course of the thesis.

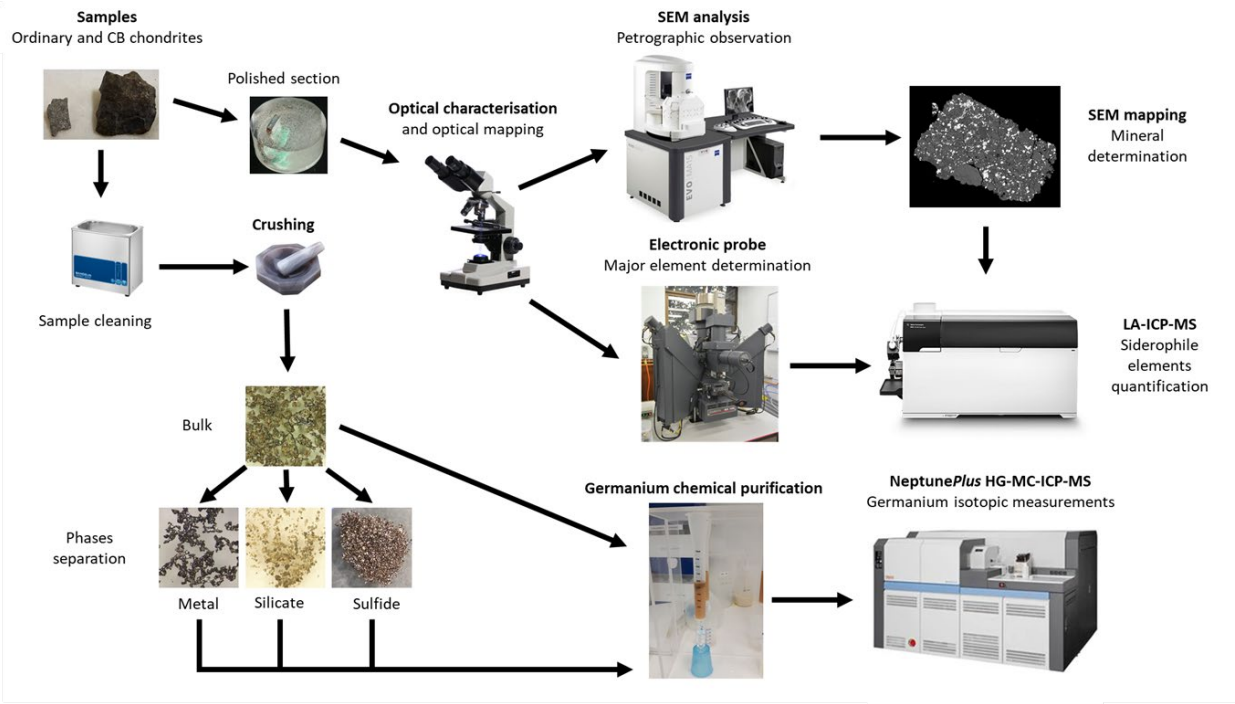

Figure 2.1: Global view of all the steps required for the chondrite analyses carried out during this PhD.

II. Preparation of meteorite polished section

A slice of sample, 1 to 3 mm thick is cut with a diamond wire or disk and cleaned with acetone for few minutes. When dry, the slice is placed in an indium ring adapted to electron microscope and the Laser Ablation–Inductively Coupled Plasma–Mass Spectrometry devices (LA-ICP-MS, ring size: 2.5 cm of diameter per 0.5 cm of thickness). This ring is filled with epoxy resin and put in an oven at 50 °C for the resin to be set during the night. As some chondrite samples are not very well consolidated, hand polish is preferred to automatic polishing that would scratch the surface by pulling off grains. The sample is polished by hand with sandpaper made of silicon carbide (SiC), starting by a coarse sandpaper P600 (600 grains/cm^2) to remove the resin and flatten the sample, then to a finer sandpaper P800 and P1200 (800 and 1200 grains/cm^2). Samples are then polished on a felt plate with a mixed of ethanol and diamond paste from 6 µm, then 3 µm, 1 µm, and finally ¼ µm grains. Between each step, the polished state is evaluated with optical microscope observation. Then, before starting another polishing step, diamond grains remaining stuck on the sample are removed by few minutes of ultrasonic vibration in ethanol. By following this protocol, it is possible to obtain a high-quality polish, even on metallic grains. For scanning electron microscope (SEM) or in the electronic probe techniques, the sample is covered with a carbon layer of 20 nm thick.

III. Optical and scanning electron microscope mapping

1 Mapping by optical microscope in reflected light

Optical microscope equipped with reflected light has been especially developed for the recognition of opaque phases in rocks. The first step is to perform optical mapping to highlight areas of interest that will be mapped by scanning electron microscope (Fig. 2.2 A; SEM) and analysed by LA–ICP–MS (chapter 3 and 4). These maps are also used to perform grain size calculations, circularity, percentages and repartition of mineral (chapter 4).

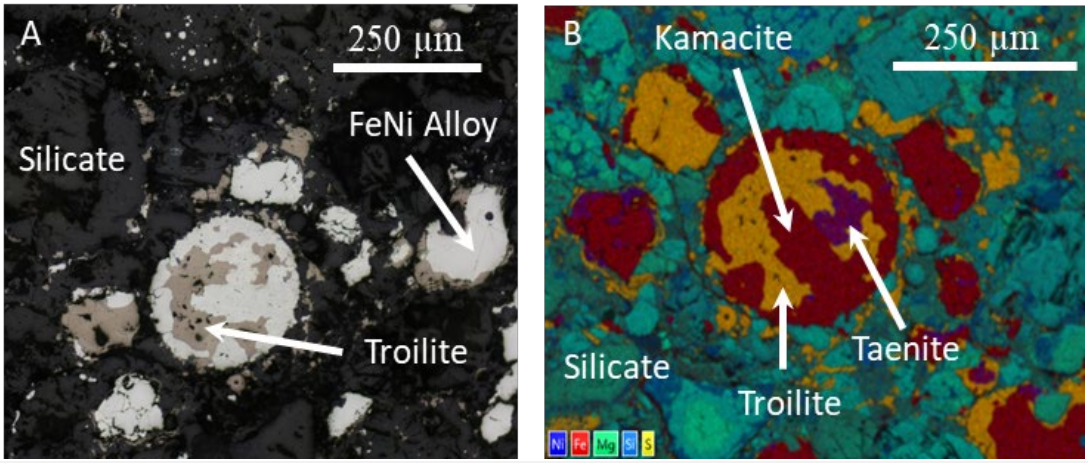

Figure 2.2: A) Optical picture of the different major minerals of Sharps (H3.4) sample. B) Combined BSE and EDX maps for the same area as in A. The different elements are represented with the following colours, Ni: dark blue; Fe: red; S: yellow; Mg: green; Si: light blue. They highlight the minerals present in the area. FeNi alloy: taenite (Ni–rich) or kamacite (Ni–poor); Troilite: FeS mineral.

2 Scanning electron microscope

The optical microscope has a maximum resolution of ~0.2 µm which can be enough in most cases. A higher magnification is sometimes needed to have a better understanding of the different phases and their relationship to each other. In this case, we used a SEM that has a maximal magnification of ~0.1 nm. This instrument can also provide qualitative or sometime quantitative elemental data that can be useful when some unknown minerals are identified. Two different scanning electron microscopes have been used, the JEOL JSM-6510 at the CRPG–Nancy and a Zeiss EVO MA15 tungsten filament SEM, at Macquarie University, Sydney, Australia, both equipped with a X-max silicon drift energy dispersive spectrometer (Bruker-AXS XFlash detector and an Oxford Instruments 20 mm^2, respectively).

The samples were mapped using a primary electron beam generated by a gun equipped of a tungsten filament heated at high temperature under a high voltage of 2 to 30 kV. This beam scans the sample surface and interacts with it, producing the emission of secondary electrons

(SE), back-scattered electrons (BSE), and Auger electrons. It also produces the emission of X–ray, as well as photons, that are used for cathodoluminescence.

The back-scattered electron process (BSE) results of the elastic interaction between the primary beam electron and the atomic core of elements. These produced electrons have a very high energy (~30 keV). The cone of electron sample-interaction is quite large (~1 μm^3), and electrons can be emitted from the inner part of the sample, such that this method of analysis is not affected by the topography of the sample. This interaction is also affected by the atomic number, which allows to have some qualitative chemical information. Thus, minerals that are composed of heavy atoms, Fe, Ni, or Cu for example, appear lighter than minerals with light atoms such as Si, Mg, Ca, or S. As a result, silicates are very dark compared to sulfide or to FeNi–alloy (Fig. 2.3 A).

The produced X–rays can be used together to the BSE images to give some semi–quantitative elemental concentrations. Elemental (Kα) X-ray spectrums (EDX map) are typical of each element, and the intensity of the X–ray emission is function of the quantity of the considered element. Thus, it is possible to deduce the elemental composition of a mineral and then to have the distribution of major elements in the sample (Fig. 2.2 B and 2.3). The association of these two techniques can highlight the difference between the kamacite (Fe–Ni–poor alloy) and the taenite (Fe–Ni–rich alloy), but also recognise different types of sulfides or secondary minerals such as chromite, and effect of the alteration on the FeNi and FeS mineral (Fig. 2.2 B and 2.3 B).

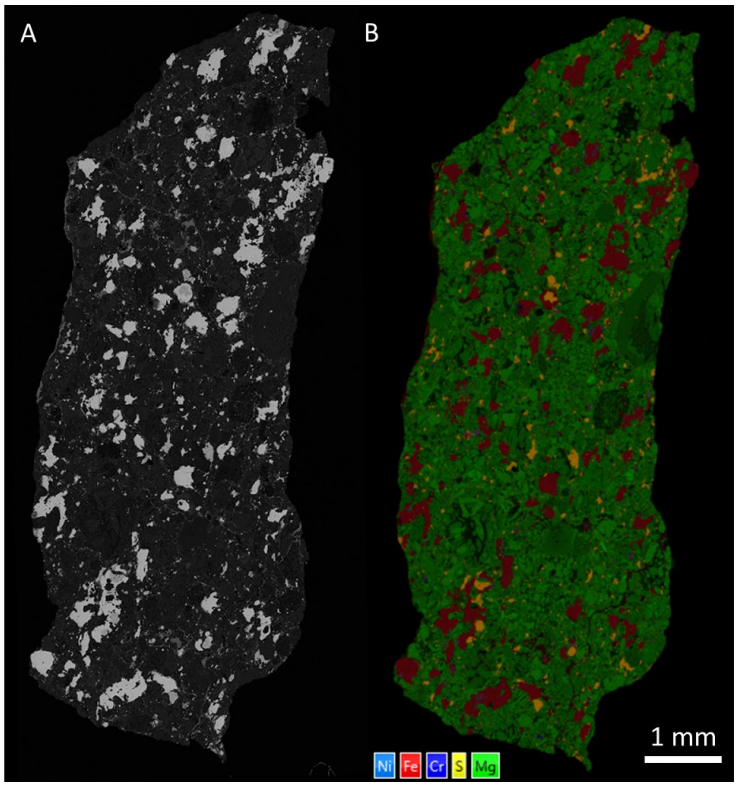

Figure 2.3: BSE (A) and EDX (B) maps of Azuna 881236. A) the dark phases are silicates; the white colour is FeNi–alloys and FeS minerals. B) The green represents the silicates; the different shades of green represent variation in the percentage of magnesium in silicates. The red is the kamacite, and the purple is the taenite. As for Mg, the difference between kamacite and taenite results of Ni proportion represented by higher tints of blue. The sulfides are in yellow.

IV. *In situ* elemental measurements by Laser Ablation–Inductively Coupled Plasma–Mass Spectrometry (LA–ICP–MS)

Ordinary and CB chondrites are primitive objects and consequently show complex petrological assemblage with large and fine metallic and sulfide grains, such that *in situ* methods are particularly suitable for elemental measurements in these types of objects. Moreover, during the two last decades the technical advances and the development of *in situ* siderophile measurements (PGE, HSE, and MSE) in metal and sulfide (e.g. Alard et al. 2000; Campbell and Humayun 1999) improved significantly the detection limits and enlarge the spectrum of elements that can be analysed.

1 Laser ablation system and ICP–MS

A Laser Ablation–Inductively Coupled Plasma–Mass Spectrometry or LA–ICP–MS is composed of two distinct parts: the Laser Ablation system, which is the method of introduction, and the Inductively Coupled Plasma–Mass Spectrometry, which is the system of elemental analysis (Fig. 2.4). The laser ablation system principle is to create laser via an Excimer source, which is used to ablate the sample on chosen mineral(s). The particles formed are then processed to be analysed by the ICP–MS.

The LA-ICP-MS used during this PhD is an Analyte G2 193 nm ArF excimer laser ablation system (Photon Machine, USA) coupled to a Agilent 7700cx ICP-MS. The laser system is composed of an ArF excimer laser source that create a 193 nm laser beam. This laser is processed by an optics that homogenised the beam, then the signal is modulated to the right spot size by the aperture. Depending of the sample that we want to analyse, the laser energy can be modified by the attenuator from 0% to 100% of the laser capacity. The final energy is the fluence, given in J/cm^2 (the fluence was 7.2 J/cm^2 for a pulse rate of 5 Hz for these studies). The laser beam is then transferred to the sample cell (HelEx cell) that is filled with a constant flow of helium (0.4 l/min^1 and 0.4 l/min^1 for the primary and the nested micro-cell, respectively). The helium gas is used for both reducing the surface deposition of ablated material and carrying ablated particles to the ICP–MS. The gas is mixed with argon after the HelEx cell (Ar flow c.a. 0.90 $\pm$ 0.05 l/min^1). Before entering in the mass spectrometer, the sample is ionised by the plasma torch. By adding hydrogen in the gas, it increases the ionisation rate in the plasma, and then, the quantity of ions created. This leads to an increase in intensity, stability and sensibility.

The created ion flux is separated after the interface from the neutral molecules and the photon by a magnetic deflector ("charge selector" on the Fig. 2.4). The ion beam is then "filtered" to remove molecular interference in the Octopole Reaction System (ORS) cell that is composed of an octopole filled with helium.

The purified beam enters in the mass analyser, which is composed of a quadrupole (Fig. 2.5 A). The role of the quadrupole is to select the ions that transit to the detector. In that aim, the quadrupole is composed of four parallel rods arrange around a central axis. On each rod a static and an alternating voltage is applied, such that two diagonally opposite rods have the same positive polarity whereas the two others have a negative polarity. The quick change in voltages modifies the polarity (~1MHz) of the rods and induces the formation and the fluctuation of an electric field. In function of the mass/charge ratio of the ion, at a given fluctuation of the field only one mass/charge ratio is stable. Ions that have a ratio that is too high or too small and that consequently are not stable with the electric field, are ejected from the quadrupole or hit the rods and are not analysed. Since we control the voltages of the rods and thus the electric field, it is possible to control which ions are stable and hence which elements are analysed. Then during analysis, the electric field changes regularly to successively analyse different elements. Once the ions have transited through the quadrupole, the ion beam enters the electron multiplier detector. The signal is first amplified by an electron multiplier (EM, Fig. 2.5 B) before reaching the detector. The principle of the EM is to increase the signal by converting a single ion in a large number of electrons. These are those electrons that are analysed by the detector. The laser parameters are given in chapter 3 and 5 as they may vary with in function of the study.

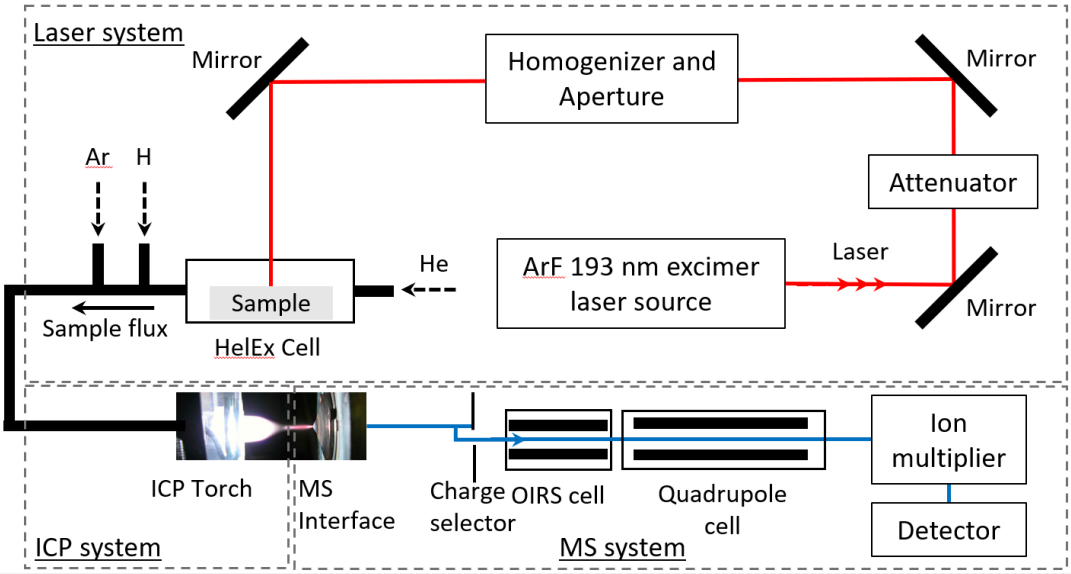

Figure 2.4: Representation of the major component of a LA–ICP–MS. The red line is the laser and the blue line is the ion beam after the plasma in the mass spectrometer.

2 Data processing and Signal selection

Different from multicollector equipped with Faraday cups, the results of this type of ICP–MS analyses are in number of counts. It implies that a standard of a known concentration is needed to convert these values in concentration. Thus a simple cross–multiplication can be achieved. Two different kinds of standards need to be distinguished, the external standard and the internal standard. The external standard refers to the standard material for which the concentrations of the elements of interest are known, and that is measured during the same analytical session than the samples. During this PhD, external standards were PGE-A (Ni–sulfide), FeS–1 (Fe–sulfide), and Filomena (IIA–magmatic iron meteorite), information on these standards are given in chapters 3 and 4. On the other hand, the internal standard refers to the elements that are used to as a reference to correct for statistical variability between standards and samples. It is also important for potential correction of physical interferences and matrix effect. During our measurements by LA–ICP–MS, we used the Fe, Ni, and S as internal standards, depending of the composition of the external standard used and of the sample measured.

V. Bulk elemental and isotopic measurements of germanium by ICP–MS and MC–ICP–MS

The development of new analytical technologies and new generations of Multicollector–Inductively Coupled Plasma–Mass Spectrometry (MC–ICP–MS), such as the Neptune*plus,* has allowed the production of high-precision and high reproducibility isotopic measurements. In cosmochemistry, the use of stable isotopes as clues for investigating processes in the Solar System and planet formation is one of the major advances these last decades (e.g. Luais 2007; Wombacher et al. 2008). These new techniques provide the opportunity to study in detail metal elements and to refine our understanding of models developed on the basis of elemental composition (e.g. ordinary chondrite formation, Kallemeyn et al. 1989). From the last two decades, techniques for germanium isotopic measurements have been developed, such that the common precision for a measurement performed on a MC–ICP–MS with a hydride generator (HG) as introducing system is better than 0.1 ‰ for 4 mass units (Escoube et al., 2012; Hirata 1997; Luais, 2007, 2012; Rouxel and Luais, 2017; Rouxel et al., 2006). This part describes the chemical procedure for germanium isolation, elemental measurements using quadrupole ICPMS, and isotopic measurements using a HG–MC–ICP–MS ThermoScienfic Neptune*Plus* at the CRPG–Nancy (France). The reader is invited to refer to Luais (2007) in which the full procedure for analysing

germanium in metal phase (iron meteorites) has been described. Further information are given in Belissont et al. (2014) for sulfide measurements, and in Luais (2012) and Florin et al. (2020) for silicate purification.

1 Sample preparation

Whereas sample measurements using LA–ICP–MS do not require a lot of preparation, elemental analyses, and isotopic analyses of germanium by Multicollector–Inductively Coupled Plasma–Mass Spectrometry (MC–ICP–MS) are more complex. As we are measuring atoms with very small difference of mass, isotopic analysis requires a high precision to be able to deconvolute each isotopic mass and thus interferences need to be minimized. Therefore, protocol for sample preparation, and germanium extraction and purification from other elements of the matrix, include three steps:

1) Sample crushing and phase separation
2) Sample digestion
3) Chemical purification of the germanium

1.1. Sample crushing and phase separation

After cutting the sample for making polished section, we also recover chip for bulk elemental and isotopic measurements. The weight of that fragment is usually 500 mg. This will allow the analyses of all mineral phases (metal, silicate and sulfide) and the bulk meteorite. However, for more rare or unique samples, we use the minimum mass of material, which is function of the germanium concentration of the sample. For one isotopic analysis composed of three replicates, around 75 ppb (75 ng/g) of germanium are needed. For example, in the case of CB chondrite, with a Ge concentration of 1 ppm (meaning 1µg/g), a minimum mass of 75 mg is processed.

After fragment selection, the sample is successively cleaned with diluted 0.2M HNO_3 for few minutes, distilled H_2O and acetone under cold ultrasonic bath, and dried under laminar flow hood. The sample is gently crushed in an agate mortar. Half of the crushed sample is further powdered for bulk elemental and isotopic measurements. The remaining will be used for separation of mineral phases. Separation of the metal phase is performed by using a hand magnet. The silicates that could be still stuck on metal grains are separated using ultrasonic bath. After metal separation, the sulfides are manually separated from the silicates under a binocular magnifier. The silicates are cleaned by successive leaching at room temperature with 6M HCl, distilled water, 2M HNO_3, and distilled water at room temperature. Finally, the metal is cleaned by leaching for few minutes at room temperature with 0.2M HNO_3, rinsed with distilled water and then with pure acetone to removed water. This protocol has been published in Florin et al.

(2020) and is described in detail in the chapter 5. Using this methodology, we obtain three pure phases (metal, silicate and sulfide) with the bulk sample.

1.2. Sample digestion

The germanium is a moderately volatile element and can behave as a highly volatile element while complexed with halogens and especially with chlorine (Luais, 2012). Then, during germanium purification, the use of HCl needs to be avoided during digestion or resin elution and in no instance, can the samples be exposed to a temperature higher than 60°C (Luais 2012). Distinct protocols are applied according to the mineral phases.

Bulk, silicate and sulfide samples are digested in a mixture of 1ml of 15 M HNO_3 and 3 ml of 29 M HF for a week in a Teflon beaker on a hotplate at 60°C. The bulk of meteorites can contain oxide mineral (e.g. chromite) that cannot be digested at 60°C, whatever the quantity of acid. Thus, bulk samples are digested under pressure (~25 bar), and at a temperature of 150°C in an oven, in sealed Bola Teflon bombs for a week (Luais et al., 2009). On the other hand, the metal is far easier to process and is usually digested overnight in 2 M HNO_3 on a hot plate at 60°C. When metal and sulfide solutions are fully digested (i.e. the solution is orange with no solid particles still present), they are evaporated to dryness and re–dissolved in diluted 1 M HF for the next steps of purification.

During the digestion of silicates and bulk samples, fluor may have complexed with silicon, such that a white Si–F complex residue is present in the solution. The solution is centrifuged, and the supernatant containing germanium is recovered. To ensure a full recovery of germanium, the white precipitate is leached with concentrated HF, and the supernatant is recovered after being centrifuged and added to the first supernatant solution. This procedure is repeated three times. The obtained solution is evaporated to form a gel, re–dissolved in concentrated 15 M HNO_3, and finally evaporated to dryness. The solution is ready for germanium purification, as well as for elemental quantification by ICP–MS when rediluted in 0.5 M HNO_3.

1.3. Chemical purification of the germanium

1.3.1. Ionic exchange resin theory

The germanium purification from the matrix is achieved with the use of ion-exchange resins by chromatography. The theory of ion-exchange chromatography has been described in numerous scientific communications (i.e. DeCarlo et al. 1981; Korkisch 1989). These resins are composed of large polystyrene chains to which functional groups are attached via a divinylbenzene molecule (Fehr et al., 2004; Korkisch, 1989; Paterson, 1970; Peters et al., 1974; Schönbächler, 2016).

In principle, during ion-exchange equilibrium, the counterion of the resin is replaced by an ion from the solution that has the same charge. Thus, when a solution is loaded on an ionic resin, the elements present in that solution will be partitioned at equilibrium between the resin and the solution. Elements that have an equilibrium distribution coefficient (Kd = concentration in the solid/ concentration in the liquid) >1 are adsorbed on the resin and stored in the ion exchange site forming electronic liaisons with this site (Schönbächler, 2016). The distribution of the elements between the resin and the solution depends on the acid type and its molarity. Then, for a specific acid volume with a given molarity, it is possible to select which elements to be adsorbed on the resin, and those to be eluted. The types of elements adsorbed on the resin depend on their nature and charge in the solution and on the functional groups of the resin. For example, during this work for Ge purification, two types of resins were used, the anionic Bio–Rad™ AG1–X8 chlorine form, 200–400 mesh resin, and the cationic Bio–Rad™ AG 50W–X8 hydrogen form.

The AG1–X8 chlorine form resin has a $CH_2N^+(CH_3)_3$ site fill with a Cl^- counterion, then the common reaction occurring with this resin is (equation adapted from the AG1–X8 anion exchange resin manual edited by Bio–Rad™):

$$\text{Resin–}CH_2N^+(CH_3)_3 \cdot Cl^- + A^- = \text{Resin–}CH_2N^+(CH_3)_3 \cdot A^- + Cl^-$$

where A^- is a negatively charged molecule such as $GeO^{2-}{}_3$ or $GeO(OH)^-{}_3$. Thus, during the equilibrium between the resin and the solution, germanate ions can be adsorbed on the resin by substitution to ion chlorine. The germanium has a high affinity for this resin that is used to separate Ge from the majority of other constituents (*i.e.* the alkalis, Mn, Al, Co, Ni, Zn, Ga, and most Fe and Mg, Figure 2.5 A).

The AG 50W–X8 hydrogen form resin reacts as follow (equation adapted from the AG 50W–X8 cation exchange resin manual edited by Bio–Rad™):

$$\text{Resin–}SO^-{}_3 \cdot H^+ + C^+ = \text{Resin–}SO^-{}_3 \cdot C^+ + H^+$$

where C^+ is a cationic constituent. In acid solutions, germanium does not occur as cation, and thus is not adsorbed on this resin. It can then be separated from all the cationic constituents, and especially mostly from Fe and Ni (Figure 2.5 B).

1.3.2. Germanium purification

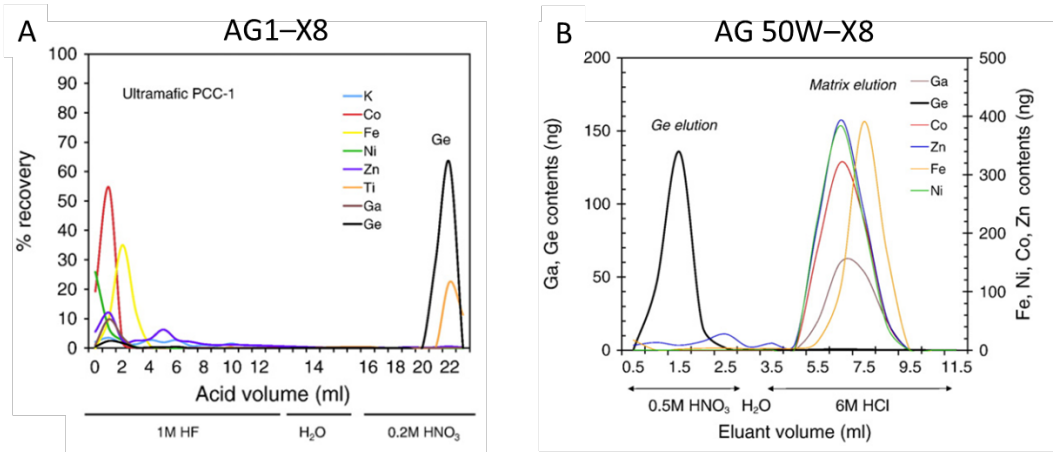

Figure 2.5: Elution curves for germanium using (A) AG1–X8 chlorine form and (B). AG 50W–X8 hydrogen form. Diagrams from Luais (2012).

After digestion, samples are processed for elemental separation in two steps of ion-exchange chromatography (Fig. 2.6). Bulk sample solutions, equivalent to about less than100mg of sample to avoid resin saturation, as well as silicates and sulfide solutions are firstly loaded on columns filled with 2 ml of the anionic Bio–Rad™ AG1–X8 chlorine form to separate the alkalis, Mn, Al, Co, Ni, Zn, Ga, and most Mg and Fe. During that step, all these elements are eluted with 12 ml of 1M HF, whereas germanium is highly compatible and remains adsorbed on the resin. Then, the resin is cleaned from HF with water, and the germanium is recovered in 4 ml of 0.2 M HNO_3. The obtained Ge fraction is evaporated to dryness at 60 °C on hot plate. Secondly, Ge fraction of sulfide, silicate, bulk samples from the first column, and metal separate solutions follow the same step of cationic exchange chromatography. They are dissolved in 0.5 M HNO_3 and an equivalent of up to 10 mg of metal is loaded on 2 ml of AG 50W–X8 hydrogen form for which the germanium has no affinity. Whereas metal elements (Fe, Ni, Co) are adsorbed on the cationic resin, germanium is eluted and 100% recovered in 2ml of 0.5 M HNO_3. At the end of that step, the solution is ready for analysis by HG–MC–ICP–MS. In the case of Bencubbin chondrites, this protocol has been adapted to large samples (up to 60 mg of metal) and the column calibrated for this purpose. This particular protocol is described in the chapter 3.

2 Elemental measurements of solution by ICP–MS

Solution ICPMS analyses provide the elemental composition of bulk samples. The digested sample from the previous digestion step (see section germanium purification) is dissolved with diluted HNO_3. The sample is introduced in the ICP–MS via a peristatic pump and the liquid is transformed in an aerosol via a nebuliser. This aerosol is transferred to the plasma where it is ionised. The created ion beam is processed in the mass spectrometer (Fig. 2.6)

Standards at higher and lower concentrations than the sample, but also close to the supposed sample concentration are analysed to create a calibration line between the number of counts and the concentrations. Then the sample is measured, and the calibration line is used to calculate its concentration from measured counts number. In addition, indium is used as an internal standard for correcting intensity drift during a session. For that, 10 ppb of In is added in each solution.

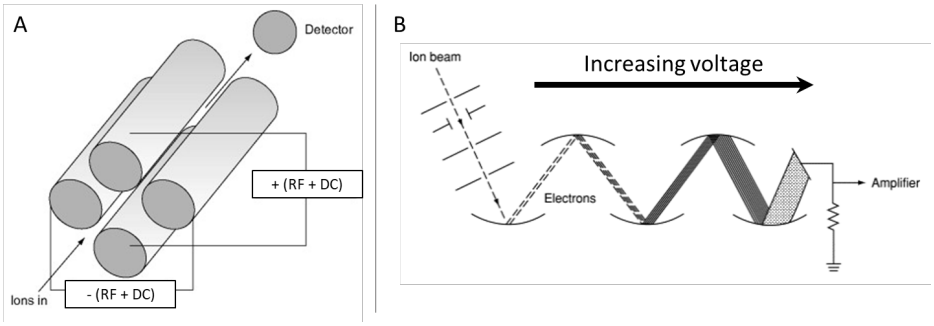

Figure 2.6: A) Representation of a quadrupole. RF voltage: alternative potential; DC voltage: Static potential. B) Schematic representation of an electron multiplier and of the increasing voltage. Figure modified from McFadden (1973).

3 Germanium isotopic measurement by Hydride Generation–Multicollector–Inductively Coupled Plasma–Mass Spectrometry

3.1. The ThermoScienfic NeptunePlus HG–MC–ICP–MS

Germanium isotopic measurements have been performed using the ThermoScientific Neptune*Plus* MC–ICP–MS at the CRPG-Nancy. The general principle of a MC–ICP–MS is to create an Argon plasma with a temperature of 8000 – 9000 K capable to ionize the elements (Fig. 2.7 A). Elements with a first ionization energy (I_E) less than 7 eV are fully ionized and the ionization yield is about 90% for elements with an I_E up to 10.5 eV. Only elements that have an $I_E > I_E(Ar)$ (i.e. 15.76 eV) are poorly ionized (Albarède and Beard, 2004). Germanium has an I_E = 7.9 eV consequently, more than 95% of Ge is ionized in a plasma at 8000 K and 99% for a temperature of 9000 K.

The solution in diluted HNO_3 (or a gas in the case of the Hydride Generator Introduction system, see below) is introduced in the plasma to be atomised. The collision with electron in the plasma ionizes the atoms. These ions are extracted from the plasma by the difference of pressure at the plasma interface, and a 2kV ion acceleration voltage lens behind the sample cone. The ion beam is focused by the ion transfer optics in order to maximise the measured intensity. Then, ions are classified in function of their energy and their mass/charge ratio by an electrostatic (Fig. 2.7 B) and a magnetic sector (Fig. 2.7 C). The ionized atoms or molecules are then analysed using Faraday cups (Fig. 2.7 D) and the signal is electronically amplified to be detectable. This

double atomic classification allows a maximal mass resolving power (MRP, see equation 2.3) of 8000 on the Neptune*Plus*.

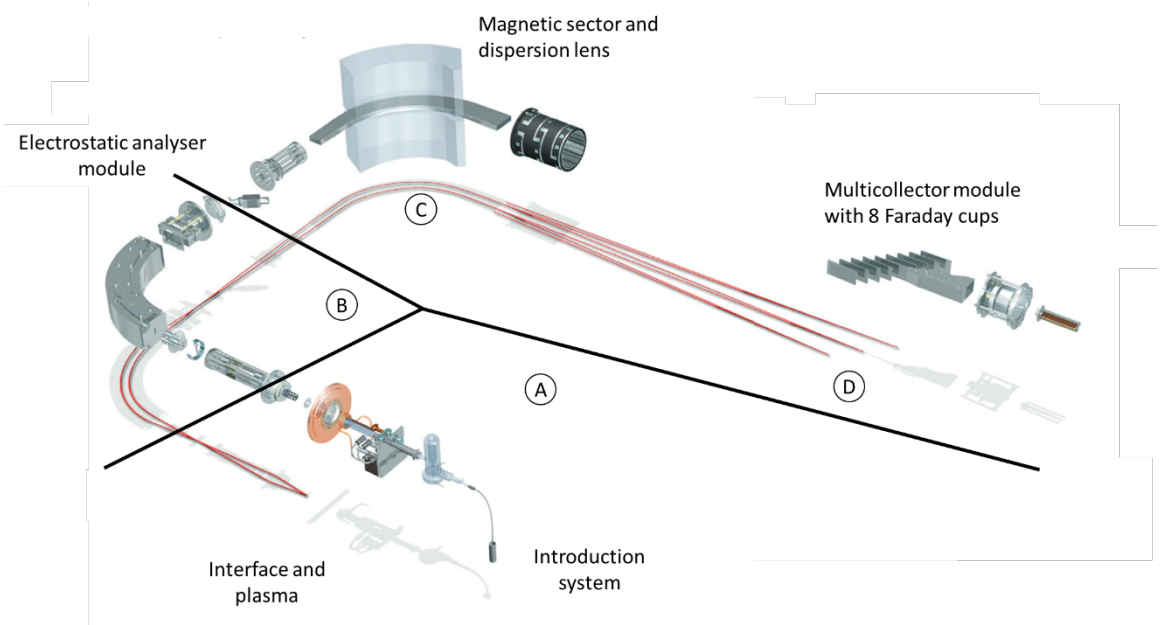

Figure 2.7: Representation of a Neptune *XT* MC-ICPMS components and the ion beam trajectory (red line). A) The ICP module with the introduction system, the plasma torch and the interphase. B) Electrostatic analyser (ESA). C) Magnetic sector and dispersion lens. D) Faraday cups. Figure adapted from ThermoFisher Scientific documentation (www.thermofisher.com)

3.1.1. Introduction system

Different types of introduction systems can be connected to the Neptune*Plus*, such as laser ablation system, multi–chamber spray, gas chromatography, or a hydride generation system. For the germanium isotopes analyses, the chosen mode is the hydride generation (HG) system (Fig. 2.9): the HGX–200 (Teledyne CETAC Technologies) (Fig. 2.8). The sample solution is mixed with a highly reducing agent, such as $NaBH_4$, in order to produce hydride species by the reduction of the elements in solution. By this process, volatile species of germanium are formed. However, elements that do not form volatile hydride, such as Zn and Se, in the case of a solution of HNO_3 reacting with $NaBH_4$, remain in the liquid. This system has two major advantages. First of all, it allows separation of the germanium from the small amount of matrix that could remain even after its chemical purification, avoiding matrix effect. It avoids the interferences of Zn or Se on the mass 70 or 76, respectively, as these elements are not creating hydrides (See table 2.1 below). However, all the ratios are corrected for ^{70}Zn interferences on ^{70}Ge. Compared to a spray chamber where 90% of the solution is wasted, 100% of the germanium of the solution can be analysed when using an

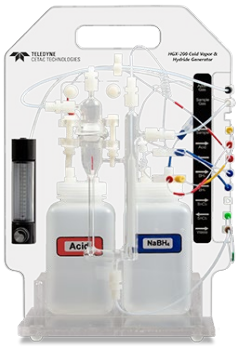

Figure 2.8: HGX–200 (Teledyne CETAC Technologies) at the CRPG-Nancy.

HGS. It implies an increase of the sensitivity and only 10 ng of Ge are needed for one analysis in routine. Also, some tests showing a good reproducibility have been done at 5 ng.

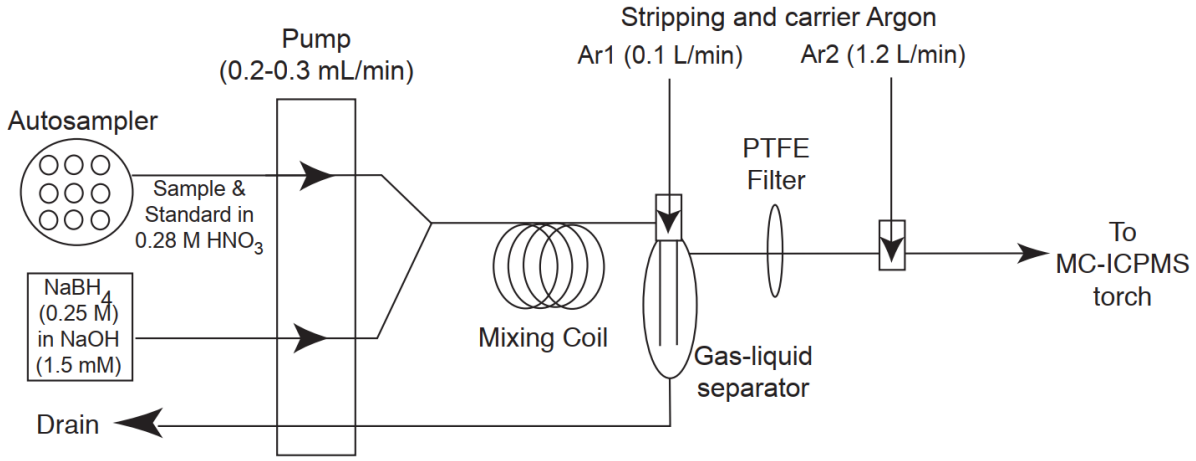

Figure 2.9: Representation of the hydride generation system. From Rouxel and Luais (2017).

3.1.2. Ion dispersion by electrostatic analyser and magnetic sector

The Electrostatic analyser module or ESA (Fig. 2.7 B) focuses ions as a function of their kinetic energy via an electrostatic field which allows filtering of ions as a function of their energy and to perform elemental selection. The principle is to change the trajectory of the different ions, by applying a difference of potential between two metallic surfaces shaped as an angle. The relation that linked the radii of curvature (R) of the ions trajectory with their kinetic energy (K_e) and the electrostatic field (E) is:

$$R = \frac{2*K_e}{E} \qquad \text{Eq. 2.1}$$

Thus, the ions are grouped according to their energy decreasing from the outer to the inner part of the curve. The final ion beam energy is of 10 keV before entering in the magnetic sector.

The magnetic sector (Fig 2.7 C) changes the angle of the ion beam trajectory, by generating a high magnetic field. The ions are separated in function of their mass with the heavier having the larger radius of curvature. The trajectory of ion (R) is linked to the mass (m), the charge (q), the kinetic energy (K_e) and the magnetic field (B) by the formula:

$$R = \frac{1}{B} * \sqrt{\frac{2*m*K_e}{q}} \qquad \text{(Eq. 2.2)}$$

The resolution of a MC-ICP-MS is expressed as the Mass Resolving Power (MRP), a ratio that quantifies the capacity of a mass spectrometer to separate two atomic or molecular ions. Thus, the closer the two ions masses are, the higher the resolution needs to be (low: 2000;

medium: 6000; high: 8000). The MRP is calculated as the ratio between the mass considered and the size of the spectrometer ray at 10% of its height. (Eq. 2.3)

$$MRP = \frac{m}{\Delta m} \qquad \text{Eq. 2.3}$$

with m the considered mass and Δm the difference in mass of the two ion species to be separated. For germanium isotopic measurements, recent developments have suggested to measure the Ge isotopes on the left part of the Ge spectrum, free from any interferences, at medium mass resolution (m/Δm = 6000, El Korkh et al., 2017).

To change the resolution and the MRP, two different slits exist on the Neptune*Plus*: one before the ESA (resolution slit) and one between the ESA and the Magnetic sector (energy slit). The resolution plate has three resolution slits corresponding to a large, medium or small width that allow to work in three modes: the low resolution, medium resolution and high resolution in order to filtrate interferences (corresponding to an MRP of 8000, 6000 and 2000 respectively). By moving the resolution plate to place the ion beam in the direction of the small width slit, hence increasing the mass resolution (MRP), we remove a large part of the molecular interferences, but also decreasing the intensity of the signal. The recent use of the Hydride Generator system that permit to avoid any interferences (see section 3.1.1) allows to perform the measurements at low resolution mode, thus increasing the intensity.

3.1.3. Faraday cups and collection mode

The Neptune*Plus* is equipped of 9 Faraday cups (H4, H3, H2, H1, C, L1, L2, L3, L4) that are associated to 10^{11} Ω resistors, and that convert each ion impact in ion current. To correct for the electronic noise, a base line is performed before each session. Additionally, the yield of Faraday cups is tested with an electronic signal to calculate the yield factor correction. Faraday cups are moved and positioned to collect the ion beams with specific masses. However, because of the maximum space between the two opposite cups (H4 and L4) is not extensible, some limitations apply to the masses that can be collected at the same time. Thus, the maximum mass difference between the two extreme cups is about 17%. In the case of germanium, the mass dispersion is such that we are using the cup from L3 to H3, and the analysis can be done in static mode. Yet for very small mass, the mass dispersion is so large that the two extreme cups are used. If it is not possible to measure all the elements at the same time, the Neptune*Plus* can be set in dynamic mode.

The germanium measurements have been done using a hydride generator in static mode, with the Faraday cups distributed as followed: ^{68}Zn, ^{69}Ga, ^{70}Ge, ^{71}Ga, ^{72}Ge, ^{73}Ge, and ^{74}Ge isotopes that correspond to the L3, L2, L1, C, H1, H2, and H3 Faraday cups (Table 2.1), respectively. Before starting a session, we verify that:

1) The different mass peaks are well centred with the Faraday cups by doing a “peak centre”

2) The correction factor of the Faraday cups

The common intensity reported for a 10-ppb solution is about 1.5 to 2.5 V, which can slightly vary between sessions in function of the instrument focalisation. Each measurement was composed of 40 cycles of 8 s signal inxtegration. The procedural blank represents less than 0.1 % of the 100 ng routinely processed for sample/standard measurements. Then no blank correction was applied.

Table 2.1: Table of isotope abundances and isobaric / molecular interferences (May and Wiedmeyer 1998). Cup configurations for Ge isotope measurements are indicated.

Isotope	Abundance	Cup	Interferences
^{68}Zn	18.75 %	L3	$^{40}Ar^{14}N_2$
^{69}Ga	60.11 %	L2	–
^{70}Ge	20.84 %	L1	$^{40}Ar^{14}N^{16}O$, $^{35}Cl^{17}O^{18}O$, $^{37}Cl^{16}O^{17}O$, $^{34}S^{18}O_2$, $^{36}S^{16}O^{18}O$, $^{36}S^{17}O_2$, $^{34}S^{36}S$, $^{36}Ar^{34}S$, $^{38}Ar^{32}S$, $^{35}Cl_2$, $^{54}Fe^{16}O$
^{71}Ga	39.89 %	Centre	–
^{72}Ge	27.54 %	H1	$^{36}Ar_2$, $^{37}Cl^{17}O^{18}O$, $^{35}Cl^{37}Cl$, $^{36}S^{18}O_2$, $^{36}S_2$, $^{36}Ar^{36}S$, $^{40}Ar^{32}S$, $^{56}Fe^{16}O$, $^{40}Ar^{16}O_2$, $^{40}Ca^{16}O_2$
^{73}Ge	7.73 %	H2	$^{36}Ar_2H$, $^{37}Cl^{18}O_2$, $^{36}Ar^{37}Cl$, $^{38}Ar^{35}Cl$, $^{40}Ar^{33}S$
^{74}Ge	36.28 %	H3	$^{40}Ar^{34}S$, $^{36}Ar^{38}Ar$, $^{37}Cl^{37}Cl$, $^{38}Ar^{36}S$

3.2. Analytical mass fractionation

Instrumental mass fractionation in an MC–ICP–MS is the result of variable transmission of the ion beam in the spectrometer. It mostly takes place in the plasma source or at the interface, between the source and the ICP–MS module. The first mass bias is due to mass dependent fractionation that may be produced in the plasma if the dissociation of the analytes and the elemental ionization is incomplete. Mass fractionation also occurs at the MS interface as some light isotopes deviate preferentially from the axial ion beam, due to loss from the expansion chamber (Albarède and Beard, 2004). Thus, the heavy isotopes are more efficiently transferred than the light ones, which means that the measured isotopic ratio is always heavier than the true one. The correction from this analytical mass fractionation can be done using power or exponential law using an internal or external standard, or by the use of sample bracketing method (Albarède and Beard, 2004).

For germanium measurements, the focusing parameters (i.e. lens focussing, flow gas, plasma position etc.) between sessions induce small variable instrumental mass fractionation (Fig. 2.10). Yet during the same session of analysis, the results lie on a similar ln ($^{72}Ge/^{70}Ge$) vs ln ($^{74}Ge/^{70}Ge$) masse fractionation line with very similar slopes and excellent correlation coefficient. All the line parameters (slope and origin intercept) also indicate that the different fractionation line intersects lie near zero and then can be forced to the origin. Thus, the slopes

of regression lines are very close from the theoretical slopes (~0.5068) calculated from exponential law:

$$a = \frac{ln\left(\frac{m^{72}Ge}{m^{70}Ge}\right)}{ln\left(\frac{m^{74}Ge}{m^{70}Ge}\right)} \quad \text{Eq. 2.4}$$

Luais (2012) demonstrate the accuracy of mass bias correction and that internal correction of the mass fractionation is not suitable for Ge as it would erase the natural mass dependent fractionations. Before the use of the hydride generator, the correction for mass fractionation was done using Ga isotopes. The chemistry removing efficiently Ga from Ge, samples (and standards) are doped using a standard of known isotopic composition (i.e. NBS SRM 994 Ga; $^{69}Ga/^{71}Ga = 1.50676$). By doing that, the samples will have different Ge isotopic ratio, but similar Ga isotopic ratios and it is possible to parameterise mass fractionation using exponential laws (Luais et al., 1997; Luais 2012; Eq. 2.5 and 2.6):

$$(^{74}Ge/^{70}Ge)_{True} = (^{74}Ge/^{70}Ge)_{meas} * (m_{74}/m_{70})^{fGe} \quad \text{Eq. 2.5}$$

$$(^{71}Ga/^{69}Ga)_{True} = (^{71}Ga/^{69}Ga)_{meas} * (m_{71}/m_{69})^{fGa} \quad \text{Eq. 2.5}$$

where m is the mass of considered isotopes, and *f*Ge, *f*Ga the mass bias parameters for Ge and Ga. Therefore, three methods can thus be used to correct for mass fractionation:

1) Sample–standard bracketing methods (SSB)
2) *f*Ga assuming that *f*Ga = *f*Ge
3) Regression line method with *f*Ga ≠ *f*Ge and *f*Ga / *f*Ge = constant

The consistency between these methods of instrumental mass bias correction allows considering that SSB method is accurate (see Luais, 2012 for more details).

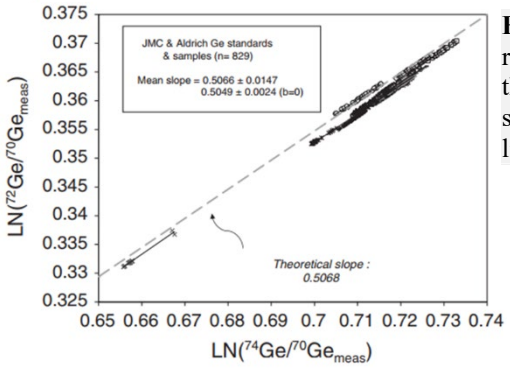

Figure 2.10: Long term data set of Ge measured isotopic ratios. On a ln($^{72}Ge/^{70}Ge$) vs ln($^{74}Ge/^{70}Ge$) diagram, all the data fall on mass fractionation lines that have the same slope, close from the theoretical mass fractionation line (see text). After Luais (2012).

The recent use of hydride generator for germanium isotopic measurements (Rouxel et al., 2006; Escoube et al., 2012; Rouxel and Luais, 2017) imply that Ga does not from hydrides, thus the Ga method is not used. The instrumental mass fractionation can be monitored by sample/standard bracketing methods and is used during this study.

3.3. Report of Germanium isotopic values

For measuring the germanium isotopic compositions of our samples, we used the sample/standard bracketing technique, which implies to measure, before and after each sample, a reference standard, with similar sample–standard intensity within 10%. This method allows correcting for the progressive shift of the intensity ratios during a session that can be up to $3.5*10^{-3}$. The germanium reference standard used for normalization is the NIST 3120a (Lot #000411, 1000µg/ g Ge, Escoube et al., 2012; Luais, 2012). Each measurement is composed of 320 s data acquisition sequence distributed in 40 cycles of 8 s each. The isotopic composition is reported in per mil delta notation, using the $^{x}Ge/^{70}Ge$ ratio and taking into account the mean intensity of the two NIST 3120a standards measured before and after each sample (Eq. 2.3).

$$\delta^{x/70}Ge_{NIST3120a} = \delta\ {}^{x}Ge/^{70}Ge = \left(\frac{(^{x}Ge/^{70}Ge)_{Sample}}{(^{x}Ge/^{70}Ge)_{NIST3120a}} - 1\right) * 1000 \qquad \text{(Eq 2.3)}$$

In order to have references to validate our measurements, known Ge standards and geostandards that have been cross-calibrated between laboratories (Escoube et al., 2012) are run during analytical sessions. The different standards used during this PhD are the JMC Ge (1000 ppm ICP standard solution, Lot # 301230S, Johnson Mattey, Karlsruhe, Germany) and the Aldrich Ge (10200 ppm ICP standard solution, Lot#01704KZ, Aldrich Chemical Co., USA) standards, the BIR–1 geostandard (Ge = 1.52 ppm, Iceland basalt, coarse-grained olivine tholeiite (dolerite), USGS, USA), and the in-house Magura iron meteorite standard for metal phase (Luais, 2007). The mean values and the long-term reproducibility of these standards during the course of the PhD project are given in table 2.2.

Table 2.2: Germanium isotopic values of standards and geostandards relative to the NIST3120a, and their reproducibility.

	This study				Rouxel and Luais (2017) and Luais (2012)			
	$\delta^{72}Ge/^{70}Ge$	$\delta^{73}Ge/^{70}Ge$	$\delta^{74}Ge/^{70}Ge$	n*	$\delta^{72}Ge/^{70}Ge$	$\delta^{73}Ge/^{70}Ge$	$\delta^{74}Ge/^{70}Ge$	n*
JMC Ge	-0.15	-0.19	-0.32	95	-0.16	-0.23	-0.32	30
2σ SD	*0.08*	*0.13*	*0.11*		*0.07*	*0.12*	*0.1*	
Aldrich Ge	-1.01	-1.52	-1.97	99	-1.03	-1.54	-2.01	182
2σ SD	*0.07*	*0.13*	*0.12*		*0.12*	*0.17*	*0.23*	
BIR-1	0.32	0.42	0.59	9	0.24	0.47	0.57	6
2σ SD	*0.04*	*0.07*	*0.06*		*0.04*	*0.06*	*0.04*	
Magura	0.42	0.58	0.78	19	0.44	0.63	0.86	13
2σ SD	*0.06*	*0.11*	*0.08*		*0.03*	*0.05*	*0.05*	

*: n is the number of measurements.

Chapter 3

Processes of metal formation by condensation

Table of contents

I. Chapter introduction

The first solids of our Solar System have been formed by the condensation of the gas of the protoplanetary disk. The sequence of condensation has been described by thermodynamic calculations. The temperature of condensation of each element being expressed as $T_{50\%\ condensation}$, corresponding to the temperature at which half of the abundance of a considered element is condensed in the solar nebula. These temperatures are only valid for specific conditions of the solar nebula, a total pressure lower than 10^{-2} bar, close or at solar metallicity, and at very low oxygen fugacity of ~IW-6 (i.e. 6 log unit bellow the Iron-Wüstite buffer, Grossman et al. 2008; Sossi and Fegley 2018). As described in the thesis introduction, condensation of the siderophile elements is function of their volatility, such that the first siderophile elements condense at ~1800 K (i.e. Os, Re, W etc.) in the form of refractory metal alloys. It is only after this first phase of condensation that the major siderophile elements (Fe, Ni, Co) will condense (around 1350 K, Wood et al. 2019). During the condensation of Fe, Ni and Co, refractory alloys will be incorporated in FeNiCo alloys because of their siderophile behaviors. Subsequently, with decreasing temperature, siderophile elements that are more volatile, such as Au, Ge, or Ga, will condense onto metal grains and then react with it, leading to their incorporation into these grains (e.g. equation 3.1, Wai and Wasson, 1979).

$$GeS_{(g)} + H_{2\ (g)} = Ge_{(s\ in\ FeNi)} + H_2S_{(g)} \qquad \text{Eq. 3.1}$$

The condensation of elements have been described by theoretical calculations with different methods of ab-initio calculation (Langhoff and Bauschlicher 1988), Calphad modeling (Saunders and Miodownik 1998) by free-energy minimization programs (e.g. Lodders 2003; Wood et al. 2019), and by experiments on equilibrium partial pressure of metal species (e.g. Knudsen Effusion Mass Spectrometry, Copland and Jacobson 2010). As a result, we have a very good understanding of how condensation of element occurs. On the other hand, the effect of condensation on isotopic composition is less constrained. From the kinetic theory of gases, the growth of a grain at equilibrium with a gas was described as a function of the molecule flux at the surface of the grain (Hirth and Pound, 1963).

$$J_{cg} = p/(2\pi mkT)^{1/2}$$

Where p is the vapor pressure at the surface of the grain, m the molecular mass, k the Boltzmann's constant and T the temperature in kelvin. At equilibrium $p = p_e$ (the equilibrium pressure of the gas), the flux of evaporation is equal to the striking flux and the grain is not growing or evaporating. However, when the system is in disequilibrium, evaporation occurs when $p < p_e$, and condensation when $p > p_e$. The related isotopic fractionation is then function of the molecular velocities (Schauble et al. 2004). Hence, isotopic fractionation in low gravity environments has been described to be a function of the kinetic energy (i.e. kinetic energy: $k_e = ½*m*v^2$; where m is the mass of the isotopes, and v the speed of this atom, Hirth and Pound,

1963; Humayun and Clayton 1995). The difference in k_e between a heavy and a light molecule is equal to,

$$v_{heavy}^2 / v_{light}^2 = m_{light} / m_{heavy}$$

Hence, the velocity of a molecule is inversely proportional to its mass, meaning that light molecules are faster than heavy ones. Based on that theory, Richter (2004) model the effects of gas pressure and cooling rate on the magnesium isotopic composition of the condensate. In an environment in which the temperature drops, the isotopic fractionation of an element will be a competition between isotope velocity and condensing rates. Richter (2004) concludes that the first solids tend to be enriched in light isotopes compared to the gas, and that this trend increases with increasing cooling rate. On the other hand, at very low cooling rate, the condensate will acquire the composition of the gas (Fig. 3.1). However, these calculations remain theoretical and need to be tested on natural samples.

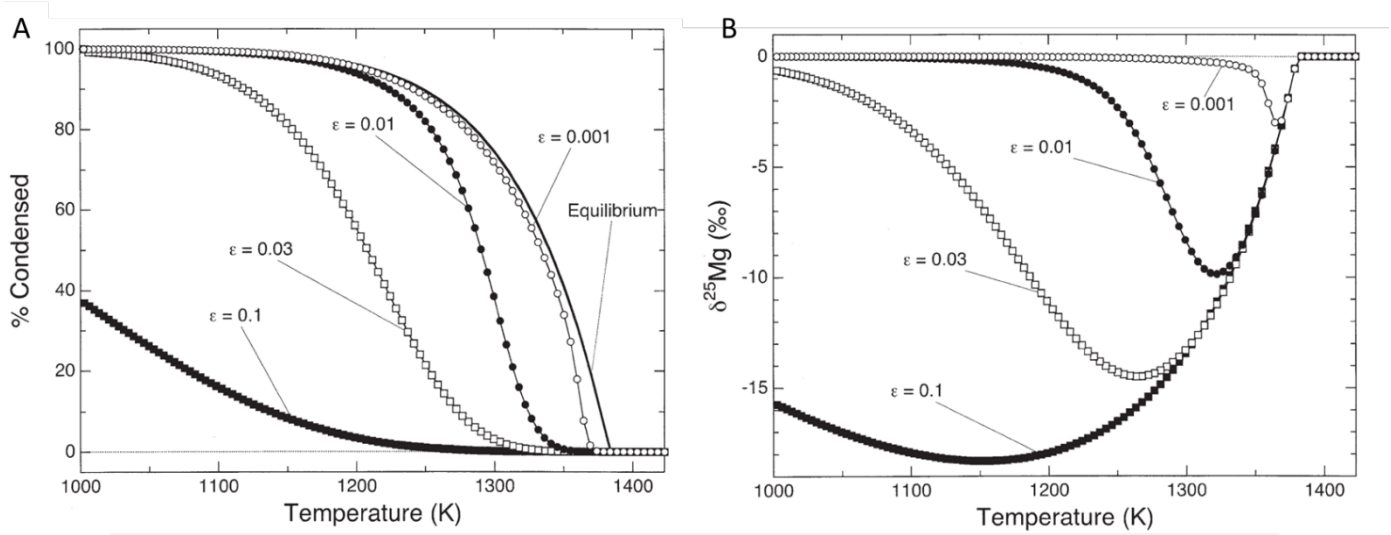

Figure 3.1: A) percentage of condensed magnesium as forsterite in function of the temperature and of low cooling rate ($\varepsilon \ll 1$) or fast cooling rate ($\varepsilon \geq 0.1$) compared to condensation timescale τ_{cond} at 10^{-3} bar. $\varepsilon = \tau_{cond} / \tau_T$ where τ_T is the timescale for temperature to change in the environment B) Effect of condensation on isotopic composition of magnesium in forsterite in function of the temperature and of the ε factor. Adapted from Richter (2004)

Condensation occurs very early in the Solar System, such that it is overprinted by following heating processes on parent bodies, such as metamorphism. Elemental and isotopic signature of condensation is only preserved in very primitive meteorites and un-reprocessed meteorite components. One of these objects are the refractory inclusions, that in some case can be pristine, are mainly composed of silicates with occasionally some refractory metallic alloys, such as calcium-aluminum-rich inclusions (CAIs) (Scott and Krot, 2014). On the other hand, it is far more difficult to find metal that retains their pristine signature. Most metal grains were reprocessed during heating events or later by oxidation. Whereas the solar nebular has a very low capability to oxidize metal (fO_2 ~IW-6), this reducing characteristic will change drastically with time, due to the decrease in temperature and then formation of oxidizing species. If the

metal was not reprocessed during heating event, such as melting in the solar nebula or during melting of undifferentiated parent bodies and subsequent metal-silicate differentiation (see Chapters 4 and 5), it can be oxidized and incorporated in silicate in the form of FeO or Fe_2O. In that case it become very difficult to study metal formation. There is no consensus on metal formation, for instance some authors argued that the metal in primitive ordinary chondrites was formed by the reduction of highly oxidized material (Kong and Ebihara, 1997), while other advocate for a vapor condensation on the planetesimal (Rubin, 1999). To further constrain metal formation a study of metal grains in the carbonaceous Bencubbin chondrites (CB) has been carried out. CBs form a very primitive and unusual meteoritic group which is composed of 60 to 80% metal, formed by condensation. It is one of the only meteorite groups to have kept their pristine elemental (Co, Ni, Fe, refractory siderophile elements) and isotopic (Fe, Ni) zonations and is thought to be due to condensation (Weyrauch et al. 2019). It has been demonstrated that they were formed ~4.2 Ma after the CAIs (Pb-Pb: Bollard et al. 2015; Ar-Ar Marty et al. 2010), thus probably too late to be formed by direct condensation from the protoplanetary disk (Campbell et al. 2002). Yet, the conditions of the environment of CB formation was very close to the latter, such that by studying CB chondrites we have the opportunity to constrain metal condensation in the protoplanetary disk. We have thus investigated the isotopic fractionation of germanium as well as the abundance and distribution of refractory and moderately siderophile elements in metallic grains.

The results are presented below as a manuscript, entitled "The formation of CB chondrites: inferences from germanium isotopes and highly siderophile element abundances", and submitted to *Meteoritical & Planetary Sciences*.

Goals of this chapter

- Studying metal condensation under conditions close to the solar nebula.
- Constrain processes occurring at intermediate temperature of condensation by using moderately siderophile elements.
- Evaluating the effect of condensation on germanium isotopic fractionation.
- Constraining the formation of Bencubbinite carbonaceous chondrites and their precursors.

II. The formation of CB chondrites: Inferences from Germanium Isotopes and Highly Siderophile Element abundances.

To be submitted to *Meteoritical & Planetary Sciences*

Guillaume Florin[a,*], Béatrice Luais[a], Olivier Alard[b,c], Tracy Rushmer[b]

[a]: Centre de Recherches Pétrographiques et Géochimiques, CRPG-CNRS- UMR 7358, Université de Lorraine, 15 Rue Notre Dame des Pauvres, 54500 Vandœuvre-lès-Nancy, France

[b]: Department of Earth and Planetary Sciences, Macquarie University, NSW 2109, Australia

[c]: Géosciences Montpellier, UMR 5243, CNRS & Université Montpellier, 34095 Montpellier, France.

*: Corresponding author guillaume.florin@univ-lorraine.fr

Abstract

We analysed the HSE content and the germanium isotopic composition of the metal phases in Bencubbin (CB_a), Gujba (CB_a), and HaH 237 (CB_b). We find that the two groups of CB are distinguishable using $\delta^{74/70}Ge_{bulk}$ +1.03±0.09‰ and -0.65±0.1‰, for CB_a and CB_b, respectively. The CB_a isotopic composition is explained by condensation at slow cooling rates, in an internal part of the plume whereas CB_b are likely formed at high cooling rates at the edge of the plume.

In Gujba metal grains we showed a gradual decrease of $\delta^{74/70}Ge$ and [Ge] from their core to their edge. This disagrees with the equilibrium condensation of Ge, or Ge diffusion through the metal. It suggests that $\delta^{74}Ge$ zonation results from condensation close to equilibrium and plume heterogeneity due to condensation/evaporation. We propose that (1) The core of each grain condensed at equilibrium; (2) grains were taken into a warmer zone where they reached temperatures lower than Fe-Ni $T_{50\%-condensation}$ but high enough to quickly evaporate Ge; (3) Loss of Ge followed by the slow cooling of metallic cores, enrich the cores in heavy isotopes and the gas in light isotopes; and (4) Gas re-condensed at equilibrium forms the light Ge isotopic zonation on the exterior of the grains.

1 Introduction

The Bencubbin chondrites (CB) are unique among the carbonaceous chondrite groups, because they show unusual enrichment in FeNi metal (60 – 80 vol % of the bulk), a lack of matrix, an enrichment in refractory elements by a factor of 1.3 for lithophile elements (with $T_{condensation} > T_{Mg\ condensation}$) and 13.7 for siderophile elements (with $T_{condensation} > T_{Pd\ condensation}$), and a depletion in moderately volatile elements according to their volatility, e.g. Ga which is more depleted than Ge compared to CI values (Campbell et al., 2002; Zipfel et al., 1998). The metal within CB chondrites has a kamacite composition, with a Ni content ranging from 4.1 to 14.8% (Weisberg et al., 2001), a Co/Ni ratio close to the solar value (~0.045, Anders and Grevesse, 1989; Weisberg et al., 1990, 1995), and an inverse Cr-Ni correlation (Weisberg et al., 2001). These features were first interpreted as the result of direct condensation from the solar nebular gas and thus reflect the primitive character of CB chondrites (Newsom and Drake 1979; Grossman et al., 1988; Meibom et al., 1999; Weisberg et al., 1999, 2001).

The bencubbinite group is divided into two subgroups: CB_a, mostly represented by Bencubbin, Gujba, and Weatherford, and CB_b, mostly represented by HaH 237 and Isheyevo. These two groups can be distinguished by the size of their metal grains, as well as the Ni content of these grains, and their elemental and isotopic zonations (Weisberg et al. 2001). in detail, when compared to CB_a, CB_b contain fine grains of metal with a rim enriched in Fe, Cr and volatile elements (e.g. Au, Cu, Ge, Ga) relative to their core (Campbell et al., 2000, Campbell et al., 2005). Fe, Ni and Co patterns follow the cosmochemical behaviour of the elements (Lodders et al., 2009) in agreement with fractional condensation from the solar nebular gas. However, compared to volatile elements, platinum group element (PGE) distribution (Campbell et al., 2001; Weyrauch et al., 2019) as well as Co and Ni concentrations (Meibom et al., 1999; Petaev et al., 2001), they show are characteristics of high cooling rates in a dense and metal-rich environment (Campell et al., 2002). Condensation at high cooling rates is also supported by the light $\delta^{56}Fe$ and $\delta^{62}Ni$ isotopic compositions of the core of CB_b metal grains relative to their edges (Richter et al., 2014; Weyrauch et al., 2019; Zipfel and Weyer, 2007). As such, their isotopic zonations reflect kinetic condensation during which light isotopes condense first (Richter, 2004).

Although processes involved in bencubbinite formation are still debated, two main models have been proposed to interpret their chemical and isotopic patterns. Based on major elemental zoning and Co-Ni covariation, the first model suggests that CB are formed by equilibrium condensation from the solar nebula gas at $P^{tot} = 10^{-4}$ bar (Meibom et al. 1999; Petaev et al. 2001). However, several lines of evidence contradicts this model: (1) the FeO content of the silicates is characteristic of high oxidation conditions (Krot et al. 2000); (2) the W, Mo depletions in zoned grains reflect a high oxygen fugacity environment (Weyrauch et al., 2019); (3) the required partial pressure for siderophile elements condensation is 7 times higher than predicted for condensation from a gas of solar composition ($P^{tot} = 10^{-4}$ bar; Campbell et al. 2002); (4) the young age of CB

chondrule formation (~ 4.2 Ma after CAIs, Bollard et al. 2015; Krot et al. 2005; Marty et al. 2010; Zhu et al. 2019). In order to accommodate a wider range of condition, Kallemeyn et al. (2001) has suggested that CB chondrites have formed by protoplanetary impact between two metal–rich bodies.

A second model has thus been put forward, arguing for CB condensation from a vapor-plume formed during the impact between two planetary embryos (Campbell et al., 2002; Krot et al., 2005). Within this frame, new Fe and Ni isotopic zonation data in metal grains suggests that unzoned metal grains (from CB_a) condense at equilibrium in the center of a plume at low cooling rates and a high partial gas pressure, whereas zoned grains (from CB_b) condense in disequilibrium in the outer part of a plume at high cooling rates and at a low partial pressure (Weyrauch et al. 2019). This model is only partly supported by numerical modelling of an impact plume at $P^{tot} = 10^{-3}$ bar. Good matches are found for Ir, Ni, Co and Cr concentrations as well as Fe and Ni isotopic compositions of unzoned and zoned metal grains. Yet, these calculations also produce large Fe and Ni isotopic zonations in cogenetic silicates, which are not found in chondrules (Fedkin et al., 2015). Moreover, the plume model cannot fully explain the composition of chondrules without the occurrence of an unlikely large numbers of starting compositions (Fedkin et al., 2015). Thus, even if the impact plume appears to be a possible hypothesis, some points need to be assessed.

Although there are some data available on moderately volatile elements in the metal phase (e.g. Cr, Au, P, As, Cu, Ga, Sb, Ge, Sn, S, Campbell et al., 2002; Kallemeyn et al., 1978; Meibom et al., 2005, Weyrauch et al., 2019), the condensation model of CB chondrites is mostly based on the study of major elements (Fe, Ni, Co) and refractory siderophile elements (e.g. Re, Os, Ir). Consequently, the model records processes happening at temperatures higher than $T_{50\% \text{ condensation}} > 1300K$ for/at $pH_2O/pH_2 = 4.2 * 10^{-4}$ atm (Lodders et al., 2009, Wood et al., 2019). The dynamics of CB metal grains condensation at high temperature have been more studied that the subsequent evolution of CB metal at intermediate and low temperatures. Processes at intermediate temperatures are well illustrated by the occurrence of fine exsolutions of kamacite and taenite, named plessite, in the core of some metal grains. These exsolution textures are consequences of prolonged reheating events (T > 400 °C) prior to accretion (Meibom et al., 2005; Zhang et al., 1993). Fe and Ni have high condensation temperatures ($T_{50\% \text{ condensation}}$ Fe = 1334K) are therefore not helpful isotopic tracers to constrain lower temperature processes. In this case, Fe and Ni isotopic variations will only trace taenite exsolutions from kamacite. According to Meibom et al. (2001), the large depletions in Ge and Ga in metal condensates would result from metal-gas separation at high temperature, which inhibit Ge and Ga condensation in metal. As a result, it is necessary to use moderately volatile elements that record intermediate and low temperature (i.e. T < 1334K that is $T_{50\% \text{ condensation}}$ of Fe, Lodders et al., 2009) processes in order to fully understand volatile depletion, low temperature processes as well as metal formation and CB evolution prior to accretion.

Germanium is a moderately siderophile and volatile element condensing in FeNi alloy (Sears, 1978; Wai and Wasson, 1979) at $T_{50\%\ condensation}$ = 883 K for pH_2O/pH_2 = 4.2 * 10^{-4} atm (Lodders et al., 2009). Germanium content and isotopes show large variations between meteorite groups and have been used to characterise iron meteorites (Wasson 1974, Luais, 2007, 2012), impact volatilisation (Luais 2007), and more recently ordinary chondrite formation (Florin et al., 2020). Therefore, we have carried out a comprehensive germanium elemental and isotopic study of metallic bulk and metal grains from CB_a, CB_b chondrites. We have first measured germanium isotopic composition of the bulk metal from CB chondrites. Then, we have sequentially digested metal grains separated from Gujba (CB_a) to provide a cross-section of germanium content and isotopes. In addition to isotopic measurements, *in situ* elemental measurements of moderately siderophile elements (W, Mo, As, Cu, Ag, Ga, Ge, Pb), and HSE: (Re, Os, Ir, Ru, Rh, Pd, Pt, and Au) have been performed on these metal grains. Elemental and isotopic results are used to discuss metal grain condensation processes and to constrain and model the environments of CB_a and CB_b formation.

2 Samples and methods

2.1. Sample selections

Two CB_a chondrites, Bencubbin and Gujba, and one CBb HaH 237 have been selected for this study. Bencubbin carbonaceous chondrites are very rare meteorites and most of them have a main mass lower than 800g. However, because Ge content is low in CB chondrites (usually <1ppm, Weyrauch et al., 2019), 300mg of pure metal is needed for isotopic studies. Only Gujba (fragment of 1.2 g) and Bencubbin (fragment of 1.9 g) have been obtained from museums with the required masses. To complete our dataset, a slice 2x1x0.2 cm (2.143 g) of Hammadah al Hamra 237 (HaH 237) was bought from the owner of the main mass.

2.2. Petrographic description of selected CB chondrites

CB chondrites are composed of 60% to 80% of rounded metal grains and 20% of silicates. Weisberg et al. (2001) also reports the occurrence of one CAI. A short petrographic description of the Bencubbin chondrites is given here. More details can be found in previous studies (Grossman and Zipfel, 2001; Meibom et al., 2005; Rubin et al., 2003; Weisberg et al., 2001). Samples were put in resin and polished with ethanol to avoid oxidation. The following mineralogical and petrographic observations were done using an optical microscope.

Bencubbin (CB_a) has been used to describe the CB grouplet. As reported by previous studies (Weisberg et al., 2001), metal grains in our samples have various sizes, from 100 µm to 4 mm, and the majority has a diameter > 1 mm. They are all deformed in the same direction due to impact compaction (Fig. 3.1A, see pages 68 – 69). Sulfides occur either as rounded or

elongated inclusions in largest metal grains (Fig. 3.2B), or as a thin film at the boundaries of small metal grains that aggregate to form larger ones (Fig. 3.2C). Metal grains are surrounded by silicates and metallic melts connected to the rim of metal grains (Fig. 3.2D). These melts are composed of sulfides and FeNi alloys and are interpreted as resulting from partial melting of the adjacent metal grains during the impact (Weisberg et al., 2001).

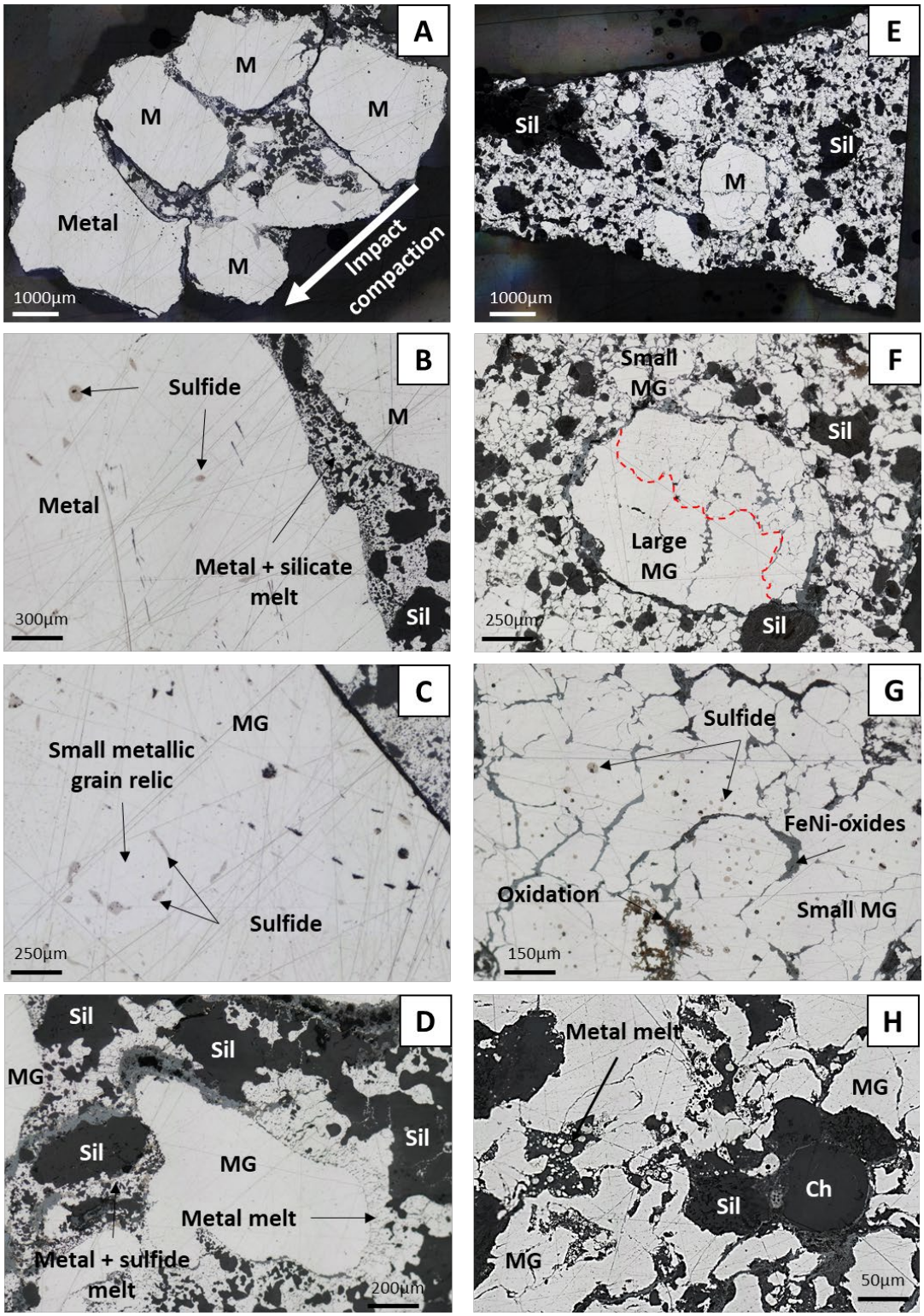

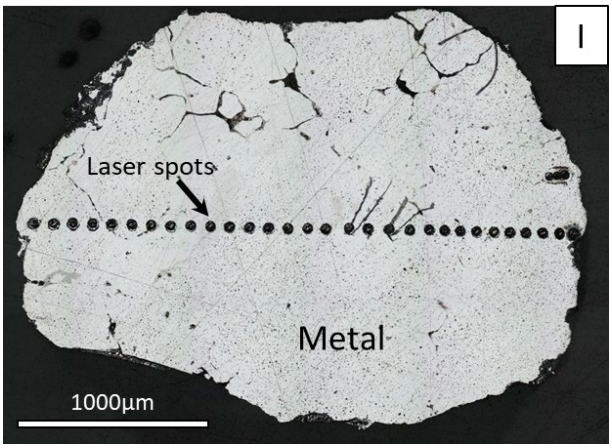

Figure 3.2 Reflected light images of Bencubbin (A, B, C, D) and HaH 237 (E, F, G, H). A) Image showing the direction of impact compaction in Benccubin. B) Sulfides inside metal grains and mixing of silicate with the impact metallic melt between grains. C) Sulfides highlighting a relic of a small metallic grain. D) Metal melt formation taking its source from the melting of the edge of metallic grains. E) Map of HaH 237 showing the silicates in black and metal in white. F) comparison of large and small metal grains in HaH 237. The red dotted line divides the large grain at the middle of the picture into two zones: in the bottom left-hand part is the fully aggregate grain, and in the upper right is the partially aggregate grain. G) Zoom on the partially aggregated part of the large grain of the "F" picture, example of the formation of large metal grain by aggregation of small metal grains. H) Example of immiscible metal liquid and silicate formed by impact. Chondrules and chondrule relics are also visible. I) Example of a rounded metal grain from Gujba. M: Metal; Mg: Metal grain; Ch: chondrule; Sil: silicate.

Gujba (CB_a) shows the same texture as Bencubbin, except that metal grains from Gujba have a size varying from 1 to 4 mm and are nearly perfectly rounded and show no deformation, although some studies have described preferential elongation in some samples (Rubin et al., 2003). Our Gujba sample shows more occurrences than Bencubbin of small metal grains delimitated by sulfide inside of large metallic ones (Fig. 3.2I). Similar metal-sulfide textures have been previously described in Gujba metal grains (Weyrauch et al., 2019).

HaH 237 (CB_b) shows a complex mixing of metal grains, metallic melts and silicates (Fig. 3.2E). Except for three grains, which are larger than 1 mm size, most of the metal grains are smaller than in CB_a studied here (~100 to 300 µm, Fig. 3.2F). Large metal grains are aggregates of smaller ones, sometimes separated by FeNi-oxides, yet these grains are less aggregated than in CB_a (Fig. 3.2G). In some of these small metal grains, troilite occurs in the form of rounded inclusions (Fig. 3.2F and G). Silicate phases are (1) chondrule relics which have been deformed or (2) silicate melt. Melt shock (Meibom et al., 2005) composed of finely intertwined metal and immiscible silicates can be found between metal and chondrules (Fig. 3.2H).

2.3. Analytical procedure

2.3.1. Elemental measurements by LA-ICP-MS

Siderophile and chalcophile trace elements were measured *in situ* by LA-ICP_MS using the method developed by Alard et al., 2000 and Mullane et al., 2004. Analyses were carried out on an Agilent 7700cx ICP-MS coupled with a Photon Machines Analyte G2 193 nm ArF excimer laser ablation system at Macquarie GeoAnalytical (MQGA, Macquarie University, Sydney,

Australia). The ICP-MS was operated at 1300 W and tuned daily in laser mode for maximum sensitivity across the mass range while keeping oxide production below 1% (^{248}ThO / ^{232}Th<0.01). The laser was operated with an estimated energy density of 7.2 J • cm^{-2} and a pulse rate of 5 Hz. Targeted minerals were ablated using beam sizes ranging between 50 and 80 µm. The laser platform is equipped with a HelEx ablation system which features a large primary cell allowing to fit numerous (or large) samples and a nested microcell with a volume of ~2.5 cm^3 in which ablation occurs (Eggins et al. 2005). The small volume of the nested cell yields a very short residence time for laser ablated particulates (≈0.5 s), resulting in high temporal resolution with minimal memory effects. Helium rather than Ar was used as the ablation medium to reduce the deposition of the surface condensate around the ablation site and to produce a complementary increase in a sample yield to the ICP-MS (Eggins et al., 1998; Horn and Gunther, 2003). Helium gas flow rates were set ca. 0.4 l • min^{-1} and 0.4 l • min^{-1} for the primary and the nested microcell, respectively. Helium and ablated material flow were then mixed before entering the torch with an Ar flow c.a. 0.90 ± 0.05 l • min^{-1}. Each measurement included 160 s of gas background measurement (i.e. laser Off), followed by 60 s (=300 laser pulses) of integrated analysed signal (i.e. laser On) and then 60 s of washout time to avoid any memory effect. The measured isotopes are: ^{57}Fe ^{59}Co, ^{60}Ni, ^{63}Cu, ^{69}Ga, ^{74}Ge, ^{75}As, ^{95}Mo, ^{101}Ru, ^{103}Rh, ^{106}Pd, ^{121}Sb, ^{125}Te, ^{182}W, ^{185}Re, ^{192}Os, ^{193}Ir, ^{195}Pt, ^{197}Au, ^{208}Pb, and ^{209}Bi. These elements were selected to cover the entire range of volatility for siderophile elements. Data was corrected and processed using the GLITTER™ software (Griffin et al., 2008), which allows for the cleanest part of the time-resolved spectrum to be selected, avoiding inclusion phases. Background values were estimated for each analysis, not interpolated throughout the session. A quenched NiS (PGE-A: Alard et al., 2000, Gilbert et al., 2013) doped with selected chalcophile and siderophile elements was used as an external calibration standard for all elements except for Re, W, Mo, Ni, Ga, Ge for which a slab of Filomena (IIAB iron meteorite) was used (Walker et al., 2008 and references therein). Furthermore, Hoba (IVB iron meteorites) and NIST1158 steel (Campbell et al., 2002; Walker et al., 2008) were systematically analysed in each session. Averages for these materials are reported in Table 3.1 and are comprised within the same error ranges as other published values. Detection limits for LA-ICP-MS analyses are calculated as average background concentrations plus three standard deviations. Typical detection limits obtained during this study are provided in appendix B Table 3.B.

Table 3.1: Comparison between our measurements and Walker et al (2008), Gilbert et al. (2013) values for Filomena, PGE-A, NIST1158 and Hoba. The error associated to each value are given as 1SD.

	This study								Walker et al. (2008)			Gilbert et al. (2013)
Element	NIST1158	SD	Hoba	SD	PGE-A	SD	Filomena	SD	NIST1158	Hoba	Filomena	PGE-A
Ni (%)	**36.05**	0.04	**16.40**	3.41	**72.54**	5.10	**5.65**	0.25	34.5	16.4	5.65	71.5
Co (ppm)	**139**	35.99	**6981**	160	**7.55**	0.48	**4595**	84.3	81	7890	4500	--
Re (ppm)	**0.12**	0.04	**3.60**	0.31	**b.d.***	0.02	**0.34**	0.14	0.005	2.732	0.175	--
Os (ppm)	**b.d.***	--	**43.56**	9.12	**73.65**	3.25	**0.88**	0.17	0.002	39.21	0.98	194
W (ppm)	**22.8**	5.4	**4.5**	0.9	**b.d.***	0.0	**2.5**	0.5	14	3.1	2.43	--
Ir (ppm)	**0.01**	0.00	**16.94**	2.61	**122.69**	5.49	**2.48**	0.43	0.006	26.86	3.22	208
Ru (ppm)	**0.20**	0.16	**20.06**	2.30	**205.82**	10.68	**14.00**	2.98	1.35	29.44	16.5	203
Mo (ppm)	**101**	13.7	**21.5**	2.5	**b.d.***	--	**6.1**	0.9	114	24.6	7.5	--
Pt (ppm)	**b.d.***	--	**20.8**	2.2	**186.2**	8.8	**19.8**	2.8	0.01	30.14	24.1	204
Rh (ppm)	**b.d.***	--	**3.1**	0.3	**223.8**	13.6	**2.3**	0.2	--	3.54	2.2	220
Pd (ppm)	**0.02**	0.01	**5.59**	0.02	**278.05**	22.54	**1.70**	0.17	--	6.244	1.6	271
As (ppm)	**28.8**	9.79	**0.58**	0.66	**134**	10	**4.4**	0.48	--	--	--	--
Au (ppm)	**b.d.***	--	**0.04**	0.32	**216**	13.62	**0.47**	0.06	--	0.064	0.61	212
Cu (ppm)	**245**	18	**1.2**	0.2	**1688**	23	**90.4**	2.1	--	--	135	2550
Ag (ppm)	**b.d.***	--	**b.d.***	--	**233**	15	**b.d.***	--	--	--	--	--
Sb (ppm)	**5.59**	2.40	**0.15**	0.08	**0.64**	0.03	**0.19**	0.11	--	--	--	--
Ga (ppm)	**8.70**	2.24	**0.31**	0.21	**b.d.***	0.10	**61**	0.87	5.6	0.192	59	--
Ge (ppm)	**18.82**	5.56	**1.34**	0.99	**b.d.***	2.61	**189**	5.65	12.5	0.049	181	--
Bi (ppm)	**b.d.***	--	**b.d.***	--	**213**	17	**0.06**	0.032	--	--	--	--
Pb (ppm)	**0.39**	0.20	**0.33**	0.16	**29.2**	2.7	**0.08**	0.033	--	--	--	--
Te (ppm)	**b.d.***	--	**b.d.***	--	**205**	12	**0.11**	0.047	--	--	--	--
Sn (ppm)	**52.07**	27.44	**2.41**	1.28	**5.98**	0.59	**b.d.***	--	--	--	--	--

*: b.d., bellow detection limit; --, no reported data for this element.

2.3.2. Sample preparation and digestion

Slices of around 300 mg of Bencubbin and HaH 237, and two fully preserved spherical metal grains (157 mg and 137 mg, respectively) separated from Gujba were cleaned with 0.2 M HNO_3 under ultrasonic agitation for 5 minutes at room temperature to remove external oxidation and possible terrestrial contamination. Samples were rinsed with ultra-pure Milli-Q water to remove acid, then with acetone to avoid oxidation. Samples were then dried overnight under laminar hood. All acids used for all steps of cleaning, digestion and resin separations were high purity acids (SeaStar®).

- Bulk metal grains: 214 mg and 230 mg of metal from Bencubbin and HaH 237, respectively, were digested overnight using 8 cc of 2 M HNO_3 at 60-65°C in Teflon beaker. After full digestion, remaining silicate grains enclosed in metal were removed by centrifugation and cleaned under ultrasonic agitation for 10 minutes with 2 cc of cold 2 M HNO_3 to fully recover the digested metal solution.

- Sequentially digested metal grains: in order to measure the elemental and isotopic variations of germanium within grains, each of the two metal grains from Gujba were sequentially digested under ultrasonic agitation using 2 M HNO_3 into three fractions: the edge, the middle

part and the core. For the first fraction (the edge of grains), digestion was stopped every 20 minutes and each grain was rinsed with water, dried in acetone and weighed. This operation was repeated until ≈33% of mass was digested. Water used to rinse grains was recovered and added to the solution. When dissolved, weight was approaching 33%. We repeated the same protocol in another beaker for the second fraction (middle part) until ~33% was digested. Finally, the last ~33% of the core fraction were entirely digested in a last beaker. Fraction weights are given in Table 3.2.

The analytical procedure for germanium purification is adapted from that of Luais (2007, 2012, and references therein), to higher mass of metal sample. The full procedure is given in appendix A: Chemistry.

Table 3.2: Germanium isotopic compositions of metallicmetal bulk from CB chondrites and of Gujba grains. % f is the percentage of each fraction (edge, middle or core). Gujba bulk is recalculated using the value of the two measured grains. Means of Gujba grains are calculated taking in account the %f. n is the number of analysis of each fraction. The 2σ SD on δ74/70Ge for grain with n = 1, is the mean maximum mean long term standard deviation.

		Ge ppm	$\delta^{72/70}$Ge	2σSD	$\delta^{73/70}$Ge	2σSD	$\delta^{74/70}$Ge	2σSD	n	%f
Bencubbin (CB_a)		0.91	0.58	0.09	0.76	0.25	1.04	0.09	5	-
Gujba (CB_a)		1.11	*0.53*	*0.12*	*0.76*	*0.32*	*0.92*	*0.20*		-
HaH 237 (CB_b)		1.34	-0.29	0.14	-0.59	0.39	-0.65	0.10	3	-
Gujba grain 1	Edge	0.7	0.46		1.07		0.65	0.20	1	34
	Middle	1.07	0.37	0.21	0.62	0.61	0.71	0.22	2	27.7
	Core	1.86	0.43	0.13	0.74	0.49	1.03	0.19	2	38.3
	Mean	**1.25**	**0.42**		**0.82**		**0.81**	**0.47**		
Gujba grain 2	Edge	0.83	0.51		0.8		0.82	0.20	1	36.5
	Middle	0.72	0.54		0.39		0.87	0.20	1	28.5
	Core	1.35	0.85		0.93		1.35	0.20	1	35
	Mean	**0.98**	**0.64**		**0.73**		**1.02**	**0.37**		

2.3.3. Procedure for germanium isotopic measurements

2.3.3.1 Germanium Isotopic and elemental measurements by HG-MC-ICP-MS

The chemistry is adapted from Luais et al. (2012, 2007) to a higher mass of metal sample because of the low concentration of Ge in CB (around 1 ppm). More details are given in the supplementary material. Sample solution in 0.5M HNO_3 were analysed for Ge elemental and isotopic composition using a NeptunePlus multiple collector inductively coupled plasma mass spectrometer (MC-ICP-MS) coupled with a hydride generator system (HG-MC-ICP-MS) at CRPG-Nancy (Florin et al. 2020, Rouxel and Luais, 2017 and reference therein). Measurements were done in static mode using the ^{68}Zn, ^{69}Ga, ^{70}Ge, ^{71}Ga, ^{72}Ge, ^{73}Ge and ^{74}Ge isotopes distributed to the L3, L2, L1, C, H1, H2 and H3 Faraday cups respectively. Intensity for a 10 ppb Ge

standard solution was 1.8 V on ^{74}Ge. Bulk Ge procedural blanks, including chemistry and MC-ICP-MS measurements were better than 70 pg (12 mV) and negligible as this corresponded to less than 0.1% of Ge processed during the chemistry, so no blank corrections were applied. Samples were measured during 320 s distributed into 40 cycles of 8 s integration each and were bracketed using the NIST3120a Ge standard solution.

Isotopic data is reported in delta (δ ‰) unit using ^{x}Ge/^{70}Ge ratios with respect to the mean ratios of the NIST3120a Ge standard analysed just before and after the sample (Luais 2012):

$$\delta^{x/70}Ge_{NIST3120a} = \delta\ {}^{x}Ge/{}^{70}Ge = \left(\frac{\left({}^{x}Ge/{}^{70}Ge \right)_{Sample}}{\left({}^{x}Ge/{}^{70}Ge \right)_{NIST3120a}} - 1 \right) * 1000$$

During the analytical session JMC (1000 ppm ICP standard solution, lot # 301230S, Johnson Matthey, Germany) and Aldrich (10200 ppm ICP standard solution, lot # 01704KZ, Aldrich Chemical Co., USA) Ge standard solutions were analysed, yielding $\delta^{74/70}$Ge = -0.32 ± 0.17‰ (n=16) and $\delta^{74/70}$Ge = -1.96 ± 0.12‰ (n=18) (2σ SD), respectively. The IAB in-house standard Magura iron meteorite yielded $\delta^{74/70}$Ge = 0.80 ± 0.09‰ (n=5). These values agree with references given in Luais (2012) and Escoube et al. (2012). On the other hand, since chemistry yield for Ge metal is 100% (Luais, 2012), germanium elemental concentrations were calculated by comparing the measured intensity of Ge isotopes of each sample with the intensities of the NIST3120a Ge standard for which the concentration is known.

3 Results

3.1. Elemental composition

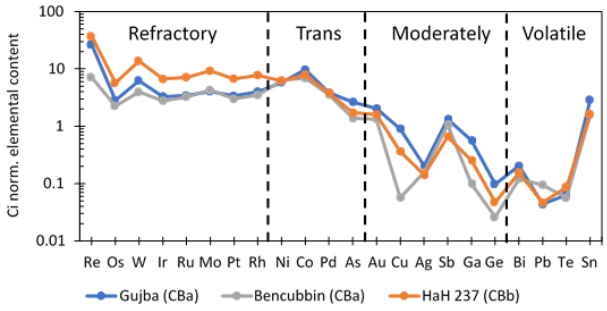

Figure 3.3: CI normalized mean elemental composition in HaH 237, Gujba, and Bencubbin. Refractory, tran. (Transitional), moderately, volatile refer to the degree of volatility of elements (Walter et al., 2000).

- *In situ analysis:* Highly and moderately siderophile elements contents of metal grains obtained by LA-ICP-MS are reported in appendix table B. The range of concentration of our analyses by LA-ICP-MS agree with previous data in CB chondrites (e.g. Re_{mean}~0.3, Os_{mean}~3.39, Ir_{mean}~2.03, Ga_{mean}~1.89, Ge_{mean}~0.76; Campbell et al., 2002; Campbell et al., 2005; Weyrauch et al. 2019). Compared to CI chondrites, metal grains are enriched in refractory siderophile elements

(ex. $2<(Ir)_N\leq 6$; $5<(Pt)_N<10$; N refers to measured values normalised to CI chondrites, chondrite values after Lodders et al., 2009). Mo and W contents range between 2.7 and 11.81 ppm (i.e. $3<(Mo)_N<12$) and between 0.9 to 1.91 ppm (i.e. $10<(W)_N<100$) respectively. Re may show extreme enrichment up to ≈100xCI1 values (0.08 to 6.52 ppm). The more volatile elements vary from 1.36 to 2.73 ppm for Pd ($1.5<(Pd)_N<4.2$), 1.52 to 6.27 ppm for As ($0.9<(As)_N<3.5$), from 0.12 to 0.4 ppm for Au ($1<(Au)_N<2.6$). On the other hand, Ag (0.02 to 0.05 ppm, $0.1<(Ag)_N<0.13$), Ge (0.6 to 6.14 ppm, $0.01<(Ge)_N<0.19$), Bi (~0.06 ppm), Pb (0.04 to 0.86 ppm, $0.015<(Pb)_N<0.32$), and Te (0.04 to 0.4 ppm, $0.017<(Pd)_N<0.17$) show strong depletion compared to chondrite and refractory HSE (Fig. 3.3).

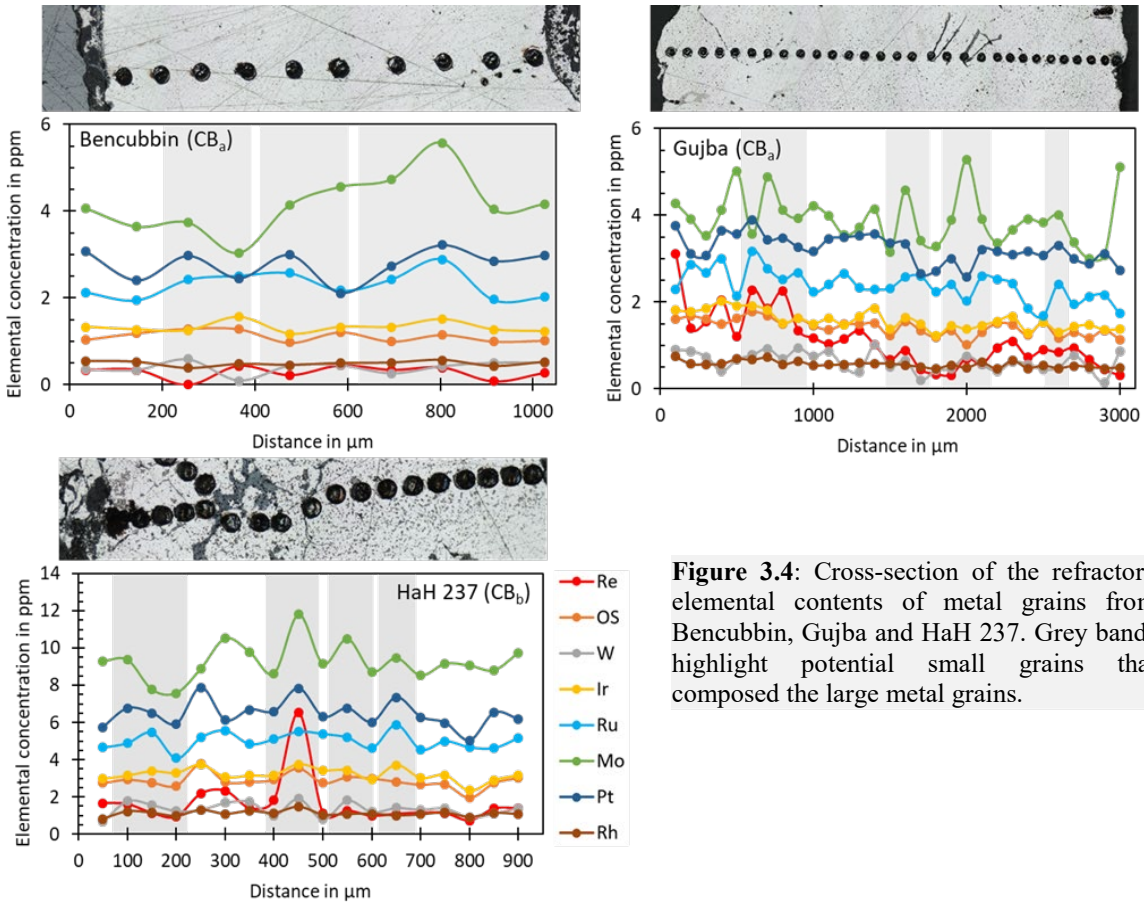

Figure 3.4: Cross-section of the refractory elemental contents of metal grains from Bencubbin, Gujba and HaH 237. Grey bands highlight potential small grains that composed the large metal grains.

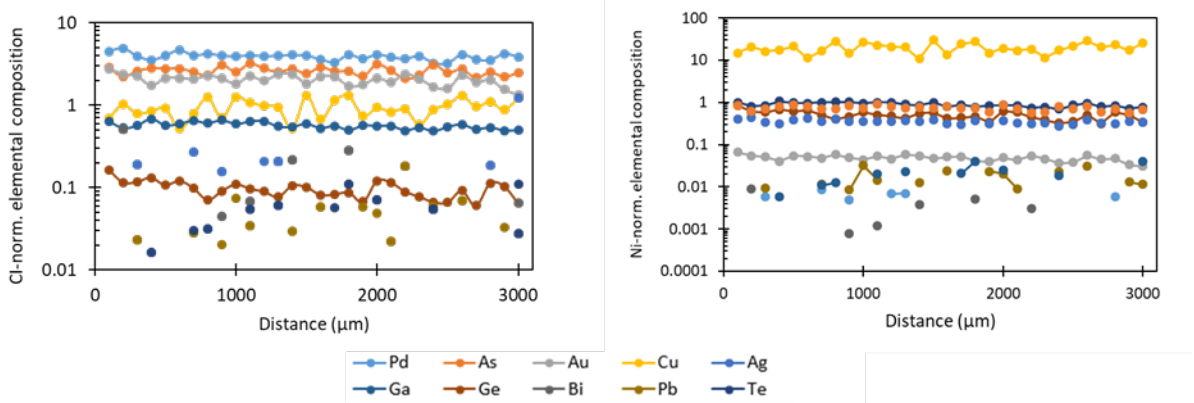

Figure 3.5: Cross section of the moderately volatile elemental content in a metal grain from Gujba, normalized to CI and Ni.

Compared to the mean composition of CB_a, the metal grains in CB_b (HaH 237) are enriched in refractory elements by a factor of two (Re, Os, W, Ir, Ru, Mo, Pt, Rh, 2.2, 2.3 2.6, 2.19, 2.1, 2.2, 2.1, 2, respectively). To be more precise, compared to Mo, Pt and Re the elements W, Os, Rh and Ir have very flat patterns (Figure 3.4) in Bencubbin and HaH 237. The largest variations concern Mo in HaH 237 (from 8 to 12 ppm, Fig. 3.4). In addition, the mean CB_b composition is depleted in volatile elements compared to mean CB_a composition (Fig. 3.3). Volatile element patterns in all grains are very flat except for Cu. We do not report a spike in refractory elements or a depletion in volatile ones in the core of each large metal grains as expected for condensation (Fig. 3.4, Fig. 3.5).

The difference in volatility between Ir, Au and Pd are helpful to constrain the condition of metal formation. In HaH 237, analysed grains have very similar compositions and define a narrow range when plotted in an Au/Ir vs Pd/Ir diagram (Fig. 3.6A). By contrast, Bencubbin and Gujba have higher ratios than HaH 237 but also more variable compositions. These compositions are very different than CI ratio and do not correspond to the variation in elemental composition reported for zoned grains by Weyrauch et al (2019). Moreover, CB_a is more depleted in W and Mo compared to CB_b (Fig. 3.6B), and there is no difference between the core and the rim of each grain, as opposed to condensation patterns.

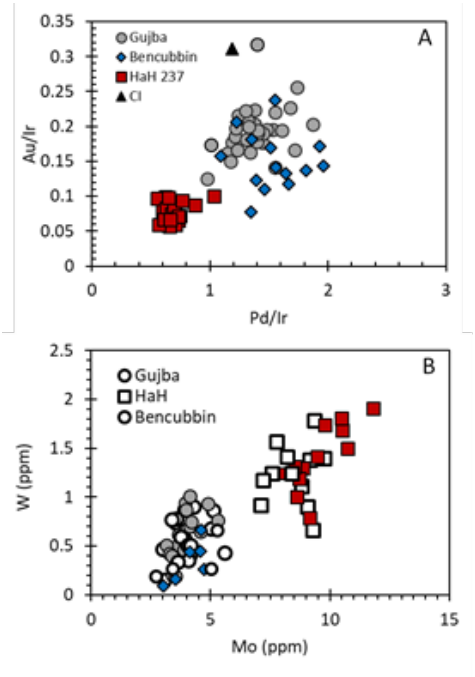

Figure 3.6: A) Au/Ir vs Pd/Ir ratio. Squares are for HaH 237 (CBb), circles for Gujba (CBa), and diamonds for Bencubbin (CBa). It should be noted that metal grains do not have CI value (Lodders et al., 2009). B) W vs Mo diagram, empty symbols are for grain edges and full symbols for grain cores. The colours are the same than in A.

CB_a and CB_b groups have similar Ni contents with a mean composition of 6.5% that is five times higher than the CI composition (1.08%, Lodders et al., 2009). The Co/Ni ratio in these metal grains varies from 0.062 to 0.099 for Gujba, 0.051 to 0.074 for HaH 237 and 0.048 to 0.056 for Bencubbin. Gujba and HaH237 have very high ratios compared to solar ones (i.e. solar ratio = 0.045, Weisberg et al., 1995, 2001), close to the ordinary chondrite ones (up to 0.070, Florin et al., 2020), whereas Benccubin shows a ratio close to the solar value (appendix Table B).

Whereas Weyrauch et al. (2019) measured small grains with a size between 180 µm and 600 µm, we have focused this study on large metal grains (>900 µm) such that the irregular variations in refractory elements might reflect the change in composition between small grains that compose large ones.

- *Germanium results:* Bulk metal from Bencubbin (CBa) and HaH 237 (CBb) displays similar Ge concentrations of 0.91 ppm and 1.34 ppm, respectively, which are within the range of variation of *in situ* measurements (0.6 to 6.14 ppm, Fig. 3.5). In the case of Gujba (CBa) the bulk Ge content for each grain was recalculated using the elemental composition and the mass of each fraction (Fig. 3.7). Elemental results show that grain 1 and 2 have elemental mean compositions of 1.25 ppm and 0.98 ppm, respectively. Previous studies have reported similar variations in germanium content in metal grains with an average bulk content of ~0.9 ppm, and variations between metal grains from 0.11 to 1.35 ppm (Campbell et al., 2002), 0.91 to 1.15 ppm (Kallemeyn et al., 1978), or by LA-ICP-MS in unzoned metal grains, from 0.38 ppm to 1.02 ppm in Bencubbin, 0.49 ppm to 1.29 ppm in Gujba and from 0.13 ppm to 2.35 ppm for HaH 237, and in zoned metal grains up to 11 ppm with a mean of 0.9 ppm (Weyrauch et al. 2019). Germanium content in CB is up to 30 times lower than in CI chondrites (33.2±0.3 ppm, Lodders, 2003, Fig. 3.6). Ge contents in CB metal grains are also very low compared to most of iron meteorite groups (from 80-180 ppm for magmatic irons, and 60-380 ppm for non–magmatic irons, Wasson, 1969; Luais, 2007), and metal in ordinary chondrites (H group ≈ 60 ppm; L group ≈ 130 ppm; LL group ≈ 250 ppm, Chou and Cohen, 1973; Florin et al., 2020). Yet, other iron groups such as the IVA - IVB (≈ 0.03 to 0.14 ppm, Schaudy et al., 1972), IIIF (≈ 0.7 to 1.1 ppm, Scott and Wasson 1976) or IIID (≈ 1.4 to 4.0 ppm, Wasson and Schaudy, 1971) have Ge contents similar to CB metal.

Germanium concentration in metal grains from Gujba increases from the edge to the core, from 0.7 to 1.86 ppm for the grain 1, and from 0.83 to 1.35 ppm for the grain 2 (Fig. 3.7, Table 3.2). These values are in the same order of magnitude as those reported for bulk metal by Weyrauch et al. (2019) (1.08 ppm). However, Weyrauch et al. (2019) do not identify any zonation in Ge in metal grains in Gujba. This may be the result of different thermal histories between grains (see part 4.3 for more details).

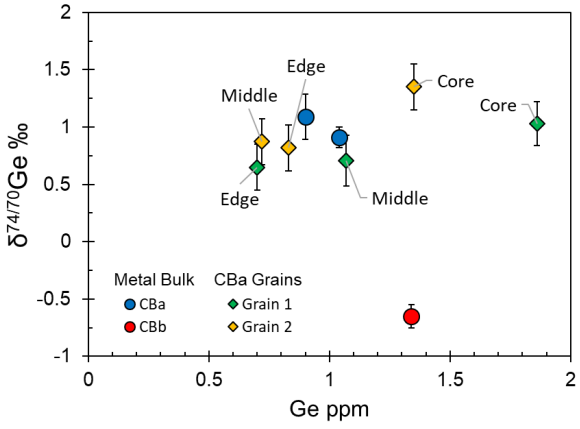

Figure 3.7: Germanium elemental and isotopic composition of CB chondrites.

3.2. Isotopic composition

Germanium isotopes were analysed on bulk metal grains of Bencubbin and HaH 237, and on the two rounded metal grains from Gujba for their core, middle and edge parts. As for Ge elemental composition of Gujba, the bulk isotopic composition of each grain was recalculated from measurements and weight mass of each fraction (Table 3.2). On a $\delta^{72/70}$Ge and $\delta^{74/70}$Ge diagram (Appendix Fig. B), all the data falls on the mass-dependent fractionation line. The data for $\delta^{74/70}$Ge is presented in Fig. 3.8.

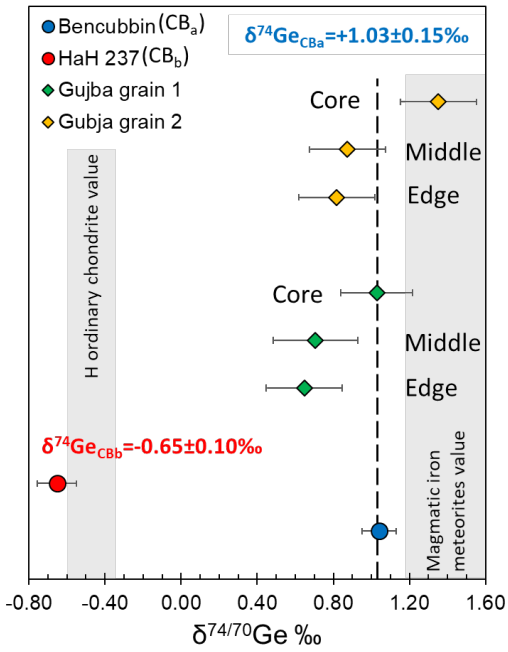

Figure 3.8: $\delta^{74/70}$Ge diagram in function of the NIST3120a standard for CB chondrites. CBa have a mean positive value of +1.03 ± 0.15‰ whereas that CB_b have very negative isotopic compositions of -0.65 ± 0.1‰. Gujba grain 1 and Gujba grain 2 display the same zonation but shifted from few per

The CB_a Bencubbin bulk metal displays high $\delta^{74/70}$Ge = +1.04 ± 0.09‰ (Table 3.2). This data agrees with the calculated $\delta^{74/70}$Ge mean value for sequentially digested fractions of metal grains 1 and 2 from the CB_a Gujba, with $\delta^{74/70}$Ge = +0.81 ± 0.47‰ and $\delta^{74/70}$Ge = +1.02 ± 0.37‰ respectively (Table 3.2). $\delta^{74/70}$Ge values for Bencubbin and Gujba are positive, just like in magmatic iron meteorites ($\delta^{74/70}$Ge= +1.41 ± 0.22‰, Luais, 2012), and in metal phases from pallasites ($\delta^{74/70}$Ge= +1,01 ± 0.04‰ Luais et al., 2017) values. In comparison, HaH 237 CB_b bulk metal displays lighter and more negative $\delta^{74/70}$Ge values of -0.65 ± 0.1‰, very close to $\delta^{74/70}$Ge = -0.54 ± 0.09‰ reported by Florin et al. (2020) for metal in H ordinary chondrites, despite very contrasted [Ge] content of 64 ± 8.8 ppm for H chondrites and ≈1.3 ppm for CB_b.

Gujba metal grains display Ge isotopic zonations that increase from the edge to the core; for grain 1: $\delta^{74/70}$Ge= +0.65 ± 0.2‰, $\delta^{74/70}$Ge = +0.71 ± 0.22‰, $\delta^{74/70}$Ge = +1.03 ± 0.19‰; and for grain 2: $\delta^{74/70}$Ge = +0.82 ± 0.2‰, $\delta^{74/70}$Ge = +0.87 ± 0.2‰, $\delta^{74/70}$Ge = +1.35 ± 0.2‰

(Fig. 3.8; Table 3.2). The occurrence of Ge isotopic variations within grains contrasts with the lack of Fe and Ni isotopic zonations in Gujba metal grains (Weyrauch et al., 2019).

4 Discussion

4.1. Formation of large metal grain

Most of the elemental variations in the analysed large metal grains are flat, except for some local positive spikes in refractory siderophile elements (i.e. Re, W, Pt and Ru, Fig. 3.4) that can be attributed to the occurrence of small metal grains, as shown in part 2, that are not equilibrated with one another. Then such elemental variations within these large grains can reflect the pristine composition of small metal grains. This confirms our petrographic observations showing that large metal grains are aggregates of smaller ones (Fig. 3.2). Furthermore, the texture of large metal grains in CB_a and CB_b as well as the larger grain size and a higher degree of homogenisation / aggregation of CB_a compared to CB_b (Fig. 3.2 C, F and G) highlight that (1) the CB_a Bencubbin grains had more time to condense and agglomerate and therefore would have spent longer at a high temperature, probably because of low cooling rates; and (2) the CB_b HaH 237 metal grains had less time to agglomerate and cooled quickly.

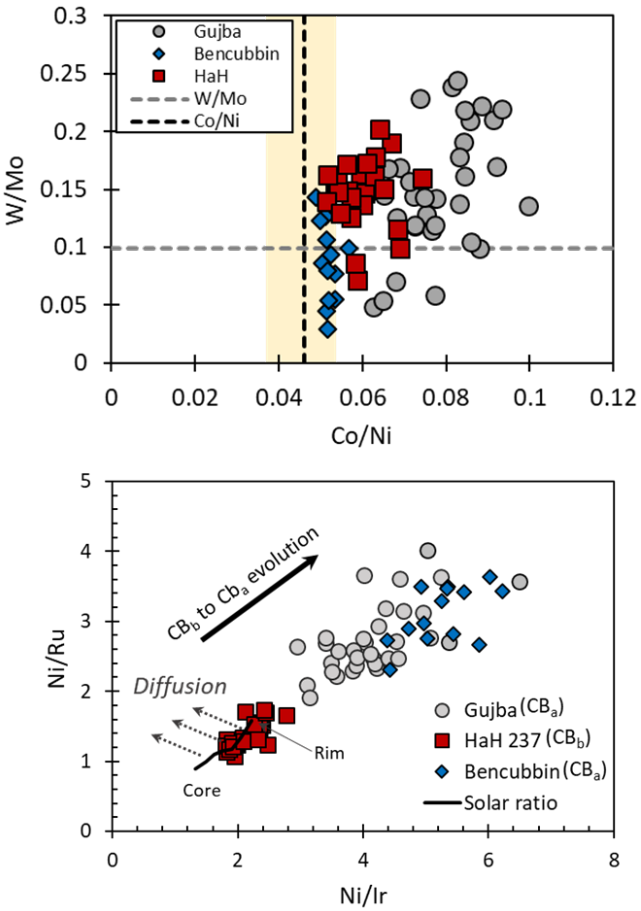

Figure 3.9: A) W/Mo vs Co/Ni ratios, the two dashed lines represent the CI ratios. The yellow area is the range of variation of the solar Co/Ni ratio, calculated as 2σ SD using the data from Campbell et al. (2002). B) Ni/Ru vs Ni/Ir ratios. The dark line represents the evolution of the solar nebular composition of the metal from the core to the rim of condensate metal grains. The dashed arrows show the expected variation of composition from the solar nebular metal by diffusion (from Richter et al., 2005 data). Squares are for HaH 237 (CBb), circles for Gujba (CBa), and diamonds for Bencubbin (CBa). It should be noted that these particular CBa grains do not have solar values

Previous studies report that CB chondrites have a Co/Ni ratio close (within the error range), to the mean solar ratio of 0.045 (Meibom et al., 1999; Newsom and Drake 1979). The latter varies from 0.037 to 0.054 using a 2σ SD = 0.008 (calculated from data of Campbell et al., 2001). By contrast, we measured a Co/Ni ratio in CB_a and CB_b metal that varied between 0.048 and 0.099 (Fig. 3.9A). These variations within large metallic grains show that small grains are not all representative of metal condensates under solar nebula conditions. Within the CB_a groups, Bencubbin has a very narrow range of Co/Ni similar to solar values (from 0.049 to 0.047), whereas Gujba shows a large range of variations (from 0.063 to 0.1) differing from solar values (Fig. 3.9A). This suggests that, within the CB_a group, small metal grains in Gujba experienced diverse conditions of formation and may sample chemically distinct regions, while the narrow Co/Ni range in Bencubbin indicates that the small metal grains were formed in a local area with homogeneous conditions of formation. Furthermore, the Co/Ni of CB_b (HaH 237) (from 0.051 to 0.074) overlaps with both Benccubin and Gujba (Fig. 3.9A), which may suggest that the difference in Co/Ni values between meteorites is linked to the mixing and the aggregation of small grains that come from chemically distinct regions.

The Co/Ni ratio disagrees with the solar Ni/Ru and Ni/Ir ratios of HaH 237 (CB_b) metal grains and with the non–solar Ni/Ru and Ni/Ir ratios of Bencubbin (CB_a) (Fig. 3.9B). Therefore, if we admit that differences between CB_a and CB_b are linked to the time spend at high temperature as suggested by our textural evidences, the well-agglomerated CB_a grains should represent the last step in the formation of large metal grains. The non-solar Ni/Ru and Ni/Ir ratios of CB_a large metal grains (Fig. 3.9B) could then be explained by the partial homogenisation of most of the refractory elements in small grains during heating events. If so, Ru that condense very close to Ir temperature (1551K, 1590K, and 1603K, respectively, Lodders et al., 2009), should have undergone the same homogenisation event. Regarding the diffusion rate of Ru, Ni and Ir in FeNi (Righter et al., 2005), a negative Ni/Ru and Ni/Ir correlation from CB_b to CB_a would be expected. However, the difference in Ni/Ru and Ni/Ir ratios in large metal grains between CB_b and CB_a cannot be explained by diffusion between small grains (Fig. 3.9B). Consequently, the temperature at which small metal grains have been aggregated in large ones is sufficiently low to inhibit the diffusion of refractory elements but high enough to sealed small grains together. Differences in composition between CB_a and CB_b could be linked to variations in gas pressure or in oxidation states.

Tungsten and Mo are siderophile and refractory elements with a distinct redox-sensitive behaviour. In an environment characterised by a high fO_2, high temperatures and high cooling rates, W would occur as a WO_3 complex, whereas Mo would occur in its metallic form in the gas (Fegley and Palme, 1985). Metal grains formed by condensation in oxidising conditions would be more depleted in W than in Mo (Fegley and Palme, 1985), as observed in both CB_a and CB_b. The fact that CB_a is even more depleted in Mo and W than CB_b (Fig. 3.6B) indicates that CB_a may have formed in a more oxidizing environment than CB_b, or at a higher temperature, or may

have stayed longer exposed to a high temperature, hence experienced lower cooling rates. Furthermore, the large W/Mo variations (0.02 to 0.15) coupled to the narrow Co/Ni ratio (~0.05) in Bencubbin indicate that Co/Ni variations in metallic grains cannot result in variations in the oxidation state within the environment of condensation (Fig. 3.9A). This observation precludes Co/Ni variations in CB_a and CB_b as the result of oxidation state variation in the environment of CB formation.

Another possibility is that the gas pressure was heterogeneous with respect to solar nebula conditions in the environment of CB formation. An increase in gas pressure modify the volatility of siderophile elements resulting in a higher RSE content in the metal at a given Ni content (Campbell et al., 2001, 2002).

Therefore, the conflict between Co/Ni, Ni/Ru and Ni/Ir ratios may be explained by this heterogeneity and by the variety of pressure affecting the formation of small metal grains.

4.2. Cooling rates and isotopic fractionation of Ge during formation of CB_a and CB_b chondrites

Richter (2004) has quantified the consequences of cooling rates on the isotopic composition of condensed phases. The isotopic composition of a solid formed by condensation from a gas mainly depends on the cooling rate. At a low cooling rate, the condensing solids reach equilibrium with the gas and acquire the same isotopic composition as the gas. On the other hand, the isotopic composition of the solids thus formed decreases with the increase of cooling rate. This means that, at a high cooling rate, the isotopic composition of the solid would be lower than at a low cooling rate. So, if CB_a and CB_b were formed from condensation of the same gas (as suggested by their common features, Weisberg et al., 2001), the heavy bulk isotopic data for the two CB_a ($\delta^{74/70}Ge = +1.04 \pm 0.09‰$, $\delta^{74/70}Ge = +0.92 \pm 0.2‰$) compared to the CB_b ($\delta^{74/70}Ge = -0.65 \pm 0.1‰$, Fig. 3.8) would imply that the environment of the CB_a has a slower cooling rate than that of the CB_b. Therefore, the metal bulk in CB_a is formed from condensation in an environment which remained warm for a long time, allowing for the metal to record a heavy composition close to that of the gas. CB_b, on the contrary, is enriched in light isotopes due to the high cooling rate, in line with petrographic observations.

To give an estimation of the cooling rates for CB_a and CB_b, we followed the method of Meibom et al. (2000), and updated their calculation, using the most recent values of total pressure for CB formation (e.g. $P^{tot} = 10^{-3}$ to 10^{-2} bar) calculated by Fedkin et al., (2015) and the revised temperature of Fe condensation ($T_{50\%\ cond}$=1338 K, Wood et al., 2019). We found that an increase in partial pressure from 10^{-4} to 10^{-3} or 10^{-2} bar dramatically increases the growth rate of metal grains from 0.14 µm/h to 1.40 µm/h to 14.08 µm/h (Fig. 3.10), respectively. Under these conditions, only 7 hours (at 10^{-2} bar) to 3 days (at 10^{-3} bar) are needed for a metallic grain of 100 µm radii to condense. Fedkin et al. (2015) suggests that CB_b was formed in a gas less dense

than CB_a (10^{-2} and 10^{-3} bar, respectively). If a 100 µm radii metal grain in CB_b condensed in 3 days, and with a temperature dropping from ~1370K to ~1270K (corresponding to the interval of temperature necessary for Fe to fully condense at equilibrium, Wood et al., 2019), the cooling rate should be ~1 K/h. This represents the highest cooling rate for CB_b. According to Meibom et al. (2000), homogenising Fe and Ni content by solid diffusion within 25 µm metal grains takes between 100 days and 2 years at 1300°K and 1200°K, respectively. This implies that the ratio between the characteristic time scale for condensation *versus* the time scale for temperature change would be very small (Richter, 2004) and explains the very low $\delta^{74/70}$Ge in CB_b. Furthermore, if CB_a formed at 10^{-2} bar, as suggested by Fedkin et al. (2015), the growth of metal grains would be one order of magnitude higher than the CB_b. Even if large CB_a metal grains formed quickly, given the low cooling rate experienced and their textural homogenisation, they must have remained at high temperature for at least 400 days. Thus, CB_a should experience a maximum cooling rate of ~0.01 K/h which seems reasonable for CB_a to acquire the heavy $\delta^{74/70}$Ge of the source.

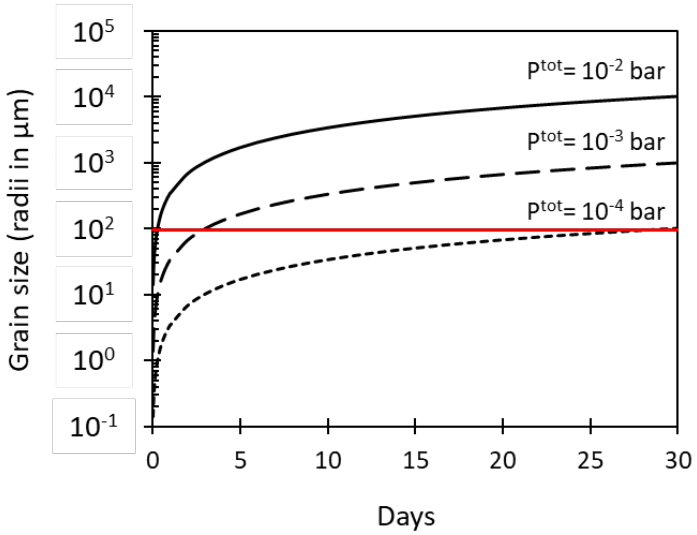

Figure 3.10: Growing rate of metal grains in function of the gas pressure. Solid curve: 0.14 µm/h; long dash curve: 1.40 µm/h; dash line: 14.08 µm/h. The red line represents a grain of 100 µm typical of the grain size observed in the CB here investigated. The calculations are based on Meibom et al. (2000).

4.3. Origin of Ge zonations in Gujba (CB_a) metal grains

Elemental and isotopic zonations of Ge in the two metal grains from CB_a Gujba are positively correlated. The cores have high Ge contents and are enriched in heavy isotopes, whereas the edge parts display lower Ge concentration and lighter isotopic compositions (grain 1: Ge varies from 1.86 to 0.7 ppm, $\delta^{74/70}$Ge from +1.03 ± 0.19‰, to +0.65 ± 0.2‰; grain 2: Ge from 1.35 to 0.83 ppm, $\delta^{74/70}$Ge from +1.35 ± 0.2‰ to +0.82 ± 0.2‰, Fig. 3.11). Compared to Ge, Fe and Ni show no isotopic zonation in most of CB_a metal grains (mean δ^{56}Fe = -0.17 ± 0.65‰ and mean δ^{62}Ni = +0.51 ± 0.9‰, Weyrauch et al., 2019). As Ge is more volatile than Fe and Ni (Ge: $T_{50\%\ cond}$= 830K; Fe: $T_{50\%\ cond}$ = 1338K; Ni: $T_{50\%\ cond}$ = 1363K; Wood et al., 2019), its elemental and isotopic zonations in the metal phase likely reflect conditions at lower

temperatures. Therefore, the zonation may suggest that: (1) Ge diffused from the core to the outer part of the grains during one or several heat event(s); or (2) CB_a formed close to equilibrium, thus the decrease of $\delta^{74/70}$Ge may indicate an early stage of condensation as described in Richter (2004, Fig.7); or (3) the isotopic composition of the starting material was heterogeneous in composition.

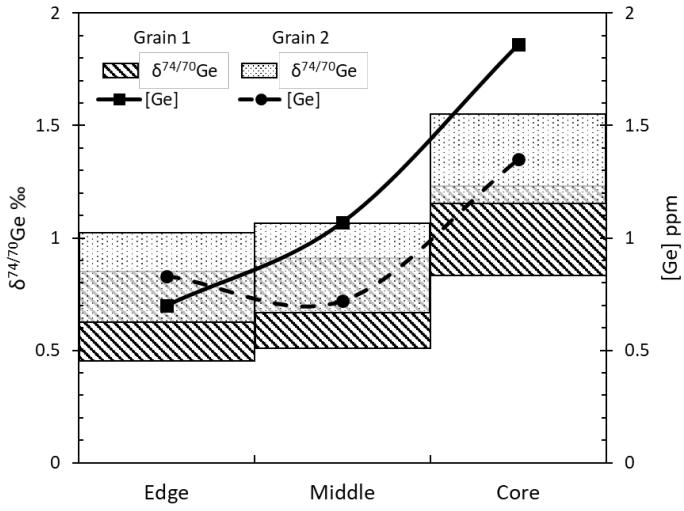

Figure 3.11: Representation of the evolution of [Ge] and $\delta^{74/70}$Ge zonation in each grain. The squares correspond to the isotopic composition and the curves to the elemental one. Isotopic composition of the two grains overlap for the edge and the middle part. See Table 2 for percentage of each fraction.

4.3.1. Diffusion of Ge in CB_a metal grains

The diffusion rate increases with the temperature and light isotopes diffuse faster than heavier ones (Richter et al., 2009); hence it would be tempting to attribute $\delta^{74/70}$Ge zonation in CB_a metal grains to isotopic diffusion. In a closed system, it is expected that diffusion would homogenise Ge contents in the grain. On the other hand, partial Ge evaporation from the grain in an open system can enrich the core in Ge contents compared to the rim, which agree with our results (Fig. 3.7 and 3.11). Experiments using radioisotopes of Ge with very short half-life (less than 10 days), show that self-diffusion of Ge is a very low process (Vogel et al., 1983), with very similar diffusion rates between heavy isotopes (^{77}Ge) and light isotopes (^{71}Ge), with 1.447 * 10^{-4} µm²/s and 1.462 * 10^{-4} µm²/s at 900°C (Campbell, 1975), respectively. In addition, the diffusion rate of Ge isotopes is higher in copper matrix (D^{73}Ge = 0.949*10-1 µm2/s at 1335 K) than in pure Ge, and similar to the diffusion rate of ^{68}Ge (Hehenkamp et al., 1979), precluding large isotopic fractionation during diffusion. Thus, small isotopic fractionation during diffusion cannot account for the significant $\delta^{74/70}$Ge zonation in Gujba metal grains characterised by large enrichment in light isotopes in the rim of grain 1 ($\delta^{74/70}$Ge = +0.82 ± 0.20) compared to its core ($\delta^{74/70}$Ge = +1.35 ± 0.20).

4.3.2. Kinetic condensation close to equilibrium

At cooling rates higher than those required for equilibrium condensation, the very first condensates would have an isotopic composition close to that of the source (see Fig. 7 in Richter,

2004). This heavy enrichment in the core compared to the intermediate section (i.e. between the core and the rim) may be very difficult to measure for high cooling rates as it represents less than 5% of the condensate (Richter, 2004). Yet, at a low cooling rate, close to equilibrium, this first decrease in isotopic composition represents up to 20% of the condensate and creates a "wave" pattern in the condensate (a slight decrease followed by a strong increase of $\delta^{74/70}$Ge). No increase of $\delta^{74/70}$Ge is shown from the core to the edge of the two Gujba metal grains (Fig. 3.11), meaning either that: (1) the variations from the highest $\delta^{74/70}$Ge and [Ge] (core of grain 2) to the lowest values (edge of grain 1) would then represent up to 20% of the quantity of condensed Ge; or that (2) the resolution of our dissolution technique may be too coarse to capture the full 'wave' pattern of $\delta^{74/70}$Ge. If the Ge zonations are the result of kinetic condensation close to equilibrium, they must represent the first steps of Ge condensation (Richter, 2004). This implies that the temperature at the end of the formation of grain 1 was higher than $T_{\text{Ge-50\% condensation}} = 830$K and that the isotopic composition of the starting material was ≥ 1.35‰. Furthermore, as large metal grains were formed by the aggregation of small ones (Fig. 3.2), different generations of grains exist. Due to fractional condensation, the first generation has a heavy $\delta^{74/70}$Ge, and was agglomerated to form the core, whereas the last one has a light $\delta^{74/70}$Ge and was agglomerated around the core to form the edge.

4.3.3. Heterogeneous $\delta^{74/70}$Ge composition of the gas source

Processes such as condensation and evaporation can create elemental and isotopic fractionation between solid and gas, leading to heterogeneity in the source. Metal grains could record these heterogeneities generating the chemical and isotopic zonations.

To test this model, we have performed a numerical modelling of evaporation / condensation based on Rayleigh fractionation laws. A specific type of solid condensing close to equilibrium acquires a bulk isotopic composition close to the gas composition. The low isotopic composition acquired during the first step of metal formation represents only 10 to 20% of the bulk Ge_{gas} (Richter, 2004) which is then balanced by the 80% of Ge remaining. If metal in CB_a chondrites condenses at a low cooling rate, as suggested by our textural and elemental data on Bencubbin, we expect no or minor fractionation between the first condensate and the gas. The bulk $\delta^{74/70}Ge_{metal}$ of Bencubbin (CB_a) is then very close to the isotopic composition of the gas source, namely $\delta^{74/70}Ge_{bencubbin} = +1.04 \pm 0.09$‰. It follows that grain cores that have a $\delta^{74/70}$Ge composition close to the bulk composition of Bencubbin (i.e. core of grain 1, $\delta^{74/70}Ge = +1.03 \pm 0.19$‰) condense at low cooling rates. The ones depleted in Ge and enriched in heavy isotopes compared to Bencubbin bulk (i.e. core of grain 2, $\delta^{74/70}Ge = +1.35 \pm 0.20$‰) experience evaporation (Fig. 3.8).

The depletion in Ge of grain core 2 (Ge = 1.35 ppm) compared to the grain 1 (Ge = 1.86 ppm) could be produced by ~25 % of evaporation (Equation 3.1):

$$\%[Ge]_{evap} = 1 - \frac{[Ge]_{core2}}{[Ge]_{core1}} \times 100 \quad \text{Eq. 3.1}$$

Where $[Ge]_x$ is the Ge content in the grain "X", and $\%[Ge]_{evap}$ the percentage of evaporation needed to decrease the Ge content from the grain 1 to 2.

To quantify evaporation, we formulate the hypothesis that grain cores of CB_a first condensed at low cooling rate, with $\delta^{74/70}Ge \approx 1.04 \pm 0.09‰$ (first step of condensation). They were then carried out to a warmer environment where they quickly reached high temperatures and experienced partial evaporation. In this scenario, the characteristic time scales for evaporation is smaller than the timescale of the temperature change, causing not only the enrichment in heavy isotopes of the solid compared to the gas (Richter, 2004), but also the formation of plessitic textures in some grain cores, as observed by Weyrauch et al. (2019). The effect of evaporation on $\delta^{74/70}Ge$ can be modelled as follows (Equation 3.2):

$$\delta^{74}Ge_f = \left[\left(1000 + \delta^{74}Ge_0\right) * f^{(\alpha-1)}\right] - 1000 \quad \text{Eq. 3.2}$$

where $\delta^{74}Ge_f$ is the isotopic composition of the solid after evaporation, $\delta^{74}Ge_0$ the initial isotopic composition of solids formed at a low cooling rate (namely $\delta^{74}Ge_0 = 1.04 \pm 0.09‰$ in this study), f the remaining fraction of Ge in the solid after evaporation, and α the fractionation factor equal to $(m70/m74)^{\beta}$ where $m70$ is the mass of ^{70}Ge, $m74$ the mass of ^{74}Ge and β an empirical parameter which is equal to 0.5 in pure Rayleigh fractionation.

Thus, as the core of metal grains loses light isotopes and become heavier, the gas becomes enriched in light isotopes. The evolution of the gas isotopic composition is calculated as a mixing between the cumulated vapour formed by Ge evaporation from metal grains and the initial gas isotopic composition (Eq. 3.3 and 3.4):

$$\delta^{74}Ge_{cumv} = \left[\left(1000 + \delta^{74}Ge_0\right) * \left(\frac{1-f^{\alpha}}{1-f}\right)\right] - 1000 \quad \text{Eq. 3.3}$$

$$\delta^{74}Ge_{gas} = \delta^{74}Ge_0 * f + \delta^{74}Ge_{cumv} * (1-f) \quad \text{Eq. 3.4}$$

where $\delta^{74}Ge_{cumv}$ is the Ge isotopic composition of the cumulated vapour formed by evaporation from the metal and $\delta^{74}Ge_{gas}$ is the evolution of Ge isotopic composition of the gas. All other parameters are the same as for equation 3.2.

Due to a constant arrival of metallic droplets that partly evaporate, the gas in these zones becomes progressively enriched in Ge-light isotopes. Also, due to the high dust pressure in warm zones, and fast FeNi condensation (see § 4.2), these metal cores act as nuclei for the aggregation of small metal grains which re-condense at equilibrium, insulating the core and preventing the complete loss of Ge. As the temperature of the gas constantly decreases, the germanium starts to re-condense at a low cooling rate, recording isotopic variations of the gas composition. This second step of condensation is responsible for the light Ge isotopic composition in the middle and edge part of metal grains, compared to the core.

The differences in bulk Ge isotopic compositions between grains 1 and 2 can be explained by the differences in their velocity / arrival time into the warmer zone. Considering the decrease in temperature of the gas with time, the grains 2 that arrive first in the warm zone experience higher temperature than the following ones. This results in a stronger evaporation rate and a higher enrichment of the core in heavy isotopes compared to the grains which follow. Grains 1 that arrive at the end of Ge condensation do not experience such a high temperature and keep their inherited equilibrium value in their core. As more grains evaporate before their arrival, the gas composition is lighter than for the previous generation, which results in a bulk isotopic composition lighter than $\delta^{74/70}Ge = +1.04 \pm 0.09‰$. This suggests that grain 1 is formed later than grain 2. The model is represented in Figure 3.12.

Therefore, we conclude that: (1) the metal grains population in CB_a results from several grain generations, (2) some grains have been reheated; (3) the isotopic zonation of Gujba metal grains can be the result of either condensation close from the equilibrium or, more likely, combined processes of condensation at low cooling rates followed by kinetic evaporation and recondensation at low cooling rates; (4) these processes are not recorded by FeNi isotopes because they occur at lower temperatures than the Fe-Ni condensation.

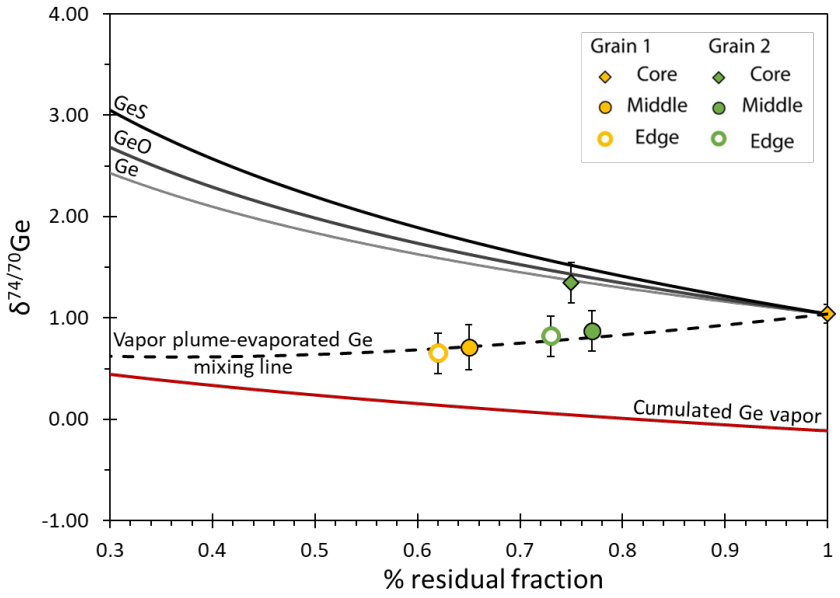

Figure 3.12: Rayleigh modelling of the $\delta^{74/70}Ge$ vs %residual fraction of Ge in the metal grain. Curves in black, gray and light gray show the isotopic evolution of the solid function of the Ge species (Ge, GeO, GeS, respectively) during evaporation with a gas-melt isotopic fractionation factor α of 0.99833, 0.99864, and 0.99885 defined as $(m^{70}/m^{74})^{\beta}$ and a β of 0.03. The red line corresponds to cumulated vapor and the dotted line represents the evolution of the plume-gas during it mixing with the cumulated vapor. The starting isotopic composition is grain 1 core (i.e. similar to the plume, see text) and its elemental composition (1.40 ppm, see text). The modeling shows that it is possible to explain the evolution of the zonation in metal grains by mixing the produced vapor and the isotopic composition of the plume.

5 Model for CB formation, disk or plume?

Two models have been suggested for the formation of CB chondrites: 1) The formation of metal by migration in the disk (Meibom et al., 2000), or 2) The formation during an impact plume (Kallemeyn et al., 2001; Campbell et al., 2002). Elemental composition of small metal grains suggests that the formation of the sub–group CB_a requires at least two different types of environments. Furthermore, the difference in germanium isotopic composition between CB_a and CB_b requires a thermally-zoned environment, as is also the case for the isotopic zonations to form in CB_a metal grains. Finally, the time scale for CB metal grains formation is very short, which means that "cold" and warm zones need to be spatially closely related. Thus, a large structure such as the protoplanetary disk seems unlikely for CB formation, and the impact plume (e.g. Campbell et al., 2002; Rubin et al., 2003) appears to be a possibility for the formation of CB groups. If so, this plume needs to be thermally zoned with the temperature dropping very fast at the exterior and the interior remaining warm for a sufficiently long time. In these conditions, CB_a may condense at low cooling rates in the inner part of the plume and CB_b at high cooling rates in the outer part. Finally, if CB_a and CB_b condense from the same gas, the higher Au/Ir and Pd/Ir ratios for CB_a compared to CB_b (Fig. 3.6A) imply that CB_a condense after CB_b as Au and Pd are more volatile than Ir. This observation is also supported by the enrichment in W and Mo of Cb_b compared to CB_a.

6 Conclusion

We have performed elemental and isotopic measurements on metal phases of two CB_a, Bencubbin and Gujba, and one CB_b, HaH 237, in order to explore the formation of these carbonaceous chondrites.

Our petrological study and *in situ* elemental analyses suggest that large metal grains are formed by the aggregation of small ones. In situ analyses of highly siderophile elements (HSE Re, W, Os, Ir, Ru, Mo, Pt, Rh) in large metal grains also show patterns in contradiction with condensation and chemical homogenisation by diffusion. We suggest that HSE composition of unzoned large metal grains might be the result of metal formation, or the aggregation of small grains already homogenised. Yet the exact process that leads to e.g. flat Ir pattern and variable Re, Ru contents remains unclear.

The $\delta^{74/70}$Ge values obtained on CB_b chondrites are very negative ($\delta^{74/70}$Ge = -0.65 ± 0.1‰), while CB_a displays a positive Ge isotopic composition ($\delta^{74/70}$Ge ≈ +1.04 ± 0.09‰ for Bencubbin bulk). We interpret this difference in bulk values in terms of cooling rates during condensation in an impact plume, with CB_b experiencing high cooling rates and kinetic condensation, acquiring negative $\delta^{74/70}$Ge. On the other hand, CB_a experiences low cooling rates

and condensation close to the equilibrium, hence acquiring positive $\delta^{74/70}$Ge. We suggest, in agreement with previous studies, that CB_b formed in the external part of the plume and CB_a in the inner part. The identification of a heterogeneous plume implies pressure constraints, thus on the growth speed of metal grains during condensation. Calculated growth rates are 1.40 µm/h for CB_b and 14.08 µm/h for CB_a metal grains.

The Ge elemental and isotopic measurements on fractions from two sequentially digested rounded metal grains from Gujba (CB_a) show that $\delta^{74/70}$Ge values and Ge contents decrease from the core to the edge. These zonations cannot result from the diffusion of Ge through metal grains. We propose that these zonations result from a condensation process close to the equilibrium, and record plume heterogeneity due to Ge evaporation from metal nucleus. We develop a model in which (1) the core of each grain is formed under equilibrium, (2) the core of each grain is then carried in a warmer zone of the plume where it experiences fast partial evaporation of Ge, (3) this kinetic evaporation increases the isotopic composition of the metallic core, (4) due to high dust pressure and temperature levels below Fe–Ni condensation, the core of each grain acts as a nucleus for the condensation and the aggregation of the metal preventing a total loss of Ge by evaporation, (5) Ge evaporation from metal grains also enriches the plume in light isotopes, a process which is recorded in the external layers of metal grains. This model explains the lighter Ge isotopic composition of the external layer of metal grains compared to their cores. This model also accounts for the occurrence of plessite in the core of some grains.

Concluding remarks

The study of metal formation by condensation is of a major importance in planetary science, as condensation is the first step of processes that will lead to formation of the mineral phases that constitute building blocks of planets. Previous studies focused on the behaviour of refractory siderophile elements to constrain condensation processes. Here we have emphasized the importance of considering moderately volatile elements to explore “lower temperature” events, for which refractory elements (from Os to major elements, Fe-Ni-Co) are not sensitive. In the next part, our attention will focus on heating processes in the solar nebula and on parent bodies, that lead to metal evolution before and after its accretion on parent bodies. This will be achieved by studying the metal composition of ordinary chondrites, and the consequences on redox conditions in the solar nebula.

7 Acknowledgments

The authors would like to acknowledge Damien Cividini for his valuable assistance on the NeptunePlus MC-ICP-MS and his advices for modifying the germanium chemistry. The authors also thank E. Florin for her careful English review. The authors thank Yoann Greau and Timothy Murphy for their help and advises during the process of analysis at Macquarie University. The authors would also like to thank Joachim Karl for providing a sample of Hammadah al Hamra 237, T. McCoy and J. Hoskin from the Smithsonian Institute for their Bencubbin and Gujba samples.

8 References

Alard O., Griffin W. L., Lorand J. P., Jackson S. E., and O'Reilly S. Y. 2000. Non-chondritic distribution of the highly siderophile elements in mantle sulphides. Nature 407:891–894.

Alard O., Griffin W. L., Pearson N. J., Lorand, J.-P. & O'Reilly, S.Y. 2002. New insights into the Re/Os systematics of sub-continental lithospheric mantle from in situ analysis of sulphides. Earth and Planetary Science Letters 203:651–663.

Anders E., and Grevesse N. 1989. Abundances of the elements: Meteoritic and solar. Geochimica et Cosmochimica Acta 53:197–214.

Bollard J., Connelly J. N., and Bizzarro M. 2015. Pb-Pb dating of individual chondrules from the CB a chondrite Gujba: Assessment of the impact plume formation model. Meteoritics & Planetary Science 50:1197–1216.

Campbell D. R. 1975. Isotope effect for self-diffusion in Ge. Physical Review B 12(6):2317–2324.

Campbell A. J., Humayun M., and Weisberg M. K. 2000. Siderophile-Element Distributions in Zoned Metal Grains in Hammadah Al Hamra 237. Meteoritics and Planetary Science Supplement 35:A38.

Campbell A. J., Humayun M., Meibom A., Krot A. N., and Keil K. 2001. Origin of zoned metal grains in the QUE94411 chondrite. Geochimica et Cosmochimica Acta 65:163–180.

Campbell A. J., Humayun M., and Weisberg M. K. 2002. Siderophile element constraints on the formation of metal in the metal-rich chondrites Bencubbin, Weatherford, and Gujba. Geochimica et Cosmochimica Acta 66:647–660.

Campbell A. J., Zanda B., Perron C., Meibom A., and Petaev M. I. 2005. Origin and thermal history of Fe-Ni metal in primitive chondrites. In Chondrites and the protoplanetary disk, edited by Krot A. N., Scott E. R. D., and Reipurth B. San Francisco: Astronomical Society of the Pacific. pp. 407–431.

Chou C.-L., and Cohen A. J. 1973. Gallium and germanium in the metal and silicates of L- and LL-chondrites. Geochimica et Cosmochimica Acta 37:315–327.

Eggins S. M., Kinsley L. P. J., and Shelley J. M. G. 1998. Deposition and element fractionation processes during atmospheric pressure laser sampling for analysis by ICP-MS. Applied Surface Science 127–129:278–286.

Eggins S. M. et al. 2005. In situ U-series dating by laser-ablation multi-collector ICPMS: new prospects for Quaternary geochronology. Quaternary Science Reviews 24:2523–2538.

Escoube R., Rouxel O. J., Luais B., Ponzevera E., and Donard O. F. X. 2012. An Intercomparison Study of the Germanium Isotope Composition of Geological Reference Materials. Geostandards and Geoanalytical Research 36:149–159.

Fedkin A. V., Grossman L., Humayun M., Simon S. B., and Campbell A. J. 2015. Condensates from vapor made by impacts between metal-, silicate-rich bodies: Comparison with metal and chondrules in CB chondrites. Geochimica et Cosmochimica Acta 164:236–261.

Fegley B., and Palme H. 1985. Evidence for oxidizing conditions in the solar nebula from Mo and W depletions in refractory inclusions in carbonaceous chondrites. Earth and Planetary Science Letters 72:311–326.

Florin G., Luais B., Rushmer T., and Alard O. 2020. Influence of redox processes on the germanium isotopic composition of ordinary chondrites. Geochimica et Cosmochimica Acta 269:270–291.

Griffin W.L., Powell W. J., Pearson N. J. & O'Reilly S. Y. 2008. GLITTER: data reduction software for laser ablation ICP-MS. In: Sylvester, P. (ed.) Laser Ablation–ICP–MS in the Earth Sciences. Mineralogical Association of Canada, Short Course Series 40, Appendix 2, 204–207

Grossman L., Beckett J. R., Fedkin A. V., Simon S. B., and Ciesla F. J. 2008. Redox conditions in the solar nebula: observational, experimental, and theoretical constrains. Reviews in Mineralogy & Geochemistry 68:93–140.

Grossman J., Rubin A., and Macpherson G. 198. ALH85085: a unique volatile-poor carbonaceous chondrite with possible implications for nebular fractionation processes. Earth and Planetary Science Letters 91:33–54.

Grossman J. N., and Zipfel J. 2001. The Meteoritical Bulletin, No. 85, 2001 September. Meteoritics & Planetary Science 36:A293–A322.

Gilbert S., Danyushevsky L., Robinson P., Wohlgemuth-Ueberwasser C., Pearson N., Savard D., Norman M., and Hanley J. 2013. A Comparative Study of Five Reference Materials and the Lombard Meteorite for the Determination of the Platinum-Group Elements and Gold by LA-ICP-MS. Geostandards and Geoanalytical Research 37:51–64.

Herzog G.F. 2007. 1.13 – Cosmic-Ray Exposure Ages of Meteorites, 1rt ed., edited by Holland H. D. and Turekian K. K. Oxford: Pergamon. pp 1–36

Hirth J. P., and Pound G. M. 1963. Progress in minerals science vol. 11: condensation and evaporation, nucleation and growth kinetics. 1st ed., London: Pergamon Press. 192p.

Horn I., and Günther D. 2003. The influence of ablation carrier gasses Ar, He and Ne on the particle size distribution and transport efficiencies of laser ablation-induced aerosols: implications for LA–ICP–MS. Applied Surface Science 207:144–157.

Humayun M., and Clayton R. N. 1995. Potassium isotope cosmochemistry: Genetic implications of volatile element depletion. Geochimica et Cosmochimica Acta 59:2131–2148.

Kallemeyn G. W., Boynton W. V., Willis J., and Wasson J. T. 1978. Formation of the Bencubbin polymict meteoritic breccia. Geochimica et Cosmochimica Acta 42:507–515.

Krot A. N., Meibom A., Petaev M. I., Keil K., Zolensky M. E., Saito A., Mukai M., and Ohsumi K. 2000. Ferrous silicate spherules with euhedral iron-nickel metal grains from CH

carbonaceous chondrites: Evidence for supercooling and condensation under oxidizing conditions. Meteoritics & Planetary Science 35:1249–1258.

Langhoff S. R., and Bauschlicher C. W. 1988. Ab initio studies of transition metal systems. Annual Reviews in Physics and chemistry 39:181–212.

Krot A. N., Amelin Y., Cassen P., and Meibom A. 2005. Young chondrules in CB chondrites from a giant impact in the early Solar System. Nature 436:989–992.

Lodders K. 2003. Solar System Abundances and Condensation Temperatures of the Elements. The Astrophysical Journal 591:1220–1247.

Lodders K., Palme H., and Gail H. 2009. 3.4 Abundances of the elements in the Solar System. In Solar System. Edited by Trümperp J. E. New York: Springer-Verlag. pp. 560–630.

Luais B. 2007. Isotopic fractionation of germanium in iron meteorites: Significance for nebular condensation, core formation and impact processes. Earth and Planetary Science Letters 262:21–36.

Luais B. 2012. Germanium chemistry and MC-ICPMS isotopic measurements of Fe–Ni, Zn alloys and silicate matrices: Insights into deep Earth processes. Chemical Geology 334:295–311.

Marty B., Kelley S., and Turner G. 2010. Chronology and shock history of the Bencubbin meteorite: A nitrogen, noble gas, and Ar–Ar investigation of silicates, metal and fluid inclusions. Geochimica et Cosmochimica Acta 74:6636–6653.

Meibom A., Petaev M. I., Krot A. N., Wood J. A., and Keil K. 1999. Primitive FeNi metal grains in CH carbonaceous chondrites formed by condensation from a gas of solar composition. Journal of Geophysical Research: Planets 104:22053–22059.

Meibom A. 2000. Large-Scale Thermal Events in the Solar Nebula: Evidence from Fe,Ni Metal Grains in Primitive Meteorites. Science 288:839–841.

Meibom A., Righter K., Chabot N., Dehn G., Antignano A., McCoy T. J., Krot A. N., Zolensky M. E., Petaev M. I., and Keil K. 2005. Shock melts in QUE 94411, Hammadah al Hamra 237, and Bencubbin: Remains of the missing matrix? Meteoritics & Planetary Science 40:1377–1391.

Mullane E., Alard O., Gounelle M., and Russell S. S. 2004. Laser ablation ICP-MS study of IIIAB irons and pallasites: constraints on the behaviour of highly siderophile elements during and after planetesimal core formation. Chemical Geology 208:5–28.

Newsom H. E., and Drake M. J. 1979. The origin of metal clasts in the Bencubbin meteoritic breccia. Geochimica et Cosmochimica Acta 43:689–707.

Petaev M. I., Meibom A., Krot A. N., Wood J. A., and Keil K. 2001. The condensation origin of zoned metal grains in Queen Alexandra Range 94411: Implications for the formation of the Bencubbin-like chondrites. Meteoritics & Planetary Science 36:93–106.

Richter F. M. 2004. Timescales determining the degree of kinetic isotope fractionation by evaporation and condensation. Geochimica et Cosmochimica Acta 68:4971–4992.

Richter F. M., Dauphas N., and Teng F.-Z. 2009. Non-traditional fractionation of non-traditional isotopes: Evaporation, chemical diffusion and Soret diffusion. Chemical Geology 258:92–103.

Richter F. M., Huss G. R., and Mendybaev R. A. 2014. Iron and nickel isotopic fractionation across metal grains from three CBb (abstract #1346). 45th Lunar and Planetary Science Conference.

Righter K., Campbell A. J., and Humayun M. 2005. Diffusion of trace elements in FeNi metal: Application to zoned metal grains in chondrites. Geochimica et Cosmochimica Acta 69:3145–3158.

Rouxel O. J., and Luais B. 2017. Germanium Isotope Geochemistry. Reviews in Mineralogy and Geochemistry 82:601–656.

Rubin A. E., Kallemeyn G. W., Wasson J. T., Clayton R. N., Mayeda T. K., Grady M., Verchovsky A. B., Eugster O., and Lorenzetti S. 2003. Formation of metal and silicate globules in Gujba: a new Bencubbin-like meteorite fall. Geochimica et Cosmochimica Acta 67:3283–3298.

Saunders N., and Miodownik A. P. 1998. CALPHAD (calculation of phase diagrams): a comprehensive guide (Vol. 1). Amsterdam: Elsevier B.V. 478p.

Schauble E. A. 2004. Applying Stable Isotope Fractionation Theory to New Systems. Reviews in Mineralogy and Geochemistry 55:65–111.

Schaudy R., Wasson J. T., and Buchwald V. F. 1972. The Chemical Classification of Iron Meteorites: VI. A Reinvestigation of iron with Ge concentration lower than 1ppm. Icarus 17:174–192.

Scott E. R. D., and Krot A. N. 2014. Chondrites and Their Components. In vol. 2 of Treatise on Geochemistry 2nd Edition. Edited by Heinrich D. Holland and Karl K. Turekian, Elsevier Science. pp. 65–135.

Scott E. R. D., and Wasson J. T. 1976. Chemical classification of iron meteorites: VIII. Groups IC. IIE, IIIF and 97 other irons. Geochimica et Cosmochimica Acta 40:103–115.

Sears D. W. 1978. Condensation and the composition of iron meteorites. Earth and Planetary Science Letters 41:128–138.

Wai C. M., and Wasson J. T. 1979. Nebular condensation of Ga, Ge and Sb and the chemical classification of iron meteorites. Nature 282:790.

Walker R. J., McDonough W. F., Honesto J., Chabot N. L., McCoy T. J., Ash R. D., and Bellucci J. J. 2008. Modeling fractional crystallization of group IVB iron meteorites. Geochimica et Cosmochimica Acta 72:2198–2216.

Wasson J. T., and Schaudy R. 1971. The chemical classification of iron meteorites: V groups IIIC and IIID and other irons with germanium concentrations between 1 and 25 ppm. Icarus 14:59–70.

Wasson J. T. 1974. Meteorites: Classification and Properties, Berlin Heidelberg: Springer-Verlag. 318p.

Weisberg M. K., Prinz M., and Nehru C. E. 1990. The Bencubbin chondrite breccia and its relationship to CR chondrites and the ALH85085 chondrite. Meteoritics 25:269–279.

Weisberg M. K., Prinz M., Clayton R. N., Mayeda T. K., Grady M. M., and Pillinger C. T. 1995. The CR chondrite clan. Antarctic Meteorite Research 8:11.

Weisberg K. M., and Prinz M. 1999. Zoned metal in the CR clan chondrites. Proceedings, 24th Symposium on Antarctic Meteorites. pp. 187–189

Weisberg M. K., Prinz M., Clayton R. N., Mayeda T. K., Sugiura N., Zashu S., and Ebihara M. 1999. QUE 94411 and the Origin of Bencubbinites (abstract #1416). 30th Annual Lunar and Planetary Science Conference.

Weisberg M. K., Prinz M., Clayton R. N., Mayeda T. K., Sugiura N., Zashu S., and Ebihara M. 2001. A new metal-rich chondrite grouplet. Meteoritics & Planetary Science 36:401–418.

Weyrauch M., Zipfel J., and Weyer S. 2019. Origin of metal from CB chondrites in an impact plume – A combined study of Fe and Ni isotope composition and trace element abundances. Geochimica et Cosmochimica Acta 246:123–137.

Wood B. J., Smythe D. J., and Harrison T. 2019. The condensation temperatures of the elements: A reappraisal. American Mineralogist 104:844–856.

Young E. D., Galy A., Nagahara H. 2002. Kinetic and equilibrium mass-dependent isotope fractionation laws in nature and their geochemical and cosmochemical significance. Geochimica Cosmochimica Acta 66:1095-1104.

Zhang J., Williams D. B., and Goldstein J. I. 1993. The microstructure and formation of duplex and black plessite in iron meteorites. Geochimica et Cosmochimica Acta 57:3725–3735.

Zhu K., Liu J., Moynier F., Qin L., Alexander C. M. O., and He Y. 2019. Chromium Isotopic Evidence for an Early Formation of Chondrules from the Ornans CO Chondrite. The Astrophysical Journal 873:82.

Zipfel J., Wlotzka F., and Spettel B. 1998. Bulk Chemistry and Mineralogy of a New “Unique” Metal-rich Chondritic Breccia, Hammadah AL Hamra 237 (abstract #1417). 29th Annual Lunar and Planetary Science Conference.

Zipfel J., and Weyer S. 2007. In situ analyses of fe isotopes in zoned metal grains of Hammadah Al Hamra 237 (abstract #1927). 38th Annual Lunar and Planetary Science Conference.

Appendix A

Chemistry

The analytical procedure for germanium purification is adapted from that of Luais (2007, 2012, and references therein), to higher mass of metal sample. The low concentration of Ge in CB (around 1 ppm) constrains to digest large amount of metal that would oversaturate the 2 ml of cationic resin used for Ge separation from the Fe-Ni matrix (Luais, 2007). Thus, we calibrated 10 ml columns of cationic resin (AG 50W-X8, Biorad, Hercules, Ca, USA) to perform Ge purification. The 8 ml solutions of 2 M HNO_3 of dissolved metal samples were evaporated on hot plate at 60°C until complete evaporation. Then the dried sample residue was diluted in 8 ml of 0.5 M HNO_3 for Ge purification using cationic-exchange resin. A solution equivalent to a maximum of 60 mg of sample was loaded onto the column in the form of 2 ml of 0.5 M HNO_3, for a given sample of about 200-300 mg, four to five columns were used. The germanium was then fully recovered in 8 ml of 0.5 M HNO_3 while Fe, Ni, Co, Zn, Ga remained adsorbed on the resin (Fig. 3A). Then the eluted Ge fractions from the different columns of the same sample were combined in a single beaker, evaporated to dryness and diluted in 2 ml of high purity (SeaStar®) 0.5M HNO_3 for subsequent NeptunePlus MC-ICP-MS isotopic measurements.

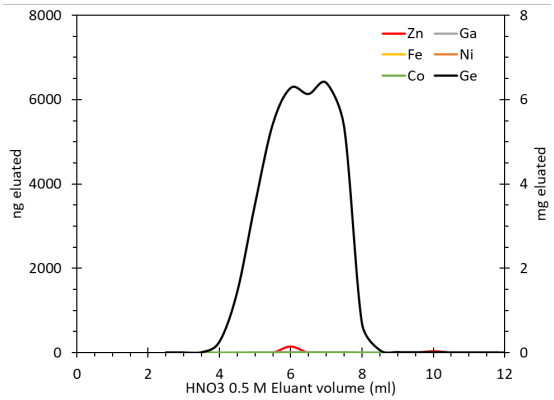

Figure 3.A: AG 50W-X8 elution curves for 35500 ng about 35mg of Ge in function of the quantity of HNO3 0.5 M eluted from the column. The first 2.5 ml corresponds to the sample loading and to the dead volume of the resin. Only germanium is eluted at this molarity. Note that a very small amount of Zn, corresponding to less than 0.01 % of total amount of loaded Zn, is eluted around 6 ml, and 10 ml of HNO3.

Mass Fractionation

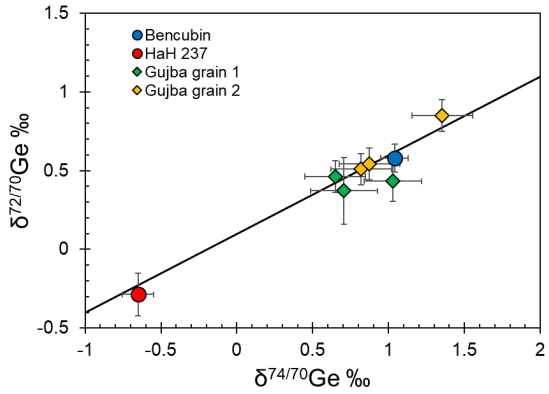

Figure 3.B: $\delta^{72/70}Ge$ vs $\delta^{74/70}Ge$ diagram for Bencubbin samples. All the data plot on the mass fractionation line, demonstrating the accuracy of our measurements. Diamonds correspond to sequentially digested metal fractions while circles correspond to bulk metal fractions.

Appendix B

Table 3.A: Elemental composition in ppm of metal grains in Gujba, Bencubbin (Ben) and HaH 237 (HaH), Elements are classified in function of their volatilities. B.L.: bellow detection limit.

Element	Re	Os	W	Ir	Ru	Mo	Pt	Rh	Ni	Co	Pd	As	Au	Cu	Ag	Sb	Ga	Ge	Bi	Pb	Te	Sn	Co/Ni	W/Mo
Gujba-1-L-1	3.120	1.600	0.900	1.810	2.290	4.280	3.750	0.742	61576	5623	2.500	5.020	0.404	90.31	B.L.	0.537	6.200	5.330	B.L.	B.L.	B.L.	B.L.	0.091	0.210
Gujba-1-L-2	1.390	1.680	0.870	1.780	2.860	3.910	3.110	0.573	63478	5616	2.730	3.880	0.347	133.2	B.L.	0.136	5.120	3.760	0.056	B.L.	B.L.	B.L.	0.088	0.223
Gujba-1-L-3	1.560	1.600	0.740	1.850	2.680	3.540	3.070	0.566	64527	5537	2.200	4.520	0.327	104.2	0.038	0.167	5.460	3.800	B.L.	0.061	B.L.	B.L.	0.086	0.209
Gujba-1-L-4	2.050	1.490	0.410	2.020	3.000	4.130	3.640	0.572	62681	5513	1.970	4.910	0.253	111.0	B.L.	0.085	6.640	4.290	B.L.	B.L.	0.037	6.650	0.088	0.099
Gujba-1-L-5	1.210	1.630	0.680	1.920	2.140	5.020	3.560	0.697	56485	5634	2.210	4.840	0.310	120.2	B.L.	0.153	5.540	3.470	B.L.	B.L.	B.L.	B.L.	0.100	0.135
Gujba-1-L-6	2.280	1.780	0.780	1.920	3.160	3.560	3.900	0.674	60413	5644	2.580	4.840	0.312	68.05	B.L.	0.180	5.740	3.920	B.L.	B.L.	B.L.	B.L.	0.093	0.219
Gujba-1-L-7	1.860	1.690	0.930	1.810	2.770	4.880	3.440	0.732	63337	5336	2.230	4.430	0.301	103.4	0.054	0.211	6.300	3.200	B.L.	0.074	0.069	B.L.	0.084	0.191
Gujba-1-L-8	2.250	1.500	0.700	1.510	2.520	4.120	3.480	0.567	57828	5325	2.340	3.980	0.333	162.1	B.L.	B.L.	5.850	2.320	B.L.	B.L.	0.072	B.L.	0.092	0.170
Gujba-1-L-9	1.340	1.620	0.940	1.630	2.670	3.940	3.260	0.639	63252	5152	2.220	5.340	0.307	92.09	0.031	0.207	6.400	2.950	0.005	0.053	B.L.	3.880	0.081	0.239
Gujba-1-L-10	1.170	1.450	0.750	1.500	2.240	4.210	3.160	0.542	60468	5036	2.170	4.430	0.265	163.2	B.L.	0.089	5.730	3.570	B.L.	0.194	B.L.	B.L.	0.083	0.178
Gujba-1-L-11	1.030	1.360	0.870	1.620	2.410	3.980	3.460	0.552	62235	5253	2.240	5.570	0.328	141.4	B.L.	B.L.	6.170	3.150	0.007	0.090	0.124	B.L.	0.084	0.219
Gujba-1-L-12	1.150	1.490	0.490	1.470	2.650	3.550	3.490	0.562	61984	5157	2.180	4.850	0.287	129.3	0.042	B.L.	6.200	2.910	B.L.	B.L.	B.L.	B.L.	0.083	0.138
Gujba-1-L-13	1.340	1.490	0.390	1.670	2.330	3.720	3.530	0.591	60146	5175	2.210	4.430	0.347	122.5	0.042	0.208	5.340	2.520	B.L.	B.L.	0.137	B.L.	0.086	0.105
Gujba-1-L-14	1.010	1.510	1.010	1.860	2.290	4.140	3.560	0.589	63398	5244	2.260	4.770	0.346	68.64	B.L.	0.502	5.280	3.440	0.024	0.078	B.L.	B.L.	0.083	0.244
Gujba-1-L-15	0.670	1.220	0.510	1.380	2.320	3.150	3.360	0.584	57388	4845	2.220	4.220	0.268	172.2	B.L.	B.L.	5.790	3.290	B.L.	B.L.	B.L.	B.L.	0.084	0.162
Gujba-1-L-16	0.890	1.550	0.650	1.640	2.570	4.580	3.350	0.548	64054	4966	2.000	5.040	0.324	87.76	B.L.	0.148	5.100	2.660	B.L.	0.153	B.L.	3.700	0.078	0.142
Gujba-1-L-17	0.440	1.340	0.200	1.490	2.600	3.410	2.650	0.508	62396	4822	1.850	4.500	0.322	149.5	B.L.	0.144	5.450	2.700	B.L.	B.L.	0.130	2.200	0.077	0.059
Gujba-1-L-18	0.340	1.180	0.420	1.220	2.240	3.280	2.720	0.458	61859	4657	2.280	4.480	0.248	169.7	B.L.	B.L.	4.800	2.840	0.031	B.L.	0.250	B.L.	0.075	0.128
Gujba-1-L-19	0.320	1.350	0.460	1.450	2.410	3.890	3.000	0.550	65574	4760	2.030	3.900	0.258	96.98	B.L.	B.L.	5.510	2.190	B.L.	0.153	B.L.	B.L.	0.073	0.118
Gujba-1-L-20	0.700	1.010	0.760	1.370	2.020	5.290	2.580	0.481	63549	4592	2.300	5.450	0.311	122.2	B.L.	0.175	5.430	3.930	B.L.	0.128	0.160	4.030	0.072	0.144
Gujba-1-L-21	0.570	1.310	0.560	1.460	2.590	3.920	3.210	0.610	64210	4796	2.120	4.540	0.278	109.0	B.L.	0.090	5.440	3.720	B.L.	0.058	B.L.	2.240	0.075	0.143
Gujba-1-L-22	0.950	1.510	0.400	1.560	2.530	3.360	3.160	0.457	64225	4658	2.030	3.660	0.347	117.4	B.L.	B.L.	4.780	2.900	0.020	B.L.	B.L.	B.L.	0.073	0.119
Gujba-1-L-23	1.100	1.480	0.620	1.670	2.420	3.670	3.090	0.655	66701	4592	2.190	4.010	0.303	76.54	B.L.	B.L.	5.190	2.530	B.L.	B.L.	B.L.	B.L.	0.069	0.169

Element	Re	Os	W	Ir	Ru	Mo	Pt	Rh	Ni	Co	Pd	As	Au	Cu	Ag	Sb	Ga	Ge	Bi	Pb	Te	Sn	Co/Ni	W/Mo
Gujba-1-L-24	0.730	1.240	0.570	1.290	1.860	3.920	3.160	0.475	67495	4395	1.810	5.400	0.245	116.2	B.L.	0.133	4.690	2.180	B.L.	0.155	0.124	4.170	0.065	0.145
Gujba-1-L-25	0.900	1.530	0.440	1.530	1.680	3.830	3.080	0.541	61502	4706	1.800	4.330	0.230	133.6	B.L.	0.147	5.280	2.160	B.L.	B.L.	B.L.	B.L.	0.077	0.115
Gujba-1-L-26	0.840	1.170	0.480	1.310	2.410	4.010	3.310	0.472	59676	4608	2.280	4.760	0.335	170.4	B.L.	0.105	5.660	2.980	B.L.	0.183	B.L.	5.110	0.077	0.120
Gujba-1-L-27	0.940	1.310	0.770	1.430	1.950	3.370	3.000	0.532	62254	4590	2.010	3.750	0.278	127.1	B.L.	0.096	4.950	1.960	B.L.	B.L.	B.L.	B.L.	0.074	0.228
Gujba-1-L-28	0.680	1.170	0.470	1.470	2.130	3.000	2.890	0.503	62457	4450	1.950	4.360	0.294	144.0	0.037	B.L.	5.220	3.670	B.L.	B.L.	B.L.	B.L.	0.071	0.157
Gujba-1-L-29	0.440	1.350	0.150	1.360	2.160	3.070	3.120	0.472	67415	4223	2.340	3.870	0.226	116.5	B.L.	B.L.	4.780	3.370	B.L.	0.087	B.L.	B.L.	0.063	0.049
Gujba-1-L-30	0.310	1.140	0.860	1.370	1.740	5.110	2.740	0.488	62763	4146	2.130	4.300	0.193	160.3	B.L.	B.L.	4.820	2.100	B.L.	0.072	0.250	4.240	0.066	0.168
Gujba-sg-1	0.240	1.190	0.190	1.010	1.840	2.700	2.960	0.448	65623	4455	2.150	6.270	B.L.	67.46	0.043	B.L.	5.470	6.140	B.L.	B.L.	B.L.	B.L.	0.068	0.070
Gujba-sg-2	0.310	1.140	0.190	1.350	1.690	3.540	2.740	0.544	67800	4394	1.360	4.680	0.234	68.55	B.L.	0.360	5.280	B.L.	0.013	B.L.	0.240	11.10	0.065	0.054
Gujba-sg-3	0.260	1.150	0.660	1.210	2.400	5.270	3.230	0.426	64967	4432	1.690	4.460	0.384	70.55	B.L.	B.L.	5.060	2.100	B.L.	0.188	B.L.	B.L.	0.068	0.125
HAH-l-1	1.670	2.750	0.660	2.970	4.660	9.290	5.750	0.814	70856	4170	1.650	2.490	0.287	42.61	B.L.	B.L.	2.360	2.010	B.L.	B.L.	B.L.	B.L.	0.059	0.071
HAH-l-2	1.610	2.930	1.780	3.140	4.900	9.360	6.760	1.228	63045	4212	2.230	2.670	0.231	47.68	0.021	0.065	2.590	2.510	B.L.	0.122	B.L.	B.L.	0.067	0.190
HAH-l-3	1.140	2.780	1.570	3.380	5.460	7.760	6.510	1.149	67440	4319	2.110	3.330	0.206	39.76	B.L.	B.L.	2.940	1.370	B.L.	0.104	B.L.	B.L.	0.064	0.202
HAH-l-4	0.930	2.600	1.240	3.290	4.090	7.570	5.920	0.973	69892	4166	1.980	2.710	0.257	36.47	0.035	B.L.	2.800	1.940	B.L.	B.L.	B.L.	B.L.	0.060	0.164
HAH-l-5	2.170	3.790	1.300	3.730	5.190	8.880	7.890	1.307	67942	4107	2.230	3.840	0.227	44.02	B.L.	B.L.	3.020	2.000	B.L.	0.054	B.L.	3.390	0.060	0.146
HAH-l-6	2.330	2.820	1.680	3.070	5.570	10.52	6.120	1.084	59659	4436	1.960	3.310	0.205	41.20	B.L.	0.083	2.440	1.620	B.L.	0.046	B.L.	B.L.	0.074	0.160
HAH-l-7	1.400	2.810	1.740	3.150	4.850	9.780	6.690	1.252	65225	4123	2.000	3.590	0.261	56.63	B.L.	0.094	2.650	1.860	B.L.	B.L.	0.123	2.060	0.063	0.178
HAH-l-8	1.830	2.930	1.000	3.180	5.110	8.630	6.590	1.139	58005	3963	2.150	3.090	0.236	93.80	0.037	B.L.	2.410	2.070	B.L.	0.233	B.L.	1.410	0.068	0.116
HAH-l-9	6.520	3.550	1.910	3.750	5.510	11.81	7.840	1.480	67527	4249	2.660	3.740	0.223	44.45	B.L.	0.098	3.150	1.600	B.L.	0.091	B.L.	5.750	0.063	0.162
HAH-l-10	1.110	2.750	0.790	3.430	5.390	9.150	6.310	1.046	67999	3960	2.260	3.080	0.196	41.04	B.L.	0.074	2.060	1.030	B.L.	0.125	B.L.	B.L.	0.058	0.086
HAH-l-11	1.260	3.070	1.810	3.430	5.200	10.49	6.760	1.078	65423	4003	2.400	3.260	0.294	42.58	B.L.	0.068	2.250	1.410	B.L.	0.042	B.L.	2.340	0.061	0.173
HAH-l-12	0.980	3.000	1.190	2.930	4.640	8.730	6.010	1.095	67370	4049	2.250	3.030	0.273	38.82	B.L.	B.L.	2.540	1.010	B.L.	B.L.	B.L.	B.L.	0.060	0.136
HAH-l-13	1.090	2.820	1.410	3.710	5.880	9.460	7.350	0.999	69151	3914	2.120	3.650	0.219	39.08	B.L.	0.162	2.300	1.340	B.L.	B.L.	0.400	B.L.	0.057	0.149
HAH-l-14	1.140	2.660	1.310	3.020	4.560	8.520	6.290	1.057	71215	3816	2.210	2.510	0.215	42.24	B.L.	B.L.	2.620	1.590	0.023	0.078	B.L.	B.L.	0.054	0.154
HAH-l-15	1.120	2.680	1.380	3.170	5.000	9.150	5.980	1.160	60890	3973	1.950	2.790	0.210	56.43	B.L.	B.L.	1.990	1.190	B.L.	0.092	B.L.	B.L.	0.065	0.151
HAH-l-16	0.730	1.950	0.900	2.350	4.680	9.050	5.030	0.911	58097	4002	2.060	2.580	0.205	84.19	B.L.	0.076	2.400	2.460	B.L.	0.200	B.L.	B.L.	0.069	0.099
HAH-l-17	1.370	2.750	1.110	2.910	4.640	8.800	6.520	1.140	68441	3917	1.890	2.480	0.284	43.56	0.021	B.L.	2.240	0.800	B.L.	0.111	B.L.	2.420	0.057	0.126
HAH-l-18	1.390	3.030	1.400	3.170	5.170	9.750	6.180	1.067	66292	3797	2.110	1.520	0.212	55.64	B.L.	B.L.	1.890	1.550	B.L.	0.095	0.148	B.L.	0.057	0.144
HAH-g-1	1.140	2.660	1.410	2.940	4.610	8.220	6.300	1.017	68938	3883	2.010	2.700	0.197	40.97	B.L.	B.L.	2.570	1.410	B.L.	B.L.	0.123	2.290	0.056	0.172

Element	Re	Os	W	Ir	Ru	Mo	Pt	Rh	Ni	Co	Pd	As	Au	Cu	Ag	Sb	Ga	Ge	Bi	Pb	Te	Sn	Co/Ni	W/Mo
HAH-g-2	0.900	2.800	1.240	3.100	4.590	7.930	6.810	0.980	70078	3775	2.310	3.410	0.223	37.82	B.L.	0.132	2.710	1.820	B.L.	B.L.	B.L.	1.780	0.054	0.156
HAH-g-3	0.950	2.890	1.240	2.930	5.170	8.400	5.960	1.120	67769	3679	2.170	3.090	0.189	41.41	B.L.	0.087	2.720	1.280	B.L.	0.232	B.L.	B.L.	0.054	0.148
HAH-g2-1	0.850	2.640	1.170	2.850	4.130	7.210	5.430	0.961	69801	3611	1.780	2.500	0.283	38.15	B.L.	0.119	1.870	1.750	B.L.	B.L.	B.L.	B.L.	0.052	0.162
HAH-g2-2	0.860	2.510	1.500	2.980	4.140	10.75	6.650	0.897	71890	3690	1.980	3.430	0.242	43.01	B.L.	0.063	2.030	0.880	B.L.	0.099	B.L.	2.480	0.051	0.140
HAH-g2-3	0.780	2.190	0.920	2.420	4.060	7.090	5.050	1.043	67191	3679	2.500	3.160	0.243	45.86	B.L.	0.113	2.590	0.600	0.011	0.240	B.L.	B.L.	0.055	0.130
Ben-l1-1	0.340	1.040	0.350	1.330	2.130	4.060	3.070	0.544	69950	3529	2.070	3.030	0.188	7.41	B.L.	B.L.	0.950	1.130	B.L.	B.L.	0.230	3.070	0.050	0.086
Ben-l1-2	0.340	1.190	0.340	1.270	1.950	3.640	2.400	0.523	68027	3567	1.860	1.770	0.139	6.73	B.L.	B.L.	0.720	B.L.	B.L.	B.L.	0.111	B.L.	0.052	0.093
Ben-l1-3	B.L.	1.290	0.590	1.250	2.420	3.740	2.970	0.379	68072	3586	1.890	1.690	0.211	7.97	0.033	B.L.	0.930	1.010	B.L.	0.071	B.L.	B.L.	0.053	0.158
Ben-l1-4	0.430	1.280	0.090	1.560	2.510	3.040	2.450	0.474	68457	3537	2.100	2.390	0.120	7.23	B.L.	B.L.	0.740	0.630	0.016	B.L.	0.105	B.L.	0.052	0.030
Ben-l1-5	0.220	0.970	0.440	1.170	2.570	4.140	2.990	0.451	68423	3512	2.120	2.180	0.160	7.86	0.035	B.L.	0.440	B.L.	B.L.	0.114	B.L.	B.L.	0.051	0.106
Ben-l1-6	0.440	1.210	0.450	1.330	2.170	4.560	2.110	0.496	62816	3561	2.180	2.200	0.177	10.46	B.L.	B.L.	1.590	B.L.	B.L.	0.211	B.L.	B.L.	0.057	0.099
Ben-l1-7	0.340	1.000	0.260	1.330	2.430	4.730	2.730	0.505	66788	3565	1.800	2.740	0.241	9.48	B.L.	0.239	1.120	B.L.	B.L.	0.177	B.L.	3.450	0.053	0.055
Ben-l1-8	0.390	1.150	0.430	1.510	2.890	5.570	3.220	0.568	66809	3579	2.100	2.790	0.186	6.54	B.L.	B.L.	1.040	B.L.	B.L.	0.181	0.110	B.L.	0.054	0.077
Ben-l1-9	0.080	1.000	0.510	1.270	1.960	4.040	2.850	0.426	67882	3476	1.970	2.110	0.302	6.61	0.025	0.144	1.020	B.L.	B.L.	0.083	B.L.	B.L.	0.051	0.126
Ben-l1-10	0.270	1.020	0.510	1.230	2.020	4.160	2.980	0.525	69000	3446	1.510	2.660	0.253	6.29	B.L.	B.L.	1.280	B.L.	B.L.	B.L.	B.L.	B.L.	0.050	0.123
Ben-g1-1	0.230	1.060	0.270	1.090	1.980	3.400	3.010	0.531	67829	3509	2.140	2.800	0.156	6.50	B.L.	B.L.	0.810	B.L.	0.010	B.L.	B.L.	B.L.	0.052	0.079
Ben-g1-2	0.220	1.020	0.660	1.400	1.980	4.620	3.040	0.444	69048	3367	1.530	2.950	0.220	6.63	B.L.	B.L.	0.910	B.L.	B.L.	0.277	0.087	1.950	0.049	0.143
Ben-g1-3	0.100	1.180	0.160	1.360	2.280	3.540	2.930	0.453	67600	3470	2.270	2.140	0.159	7.01	B.L.	0.080	1.010	B.L.	B.L.	0.860	B.L.	2.280	0.051	0.045
Ben-g1-4	0.240	1.160	0.270	1.120	1.860	5.030	3.020	0.464	67508	3500	2.160	2.220	0.192	7.69	0.033	B.L.	0.960	0.620	B.L.	0.268	B.L.	2.070	0.052	0.054

Table 3.B: Detection limits in ppm for Filomena calculated as the mean background multiplied by 3 times the standard deviation.

Elements	Detection limits in ppm (3SD)
Co	0.005
Ni	3.126
Cu	0.177
Ga	0.043
Ge	0.373
As	0.358
Se	4.43
Mo	0.084
Ru	0.032
Rh	0.01
Pd	0.013
Ag	0.025
Sn	1.91
Sb	0.078
Te	1.369
W	0.028
Re	0.013
Ir	0.015
Os	0.009
Pt	0.031
Au	0.012
Pb	0.076
Bi	0.015

Chapter 4

Processes of metal evolution by heating before and after accretion

Table of contents

I. Chapter introduction

In the previous chapter, we have explored the effect of metal condensation on isotopic composition. In this chapter, we will look toward heating processes leading to metal evolution in the solar nebula and in the parent bodies. The problem of metal evolution during heating processes is important for at least two reasons. First, early theories about magmatic iron meteorites have argued for their formation via primitive differentiation of planetesimals (i.e. metal–silicate segregation). However, recent advances in isotopic chronology have demonstrated that the formation of iron meteorites happens very early after condensation of first solids (CAIs, 4567.94±0.31 Ma, Bouvier et al. 2011), and before primitive chondrites (Figure 4.1, Elkins–Tanton et al., 2011). Understanding how metal was formed during the first steps of the solar nebula evolution is required to constrain magmatic iron formation. If differentiated bodies formed so early in the Solar System, then primitive chondrites cannot be their precursors. *If so, what are the precursors of primitive chondrites*?

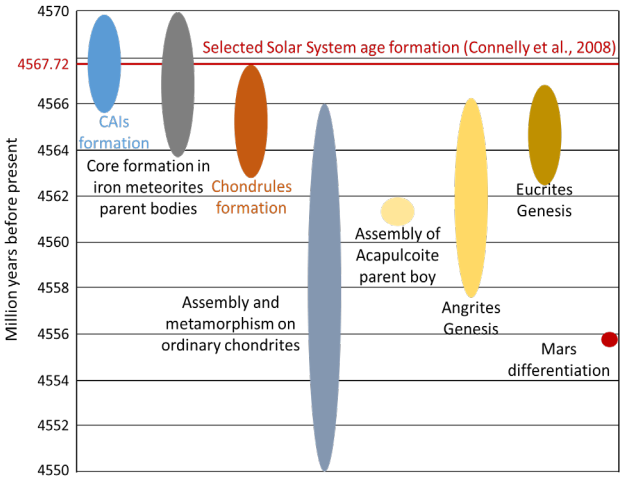

Figure 4.1: Ages of accretion and formation of object in the Solar System relative to CAIs formation, for magmatic irons meteorites are corrected from the cosmogenic effect, modify from Elkins–Tanton et al. (2011) compilation.

This question leads to the second point: the formation of the primitive meteorites. There are two types of primitive meteorites that contain significant amount of metal, (1) those that formed by direct condensation from a gas (i.e. CB–CH; as developed in the previous chapter), and (2) the ones that lost their condensation features due to heating event(s) in the solar nebula (e.g. ordinary chondrites). Whereas most authors agree that metal of ordinary chondrites was heated in the solar nebula at the same time as chondrules (e.g. Kong and Ebihara, 1997), it is unclear how metal in ordinary chondrites was formed. Multiple theories have been suggested, from silicate reduction to sulfide desulfurization or by FeNi–alloy melting (Campbell and Humayun, 2003; Cohen and Hewins, 2004; Horan, 2009; Kong and Ebihara, 1996, 1997; Okabayashi et al., 2019). By constraining the composition of the metal precursors of ordinary chondrites, this can help understand (1) the gas/dust composition in the inner protoplanetary disk, (2) the textural and chemical evolution of metal from H, to L, to LL groups, as well as (3) the elemental fractionation between silicate and metal in ordinary chondrites.

Ordinary chondrites (OCs) also underwent metamorphism and this is expressed as petrographic types, as described in the introduction. Some petrographic mineralogy studies suggest that their parent bodies might undergo some very early stages of metal–silicate differentiation (OCs H7, Tait et al., 2014). Also, some textures of meteorites show evidence of metal migration, such as H5 Portales Valley (Tomkins et al., 2013). The cooling rate and the ages are well correlated with their petrographic types, which has led authors to argue that the petrographic types reflect metamorphism in different layers and depths in the planetesimal (Monnereau et al., 2013) in the classical "onion shell model" (Minster and Allègre, 1979). If the metal has migrated through the parent bodies of ordinary chondrites planetesimal to form a core, this should be recorded in the metal composition of ordinary chondrites.

Here we explore the highly and moderately siderophile element contents in the metal phase of ordinary chondrites. To do so, we track the early evolution of metallic and sulfide phases with the aim of determining the composition of metal precursors. We then use the textural shape of metal/sulphide, and siderophile elements repartitioning to map the possible migration of metal in the H parent body. The results are presented below in the form of a paper draft entitled "Elemental composition of the metallic phases in H ordinary chondrites, formation and evolution" that is in preparation for *Meteoritical & Planetary Sciences*.

Goals of this chapter

- Studying the large range of siderophile elemental content of metallic grains hosted in H ordinary chondrites.
- Testing the metal melting model prior to the accretion of the parent body
- Constraining the composition of the metal precursor as well as metal formation during the heating event(s).
- Searching for elemental and textural clues of metal migration in the H ordinary chondrites parent body

II. Siderophile element composition of the metallic phases in H ordinary chondrites, formation and evolution

Abstract

Understanding the evolution of metal in the protoplanetary disk is important to constrain planetary formation and metal-silicate fractionation. Here, we have studied the siderophile element composition of metal and sulfide in ordinary chondrites from *in–situ*, measurements by laser ablation-inductively coupled plasma-mass spectrometry (LA-ICP-MS). Unequilibrated and equilibrated ordinary chondrites (UOC and EOC, respectively) were chosen to study the evolution of the metal from its formation in the protoplanetary disk to its evolution on the parent body. We highlight large elemental variation between grains in UOC compared to EOC, as metamorphism has homogenized the metal composition, with Portales Valley having the most homogeneous composition. The sulfides in H3 meteorites have a composition close to the metal, which is overprinted with increasing metamorphism.

We report the siderophile elements contained in the metallic phase against the Ge/Ir ratio which is a tracer of metal melting and we highlight correlations between this ratio and Re, Os, Ru, Pt, Pd. In UOC, metallic grains can be classified into three groups according to their compositions: (1) high Ge/Ir–low HSE; (2) low Ge/Ir–high HSE; (3) and grains with intermediary compositions. We have modelled the evolution of the metal during melting and we show that the range of composition in metal grains of UOC can be mostly explained by the melting of a single metallic precursor that had contained up to 5.2 wt% of carbon. This high carbon content in H chondrites is in line with their reduced composition when compared to L and LL that contain 3 wt% of carbon (Okabayashi et al. 2019). Our melting model cannot reproduce the high Re content in Dhajala and we suggest that some refractory particles may be heterogeneously distributed within metal precursors. Also, the W and Mo variation is unlikely to result from metal precursor melting. We suggest that the range of composition reflects various oxidation states at grain scale during melting event(s), buffered by the heterogeneous distribution of oxidizing components within the precursors. Similarly, Ga varies by more than 4 orders of magnitude. As previous studies have demonstrated, Ga can condense in the silicate phases and be redistributed during metamorphism in the metal, it also provides evidence for the interaction of metal and silicate under various oxidation states before accretion. Our model can also explain the large range of olivine and pyroxene composition in UOC.

Finally, the metal composition of EOC can be explained by the mixing of the grains that composed UOC. We suggest that metamorphism occurs in a closed system which has

homogenized the composition of the metal and propose that the large majority of siderophile elements were already in the metal before accretion.

1 Introduction

Chondrites are undifferentiated and primitive objects composed of a mixture of multiple components with various compositions and textures that witness their diverse origins and processes of formation. They include chondrules, metal, sulfide, calcium-aluminum inclusions (CAIs) and a fine-grained matrix. Among these components, understanding how the metal formed in primitive chondrites is important to constrain the early stages of planetary formation. Recent studies have demonstrated that differentiated objects, with a metallic core, may have existed at the very beginning of the Solar System only 1-2 My after CAIs formation, even before chondrites (Kruijer et al. 2014; Qin et al. 2008). Processes of metal formation vary from one chondritic group to another. Metal formation can result from (1) direct condensation from the solar nebula (Campbell et al. 2005; Newsom and Drake 1979) or impact plume (Campbell et al. 2002; Weyrauch et al. 2019); (2) reduction of iron from silicate (Kong and Ebihara 1997) due to interaction with carbon (Connolly et al. 2001; Lauretta et al. 2001) or nebular gas (Zanda et al. 1994); (3) sulfide desulfurization due to evaporation (Cohen and Hewins 2004); (4) recondensation of vapor following chondrule evaporation (Connolly et al. 2001).

The H ordinary chondrite (OC) group is the most reduced group in the ordinary chondrite sequence and contain up to 8.4 vol. % of metal (Krot et al. 2014). It has been demonstrated that the ratio Co/Ni of the metal can be higher or lower than the solar Co/Ni ratio, which rules out the possibility that metal in H OCs was formed by condensation (Kong and Ebihara, 1997). The agreement between metal-silicate partitioning coefficient of siderophile elements measured in ordinary chondrites (Kong and Ebihara, 1997) and by melting experiments at conditions of chondrule formation (Schmitt et al., 1989) suggest that the metal can be formed by the reduction of FeO in silicate precursors during chondrule formation (Kong and Ebihara, 1997). Despite this apparent consistency, *in-situ* measurements using laser ablation-inductively coupled plasma-mass spectrometry (LA-ICP-MS) techniques highlight large variations in highly siderophile elements (HSE) from one metal grain to another within the same chondrite (Campbell and Humayun, 2003). The lack of correlation between refractory HSE (Re, Os, Ir, Ru, Pt) and moderately refractory HSE (Pd, Au), suggest that it is impossible to explain the metal formation in H OCs by the reduction of FeO in silicates (Campbell and Humayun, 2003).

One of the most interesting characteristics of metal grains in ordinary chondrites is the enrichment in HSE in small grains compared to large ones (Horan et al. 2009). These authors have suggested that the high HSE content of small grains is due to their condensation at high temperature, while low HSE content of large grains results from their condensation at lower temperatures. Grossman and Wasson (1985) have then suggested that the large range of composition is the result of mixing between these two types of metal. In addition to the mixing, Horan et al., (2009) have shown that these two fractions might form separately and never equilibrate. The high Pd content compared to Fe in the high HSE metal phase must be formed

at high to moderate temperatures and high pressure (>10^{-4} bar), otherwise Pd and Fe would condense at the same temperature with constant Pd/Fe ratio in the metal. On the other hand, Campbell and Humayun (2003) suggested that the large variability of metal composition is more likely the result of incomplete homogenization of HSE carriers in the metal of ordinary chondrites. A third possibility (Hewins et al., 1997) is that metal from ordinary chondrite was produced by troilite desulfurization as observed in the experiments of McCoy et al. (1999). Finally, recent *in-situ* measurements by Okayabashi et al. (2019) tend to demonstrate that the variability of metal composition was the result of fractional melting of precursors. As can be seen, no consensus about the metal formation in ordinary chondrites.

The evolution of metal phases with metamorphism and its migration through a planetesimal is also a subject of debate. Textural studies of the metal phase have shown an increase in the percentage of metal in highest metamorphic grades (i.e. H6), as well as an increase in grain circularity and a decrease of the length of metal-sulfide contact (Guignard and Toplis, 2015). This evolution has been linked to thermal processes during metamorphism. The link between metamorphism and the migration of metal (i.e. very early stage of differentiation), is not easy to demonstrate and experimental studies point to the fact that metal migration is hampered when associated with sulfides (Néri et al., 2019). On the other hand, petrological evidence highlight that migration of metal and sulfide during an impact is feasible (Tomkins et al. 2013).

In this study, we measured the concentrations of highly siderophile elements (HSE) and moderately siderophile elements (MSE) by LA-ICP-MS in opaque phases associated with both unequilibrated and equilibrated ordinary chondrites (UOC and EOC, respectively). Metallic and sulfide grains were analysed inside, and outside of chondrules. This has been combined to a petrological investigation of the textural evolution of the metal and the sulfide phases. Primitive meteorites were used to constrain the formation of metallic phases in the solar nebula and provide new constraints on metal and silicate precursors. The study of UOC and EOC highlight metal migration process with increasing metamorphism.

2 Methods

2.1. Sample selection

For this study, ordinary chondrites were selected according to the classification of Van Schmus and Wood (1967). To constrain the metal formation in H ordinary chondrites, 3 unequilibrated H3 chondrites (UOC), A-881236 (H3.1), Sharps (H3.4), and Dhajala (H3.8), were chosen. To assess the effect of metal evolution and migration with metamorphism we have selected five equilibrated H ordinary chondrites (EOC), Ste Marguerite (H4), Allegan (H5), Portales Valley (H5), Kernouvé (H6) Guareña (H6). The samples are summarized in Table 4.1.

Table 4.1: Used samples and their petrologic types.

Samples	Sample N° (Sources)	Petrologic types
Sharps	USNM 640 (SI)	H3.4
Dhajala	USNM 5832 (SI)	H3.8
St Marguerite	MNHN 3290 (MNHN)	H4
Allegan	USNM 215 (SI)	H5
Guareña	(MNCN)	H6
Kernouvé	(Smithsonian)	H6
Portales Valley	USNM 6975 (SI)	H6

Abbreviations: NIPR: National Institute of Polar Research, Tokyo; SI: Smithsonian, Washington; MNHN: Museum National d'Histoire Naturel, Paris; MNCN: Museo Nacional de Ciencias Naturales, Madrid.

2.2. Analytical Procedures

Selected samples were cut using a diamond saw, mounted in resin and processed as polished sections. Samples were first examined by reflected light optical microscopy, and then by scanning electron microscope (SEM) with a Zeiss EVO MA15 tungsten filament SEM at Macquarie University, Sydney, Australia. Elemental (Kα) X-ray maps were collected using an Oxford Instruments 20 mm^2, X-max silicon drift energy dispersive spectrometer; data were processed using the Oxford Instruments AZtec acquisition software 3.2. Optical maps were processed using the *Image J* software. To extract the size distribution of grains and their circularities, the images were firstly converted in 8-bit grey scale, then a threshold base on the colour of grains is used to separate and measure each type of particle. The circularity is calculated as $(4\pi*area)/perimeter^2$. Based on this information, grains of interest outside, inside, and at the edge of chondrules were selected for siderophile element analysis by laser ablation-inductively coupled plasma-mass spectrometry (LA-ICP-MS).

Table 4.2: Values of external standards

Element	Standard	Literature data	Sources
Ni (%)	Filomena	5.65	Walker et al. (2008)
Co (ppm)	Filomena	4500	Walker et al. (2008)
Re (ppm)	Filomena	0.175	Walker et al. (2008)
Os (ppm)	PGE-A	72.7	PGE-A certified value
W (ppm)	Filomena	2.43	Walker et al. (2008)
Ir (ppm)	PGE-A	121	PGE-A certified value
Ru (ppm)	PGE-A	204	PGE-A certified value
Mo (ppm)	Filomena	7.5	Walker et al. (2008)
Pt (ppm)	PGE-A	184	PGE-A certified value
Rh (ppm)	PGE-A	223	PGE-A certified value
Pd (ppm)	PGE-A	274	PGE-A certified value
Au (ppm)	PGE-A	212	PGE-A certified value
Cu (ppm)	Filomena	135	Walker et al. (2008)
Ga (ppm)	Filomena	59	Walker et al. (2008)
Ge (ppm)	Filomena	181	Walker et al. (2008)

The LA-ICP-MS used for this study was composed of a G2 photon machine 193 nm HelEx Cell as laser ablation peripheral connected to a 7500 Agilent ICP-MS. The gas injected in

the laser chamber was a mixed of Helium and Nitrogen, and the fluence was 7.2 J/cm². Measurements were performed using a 50 to 80 µm spot size depending of the size of the grain that we analyzed. A measurement is composed of 160 s of blank, 60 s of integrated signal analyses, and then 60 s of blank. Each analyzed point was ablated by 300 laser pulses at 5Hz. The isotopes ^{34}S, ^{57}Fe ^{59}Co, ^{60}Ni, ^{63}Cu, ^{69}Ga, ^{74}Ge ^{95}Mo, ^{101}Ru, ^{103}Rh, ^{106}Pd, ^{182}W, ^{185}Re, ^{192}Os, ^{193}Ir, ^{195}Pt, and ^{197}Au were monitored during all the analysis. These elements have been selected to represent a range of volatility from refractory elements (Re, Os, Ir, Pt, Ru, Rh, Mo, W) to volatile elements (Au, Ga, Ge), and chemical behaviour from highly siderophile, (Re, Os, Ir, Pt, Ru, Rh, Pd, Au) to moderately siderophile (Ni, Co, Fe, Cu, Ga, Ge,) and chalcophile (*e.g.* Cu, Ge). External standards were run five times during each session. These are PGE-A (HSE rich Ni–sulfide, Alard et al., 2011; Gilbert et al., 2013) for Os, Ir, Ru, Pt, Rh, Co Pd, Au and Cu, and Filomena (North Chile) (IIAB iron meteorite) commonly used for LA-ICP-MS measurements (Walker et al., 2008 and references therein) for Re, W, Mo, Ni, Ga, and Ge (Table 4.2). Data were validated by comparing our analyses with Hoba (IVB iron meteorite), and the NIST (National Institute of Standards and Technology) standard reference material 1158 with literature data (Campbell et al., 2002; Walker et al., 2008). The reproducibility of standard values is given in Table 4.3. Internal standards were ^{57}Fe, ^{60}Ni and ^{34}S.

Table 4.3: Concentrations and reproducibility of standards

	This study						Walker et al. (2008)		
Element	Filomena	2σ SD	Hoba	2σ SD	SRM 1158	2σ SD	Filomena	Hoba	SRM 1158
Ni (%)	**5.63**	0.15	**17.64**	0.95	**39.30**	2.70	5.65	16.4	34.5
Co (ppm)	**4515**	98	**7453**	208	**79**	33	4500	7890	81
Re (ppm)	**0.18**	0.08	**3.15**	0.64	**0.003**	0.008	0.175	2.732	0.005
Os (ppm)	**1.06**	0.90	**43.04**	22.04	**0.19**	0.11	0.98	39.21	0.002
W (ppm)	**2.48**	0.66	**2.88**	2.87	**13.63**	14.57	2.43	3.1	14
Ir (ppm)	**3.23**	1.39	**26.57**	7.95	**0.004**	--	3.22	26.86	0.006
Ru (ppm)	**17.27**	4.70	**27.52**	4.91	**0.30**	0.21	16.5	29.44	1.35
Mo (ppm)	**7.52**	0.59	**30.81**	7.03	**158.04**	39.38	7.5	24.6	114
Pt (ppm)	**26.76**	8.57	**31.53**	5.68	**0.13**	0.10	24.1	30.14	0.01
Rh (ppm)	**2.69**	0.76	**4.12**	0.69	**0.01**	0.02	2.2	3.54	--
Pd (ppm)	**2.07**	0.51	**7.03**	0.81	**0.05**	0.08	1.6	6.244	--
Au (ppm)	**0.43**	0.17	**0.06**	0.08	**0.03**	0.06	0.610	0.064	--
Cu (ppm)	**133.86**	7.11	**1.57**	0.70	**480.02**	160.95	135	2.15	390
Ga (ppm)	**58.83**	2.14	**0.17**	0.06	**6.54**	2.13	59	0.192	5.6
Ge (ppm)	**179.81**	5.70	**0.45**	0.40	**14.51**	5.22	181	0.049	12.5

3 Results

3.1. Texture of metal and sulfide in H OCs

We have performed a textural analysis of metal and sulfide using an optical microscope. Example of each analysed sample is given in Figure 4.2 (see next page). The distribution between

metal and sulphides evolved with increasing metamorphism. In type 3, sulfides are mostly encrusted around metal and silicates (Fig. 4.2 A, C, D). Yet, some sulfides grains have sharp edges with metal which suggest sulfide–metal immiscibility (Fig. 4.2 B) and confirmed by the occurrence of taenite associated with kamacite and sulfide (Fig. 4.3). The distribution of sulfide is heterogeneous in H3 samples and grains are small, between 10 µm to 0.1 mm. (Fig. 4.4). However, the evolution of circularity is homogeneously distributed and no spike in the data exists (Fig. 4.4). With the increase of metamorphism, sulfide grains become large and their relative circularity increase (Fig. 4.4). They are not encrusted around metal and chondrules anymore and their boundaries with metal grains become less complex and sharper from H4 to H5(Fig. 4.2 E–H) and are perfectly straight in H6 (Fig. 4.2 I–J), which agree with Guignard and Toplis (2015) that show a decrease of the length contact between sulfide and metal with increasing metamorphism. In EOC, the sulfide–metal boundaries are characteristic of sulfide wetting on metal instead of a metal silicate reaction, Portales Valley is an exception. In this meteorite, sulfides are large, well separated from metal and are enclosed in silicate clasts (Fig. 4.2K), in agreement with Tomkins et al. (2013).

The reparation of the metal grain size in the primitive H is heterogeneous, as for the sulfide. It mostly occurs in the form of rounded grains inside and outside of chondrules but contrary to sulfide, it is not significantly encrusted around chondrules (Fig. 4.2 A to D). In H3, the grain size of metal is more various than for sulfide, whereas when small grains exist, they can be larger (Fig. 4.4). The metal grains are also more circular than sulfide ones and are not characterized by a flat circularity pattern. Most data are centred around 0.6 and shows an increase in circularity from 0.5 (15 % of the grains) to 0.9 (~10%), with a peak of occurrence at 0.7 (20% of the grains) (Fig. 4.4). Metal grains seem more circular than sulfide ones. Also, small grains are usually more circular than large one (Fig. 4.5). With metamorphism, grain shapes are evolving, and metal grains become larger but also more circular (Fig. 4.2 E to J and 4.4). Also, small grains do not show a large range of circularity in H6 compared to H3 (Fig. 4.5). Our results on sulfide and metal grains shape and circularity agree with Guignard and Toplis (2015). Finally, metal in Portales Valley are in the form of large veins, surrounding clasts composed of silicate, large sulfide and a small amount of metal (Fig. 4.2K). The boundaries between metal and sulfide are well defined and seem to be the result of FeNi–FeS immiscibility.

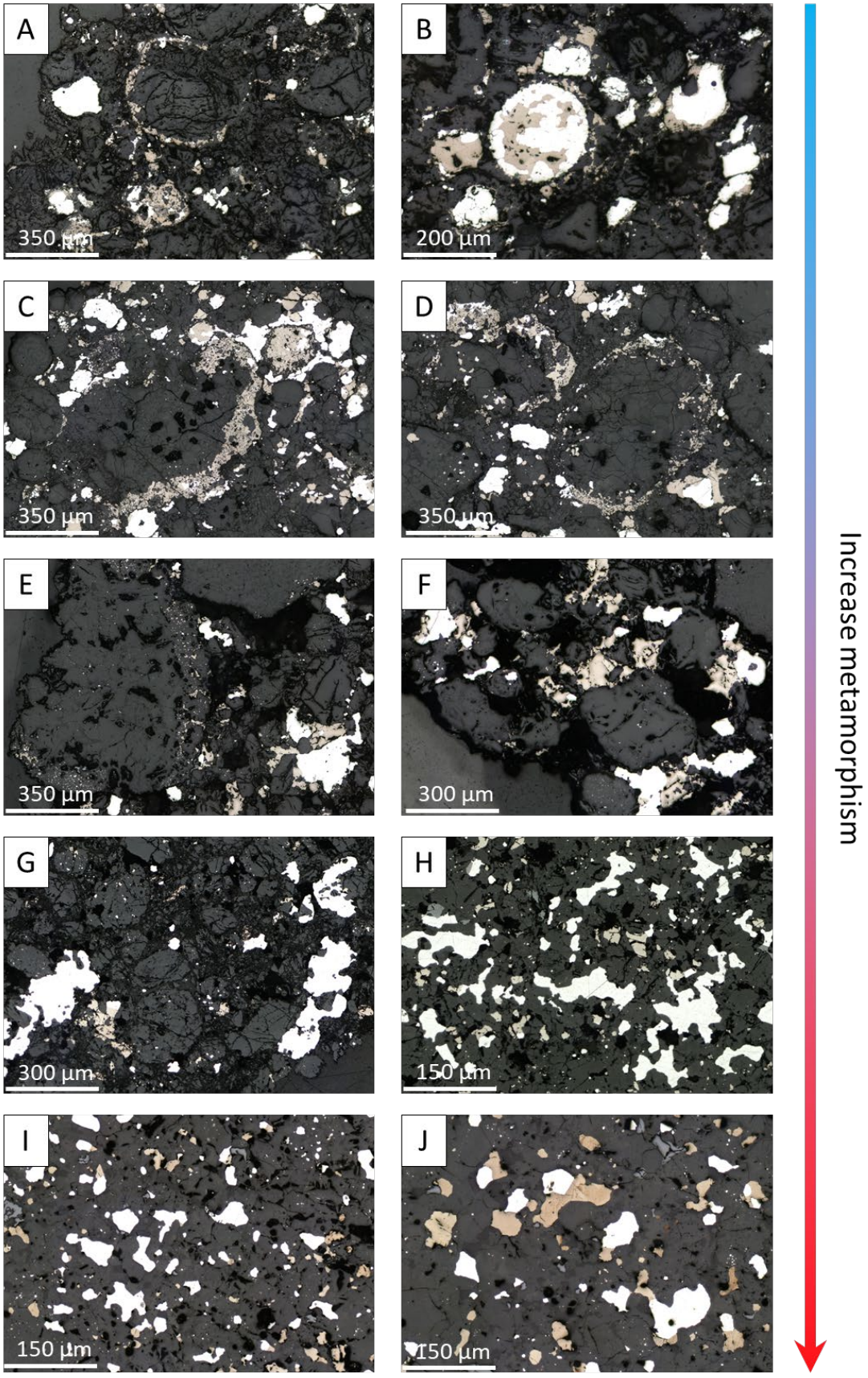

Figure 4.2: Optical microscope images in reflected light of the different ordinary chondrites: A–B, Sharps (H3.4); C–D, Dhajala (H3.8); E–F, Sainte Marguerite (H4); G, Allegan (H5); H, Kernouvé (H6); I–J, Guareña (H6). In all pictures, dark grey is silicate, white is FeNi alloy, and yellowish–brown is troilite.

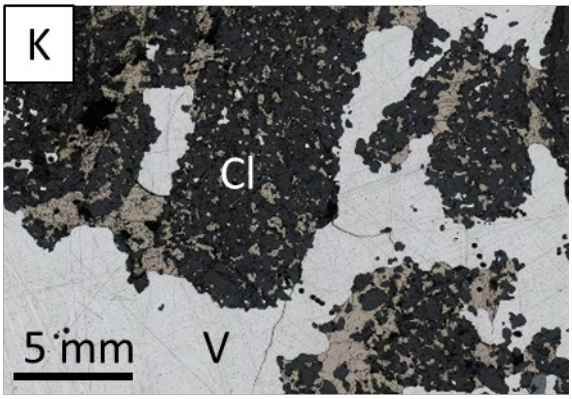

Figure 4.2 bis: Image of Portales Valley (H6, metal breccia) by optical microscope. V: Vein, Cl: Clast. The colour char is the same than for other pictures.

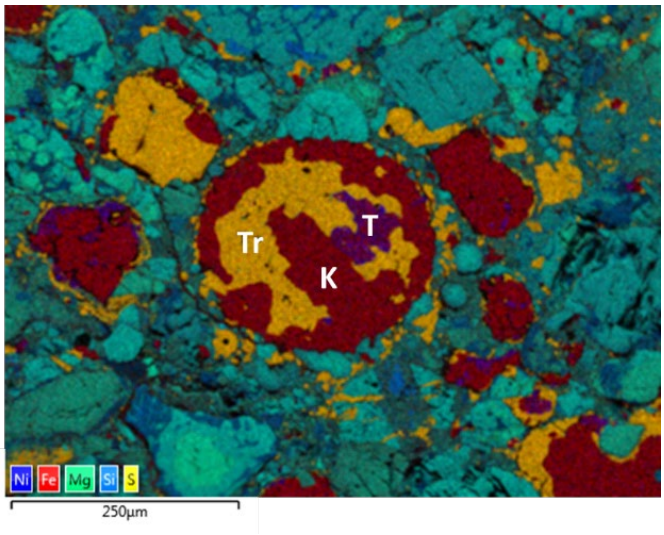

Figure 4.3: SEM image of the metal grains in Sharps (H3.4) presented in the Figure 4.2 B (see next page for the optical image. T: Taenite, K: Kamacite, Tr: Troilite.

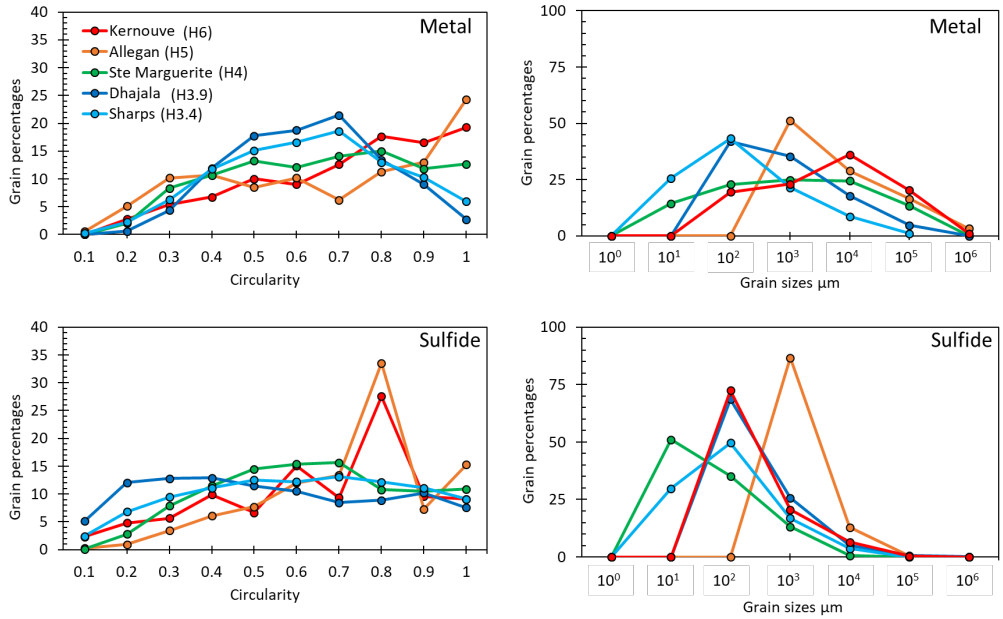

Figure 4.4: Distribution of the circularity and of the grain sizes in function of the metamorphism. A circularity is calculated as (4π*area)/perimeter². A circularity of 1 mean that the grain is perfectly rounded, while the circularity decrease, the roundness decreases of grains decrease too.

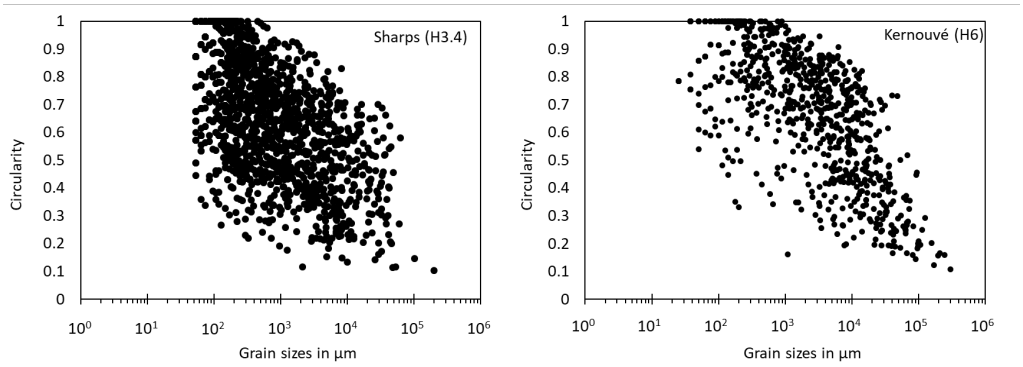

Figure 4.5: Correlation between circularity and grain sizes in metal of the two ordinary chondrites,, UOC Sharps (H3.4) and EOC Kernouvé (H6).

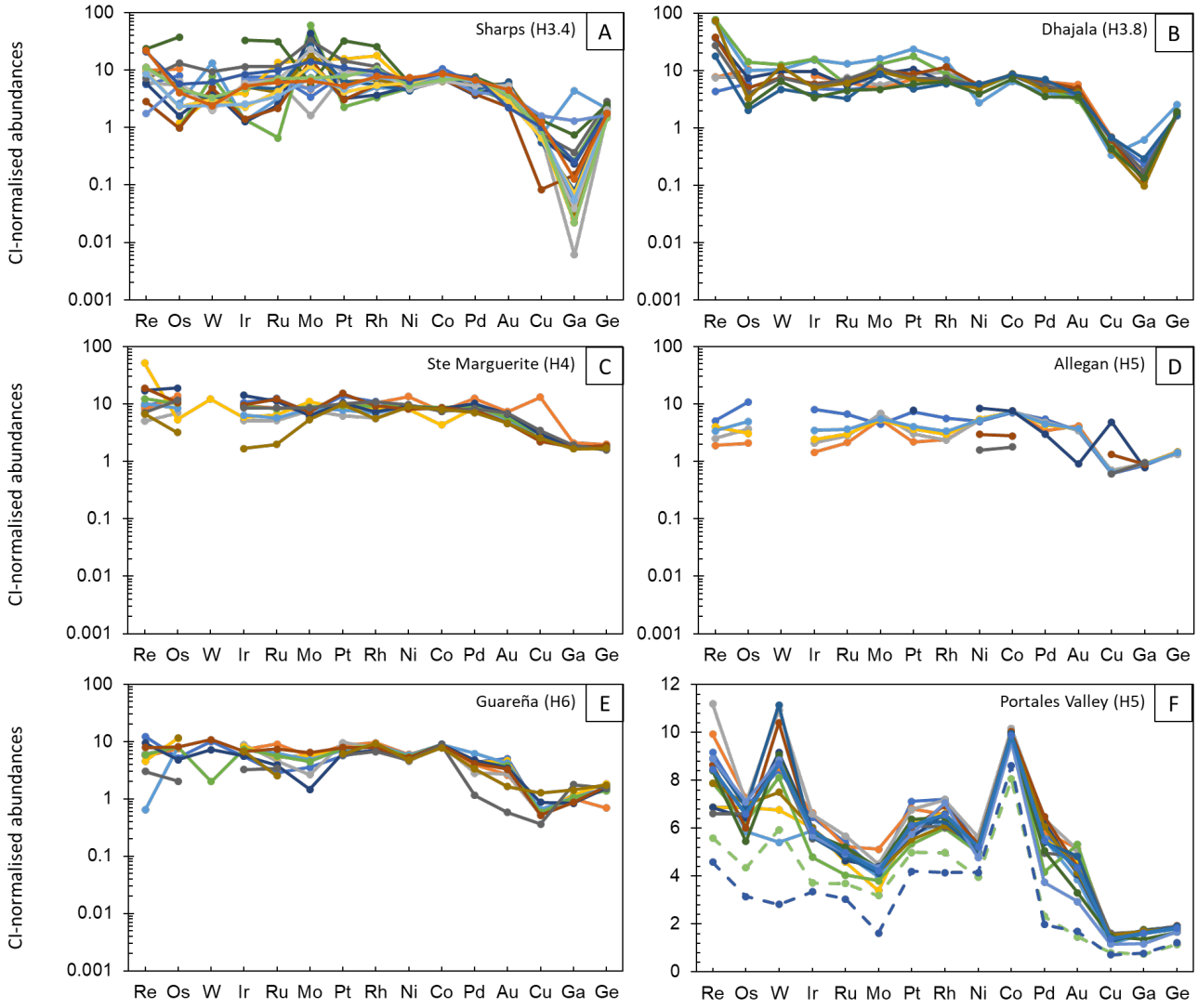

Figure 4.6: Spider diagrams for kamacite metal phase. Elements are classified by increasing volatility. Dotted lines in Portales Valley represent measurements in clasts, while full line represents measurements in veins, Portales Valley condensation are not reported in log scale. Values are normalized to CI chondrites (Lodders et al., 2009).

3.2. Metal composition

Our LA-ICP-MS analyses of metal and sulfide phases are given in the Table 4.A in the appendix. The FeNi metal grains were classified into taenite or kamacite as a function of their Ni contents, with Ni <10 wt.% for kamacite and Ni>10 wt. % for taenite. Our results in Fig. 4.6 show that, HSE and refractory elements in metallic grains are superchondritic, up to one order of magnitude more concentrated than in CI (Lodders et al., 2009), in agreement with previous studies (e.g. Kong et al., 1998). Kamacite composition in H3 unequilibrated chondrites show large variations in highly and moderately siderophile elements (Fig. 4.6 A and B), when compared to H4 to H6 equilibrated ordinary chondrites (Fig. 4.6 C and D). This range of variation is similar to HSE concentrations reported by Okabayashi et al. (2019) in unequilibrated L3 and LL3 chondrites. The range of concentration decreases with increasing metamorphic grade and the metal composition tends to become more homogeneous in equilibrated OCs than in unequilibrated ones, with a very flat PGE pattern (Fig. 4.6 C to E). Veins of Portales Valley H6 for which the metal experiences complete melting (Tomkins et al., 2013) exhibit remarkable homogeneous concentrations (Fig. 4.6 F). Refractory elements are showing flat pattern, yet, the volatile elements and more chalcophile elements (Pd, Au, Cu) are slightly depleted.

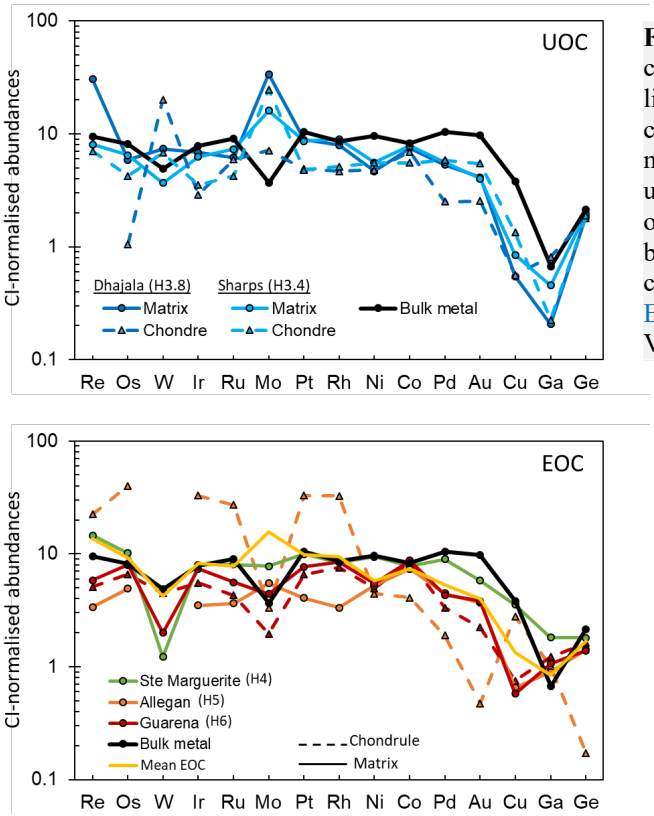

Figure 4.7: Spider diagrams of the mean composition of kamacite in each meteorite. Dotted lines represent metal in chondrules or on the edge of chondrules,and full lines represent measurements of metal grains in the matrix. Top diagram refers to unequilibrated ordinary chondrites (UOC), bottom one to equilibrated ordinary chondrites (EOC). The black line represents the metal bulk of H3 chondrites calculated on 5 different H3 (3.4 to 3.9) by Kong and Ebihara (1997) from their elemental measurements. Values are normalized to CI chondrites.

HSE (Ir, Re, Os, W, Ru, Mo, Pt, Rh), content vary from 0.59 to 15.48 ppm in H3.4 Sharps while it varies from 1.52 to 4.11 ppm and from 1.57 to 3.09 ppm in H6 Guareña and H6

Portales Valley, respectively, with a decrease from H3 to H6 goes from ppm to 10xCI. This pattern is also observed for the moderately siderophile elements (Mo, W, and from Ni to Ge), especially Ga, which show very large variations in primitive H3, from 0.06 to 42.71 ppm (H3.4, Sharps), that mostly disappear even at lower metamorphic grade, from 0.95 to 13.08 ppm (H3.8, Dhajala), and become broadly homogeneous at high metamorphic grade, e.g. 8.12 to 17.04 ppm and 7.19 to 17.14 ppm in Guareña and Portales Valley, respectively. Moreover, we do not report significant differences in concentration between metal in the chondrules and in the matrix, but the chondrule metal is more heterogeneous and has a more variable composition compared to metal in the matrix (Fig. 4.3). Also, apart from Mo, W and Re, the mean refractory siderophile element content in kamacite of UOC compared very well, within analytical error, to Kong and Ebihara. (1997) bulk data (Fig. 4.6 and 4.7). Rhenium in Dhajala and Mo in Sharps show enrichments up to one order of magnitude compared to other samples, and significantly deviate from Kong and Ebihara (1997) bulk data (Fig. 4.7). Our data on the kamacite show a depletion in Ni, Pd, Au, Cu, and Ga compared to the metal bulk, which is the result of their enrichment in taenite (Okayabashi et al., 2019). In contrast to the variability of HSE, for example Ir ($[Ir]_{mean\ H3}$ = 2.86 ± 5.31 ppm 2σ SD) and others MSE (moderately volatile elements), the Ge concentration is very homogeneous from one grain to another ($[Ge]_{mean\ H3}$ = 62.47 ± 18.93 ppm 2σ SD). Reporting HSE contents against Ge/Ir ratios (Fig. 4.8) can differentiate high and low HSE contents groups (Horan et al., 2009), with low and high Ge/Ir ratios, respectively. Metal grains analysed in that study can be divided into high Ge/Ir > 25, and low Ge/Ir < 25 ratio. High Ge/Ir ratio is characterised by a constant and very low HSE content while low Ge/Ir ratio shows a high and variable HSE content. It creates a negative correlation that is well constrained for Os, Re, Ru, Pt, Rh, and Pd. Mo and Au are special and show a weak positive correlation for Ge/Ir<35. The Ga is a special case and show very low content in H3 at any Ge/Ir ratio compared to equilibrated ordinary chondrites

In detail, in H3 chondrites, Ge/Ir varies from 5.2 to 115.8 in Sharps and from 8.0 to 81.0 in Dhajala. In this chondrite, the Ge/Ir ratio shows a negative correlation with most of the HSE (Re, Os, Ru, Rh, Pt), negative weak correlation with Pd, and positive with Au, and does not correlate with W, Mo and Ga. The high HSE-low HSE dichotomy become less evident with increasing metamorphism. Whereas some grains in H4 and H5 can have a very low or high Ge/Ir ratio (e.g. $Ge/Ir_{Ste\ Marguerite}$ varies from 9.05 to 70.80 with a mean of 21.27 ± 35.99 2σ SD), most of the analysed grains in H6 equilibrated OCs have a Ge/Ir ratio between 10 and 35 (16.73 ± 13.16 2σ SD in H6, Guaréña). In Portales Valley, metal veins have a very consistent mean Ge/Ir ratio of 21.91 ± 4.09 2σ SD.

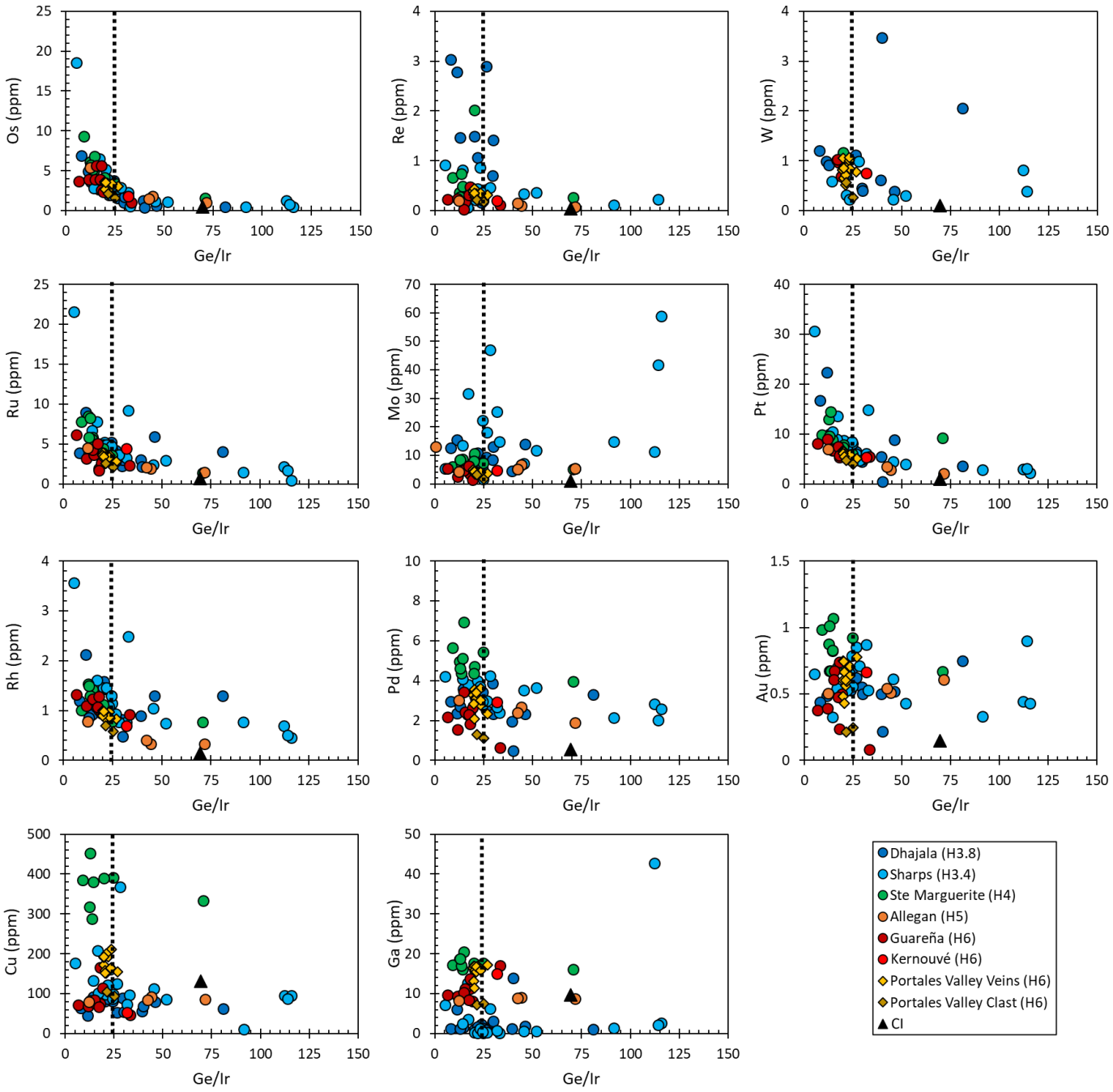

Figure 4.8: Highly siderophile element concentration *versus* Ge/Ir ratio in kamacite from unquilibrated (H3) and equilibrated (H4, H2, H6) ordinary chondrites. The dotted line represents the dichotomy between high Ge/Ir < 25 and low Ge/Ir > 25.

3.3. Sulfide composition

Sulfides have been analysed in all petrologic groups of the H OCs. Sulfides in the very primitive Sharps (H3.4) sample have siderophile elements contents close to metal composition (Fig. 4.9). The highly siderophile element content decreases during the first step of metamorphism (from H3 to 4) to become depleted by 2 orders of magnitude compared to metal phase. The sulfides have very flat patterns in PGE (Os, Ir, Ru, Pt, Rh, Pd, Au) which disagrees

somewhat with metal–sulfide melting and crystallisation. They also show an enrichment in Re, W, Mo and Cu. This enrichment increases with increasing metamorphism from UOC to EOC, with Mo being more enriched than W and Re, and to a lesser extent than Cu. Finally, other elements that are more volatile than Pt have a relatively flat pattern.

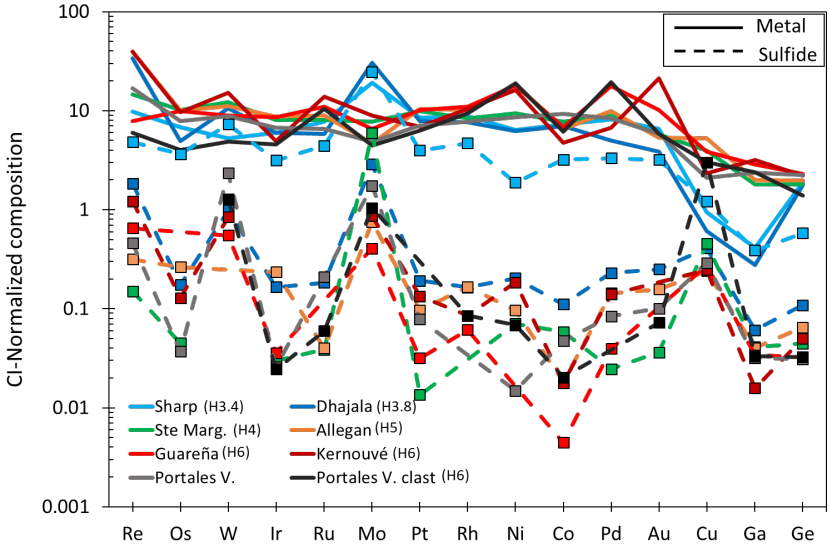

Figure 4.9: Mean composition (kamacite + taenite) of metal grains (full line) and sulfides (dotted line) in the different samples that we analysed. Values are normalized to CI composition (Lodders et al., 2009).

4 Discussion

4.1. Texture of metal and sulfide in ordinary chondrites

Guignard and Toplis (2015) have studied the variation of the texture of metal and sulfide phases with increasing metamorphism from type H4 to H6. They suggest that metamorphism has a significant influence on the textural evolution of metal and sulfide. With increasing metamorphism, they show an increase in grain circularity as well as in mean grain size and a diminution of length contact between metal and sulfide. Our conclusions agree with previous observations. However, we do not report textural evidence of metal–sulfide reaction with increasing the metamorphism. We show that sulfide grains in H6 are wetting on metal, which means that the metal has likely not been melted during metamorphism, whereas sulfides have melted. This agrees with the temperature spike for H6 (~1000 °C, Tait et al., 2014), the high temperature of melting for a FeNi alloy (~1500 °C, e.g. Swartzendruber et al., 1991) and the low ones for the FeNi–S alloy (~988°C, Fei et al., 1997).

In figures 4.4 and 4. 5, we show the circularity and the size of metal and sulfides grains in UOCs and EOCs. The typical grain size increases from UOCs to EOCs, which means that first metal grains in the protoplanetary disk were small and then they were aggregated during parent body metamorphism (Fig. 4.4). Our data in UOCs also show a smaller range of circularity

distribution and a smaller circularity mean than for EOCs which suggests different modes of formation. Whereas spherical metal grain shapes result from their formation in the solar nebula (Fig. 4.2 B and 4.3). UOC metal grains with lower circularity cannot be formed in an environment with a low gravitational effect and/or low density of particles. Indeed, the minimization of surface tensions due to low gravity should form spherical grains, as for chondrules. A possibility to explain aspherical metal shape is that they were formed in a high-density region of the disk where the spatial constrains makes it difficult to form spheres of metal which were still hot during accretion. If so, spherical metal grains should form in environments with a lower particle density than aspherical ones. This suggests the less a grain is spherical the more it has interacted with silicate. This interpretation could suggest that metal grains were formed in a reservoir in which grain density was heterogeneous.

At low metamorphic grades, sulfide grains can be divided into two major types, the ones around chondrules and metal and those inside metal with sharp boundaries. The first type may be associated with H_2S–$FeNi_{metal}$ reactions and then formed by condensation by sulfur on metal during a heating event. Yet, the paragenesis is not clear and a deeper characterisation of the fine sulfide–metal relation is needed. The formation of the second type of sulfide is less ambiguous and the occurrence of FeS with kamacite–taenite suggest a formation by metal–sulfide melting. It emphasizes the precursors of this sulfide–metal assemblage experience temperatures higher than 1500 °C (FeNi melting temperature) and have been liquid before accretion. Also, the tortuous FeS–FeNi association display in figures 4.2 B and 4.3 suggest that metal and sulfide have quenched quickly.

4.2. Elemental constrains on metal formation before accretion

Previous models for understanding the variations in metal compositions in ordinary chondrites have been based on the decoupling of highly siderophile elements during complex condensation and melting processes (Horan et al., 2009; Okabayashi et al., 2019). Here we are coupling the use of HSE with moderately siderophile elements. We specifically address the variation of Ge/Ir ratios and the correlation with refractory elements, as well the large range of Ga, Mo and W composition.

4.2.1. Melting model and C, S content of the metal

Type 3 chondrites do not reach temperatures that can melt any FeNi alloy (H3 < 673°C, Tait et al., 2014). If the range of HSE composition in H3 metal results from melting event prior to the accretion, as suggested by Okabayashi et al. (2019) for the L and LL groups, then the observed correlations between Ge/Ir and the HSE in pristine H chondrites (Fig. 4.4) must be related to that event. Thus, the key question for understanding and modelling the elemental

evolution of metal during melting is to consider the occurrence of "light elements", *i.e.* S and C, in FeNi alloys as they modify the behaviour of siderophile elements between liquid and solid metal phases.

Table 4.4: Parameters used for the melting and mixing models.

	Re	Os	W	Ir	Ru	Pt	Rh	Pd	Au	Ga	Ge
Fractional melting											
D0[1]	1.65	1.71	0.95	1.49	1.18	0.95	0.97	0.54	0.37	0.76	0.63
Beta C[1]	-0.27	2.8	-3.36	4.23	1.6	4.81		3.38	4.29	3.7	2.57
D[1]	1.53	3.62	1.06	4.62	1.81	3.44		1.33	1.17	2.05	1.25
Starting composition[2]	0.41	3.20	0.49	2.93	5.02	8.16	1.25	3.13	0.6	4.4	64.3
Mixing[3]											
Last solid composition	0.83	21.62	$1.9*10^{-5}$	22.61	19.33	60.74		13.96	2.9	26.2	226.0
First liquid composition	0.282	0.452	2.96	0.232	1.826	0.764		1.116	0.2	0.9	28.8

1: Value from Chabot et al. (2017). D is calculated for 5.3% C, See Chabot et al. (2003, 2017) for more details.
2: the starting composition corresponds to the mean values of kamacite in Sharps.
3: Value for the mixing are in ppm.

Chabot and Jones (2003) and Chabot et al. (2017) provide parameterization of siderophile partition coefficients in the Fe-Ni, Fe-Ni-S, and Fe-Ni-C systems as a function of metal content with light elements (Table 4.4). The Ge/Ir ratio is a tracer of melting and crystallization of the metal as Ge behaves as an incompatible element with respect to FeNi solid ($D(Ge)_{\text{solid metal-liquid metal}} = 0.63$) and Ir as a compatible element ($D(Ir)_{\text{solid metal-liquid metal}} = 1.49$) as well as in the Fe-Ni-S system ($D(Ge)_{\text{solid metal-liquid metal}} = 0.69$, and $D(Ir)_{\text{solid metal-liquid metal}} = 1.71$, for 2 wt% of sulfur). In the case of a metal containing carbon, Ge becomes compatible ($D(Ge)_{\text{solid metal-liquid metal}} = 1$) for 3.18 wt. % C in the metal while $D(Ir)_{\text{solid metal-liquid metal}}$ increase to 3.16. Thus, even at high carbon contain, Ge is still less compatible than Ir, and the liquid will have a high Ge/Ir ratio.

In a pure FeNi system, Chabot et al. (2017) demonstrate that Re, Os, and Ru are compatible whereas Pt, Rh, and Pd are incompatible. However, as Pt, Rh, and Pd correlate with Ge/Ir, they might be compatible during metal melting. Thus, the starting material was not a pure FeNi metal phase and must have contained sulfide and/or carbon. By adding sulphur, Pt and Rh become compatible and Pd remains incompatible, whereas they all become compatible with carbon. Additionally, a minimal temperature of 988°C is needed to melt an Fe-Ni-S alloy at 1 bar (Fei et al., 1997), and 1153 °C for Fe-Ni-C alloy (Hirayama et al., 1993, and references therein). Sulphur is the most volatile species among these elements and will evaporate from the FeNi–S melt above eutectic temperature (Tachibana and Huss, 2005), whereas carbon dissolved in the metal (e.g. in a form of Fe_3C) is more refractory (Mikhail and Füri 2019). As a result, during peak temperatures leading to metal and chondrule melting (~1800 to 2000K, Hewins and Connolly, 1996), sulfur is more likely to be lost from the metal compared to carbon. The carbon species incorporated in metal during nebula processes , either as MAC inclusion (metal-associated carbon), or pure carbon, is however difficult to identify, as it can be modified during the nebular processes (Mostefaoui et al., 2000, 2005). Considering the behaviour of HSE in the different systems (i.e. FeNi, FeNi-S and FeNi-C), and the volatility of Fe_3C compared to FeS, it is likely that the metal precursor contained significant amount of C compared to S. To model metal

melting, the Fe-Ni-C system must be considered instead of a Fe-Ni-S or FeNi alloy, in agreement with Okabayashi et al. (2019).

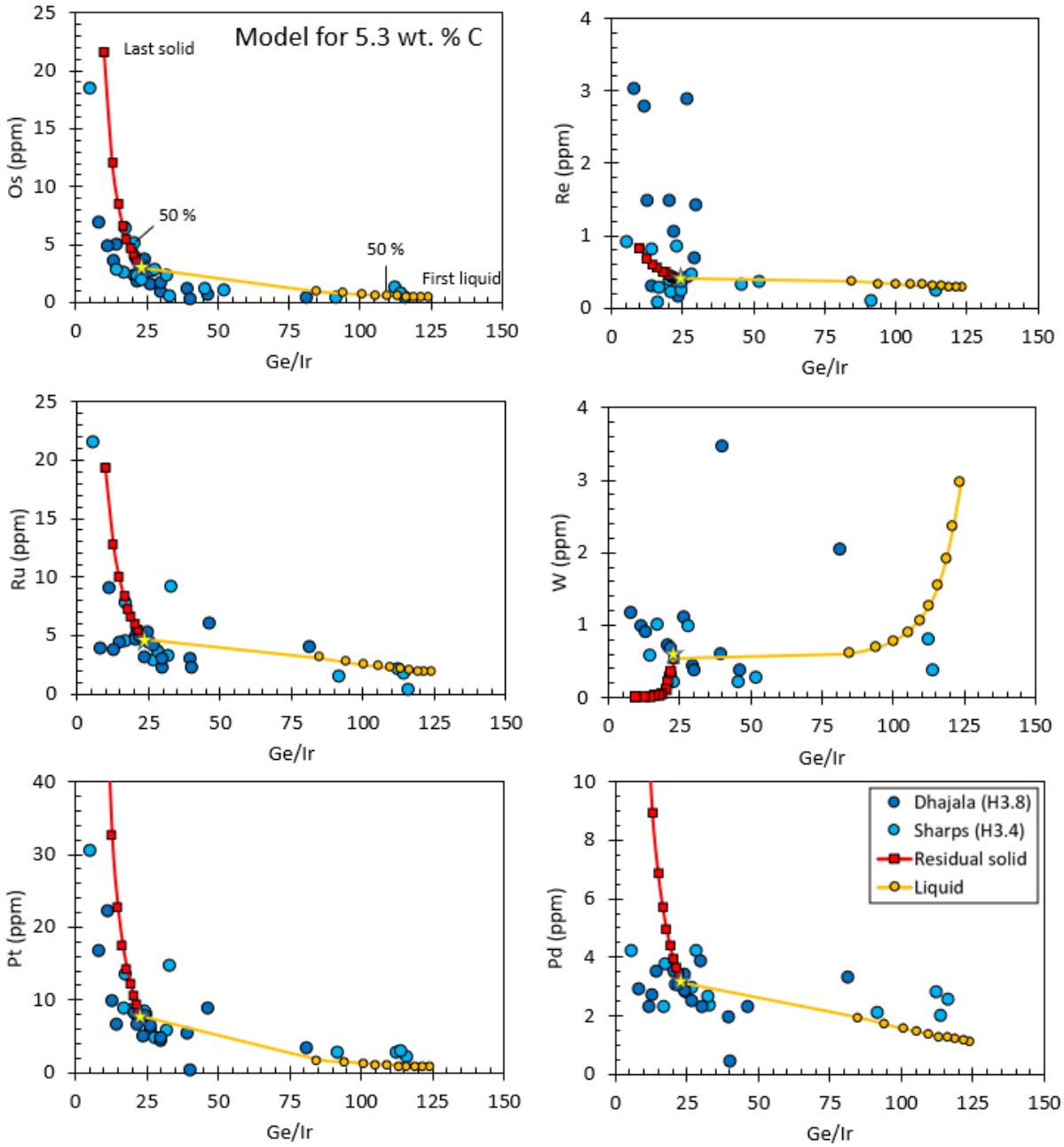

Figure 4.10: Melting model of the metal phase in H3 chondrites for 5.3 wt. % of carbon in the metal. The yellow line represents the evolution of the liquid and the red line the evolution of the remaining solid. The yellow star shows the starting composition. Each dot on model–lines corresponds to a 10% incrementation starting at 0.001% of melting. Ru is not represented because of the lack of parameterization parameters.

We have used the parameterization of Chabot et al., (2017) to model the evolution of HSE siderophile elements during metal melting in the Fe-Ni-C system, as this is the most representative one. The starting composition is defined as the mean composition of the less metamorphosed chondrite sample (Sharps, H3.4). Two models were made, a batch melting model

and a fractional melting model, at different carbon contents ranging from 1 to 6 wt. %. Both models display similar results, but the best match to our data is achieved with the fractional melting model containing 5.3 wt. % of carbon in the metal (Fig. 4.10). During the melting of a FeNiC alloy, the first liquids are depleted in HSE with a high Ge/Ir ratio, while the solids are enriched in HSE with a low Ge/Ir. As the percentage of melting increases, the liquid becomes progressively enriched in HSE and *slowly* decreasing its Ge/Ir ratio with the solid becoming highly enriched in HSE, *strongly* decreasing its Ge/Ir ratio. The compositional range of metal in H OCs, especially metal grains with very low or high HSE content, appear to be the result of melting of metallic precursors (Fig. 4.10 and 4.11).

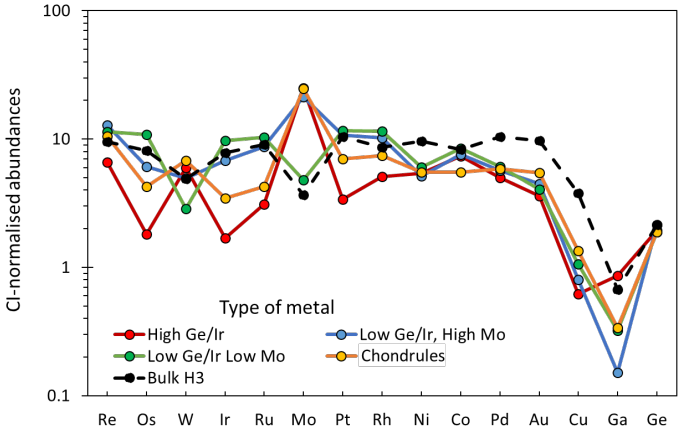

Figure 4.11: Spider–diagram of the means different types of metal in Sharps. The high Ge/Ir type is depleted in HSE while the two low Ge/Ir lines are enriched in HSE. The bulk H3.5–H3.9 (dark line) is the elemental composition measured by Kong and Ebihara, (1997). Values are normalized to CI chondrites. (Lodders et al., 2009).

Only a few grains in the H3 chondrites show extreme compositions (i.e. Ge/Ir>75 and Ge/Ir<10). Most metal composition ranges between Ge/Ir =15 and 30 and is close to the bulk metal from equilibrated H chondrites (Fig. 4.8 and 4.10). These two different types of compositions have been identified in previous studies and have been associated with a size effect (Horan et al., 2009; Kong et al., 1998; Okabayashi et al., 2019; Widom et al., 1986). These authors suggest that the range in composition is a result of either, (1) from an addition, in various proportions, of HSE-depleted grains to previously condensed HSE-rich grains (Horan et al., 2009); or (2) from the mixing during crystallisation of liquid and solid formed during metal melting (Okabayashi et al., 2019); or (3) from evaporation/recondensation during metamorphism (Kong et al., 1998).

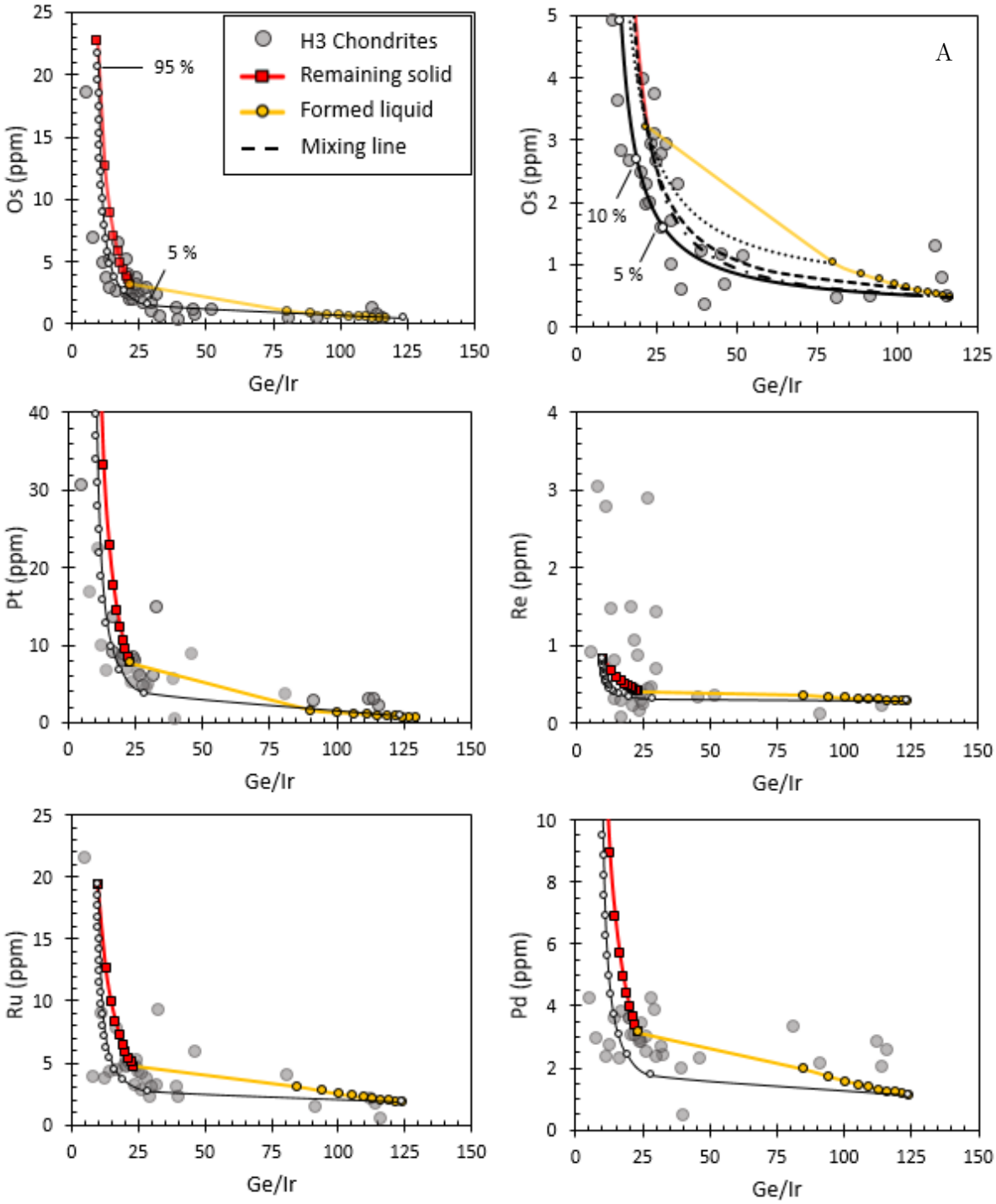

Figure 4.12: Example of mixing model between the formed liquid and the remaining solid. The dotted black line represents the mixing between the first formed liquid and the last remaining solid which is an example to highlight the the entire range of possible mixing. It shows that the grains that have an intermediate Ge/Ir composition can be the result of that mixing. Only H3 chondrites are represented in the diagram. Each white circles are 5% mixing steps. The diagram with the A is a zoom of the Os vs Ge/Ir. The different dashed lines are mixing lines between liquids and solids at various degrees of partial fusion. The area between the black full line and the fusion partial models (yellow and red lines) represents the entire range of composition by mixing.

We have modelled mixing between the two extreme compositions that we have obtained with our melting model: the first metallic liquid and the last remaining solid (See table 4.4 for parameters). This way, we are covering the full range of compositions that can be achieved by the mixing of solid and liquid formed by different percentage of metal melting. Figure 4.12 shows that mixing model based on the fractional melting model. Here, the entire range of HSE elemental composition can be modelled by mixing between solid and liquid metal. As a result, the range of kamacite composition between the high Ge/Ir (>20) with low HSE kamacite corresponding to the liquid phase, and the low Ge/Ir (<20) with high HSE kamacite representing the solid, can be explained by the melting and the mixing of metal which had contained up to 5.3 wt. % of carbon. It means that the size effect and the enrichment in refractory siderophile elements of small metal grains can be the last unmelted particles that were separated from the melted metal prior to accretion. Also, the bulk composition of some grains can be the result of mixing / homogenisation between the two compositions of metal produced during melting. Regarding this model, the formation of metal in H3 chondrites agrees with the model of metal formation in L and LL chondrite in Okabayashi et al., (2019). This suggests that a portion of the elemental variation in metal of H3 chondrites can be the result of metal melting and mixing with residual metallic solid in the protoplanetary disk.

4.2.2. Metal–silicate interaction prior to the accretion

Os, Ru, Pt and Rh variations in metal from UOCs can be interpreted with melting models, but W and Mo concentrations are more complex to explain (Fig. 4.6). With 5.3 wt. % of carbon contents in the metal, W should behave as an incompatible element ($D(W)_{\text{solid metal-liquid metal}} = 0.18$, Table 4.4). Yet, it shows no correlation with the melting model (Fig. 4.10). Additionally, as Chabot et al. (2017) do not report parametrisation for Mo in the Fe-Ni-C system, we cannot determine the reason for the lack of correlation between Mo and Ge/Ir.

It has been demonstrated that W and Mo are very sensitive to fO_2 with W more easily oxidized than Mo (Fegley and Palme, 1985). If W and Mo metal contents cannot be explained by fractional melting, the oxidation state may have played an important role in their fractionation. Kong and Ebiahra (1996) suggest that the enrichment in Mo, compared to W, in the bulk metal of UOC can be explained by the partial reduction of highly oxidized precursor formed at high $\log(fO_2)$ (between 10^{-13} to 10^{-11}), during melting. As Mo is more easily reduced than W, the metal will be less depleted in Mo than W. The mean compositions of metallic grains show a higher enrichment in Mo compared to W, which agree with W being incorporated more in the silicates compared to Mo (Fig. 4.11). This enrichment is more significant than reported for H3.5 to 3.9 by Kong and Ebiahra (1996) and suggests that the metal grains from Sharps has been formed under more reduced conditions than predicted by the Kong and Ebihara (1996) model. The distribution of W and Mo in UOCs metallic grains is highly variable from one grain to another (Fig. 4.6) and implies that multiple species of W (i.e. W_{metal} WO_2, WO_3) and Mo (i.e.

Mo_{metal}, MoO_2, MoO_3) can occur in the environment during the heating event. The occurrence of multiple Mo and W species at the same time, in the same environment, can be examined in the case when mineral precursors buffered the redox conditions of chondrite precursors, instead of being determined by the nebula (Connolly et al., 1994). The melting of an assemblage of dust and oxidizing agent can create, at a grain scale, a local oxidizing environment independent from the solar nebula (Fegley and Palme, 1985). We suggest that during melting of metal and silicate ordinary chondrite precursors, the redox state was locally defined by evaporation of variable quantities of hydrated dust grains (e.g. silicates or hydrated phyllosilicates, Florin et al., 2020) which can led to the local formation of W_{metal}, WO_2, or WO_3 and Mo_{metal}, MoO_2, or MoO_3, and thus to different W and Mo contents in the metal. This conclusion also implies that, in the environment where H OCs formed, the precursor material was heterogeneously distributed, leading to areas being more oxidized than others during the heating event (see section 5.3).

Gallium (Ga) is an element that can be siderophile and lithophile during condensation depending on its redox state (Wai and Wasson, 1979; Lodders et al., 2009). During metal melting, it is expected that the moderately volatile Ga will mostly evaporate from precursors ($T_{50\%}$(Ga) = 968 K, Lodders et al., 2009) which explains its depletion in most of the analysed metal grains (from ~0.1 to 3.56 ppm, although three outliers exist: 7.15, 12.59 and 42.71 ppm) compared to CI (9.71 ppm, Lodders et al., 2009) (Fig. 4.6 A). However, because Ga is less volatile than Ge, it is expected to be less depleted than Ge in the metal, which is not the case (Fig. 4.6 A). This difference can be explained by the lower siderophile behaviour of Ga compared to Ge during condensation. Indeed, during re-condensation Ga behaviour is going to be affected by environmental redox states and thus will be fractionated in silicate and metal accordingly. Therefore, the range of Ga depletion in the metal can be attributed to the multiple local redox conditions.

An implication of metal–silicate interaction in a local variable oxidation state is the variable incorporation of iron in pyroxenes and olivines during the heating event. This scenario is confirmed by the very large range in %Fa and %Fs (i.e. Fe content in olivine and pyroxene) in very primitive UOCs (type 3.0 to 3.4) compared to EOC.

Finally, local dust grain evaporation implies that volatile elements (such as Na) instead of being enriched at nebula scale (and then incorporated in chondrules) could be locally enriched due to precursors evaporation and then recondensed, in line with Hewins and Zanda (2012).

4.2.3. Rhenium issue

The high Re content in Dhajala metal grains do not follow the fractional melting model of a FeNi-C metal. The high Re content also disagrees with Kong and Ebihara (1997) bulk measurements. Florin et al. (2020) have shown a high $\delta^{74/70}Ge_{metal}$ of Dhajala compared to and other H OCs and suggest that Dhajala formed in a different environment than other H chondrites.

Alternatively, the refractory siderophile carrier may not occur as one phase but as different metal precursors with different characteristics (such as refractory grains like W–Re alloys) that were then not melted during the heating event.

4.3. The H, L/LL dichotomy

4.3.1. Carbon content in FeNi and its influence on H, L/LL dichotomy

Kong and Ebihara (1997) suggest that the metal in primitive H, L and LL chondrites formed at the same conditions (oxygen fugacity, temperature) and initially had similar elemental compositions. They proposed that the difference of siderophile content in the metal between OCs groups is the result of accretion time and equilibration with the solar nebula before accretion. Thus, the H group has accreted at higher temperature, before L and LL and under more reduced conditions than the L and LL groups. However, recent studies have shown that OC groups were accreted at the same time (Desch et al., 2018; Hellmann et al., 2019). Moreover, evidence from fractionation of Hf–W highlight that metal and chondrules were formed during related event(s), and that the differences between H, L and LL were established during that thermal event (Hellmann et al., 2019).

According to our model, before melting, H OCs metal contains up to 5.3 wt. % of C and higher than the 3.8 wt. % of C reported by Okayabashi et al. (2019) for L and LL chondrites. This agrees with the most reduced feature of the H group compared to L and LL. However, according to thermodynamic calculation, H OC metal is unlikely to incorporate carbon during high temperature condensation (Grossman et al., 2012) and OCs bulk contain less than 1 wt. % C, even in type 3 chondrites (Jarosewich et al., 1990). As a result, the following questions need to be assessed:

1) How has carbon been incorporated in OCs metal?
2) Why is the carbon content in OCs now lower that 1 wt. %?
3) How has the carbon influenced the H-L-LL trichotomy?

A gas component enriched in CO and/or CH_4 can react with metal at low temperature (<750°C, Sohn and Sridhar, 2006) to form iron carbide (Fe_3C or $[FeNi]_3C$) following equations 1 and 2:

$$3\ Fe_{(s)} + 2CO_{(g)} \Leftrightarrow Fe_3C_{(s)} + CO_{2\ (g)} \qquad \text{Eq. 1}$$

$$3\ Fe_{(s)} + CH_{4\ (g)} \Leftrightarrow Fe_3C_{(s)} + 2H_{2\ (g)} \qquad \text{Eq. 2}$$

Mostefaoui et al. (2000) suggest that organic matter (OM), in the form of kerogen-like macro-molecule, was associated with metal and chondrule precursors and was decomposed to graphite and trapped into the metal during the heating event that led to chondrule formation.

They also note that oxidized carbon formed from OM by reduction of Fe from the oxidized precursor, could escape as CO. If so, the gas would be locally enriched in CO. The produced CO would then react with the metal, dissolving carbon in FeNi alloy (Eq. 1 and 2) and influencing the fractionation of siderophile elements. This carbon can later be exsolved at low temperature (~400 °C, Gabriel et al., 1987).

According to our model and Okayabashi et al. (2019), UOCs metal contains between 3 and 5.3 wt. % of carbon when melted. Today, if we consider that all the carbon of H3 chondrite is in the metal, the maximum carbon content in H3 metal is 1.93 wt. % (Jarosewich, 1990). Hence, loss of C occurs prior to the accretion of OCs parent body is mostly related to volatilisation processes in the disk rather than variations in temperature during metamorphism (Mostefaoui et al., 2000, Mostefaoui et al, 2005).

The low C content calculated for the H group indicates that the environment of H OCs was more reduced than for L and LL due to a lower percentage of hydrated phyllosilicates of metal precursors (Florin et al., 2020). When precursors were heated, the ratio CO/CO_2, was higher in the environment of H groups compared to L and LL types. The differences in CO/CO_2 ratio can account for the difference in %Fa between H and L, LL. If metal and chondrules were formed during the same melting event (Okayabashi et al., 2019), the lower metal content and the higher %Fa in L and LL compared to H can be explained by the reaction of Fe with CO_2 (Eq. 5):

$$Fe_{(s)} + CO_{2\,(g)} = CO_{(g)} + FeO \qquad \text{Eq. 5}$$

And the formation of fayalite by the reaction of FeO with SiO_2:

$$2\ FeO + SiO_2 = Fe_2SiO_4 \qquad \text{Eq. 6}$$

4.3.2. Constraining siderophile elements in the H-L/LL dichotomy

The difference in metal content between H and L/LL OCs highlighted by the Urey and Craig-type diagram, *i.e.* $Fe_{metal\ +\ sulfide}$ vs FeO (e.g. Cartier and Wood, 2019), can be assessed by siderophile elements in the metal. In figure 4.13, we compare the Re, Os, Ir, Pt, Pd and Au metal content of H and L/LL OCs groups. The two groups show a similar elemental composition (Fig 4.13). Therefore, the highest metal content in H OCs compared to L and LL cannot be the result of thermodynamic processes such as an increase of Fe oxidation / evaporation from H to LL nor a higher proportion of iron condensate in the environment of H formation. Indeed, in these cases the decrease of Fe relative to refractory elements from H to LL will create a dilution effect of these elements. Thus, a lower content of refractory PGEs would be expected in the metal of H compared to L and LL, and moderately volatile PGE and gold would be enriched in the H metal grains compared to L and LL.

The metal variation content in ordinary chondrites groups can consequently be linked to mechanical distribution of metal grains in the disk that contribute to enrich the region of H in Fe–Ni–metal at the expense of L and LL region. It means that the proportions of PGE and metal are linked and have not changed in primitive OCs since last metal modification in the protoplanetary disk. Thus, if the large range of %Fa and %Fs in primitive H and L and LL OCs (Rubin, 2005) results from iron oxidation during heating event, the lack of oxidation effect on the metal from H to LL (i.e. dilution effect) also suggests that the mechanical distribution of metal occurred after the heating event.

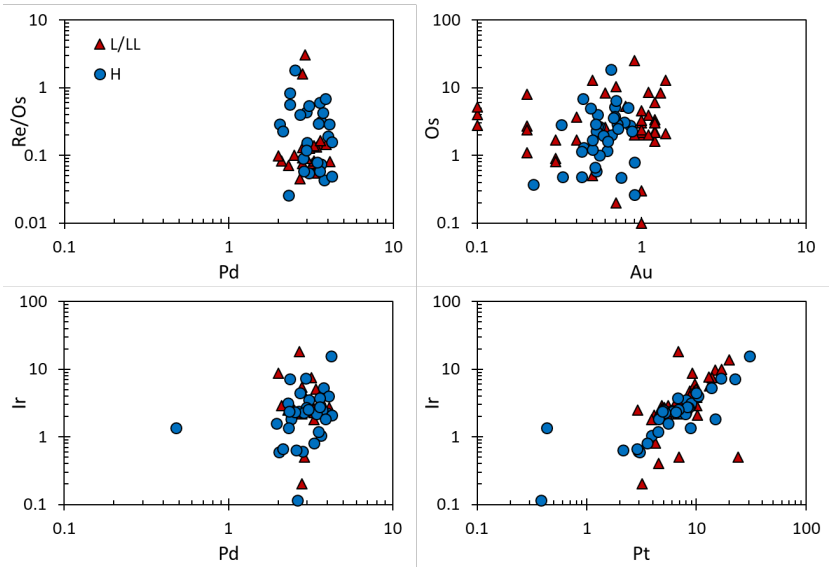

Figure 4.13: Siderophile elements content in kamacite from H chondrites (blue circles) and L–LL chondrites (red triangles). Values are in ppm. L and LL data after Okabayashi et al. (2019).

Recent studies suggest that the protoplanetary disk could have been structured so that pressure bumps were present creating pressure gradients in OCs environment (Brasser and Mojzsis, 2020). The effect of a pressure gradient can be a possible explanation for mechanical distribution of metal between H and L/LL. Another possibility is the presence of high turbulence in the region of L and LL formation compared to H (Rubin et al., 2005).

4.4. Effect of metamorphism on the metal-sulfide assemblage

Sulfides that we have measured in the most unequilibrated OC of our sample set (Sharps) shows a strong enrichment in refractory elements, close to metal composition, (Fig. 4.9). This contrast with sulfides from Dhajala that are depleted in siderophile elements as the EOC sulfides. The partition coefficient of siderophile elements between metal and sulfide ($Kd_{metal\text{-}sulfide} = [X]_{metal}/[X]_{sulfide}$, where X is the elemental composition of the phase) increase as a function of increasing degrees of thermal metamorphism to (Fig. 4.14). This suggests that the sulfide composition in Sharps reflects primary processes taking place in the protoplanetary disk.

Tachibana and Huss (2005) suggest that different types of sulfides occur in ordinary chondrites: (1) pristine troilites in chondrules that were protected from evaporation during precursors melting; (2) Fe–Ni–S droplets that were expelled from the chondrules; (3) sulfide formed by sulfurization of the metal during recondensation. In this study, we report values for

sulfides outside chondrules as sulfides inside chondrules are too small for accurate siderophile elemental measurements. According to Rubin et al., (1999) and Tachibana and Huss (2005), the measured sulfides in H3 Sharps cannot be "primary" troilite as they were not located inside chondrule, within metal grains and thus not protected from heating events. A possibility is that they result from the recondensation of sulfide on metal grains after the heating event(s) in the protoplanetary disk.

The difference in sulfide composition between Sharps (H3.4) and Dhajala (H3.8) (Fig. 4.9) could be explained by re-equilibration of the two types of sulfide texturally identify triggered by an increasing in temperature during metamorphism, from ~350-400°C in H3.4 (Huss et al., 2006; Rietmeijer and Mackinnon, 1985) to ~625-680 °C in H3.8 (Wlotzka, 1985, 1987, 2005).

During metal melting and crystallisation of a FeNiS assemblage on a parent body, the formed sulfides are expected to become enriched in Au and Pd at the expense of the metal. Here, the PGE and Au sulfide patterns are flat (Fig. 4.14), meaning that they cannot be produced by the crystallisation of a FeNiS liquid. Therefore, the lack of the evolution of sulfide composition with increasing metamorphism from H4 to H6 as well as the flat elemental pattern of metal (Fig. 4.10 and 4.14) suggests that no significant exchange occurred during metamorphism between metal and sulfides. Also, these observations agree with the lack of textural reaction between sulfide and metal. This suggests that the sulfide may have been melted and then wetted the metal surface. A reason is likely the temperature peak of H6 (~1000°C, Tait et al., 2014), that is too low to melt metal (solidus for pure FeNi ~1500°C, Swartzendruber et al., 1991) compared to FeS (988°C, Fei et al., 1997).

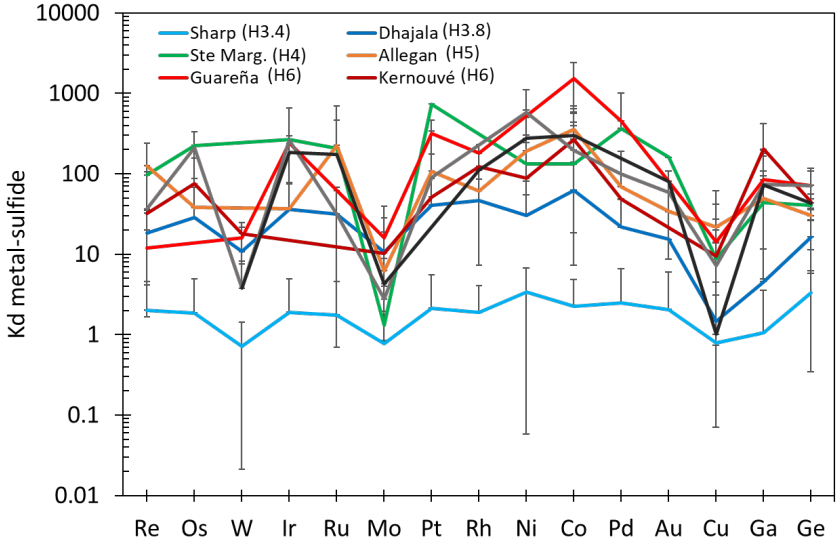

Figure 4.14: Evolution of the partition coefficient of siderophile elements between metal and sulfides (Kd = $[X]_{metal}$ / $[X]_{sulfide}$ where X is an specific element and [X] its content in metal or sulfide).

The increase of metamorphism induced a homogenization of metal composition (Fig. 4.6). In Ge/Ir vs siderophile elements diagrams. This evolution is highlighted by the disappearance of the high and very low Ge/Ir metal grains with increasing metamorphism. Also, the variations of volumetric percentage of the metal in OC samples show a decrease of the metal content from H4 to H5 chondrites and an increase in from H5 to H6 (Guignard and Toplis, 2015). It would be

tempting to attribute textural and chemical evolution to metal migration from H4 to H6. However, the metal melt flow within a silicate network is highly dependent on the interconnectivity of the metal droplets and the presence of a high percentage of sulfide can inhibit the migration of metal by closing pores (Néri et al., 2019). Therefore, the sulfide wetting on metal observed in H6 may preclude the migration of metal. Thus, the textural change and chemical homogenisation of the metal might be due to a slow viscous effect associated with a pressure gradient.

4.4.1. Metal migration in the parent body?

Metal in H6 apparently is not able to migrate freely in a planetesimal. Tomkins et al. (2013) study highlighted evidence of metal migration in the metal breccia Portales Valley (H6). On the basis of vein distribution and occurrence (Fig 4.6 I), the authors suggest that an impact can trigger metal migration on a large scale inside the planetesimal due to pressure bump at mineral interphases.

Metal in the clasts of Portales Valley is slightly depleted in HSEs compared to the veins. However, metal composition between these two objects do not show a strong elemental fractionation. Tomkins et al., (2013) suggest that the sulfide inside the clasts result from the injection of a residual Fe–Ni–S_{rich} liquid. The lack of Au and Pd depletion in the metal veins suggest that the last residual liquid had a very high S content (~25%, Chabot and Jones, 2003) which leads Au and Pd to be more incorporated in the solid metal compared to the liquid metal. Therefore, the elemental analysis agrees with the injection of Fe–Ni–S_{rich} liquid in the clasts which is the residue of Fe–Ni–S liquid that formed the veins. This observation may explain the slight depletion in HSE in metal grains from clasts compared to veins (Fig. 4.6)

The mean composition of metal in Portales Valley is identical to the mean composition of other H chondrites (Fig. 4.9). If Portales Valley formed by impact, this metal has to originate from the H parent body if not, the impactor has to have the same elemental composition, suggesting that multiple H parent bodies have existed. Also, according to Stöffler et al. (1991) the lack of shock evidence in clasts mean that Portales Valley has been deeply buried in the planetesimal.

5 Conclusions

In this study, we have performed *in-situ* analysis of siderophile elements by LA-ICP-MS in metal and sulfide grains in ordinary chondrites from types 3 to 6. In agreement with previous studies, we show a large variability of elemental composition in unequilibrated ordinary chondrites. These variations in siderophile element decrease with increasing metamorphism. We report correlations between Ge/Ir, a tracer for metal melting, and siderophile elements (e.g. Os,

Re, Ru, Pt, Rh). We have shown that this variation in composition can be modelled for melting of the metallic phase containing up to 5.2% of carbon. This carbon content is lower than reported by Okabayashi et al. (2019) for L and LL ordinary chondrites. This difference agrees with the more reduced feature of the H group compared to L and LL groups and is related to the higher occurrence of an oxidizing agent within L and LL precursors than in H precursors. Also, the similarity between H, L and LL metal compositions implies that the metal is from similar precursors. We conclude that the difference of metal content through the OC groups is not the result of chemical processes but more of mechanical distribution of the metal after its formation in the protoplanetary disk.

The large variation in Mo, W and Ga in metal grains from H3.4 suggest that metal has been formed by melting and reduction of highly oxidized precursor during chondrule formation (Fig. 4.15 A), as the consequences of local variations of the oxidation state that result in the formation of different molecules species (e.g. Mo^0, MoO_2, MoO_3, W^0, WO_3). The preferential incorporation of these species in metal and silicate would then produce the depletion / enrichment in the metal. The variation in oxidation state can be due to heterogeneous distribution of oxidizing agents (Fig. 4.15 B). The depletion of W and Mo in the metallic bulk composition is therefore a better reflection of the global oxidation state acquired during the melting event than the oxidation environment occurring before melting (Fig. 4.15 C). The large variation in %Fa and %Fe in primitive OCs (<= H3.4) can be explain by these local variations in oxidation states during metal and silicates precursors heating (Fig. 4.15 B). Also, the interaction between metal and silicate prior to the accretion is highlighted by the variation of Ga in H3 chondrites. Therefore, the global oxidation state of the metal in an OC cannot be used to assess the oxidation state of metal precursors.

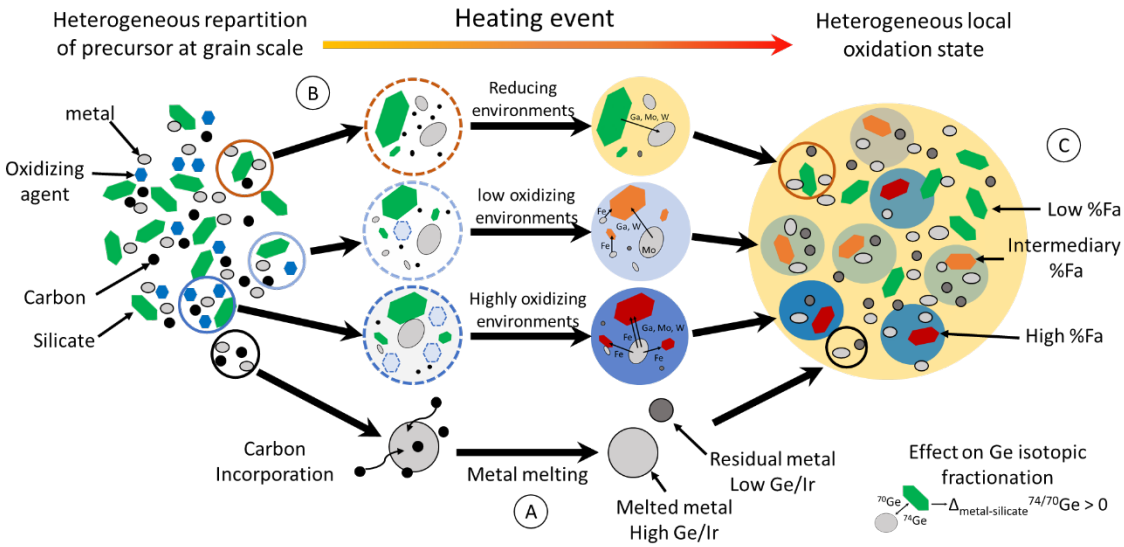

Figure 4.15: Representation of the formation of metal and of metal silicate exchange during melting event in the protoplanetary disk.

Lastly, the progressive homogenization of the elemental composition of the metal with increasing the metamorphic grade highlights metal equilibration with increasing thermal metamorphism. Models of metal migration within the planetesimal have to involve impact brecciation which allow the formation of porosity and the migration of metal such as seen in Portales Valley.

Concluding remarks

Previous studies highlighted that silicate and metal have interacted in the protoplanetary disk prior to their accretions due to complex precursor melting and evaporation / recondensation. In this study, we have considered the *in situ* elemental composition of metal and sulfide grains in primitive ordinary chondrites. We have emphasized the potential of Ge to track metal melting in the protoplanetary disk. Also, we have demonstrated the heterogeneous distribution of particles within the precursors and have highlighted that strong mechanical effect of the distribution of metal in the disk.

Whereas the range of %Fa in primitive chondrites can be explain by various local oxidation state, the increase of %Fa from H to L and LL needs an additional process. In the next section, we focus on the effect metal oxidation after accretion and on the relation between oxygen and germanium using germanium isotopes in the metal, silicate, sulfide and bulk of ordinary chondrites.

6 Acknowledgments

The authors thank Timothy Murphy for its help for SEM imaging. The authors also thank M. Gounelle and the "Comité de gestion" at the "Muséum National d'Histoire Naturelle" (MNHN) of Paris, T. McCoy and J. Hoskin from the Smithsonian Institute, A. Nieto Codina from the "Museo Nacional de Ciencias Naturales" (MNCN) of Madrid, and A. Yamaguchi from the "National Institute of Polar Research" of Tokyo for providing the meteorite samples.

7 Reference

Alard O., Lorand J.-P., Reisberg L., Bodinier J.-L., Dautria J.-M., and O'Reilly S. Y. 2011. Volatile-rich Metasomatism in Montferrier Xenoliths (Southern France): Implications for the Abundances of Chalcophile and Highly Siderophile Elements in the Subcontinental Mantle. *Journal of Petrology* 52:2009–2045.

Campbell A. J., Humayun M., and Weisberg M. K. 2002. Siderophile element constraints on the formation of metal in the metal-rich chondrites Bencubbin, Weatherford, and Gujba. *Geochimica et Cosmochimica Acta* 66:647–660.

Campbell A. J., and Humayun M. 2003. Formation of metal in Grosvenor Mountains 95551 and comparison to ordinary chondrites. *Geochimica et Cosmochimica Acta* 67:2481–2495.

Campbell A. J., Zanda B., Perron C., Meibom A., and Petaev M. I. 2005. Origin and Thermal History of Fe-Ni Metal in Primitive Chondrites. *Chondrites and the Protoplanetary Disk ASP Conference Series* 341:407.

Cartier C., and Wood B. J. 2019. The Role of Reducing Conditions in Building Mercury. *Elements* 15:39–45.

Chabot N. L., and Jones J. H. 2003. The parameterization of solid metal-liquid metal partitioning of siderophile elements. *Meteoritics & Planetary Science* 38:1425–1436.

Chabot N. L., Wollack E. A., McDonough W. F., Ash R. D., and Saslow S. A. 2017. Experimental determination of partitioning in the Fe-Ni system for applications to modeling meteoritic metals. *Meteoritics & Planetary Science* 52:1133–1145.

Chou C.-L., Baedecker P. A., and Wasson J. T. 1973. Distribution of Ni, Ga, Ge and Ir between metal and silicate portions of H-group chondrites. *Geochimica et Cosmochimica Acta* 37:2159–2171.

Cohen B. A., and Hewins R. H. 2004. An experimental study of the formation of metallic iron in chondrules 1 1Associate editor: C. Koeberl. *Geochimica et Cosmochimica Acta* 68:1677–1689.

Connolly H. C., Hewins R. H., Ash R. D., Zanda B., Lofgren G. E., and Bourot-Denise M. 1994. Carbon and the formation of reduced chondrules. *Nature* 371:136–139.

Connolly H. C., Huss G. R., and Wasserburg G. J. 2001. On the formation of Fe-Ni metal in Renazzo-like carbonaceous chondrites. *Geochimica et Cosmochimica Acta* 65:4567–4588.

Desch S. J., Kalyaan A., and Alexander C. M. O. 2018. The Effect of Jupiter's Formation on the Distribution of Refractory Elements and Inclusions in Meteorites. *The Astrophysical Journal Supplement Series* 238:11.

Fegley B., and Kornacki A. S. 1984. The geochemical behavior of refractory noble metals and lithophile trace elements in refractory inclusions in carbonaceous chondrites. *Earth and Planetary Science Letters* 68:181–197.

Fegley B., and Palme H. 1985. Evidence for oxidizing conditions in the solar nebula from Mo and W depletions in refractory inclusions in carbonaceous chondrites. *Earth and Planetary Science Letters* 72:311–326.

Fei Y., Bertka C. M., and Finger L. W. 1997. High-Pressure Iron-Sulfur Compound, Fe3S2, and Melting Relations in the Fe-FeS System. *Science* 275:1621–1623.

Florin G., Luais B., Rushmer T., and Alard O. 2020. Influence of redox processes on the germanium isotopic composition of ordinary chondrites. *Geochimica et Cosmochimica Acta* 269:270–291.

Gabriel A., Gustafson P., and Ansara I. 1987. A thermodynamic evaluation of the C-Fe-Ni system. *Calphad* 11:203–218.

Gilbert S., Danyushevsky L., Robinson P., Wohlgemuth-Ueberwasser C., Pearson N., Savard D., Norman M., and Hanley J. 2013. A Comparative Study of Five Reference Materials and the Lombard Meteorite for the Determination of the Platinum-Group Elements and Gold by LA-ICP-MS. *Geostandards and Geoanalytical Research* 37:51–64.

Goldstein J. I., Huss G. R., and Scott E. R. D. 2017. Ion microprobe analyses of carbon in Fe–Ni metal in iron meteorites and mesosiderites. *Geochimica et Cosmochimica Acta* 200:367–407.

Grossman J. N., and Wasson J. T. 1985. The origin and history of the metal and sulfide components of chondrules. *Geochimica et Cosmochimica Acta* 49:925–939.

Guignard J., and Toplis M. J. 2015. Textural properties of iron-rich phases in H ordinary chondrites and quantitative links to the degree of thermal metamorphism. *Geochimica et Cosmochimica Acta* 149:46–63.

Hellmann J. L., Kruijer T. S., Van Orman J. A., Metzler K., and Kleine T. 2019. Hf-W chronology of ordinary chondrites. *Geochimica et Cosmochimica Acta* 258:290–309.

Hewins R. H., and Connolly H. C. Jr. 1996. Peak temperatures of flash-melted chondrules. In *Chondrules and the Protoplanetary Disk*. Cambridge ; New York: Cambridge University Press. pp. 197–204.

Hewins R. H., Yu Y., Zanda B., and Bourot-Denise M. 1997. Do nebular fractionations, evaporative losses, or both, influence chondrule compositions? *Antarctic Meteorite Research* 10:275–298.

Hewins R. H., and Zanda B. 2012. Chondrules: Precursors and interactions with the nebular gas. *Meteoritics & Planetary Science* 47:1120–1138.

Hirayama Y., Fujii T., and Kurita K. 1993. The melting relation of the system, iron and carbon at high pressure and its bearing on the early stage of the Earth. *Geophysical Research Letters* 20:2095–2098.

Horan M. F., Alexander C. M. O., and Walker R. J. 2009. Highly siderophile element evidence for early Solar System processes in components from ordinary chondrites. *Geochimica et Cosmochimica Acta* 73:6984–6997.

Huss G. R., Rubin A. E., and Grossman J. N. 2006. Thermal Metamorphism in Chondrites. *Meteorites and the Early Solar System II* 567–586.

Kong P., Ebihara M., and Xie X. 1998. Reevaluation of formation of metal nodules in ordinary chondrites. *Meteoritics & Planetary Science* 33:993–998.

Krot A. N., Keil K., Scott E. R. D., Goodrich C. A., and Weisberg M. K. 2014. Classification of Meteorites and Their Genetic Relationships. In *Treatise on Geochemistry*. Elsevier. pp. 1–63.

Kruijer T. S., Touboul M., Fischer-Godde M., Bermingham K. R., Walker R. J., and Kleine T. 2014. Protracted core formation and rapid accretion of protoplanets. *Science* 344:1150–1154.

Lauretta D. S., Buseck P. R., and Zega T. J. 2001. Opaque minerals in the matrix of the Bishunpur (LL3.1) chondrite: constraints on the chondrule formation environment. *Geochimica et Cosmochimica Acta* 65:1337–1353.

Lodders K., Palme H., and Gail H.-P. 2009. 4.4 Abundances of the elements in the Solar System. In *Solar System*, edited by Trümper J. E. Berlin, Heidelberg: Springer Berlin Heidelberg. pp. 712–770.

Marrocchi Y., Villeneuve J., Batanova V., Piani L., and Jacquet E. 2018. Oxygen isotopic diversity of chondrule precursors and the nebular origin of chondrules. *Earth and Planetary Science Letters* 496:132–141.

McCoy T. J., Dickinson T. L., and Lofgren G. E. 1999. Partial melting of the Indarch (EH4) meteorite: A textural, chemical, and phase relations view of melting and melt migration. *Meteoritics & Planetary Science* 34:735–746.

Mikhail S., and Füri E. 2019. On the Origin(s) and Evolution of Earth's Carbon. *Elements* 15:307–312.

Monnereau M., Toplis M. J., Baratoux D., and Guignard J. 2013. Thermal history of the H-chondrite parent body: Implications for metamorphic grade and accretionary time-scales. *Geochimica et Cosmochimica Acta* 119:302–321.

Mostefaoui S., Perron C., Zinner E., and Sagon G. 2000. Metal-associated carbon in primitive chondrites: structure, isotopic composition, and origin. *Geochimica et Cosmochimica Acta* 64:1945–1964.

Mostefaoui S., Zinner E., Hoppe P., Stadermann F. J., and Goresy A. E. 2005. In situ survey of graphite in unequilibrated chondrites: Morphologies, C, N, O, and H isotopic ratios. *Meteoritics & Planetary Science* 40:721–743.

Néri A., Guignard J., Monnereau M., Toplis M. J., and Quitté G. 2019. Metal segregation in planetesimals: Constraints from experimentally determined interfacial energies. *Earth and Planetary Science Letters* 518:40–52.

Newsom H. E., and Drake M. J. 1979. The origin of metal clasts in the Bencubbin meteoritic breccia. *Geochimica et Cosmochimica Acta* 43:689–707.

Okabayashi S., Yokoyama T., Nakanishi N., and Iwamori H. 2019. Fractionation of highly siderophile elements in metal grains from unequilibrated ordinary chondrites: Implications for the origin of chondritic metals. *Geochimica et Cosmochimica Acta* 244:197–215.

Qin L., Dauphas N., Wadhwa M., Masarik J., and Janney P. E. 2008. Rapid accretion and differentiation of iron meteorite parent bodies inferred from 182Hf–182W chronometry and thermal modeling. *Earth and Planetary Science Letters* 273:94–104.

Radomsky P. M., and Hewins R. H. 1990. Formation conditions of pyroxene-olivine and magnesian olivine chondrules. *Geochimica et Cosmochimica Acta* 54:3475–3490.

Rietmeijer F. J. M., and Mackinnon I. D. R. 1985. Poorly graphitized carbon as a new cosmothermometer for primitive extraterrestrial materials. *Nature* 315:733–736.

Righter K., Campbell A. J., and Humayun M. 2005. Diffusion of trace elements in FeNi metal: Application to zoned metal grains in chondrites. *Geochimica et Cosmochimica Acta* 69:3145–3158.

Rubin A. E., Sailer A. L., and Wasson J. T. 1999. Troilite in the chondrules of type-3 ordinary chondrites: implications for chondrule formation. *Geochimica et Cosmochimica Acta* 63:2281–2298.

Schmitt W., Palme H., and Wänke H. 1989. Experimental determination of metal/silicate partition coefficients for P, Co, Ni, Cu, Ga, Ge, Mo, and W and some implications for the early evolution of the Earth. *Geochimica et Cosmochimica Acta* 53:173–185.

Scott E. R. D., Mandell D., Yang J., Goldstein J. I., Krot T., and Taylor G. J. 2010. Metamorphism and Impacts on the Parent Asteroid of H Chondrites. 41:1529.

Siebert J., Corgne A., and Ryerson F. J. 2011. Systematics of metal–silicate partitioning for many siderophile elements applied to Earth's core formation. *Geochimica et Cosmochimica Acta* 75:1451–1489.

Sohn H. Y., and Sridhar S. 2006. Descriptions of High-Temperature Metallurgical Processes. *ChemInform* 37.

Tachibana S., and Huss G. R. 2005. Sulfur isotope composition of putative primary troilite in chondrules from Bishunpur and Semarkona. *Geochimica et Cosmochimica Acta* 69:3075–3097.

Tait A. W., Tomkins A. G., Godel B. M., Wilson S. A., and Hasalova P. 2014. Investigation of the H7 ordinary chondrite, Watson 012: Implications for recognition and classification of Type 7 meteorites. *Geochimica et Cosmochimica Acta* 134:175–196.

Tomkins A. G., Weinberg R. F., Schaefer B. F., and Langendam A. 2013. Disequilibrium melting and melt migration driven by impacts: Implications for rapid planetesimal core formation. *Geochimica et Cosmochimica Acta* 100:41–59.

Van Schmus W. R., and Wood J. A. 1967. A chemical-petrologic classification for the chondritic meteorites. *Geochimica et Cosmochimica Acta* 31:747–765.

Walker R. J., McDonough W. F., Honesto J., Chabot N. L., McCoy T. J., Ash R. D., and Bellucci J. J. 2008. Modeling fractional crystallization of group IVB iron meteorites. *Geochimica et Cosmochimica Acta* 72:2198–2216.

Weyrauch M., Zipfel J., and Weyer S. 2019. Origin of metal from CB chondrites in an impact plume – A combined study of Fe and Ni isotope composition and trace element abundances. *Geochimica et Cosmochimica Acta* 246:123–137.

Widom E., Rubin A. E., and Wasson J. T. 1986. Composition and formation of metal nodules and veins in ordinary chondrites. *Geochimica et Cosmochimica Acta* 50:1989–1995.

Wlotzka F. 1985. Olivine-Spinel and Olivine-Ilmenite Thermometry in Chondrites of Different Petrologic Type. In *16th Lunar and Planetary Science Conference*. Houston. pp. 918–919.

Wlotzka F. 1987. Equilibration Temperatures and Cooling Rates of Chondrites: A New Approach. *Meteoritics* 22:529.

Wlotzka F. 2005. Cr spinel and chromite as petrogenetic indicators in ordinary chondrites: Equilibration temperatures of petrologic types 3.7 to 6. *Meteoritics & Planetary Science* 40:1673–1702.

Zanda B., Bourot-Denise M., Perron C., and Hewins R. H. 1994. Origin and Metamorphic Redistribution of Silicon, Chromium, and Phosphorus in the Metal of Chondrites. *Science* 265:1846–1849.

Appendix

Table 4.A: Elemental composition of metal and sulfides grains in ordinary chondrites. Values are in ppm except for Ni that are in %. M: Matrix; C.E.: Chondrule Edge; C.I.: Chondrule Interior; V: Vein; C: Clast. K: kamacite; t: taenite; s: sulfide.

			Re ppm	Os ppm	W ppm	Ir ppm	Ru ppm	Mo ppm	Pt ppm	Rh ppm	Ni %	Co ppm	Pd ppm	Au ppm	Cu ppm	Ga ppm	Ge ppm	Ge/Ir
Sharp																		
ShS_HM_001	M	k	0.218	3.97	b.d	3.51	5.22	3.29	8.05	1.44	6.35	5355	3.08	0.54	97.9	0.49	73.40	20.91
ShS_HM_002	M	k	0.387	5.18	b.d	2.92	4.86	4.50	8.77	1.46	6.53	4176	3.62	0.69	112.1	0.26	59.31	20.31
ShS_HM_005	M	k	0.242	2.67	b.d	2.27	4.31	1.58	8.07	1.15	6.21	4541	2.82	0.56	97.8	0.06	56.28	24.79
SHS_HM_010	M	k	b.d	0.59	b.d	1.85	9.23	14.87	14.81	2.48	5.51	4135	2.40	0.53	97.6	0.22	60.84	32.89
SHS_HM_011	M	k	b.d	1.29	0.82	0.61	2.16	11.20	2.93	0.70	4.84	3511	2.82	0.44	94.9	42.71	68.41	112.1
SHS_HM_012	M	k	b.d	0.48	b.d	0.64	0.45	58.96	2.14	0.46	5.33	3612	2.58	0.43	95.9	2.57	74.16	115.9
SHS_HM_012B	M	k	0.230	0.79	0.39	0.59	1.71	41.71	3.01	0.51	5.51	3469	2.03	0.90	87.9	2.25	67.27	114.0
SHS_HM_013	M	k	0.110	0.48	b.d	0.66	1.48	14.86	2.86	0.77	5.62	3532	2.13	0.33	10.9	1.45	60.36	91.45
SHS_HM_015	M	k	0.280	6.49	1.02	5.35	7.80	31.63	13.63	1.61	4.94	3322	3.79	0.70	101.1	3.56	91.21	17.05
SHS_HM_016	M	k	0.430	2.78	b.d	2.42	2.82	18.08	6.01	0.93	5.62	3243	2.99	0.85	124.5	0.33	64.24	26.55
SHS_HM_017	M	k	b.d	2.28	b.d	2.36	3.24	25.31	6.02	0.77	4.74	4014	2.66	0.87	72.6	0.78	75.17	31.85
ShS_HM_40	M	k	0.920	18.56	b.d	15.48	21.54	5.45	30.61	3.56	6.25	4138	4.22	0.65	177.4	7.15	81.81	5.28
ShS_HM_41	M	k	0.068	2.66	b.d	3.18	4.40	4.54	8.95	1.07	6.34	3882	2.30	0.54	208.2	12.59	53.12	16.70
SHS-HM-030	M	k	0.360	1.14	0.30	1.05	2.91	11.73	3.89	0.75	6.48	4264	3.64	0.43	86.6	0.68	54.52	51.92
SHS-HM-031	M	k	0.340	1.16	0.23	1.19	2.38	7.14	4.45	1.05	7.12	4014	3.52	0.61	112.0	0.54	54.26	45.60
SHS-HM-032	M	k	0.440	2.30	0.32	2.22	4.87	7.06	7.33	1.46	5.80	3461	4.00	0.53	121.4	0.22	48.22	21.72
SHS-HM-033	M	k	0.810	2.82	0.59	3.97	6.70	13.55	10.41	1.29	6.88	4427	4.07	0.33	132.6	2.45	56.96	14.35
SHS-HM-035	M	k	0.860	2.00	0.23	2.46	4.21	6.21	5.01	1.08	7.96	4370	3.72	0.65	160.4	1.22	57.00	23.17
SHS_HM_012	M	t	0.150	12.51	b.d	5.44	22.22	63.93	20.56	3.12	22.16	2544	35.96	8.37	b.d	1.93	85.03	15.63
SHS_BM_014	C.E.	k	0.370	3.10	b.d	2.74	4.70	22.18	8.48	1.29	5.10	3292	2.96	0.79	86.8	0.37	66.61	24.31
SHS_BM_014B	C.E.	k	0.460	2.92	0.99	2.11	3.68	47.05	4.74	0.77	6.65	1842	4.24	0.71	367.2	6.19	59.33	28.12
SHS_CM_019	C.I.	k	b.d	0.26	b.d	0.12	0.35	2.64	0.38	0.08	6.21	3244	2.62	0.90	72.9	b.d	58.11	

			Re	Os	W	Ir	Ru	Mo	Pt	Rh	Ni	Co	Pd	Au	Cu	Ga	Ge	Ge/Ir
			ppm	ppm	ppm	ppm	ppm	ppm	ppm	ppm	%	ppm	ppm	ppm	ppm	ppm	ppm	
SHS_CM_018	C.I.	t	0.210	0.87	0.13	1.28	1.79	13.26	3.28	0.46	9.82	2131	2.87	0.69	211.0	0.14	1.77	1.38
mean metal			**0.383**	**3.36**	**0.50**	**2.80**	**5.35**	**18.73**	**8.02**	**1.23**	**6.87**	**3675**	**4.57**	**0.96**	**124.1**	**4.01**	**62.06**	
1SD			**0.272**	**4.24**	**0.33**	**3.11**	**5.65**	**18.10**	**6.75**	**0.83**	**3.51**	**790**	**6.88**	**1.62**	**73.7**	**8.98**	**17.12**	
ShS_HS_001	M	s	0.008	0.06	b.d	0.03	0.04	2.66	0.08	0.02	0.09	92	0.07	0.01	70.1	4.42	1.92	58.72
SHS_BS_014	C.E.	s	0.160	2.40	1.42	1.83	3.34	34.24	3.03	0.42	2.46	902	1.87	0.48	336.7	4.69	15.94	8.71
SHS_BS_015	C.E.	s	0.031	0.04	0.29	0.04	0.71	17.73	0.14	0.15	1.99	130	1.15	0.22	153.2	2.74	18.08	488.6
SHS_HS_012	M	s	b.d	b.d	0.57	b.d	b.d	54.50	b.d	1.51	0.04	1724	2.63	1.00	b.d	2.50	1.95	
SHS_HS_016	M	s	0.520	4.60	b.d	4.15	9.02	10.59	12.41	1.34	3.34	4946	4.18	0.90	175.9	7.75	37.63	9.07
SHS_HS_017	M	s	0.230	1.88	0.51	1.33	2.11	24.68	3.13	0.48	4.24	1929	1.20	0.18	55.9	0.59	37.61	28.28
mean sufide			**0.190**	**1.80**	**0.70**	**1.48**	**3.04**	**24.07**	**3.76**	**0.65**	**2.03**	**1620**	**1.85**	**0.47**	**158.4**	**3.78**	**18.86**	
1SD			**0.200**	**1.85**	**0.53**	**1.63**	**3.43**	**18.49**	**4.78**	**0.63**	**1.70**	**1802**	**1.42**	**0.40**	**119.4**	**2.45**	**16.04**	
Dhajala	3		b.d	b.d	1.20	b.d	b.d	42.79	b.d	b.d	b.d	b.d	b.d	b.d	b.d	b.d	b.d	b.d
Dh_HM_001	M	k	0.169	2.92	b.d	2.30	3.12	5.24	5.19	1.04	5.98	4263	2.86	0.53	82.7	2.28	54.55	23.72
Dh_HM_003	M	k	0.301	5.12	b.d	3.79	4.32	4.75	6.75	0.91	6.28	4255	3.57	0.82	92.2	1.53	54.53	14.39
Dh_HM_004	M	k	0.298	3.74	b.d	2.17	5.23	5.35	7.93	1.30	6.04	4253	3.43	0.68	80.6	1.33	52.84	24.35
DHJ_HM_01	M	k	b.d	0.47	2.06	0.81	4.03	319.1	3.57	1.29	2.96	2351	3.30	0.75	62.8	1.14	65.67	81.07
DHJ_HM_020	M	k	2.780	4.93	0.99	7.20	8.95	15.54	22.37	2.12	2.94	3260	2.35	0.49	44.5	6.03	82.26	11.43
DHJ_HM_021	M	k	3.030	6.93	1.20	7.38	3.88	12.50	16.75	1.20	5.25	4147	2.95	0.44	63.5	1.28	59.72	8.09
DHJ_HM_022	M	k	1.470	3.63	0.92	4.48	3.77	8.37	9.97	0.86	5.80	4203	2.71	0.67	82.7	1.31	57.41	12.81
DHJ_HM_023	M	k	1.490	2.47	0.74	2.78	4.62	9.81	8.29	1.59	5.98	4283	3.57	0.72	81.4	1.14	56.77	20.42
DHJ_HM_025	M	k	1.070	1.96	0.71	2.55	4.90	10.88	6.79	1.02	5.95	4188	3.06	0.59	87.5	1.70	55.71	21.85
DHJ_HM_026	M	k	2.890	1.60	1.12	2.33	4.16	9.36	6.51	0.86	5.18	4457	2.53	0.62	53.7	0.95	61.73	26.49
DHJ_HM_027	M	k	0.700	1.01	0.45	1.83	2.22	8.51	4.51	0.82	6.32	4274	3.87	0.55	89.8	2.84	54.20	29.62
DHJ_HM_028	M	k	b.d	1.22	0.62	1.59	3.05	4.58	5.50	0.89	4.20	3625	1.96	0.50	56.7	1.31	62.55	39.34
DHJ_HM_029	M	k	1.420	1.69	0.40	2.40	2.99	13.11	4.91	0.48	2.75	1492	2.34	0.50	54.8	3.18	71.88	29.95
DHJ_HM_024	M	t	0.230	0.38	0.14	0.40	0.63	2.54	0.85	0.23	31.73	248	3.33	0.39	193.1	1.08	18.78	46.95
DHJ_BM_01	C.E.	k	b.d	0.67	0.39	1.37	5.94	13.90	8.86	1.30	4.80	3453	2.32	0.52	79.1	1.91	63.24	46.16
DHJ_CM_030	C.I.	k	b.d	0.37	3.48	1.35	2.18	b.d	0.43	b.d	5.53	3544	0.48	0.22	68.6	13.88	53.92	39.94

			Re	Os	W	Ir	Ru	Mo	Pt	Rh	Ni	Co	Pd	Au	Cu	Ga	Ge	Ge/Ir
			ppm	ppm	ppm	ppm	ppm	ppm	ppm	ppm	%	ppm	ppm	ppm	ppm	ppm	ppm	
mean metal			**1.321**	**2.44**	**1.02**	**2.80**	**4.00**	**29.57**	**7.45**	**1.06**	**6.73**	**3519**	**2.79**	**0.56**	**79.6**	**2.68**	**57.86**	
1SD			**1.091**	**1.96**	**0.89**	**2.02**	**1.86**	**77.83**	**5.49**	**0.51**	**6.78**	**1190**	**0.82**	**0.15**	**33.6**	**3.24**	**12.99**	
DHJ_HS_002	M	s	b.d	0.18	b.d	0.06	0.05	2.12	0.15	b.d	0.14	3	0.11	b.d	28.4	0.31	2.53	
DHJ_HS_01	M	s	0.090	b.d	0.06	b.d	b.d	2.31	b.d	0.02	0.11	5	0.05	b.d	39.5	0.11	2.82	
DHJ_HS_021	M	s	0.100	0.01	0.13	0.04	0.02	4.87	0.18	0.01	0.11	95	0.02	0.02	9.1	1.38	2.21	52.62
DHJ_HS_024	M	s	0.049	0.06	b.d	0.05	0.10	1.90	0.21	0.02	0.91	18	0.43	0.09	314.5	0.44	6.68	126.0
DHJ_HS_026	M	s	b.d	0.02	b.d	0.03	0.05	2.49	0.03	0.01	0.06	31	b.d	b.d	5.1	0.04	2.23	65.59
DHJ_HS_026B	M	s	b.d	0.26	0.16	0.23	0.38	2.64	0.50	0.06	0.31	171	0.14	b.d	20.8	1.50	6.99	30.39
DHJ_HS_028	M	s	0.090	0.05	0.05	0.09	0.16	3.72	0.20	0.03	0.11	125	0.03	b.d	4.0	b.d	3.62	40.22
DHJ_HS_029	M	s	0.033	0.02	0.07	0.04	b.d	2.36	0.02	0.01	0.01	2	b.d	0.01	8.5	0.35	1.21	34.57
mean sufide			**0.072**	**0.09**	**0.09**	**0.08**	**0.13**	**2.80**	**0.18**	**0.02**	**0.22**	**56**	**0.13**	**0.04**	**53.7**	**0.59**	**3.54**	
1SD			**0.044**	**0.09**	**0.06**	**0.07**	**0.13**	**1.00**	**0.16**	**0.02**	**0.29**	**65**	**0.14**	**0.03**	**106.1**	**0.59**	**2.15**	
<u>Ste Marguerite</u>	3																	
Stm_HM_001	M	k	0.363	6.11	b.d	4.94	8.51	6.96	13.03	1.53	9.86	4278	4.96	0.88	317.2	18.68	61.85	12.52
Stm_HM_004	M	k	0.198	3.43	b.d	2.41	3.55	7.40	5.91	0.78	9.97	4328	5.43	0.92	391.8	17.74	59.78	24.80
Stm_HM_010	M	k	2.020	2.63	1.17	2.74	4.46	10.63	7.85	1.12	8.78	2193	4.70	0.70	b.d	16.06	55.20	20.15
Stm_HM_40	M	k	0.396	4.15	b.d	2.98	3.90	8.10	7.38	0.95	9.83	4182	4.37	0.73	390.0	17.62	59.05	19.82
Stm_HM_41	M	k	0.485	5.01	b.d	4.24	5.63	8.59	8.84	1.27	9.76	4347	5.13	0.83	380.3	16.11	60.81	14.34
Stm_HM_42	M	k	0.670	9.30	b.d	6.65	7.76	6.02	9.87	1.01	9.92	4198	5.65	0.98	385.0	17.18	60.21	9.05
Stm_HM_43	M	k	0.740	5.21	b.d	4.50	8.29	7.11	14.46	1.30	8.81	4292	4.38	0.67	288.5	17.08	61.38	13.64
Stm_HM_44	M	k	0.276	5.72	b.d	3.98	5.87	8.34	9.61	1.50	10.39	3754	4.62	1.01	452.7	18.78	51.14	12.85
Stm_HM_45	M	k	0.264	1.57	b.d	0.78	1.35	5.20	9.24	0.77	9.71	4037	3.95	0.67	333.3	16.13	55.23	70.81
Stm_HM_003	M	t	0.320	6.80	b.d	4.37	5.82	7.34	8.22	1.43	14.52	3760	6.93	1.07	1718	20.47	64.45	14.75
mean metal			**0.573**	**4.99**	**1.17**	**3.76**	**5.51**	**7.57**	**9.44**	**1.17**	**10.16**	**3937**	**5.01**	**0.85**	**517.5**	**17.59**	**58.91**	21.27
1SD			**0.538**	**2.21**	**0.37**	**1.61**	**2.28**	**1.49**	**2.57**	**0.28**	**1.61**	**650**	**0.85**	**0.15**	**457.3**	**1.41**	**3.93**	
Stm_HS_010	M	s	0.050	b.d	0.04	3.99	b.d	9.45	b.d	1.88	0.02	6339	13.45	b.d	10972	0.03	1.31	0.33
Stm_HS_001	M	s	0.006	0.02	b.d	0.01	0.05	6.60	0.01	b.d	0.04	33	0.02	0.01	57.8	0.74	1.48	105.4
Stm_HS_003	M	s	b.d	b.d	b.d	b.d	b.d	4.84	b.d	b.d	0.01	21	b.d	b.d	34.9	b.d	1.44	

			Re	Os	W	Ir	Ru	Mo	Pt	Rh	Ni	Co	Pd	Au	Cu	Ga	Ge	Ge/Ir
			ppm	ppm	ppm	ppm	ppm	ppm	ppm	ppm	%	ppm	ppm	ppm	ppm	ppm	ppm	
Stm_HS_004	M	s	b.d	b.d	b.d	b.d	0.01	5.98	b.d	b.d	0.18	35	0.01	b.d	85.3	0.06	1.45	
mean sufide			**0.028**	**0.02**	**0.04**	**2.00**	**0.03**	**6.72**	**0.01**	**1.88**	**0.06**	**1607**	**4.49**	**0.01**	**2787**	**0.27**	**1.42**	
1SD			**0.024**	**0.01**	**0.02**	**1.99**	**0.02**	**1.96**	**0.01**	**0.94**	**0.08**	**3154**	**6.72**	**-**	**5456**	**0.35**	**0.07**	
Allegan	4																	
Al_HM_002	M	k	0.200	5.38	b.d	3.78	4.52	4.29	6.97	0.78	5.37	3595	3.01	0.51	80.4	8.33	46.39	12.27
Al_HM_003	M	k	0.075	1.02	b.d	0.67	1.46	5.28	2.06	0.34	5.61	3813	1.90	0.61	85.4	8.69	48.27	71.62
Al_HM_41	M	k	0.099	1.81	b.d	0.98	1.93	6.63	2.88	0.33	5.72	3790	2.69	0.51	92.1	9.03	43.43	44.32
Al_HM_45	M	k	0.157	1.51	b.d	1.13	2.06	5.16	3.47	0.41	5.94	3693	2.38	0.54	83.8	8.93	47.71	42.22
Alg-mm-b-1	M	k	3.650	1.08	1.72	1.21	2.23	3.27	2.95	0.55	6.90	10257	2.60	0.54	49.9	18.26	121.8	100.7
Alg-mm-b-3	M	k	1.670	0.99	1.65	1.11	2.49	4.74	2.85	0.48	7.35	9929	1.98	0.59	61.0	21.64	121.8	109.7
Alg-mm-b-5	M	k	2.100	1.30	1.30	1.46	2.56	3.62	3.90	0.71	7.39	10389	2.61	0.63	57.4	20.99	125.6	86.03
Al_HM_46	M	t	2.380	22.42	b.d	18.02	21.65	7.73	47.09	2.99	40.88	1485	22.59	2.11	5329	58.17	122.4	6.79
Al_HM_001	M	t	0.590	2.06	b.d	1.43	2.73	7.67	2.85	0.60	30.67	1418	2.72	0.26	1705	52.18	94.33	65.97
Al_HM_42	M	t	1.130	16.64	b.d	14.85	28.55	13.62	34.59	7.41	33.22	1498	17.73	1.99	1504	39.67	88.10	5.93
Al_HM_44	M	t	0.940	12.84	b.d	10.04	22.61	5.40	30.07	5.49	31.76	1530	16.43	1.73	1496	28.49	74.39	7.41
Alg-mm-m-2	M	t	1.880	1.34	0.34	1.37	2.86	1.67	3.51	0.56	37.89	824	2.51	0.36	177.8	15.93	39.22	28.54
Alg-mm-m-4	M	t	3.370	0.91	0.34	0.94	2.54	1.54	4.12	0.57	42.16	674	3.50	0.49	200.9	19.09	43.02	45.72
Al_CM_40	C.I.	k	b.d	b.d	b.d	b.d	b.d	b.d	7.40	b.d	9.11	3813	1.64	0.13	631.3	7.51	b.d	
Al_CM_43	C.I.	k	3.530	78.88	b.d	61.40	74.66	13.01	117	18.19	5.20	2189	2.58	0.15	578.8	13.91	22.44	0.37
Al_CM_47	C.I.	k	b.d	b.d	b.d	b.d	b.d	b.d	b.d	b.d	3.17	1398	b.d	b.d	172.5	8.61	b.d	
Al_CM_48	C.I.	k	b.d	b.d	b.d	b.d	b.d	b.d	b.d	b.d	1.69	898	b.d	b.d	80.3	9.24	b.d	
mean metal			**1.555**	**10.58**	**1.07**	**8.46**	**12.35**	**5.97**	**18.11**	**2.81**	**16.47**	**3600**	**5.79**	**0.74**	**728.5**	**20.51**	**74.21**	
1SD			**1.329**	**19.24**	**0.61**	**15.04**	**18.84**	**4.03**	**29.43**	**4.59**	**15.27**	**3344**	**6.75**	**0.65**	**1315**	**15.65**	**44.49**	
Al_HS_001	M	s	0.012	0.13	b.d	0.11	0.07	0.61	0.18	0.04	0.20	11	0.16	0.02	33.3	0.51	2.03	18.45
Al_HS_002	M	s	b.d	b.d	b.d	b.d	0.01	0.60	0.01	b.d	0.01	11	0.01	b.d	26.8	0.18	2.93	
Al_HS_003	M	s	b.d	b.d	b.d	b.d	0.01	1.00	b.d	0.01	b.d	6	b.d	b.d	34.6	0.49	1.40	
mean sufide			**0.012**	**0.13**	**b.d**	**0.11**	**0.03**	**0.74**	**0.09**	**0.02**	**0.10**	**9**	**0.08**	**0.02**	**31.6**	**0.39**	**2.12**	
1SD			**0.007**	**0.08**	**-**	**0.06**	**0.04**	**0.23**	**0.10**	**0.02**	**0.11**	**3**	**0.09**	**0.01**	**4.2**	**0.19**	**0.77**	

			Re	Os	W	Ir	Ru	Mo	Pt	Rh	Ni	Co	Pd	Au	Cu	Ga	Ge	Ge/Ir
			ppm	ppm	ppm	ppm	ppm	ppm	ppm	ppm	%	ppm	ppm	ppm	ppm	ppm	ppm	
Guarena	5																	
Gn_HM_003	M	k	0.480	2.56	0.96	2.59	1.93	3.45	5.34	1.01	5.90	4511	2.43	0.74	75.2	11.23	46.52	17.96
Gn_HM_40	M	k	0.222	3.69	b.d	3.36	6.18	5.37	8.06	1.32	6.40	4381	2.17	0.38	71.7	9.65	22.48	6.69
Gn_HM_42	M	k	0.239	3.89	b.d	4.11	3.16	2.58	9.00	1.10	4.84	4331	1.56	0.39	69.4	9.44	48.34	11.76
Gn_HM_43	M	k	0.179	5.61	b.d	3.82	3.66	5.40	7.13	1.21	6.01	4419	2.44	0.68	75.6	11.20	59.49	15.57
Gn_HM_44	M	k	0.025	3.92	b.d	3.36	4.29	4.67	6.71	1.23	6.25	4453	3.43	0.61	85.0	10.25	50.20	14.94
Gn_HM_001	M	t	0.640	7.73	0.59	5.28	11.64	11.42	12.09	2.22	38.33	1728	20.33	2.36	646.7	38.00	83.37	15.79
Gn_HM_002	M	t	0.180	5.43	1.07	5.06	10.67	10.12	12.98	2.26	43.18	1697	22.96	1.92	297.8	46.49	104.6	20.68
Gn_HM_41	M	t	0.560	8.98	b.d	6.51	17.48	10.90	16.62	2.72	39.18	1643	21.16	2.02	1811	46.19	78.90	12.12
Gn_HM_42B	M	t	0.320	8.11	b.d	7.09	23.48	11.00	20.34	2.36	61.55	1455	34.63	6.81	3535	105.4	203.1	28.64
Gn_CM_002	C.I.	k	0.370	2.37	0.69	2.61	2.65	1.41	6.07	0.95	5.58	4511	2.65	0.50	113.5	8.12	50.19	19.23
Gn_CM_003	C.I.	k	0.310	3.95	1.03	3.12	5.03	6.21	7.44	1.07	5.65	4412	2.29	0.48	67.3	8.39	54.17	17.36
Gn_CM_45	C.I.	k	0.118	1.00	b.d	1.52	2.34	b.d	5.49	0.92	5.04	4387	0.64	0.08	47.2	17.04	50.85	33.45
Gn_CM_47	C.I.	k	b.d	5.65	b.d	3.14	1.72	b.d	5.76	1.28	5.11	3907	1.84	0.24	166.0	13.81	56.69	18.05
Gn_CM_001	C.I.	t	0.290	5.45	0.78	3.65	13.81	8.95	10.92	2.01	46.36	1511	24.06	4.29	340.9	66.43	153.8	42.15
Gn_CM_46	C.I.	t	0.390	4.90	b.d	5.24	4.59	0.94	10.45	1.23	10.37	4362	6.49	0.73	200.5	17.08	61.94	11.82
mean metal			**0.309**	**4.88**	**0.85**	**4.03**	**7.51**	**6.34**	**9.63**	**1.53**	**19.32**	**3447**	**9.94**	**1.48**	**506.9**	**27.91**	**74.98**	b.d
1SD			**0.182**	**2.20**	**0.45**	**1.53**	**6.53**	**4.14**	**4.38**	**0.60**	**20.01**	**1356**	**11.26**	**1.85**	**951.1**	**28.05**	**46.95**	**b.d**
Gn_HS_001	M	s	0.020	b.d	b.d	0.02	b.d	0.35	b.d	b.d	0.01	1	b.d	b.d	15.7	b.d	1.00	59.76
Gn_HS_002	M	s	0.036	b.d	0.04	b.d	b.d	0.49	0.03	0.01	0.02	3	0.02	b.d	30.5	0.19	1.13	
Gn_HS_003	M	s	b.d	b.d	b.d	b.d	b.d	0.58	b.d	b.d	0.01	b.d	b.d	b.d	27.9	0.50	0.96	
Gn_CS_001	C.I.	s	b.d	b.d	b.d	b.d	b.d	b.d	b.d	b.d	0.02	3	b.d	b.d	70.3	0.30	1.00	
Gn_CS_002	C.I.	s	0.021	b.d	0.07	b.d	b.d	0.16	0.03	b.d	0.01	2	b.d	b.d	33.7	b.d	1.19	
mean sufide			**0.026**	**b.d**	**0.05**	**0.02**	**b.d**	**0.40**	**0.03**	**0.01**	**0.01**	**2**	**0.02**	**b.d**	**35.6**	**0.33**	**1.06**	
1SD			**0.015**	**-**	**0.03**	**0.01**	**-**	**0.24**	**0.02**	**-**	**0.01**	**1**	**0.01**	**-**	**20.5**	**0.21**	**0.10**	
Kernouve	6		b.d	b.d	0.91	b.d	b.d	6.74	b.d	b.d	b.d	b.d	b.d	b.d	b.d	b.d	b.d	
Kn_HM_003	M	k	0.200	1.82	0.75	1.73	4.42	4.74	5.31	0.70	6.25	4316	2.94	0.66	52.7	15.06	55.09	31.84
Kn_HM_002	M	t	0.730	4.35	2.18	2.56	6.62	12.58	1151	1.65	43.85	2384	117	6.22	456.6	63.48	90.15	35.21

			Re	Os	W	Ir	Ru	Mo	Pt	Rh	Ni	Co	Pd	Au	Cu	Ga	Ge	Ge/Ir
			ppm	ppm	ppm	ppm	ppm	ppm	ppm	ppm	%	ppm	ppm	ppm	ppm	ppm	ppm	
Kn_CM_001	C.I.	k	3.740	8.15	b.d	2.64	17.62	b.d	7.8	2.01	2.38	523	4.60	2.41	411.7	14.54	b.d	
mean metal			**1.557**	**4.77**	**1.47**	**2.31**	**9.55**	**8.66**	**388.2**	**1.45**	**17.49**	**2408**	**41.61**	**3.10**	**307.0**	**31.03**	**72.62**	
1SD			**1.909**	**3.19**	**1.11**	**0.50**	**7.07**	**6.35**	**661.0**	**0.68**	**22.90**	**1897**	**65.54**	**2.84**	**221.3**	**28.11**	**45.44**	
Kn_HS_001	M	s	b.d	0.10	0.08	b.d	b.d	1.15	0.13	0.01	0.37	14	0.08	b.d	51.1	0.22	2.24	
Kn_HS_002	M	s	0.048	0.03	b.d	b.d	b.d	0.53	b.d	b.d	0.03	4	b.d	b.d	13.5	0.09	1.02	
mean sufide			**0.048**	**0.06**	**0.08**	**b.d**	**b.d**	**0.84**	**0.13**	**0.01**	**0.20**	**9**	**0.08**	**b.d**	**32.3**	**0.15**	**1.63**	
1SD			**0.034**	**0.05**	**0.06**	**-**	**-**	**0.44**	**0.09**	**0.01**	**0.24**	**7**	**0.06**	**-**	**26.6**	**0.10**	**0.86**	
Portales Valley	6																	
PV_M_001a	V	k	0.360	3.40	0.81	3.03	3.70	4.03	6.75	1.00	5.72	4895	3.27	0.60	171.3	16.91	60.33	19.91
PV_M_001b	V	k	0.390	3.58	0.82	3.11	3.59	4.98	6.46	0.92	5.88	5036	3.26	0.75	190.6	16.42	61.49	19.77
PV_M_001c	V	k	0.440	3.49	1.05	3.09	3.89	4.38	6.42	1.00	6.08	5142	3.56	0.74	192.7	16.92	62.31	20.17
PV_M_003	V	k	0.270	3.39	0.65	2.83	3.14	3.31	5.93	0.92	5.58	4932	3.11	0.67	157.4	15.96	57.91	20.46
PV_M_004	V	k	0.340	2.89	0.52	2.76	3.37	3.86	5.42	0.87	5.47	4999	3.10	0.56	151.5	15.55	58.55	21.21
PV_M_005	V	k	0.310	3.08	0.78	2.25	2.77	3.70	5.06	0.84	5.39	5070	2.33	0.78	154.9	17.14	60.43	26.86
PV_M_006a	V	k	0.270	3.17	0.88	2.82	3.19	4.28	5.32	0.92	5.64	5020	3.49	0.59	191.8	16.90	61.97	21.98
PV_M_006b	V	k	0.340	2.96	1.00	2.69	3.57	4.07	5.67	0.97	5.75	5078	3.62	0.64	209.1	15.89	62.75	23.33
PV_M_006C	V	k	0.260	3.26	0.84	2.61	3.55	4.09	5.77	0.84	5.73	5032	2.77	0.70	210.4	16.29	61.54	23.58
PV_M_006d	V	k	0.310	3.45	0.72	2.81	3.35	4.07	5.24	0.85	5.71	4999	3.39	0.61	199.9	16.68	59.86	21.30
PV_M_006e	V	k	0.350	3.39	1.07	2.64	3.31	4.01	5.83	0.88	5.46	5042	3.02	0.71	164.0	15.79	61.72	23.38
PV_M_007a	V	k	0.330	2.69	0.87	2.71	3.58	4.21	6.04	0.90	5.62	4910	2.82	0.48	192.7	13.12	54.11	19.97
PV_M_008a	V	k	0.350	3.50	0.85	2.67	3.39	4.24	5.45	0.98	5.15	4865	2.09	0.43	152.4	11.45	54.45	20.39
PV_M_008b	V	t	5.320	b.d	b.d	b.d	b.d	b.d	b.d	b.d	19.26	3704	b.d	b.d	865.2	78.90	208.3	
PV_M_008c	V	t	0.760	7.04	1.11	5.50	11.36	8.29	11.83	1.97	25.53	3264	15.34	2.29	516.1	38.14	84.34	15.33
PV_M_007b	V	t	0.500	7.79	0.84	5.82	11.52	9.26	11.38	2.18	29.68	3007	15.29	2.40	514.4	47.79	97.39	16.73
PV_M_002	V	t	0.300	4.48	0.81	3.33	4.91	b.d	8.25	1.25	11.11	4823	4.44	0.76	452.3	17.94	70.92	21.30
mean metal			**0.659**	**3.85**	**0.85**	**3.17**	**4.51**	**4.72**	**6.68**	**1.08**	**9.34**	**4695**	**4.68**	**0.86**	**275.7**	**22.81**	**72.84**	
1SD			**1.207**	**1.69**	**0.25**	**1.24**	**2.87**	**2.23**	**2.58**	**0.47**	**7.73**	**671**	**4.21**	**0.61**	**196.6**	**17.15**	**36.56**	
PV_S_001	V	s	b.d	0.01	b.d	b.d	0.22	4.67	b.d	b.d	b.d	1	b.d	b.d	22.0	0.83	1.01	

			Re	Os	W	Ir	Ru	Mo	Pt	Rh	Ni	Co	Pd	Au	Cu	Ga	Ge	Ge/Ir
			ppm	ppm	ppm	ppm	ppm	ppm	ppm	ppm	%	ppm	ppm	ppm	ppm	ppm	ppm	
PV_S_002	V	s	0.012	b.d	b.d	b.d	0.07	0.84	b.d	b.d	b.d	10	b.d	b.d	30.9	b.d	1.07	
PV_S_003	V	s	b.d	0.02	b.d	b.d	b.d	0.27	b.d	b.d	0.01	18	b.d	0.01	30.9	0.02	0.96	
PV_S_004	V	s	0.024	b.d	0.23	0.01	b.d	1.01	0.07	b.d	0.02	67	0.05	0.02	68.5	0.07	1.03	84.96
mean sufide			**0.018**	**0.02**	**0.23**	**0.01**	**0.14**	**1.70**	**0.07**	**b.d**	**0.02**	**24**	**0.05**	**0.01**	**38.1**	**0.31**	**1.02**	
1SD			**0.011**	**0.01**	**0.11**	**0.01**	**0.10**	**2.01**	**0.04**	**-**	**0.01**	**30**	**0.02**	**0.01**	**20.7**	**0.40**	**0.04**	
Portales Valey Clast	7																	
PVC_M_002	C	k	0.220	2.14	0.57	1.74	2.53	3.10	4.72	0.69	4.29	4079	1.29	0.21	105.2	7.19	37.56	21.59
PVC_M_003	C	k	0.180	1.55	0.27	1.57	2.09	1.58	3.98	0.58	4.47	4355	1.10	0.25	93.7	7.57	39.50	25.16
PVC_M_004	C	t	0.160	1.33	0.32	1.22	5.53	4.90	6.86	1.38	31.09	2100	13.84	0.80	506.1	20.24	38.66	31.69
PVC_M_001	C	t	0.380	2.88	0.70	4.02	18.46	7.84	8.40	2.61	42.11	1866	26.81	2.16	883.1	58.22	65.30	16.24
mean metal			**0.235**	**1.98**	**0.47**	**2.14**	**7.15**	**4.36**	**5.99**	**1.31**	**20.49**	**3100**	**10.76**	**0.86**	**397.0**	**23.31**	**45.26**	
1SD			**0.100**	**0.69**	**0.20**	**1.27**	**7.69**	**2.69**	**2.02**	**0.93**	**19.14**	**1298**	**12.25**	**0.91**	**376.5**	**24.05**	**13.39**	
PVC_S_001	C	s	b.d	b.d	0.03	b.d	0.04	0.63	b.d	b.d	0.08	20	b.d	b.d	26.2	0.46	1.08	
PVC_S_002	C	s	b.d	b.d	0.31	b.d	b.d	2.34	b.d	0.02	0.03	3	b.d	b.d	1473	0.48	1.00	
PVC_S_003	C	s	b.d	b.d	0.03	0.01	b.d	0.36	b.d	0.01	0.16	15	b.d	b.d	47.4	0.03	1.04	86.75
PVC_S_004	C	s	b.d	b.d	0.11	0.01	b.d	0.73	b.d	b.d	0.03	3	b.d	0.01	29.3	b.d	1.11	100.5
mean sufide			**b.d**	**b.d**	**0.12**	**0.01**	**0.04**	**1.02**	**b.d**	**0.01**	**0.07**	**10**	**b.d**	**0.01**	**393.9**	**0.32**	**1.06**	
1SD			**0.000**	**-**	**0.13**	**0.01**	**0.02**	**0.90**	**-**	**0.01**	**0.06**	**9**	**-**	**0.01**	**719.2**	**0.26**	**0.04**	

Chapter 5

Role of oxidizing processes on the evolution of metal

Table of contents

I. Chapter introduction

In the previous chapter we have discussed metal formation during heating events in the solar nebula. One of the major conclusions is that precursors experienced variation of redox conditions at grain scale in the solar nebula, such that the elemental composition of the metal phase can vary from a metal grain to another. Meteorite groups are also subject to oxidizing processes at larger scale (i.e. solar nebula scale). In the protoplanetary disk, variations in oxidation state are mainly the result of the increase of oxygen fugacity in the protoplanetary disk. The oxidation state in the solar nebula is usually expressed in terms of log unit relative to the Iron–Wüstite equilibrium (IW), a negative IW means that the Fe metal is stable while at positive IW oxidized iron is stable. Another way to express the oxidation state is to refer to the C/O ratio. The solar gas is very reduced with an oxidation state of IW-7 or a C/O ratio of 0.5 (Figure 5.1, Cartier and Wood, 2019).

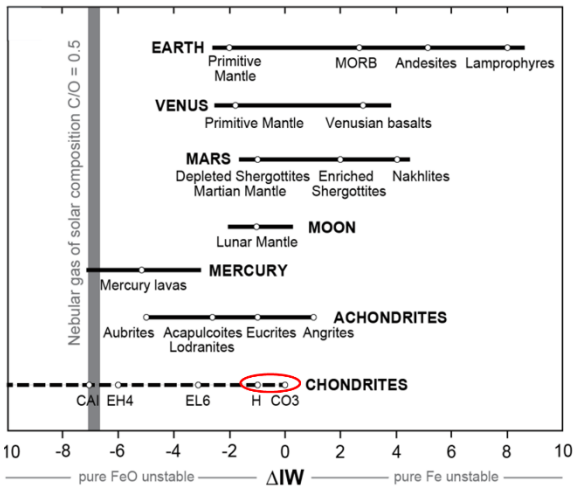

Figure 5.1: Representation of the redox state of planets, achondrites and chondrite in the Solar System as a function of the Iron–Wüstite buffer. The oxidation state of a gas of solar nebula composition is given by the C/O ratio. The red circle represents the ordinary chondrite group. CAI: Calcium–aluminium inclusions, EH: High Enstatite chondrites, EL: Low Enstatite chondrites, H: Reduced ordinary chondrite group, CO: Carbonaceous Ornans–type. The number next to chondrite groups are petrologic groups according to Van Schmus et al. (1967). Diagram from Cartier and Wood (2019)

The heat created by the proto sun divides the disk into two parts (Fig. 5.2), (1) the inner part that is hot and dry, and (2) the outer part which is colder and contains more water. The delimitation between these two parts is named the snow line. This snow line migrates inward with time and the temperature decrease in the inner part of the disk (Desch et al., 2018). This migration has changed the oxidation state of the inner Solar System, which has influenced the formation and the evolution of meteorites. Today, studying the evolution of redox condition in the disk is important to have a better understanding of planetary formation, as the redox condition during the accretion of a celestial object can change the behaviour of the elements and have significant impact on its evolution. As an example, Cartier and Wood (2019) demonstrated that the formation of the Mercury in a highly reduced environment has induced latter the incorporation of large amount of Si in the core and the formation of an intermediate layer of sulfide between the mantle and the core. This specific evolution has drastically changed the surface and the atmosphere composition of the planet emphasizing the importance of the study of early redox condition of material in the Solar System to appreciate Earth evolution.

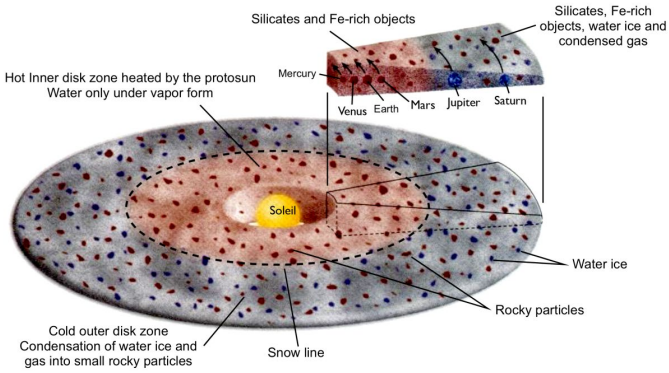

Figure 5.2: Representation of a star surrounded by its accretion disk. The red part represents the hot inner Solar System and the grey part the cold outer Solar System. The snow line is figured by the Dashed line. (Figure reproduced from Vacher, 2018 and modify after Paris Observatory)

These large variations in oxidation state in the Solar System are recorded by meteorite groups through the repartition of redox-sensitive elements between silicate, metal, and sulfide. Multiple buffers able to quantify the oxidation state exist (e.g. Ni/NiO, Ti_3O_5/TiO_2 or Os/OsO_4 etc.). Thus, meteorite oxidation state is well illustrated by the incorporation of iron in olivine as it highlights the progressive oxidation of early-formed enstatite (Mg–olivine) into fayalite (Fe–olivine), leading to the use of percentage of fayalite of olivine (%Fa) as a proxy of the oxidation state of meteorites. The speciation of iron in meteorite groups and then the relative meteorite oxidation state is usually represented in a diagram of $FeS+Fe_{silicate}$ vs Fe_{metal} (Figure 5.3, Urey and Craig 1953). In this diagram, the oxidation state increases from the left to the right while reduction features increase with increasing the percentage of reduced iron in meteorite bulk. According to that, the sequence of ordinary chondrites appears to be the meteorite groups with the largest variation in oxidation state, increasing from H (High total Fe) to L (Low total Fe) to LL (Low total Fe, Low metallic Fe). These variations in oxidation state are also correlated with a decrease in metal content, an increase in volatile elements contents of the metal (Wasson, 2017), and with an enrichment in heavy oxygen isotopes. Thus, the ordinary chondrites are the meteorite group of great interest for the study of oxidation state evolution in the Solar System.

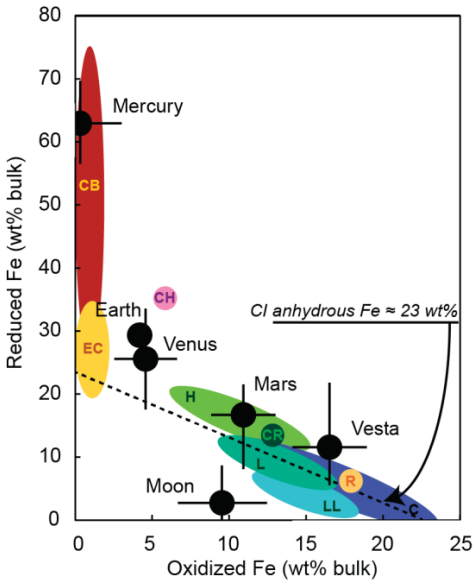

Figure 5.3: Urey–Craig type diagram representing the reduced metal (Fe^0) *versus* the oxidized metal ($FeO + Fe_2O_3 + FeS$) in the bulk of meteorites and planets. H, L, and LL: Ordinary chondrite groups, EC: Enstatite chondrite group. CB: Carbonaceous–Bencubbin type chondrite, CR: Carbonaceous–Renazzo type chondrite, CH: High metal carbonaceous chondrites, C: Other carbonaceous groups, R: Rumuruti chondrites. Diagram from Cartier and Wood (2019).

In this chapter we are exploring the effect of the oxidation state on the evolution of the metal phase from the three ordinary chondrite groups using isotopes. The key element is germanium, being siderophile and strongly fractionated in the metal phase, and sensitive to redox variations. We have measured the germanium isotopes in the bulk, as well as in the metal, silicate and sulfide phases of ordinary chondrites. The results were applied to constrain the metal evolution with oxidation state between ordinary chondrite groups, as well as with petrologic groups on the parent bodies. The results of this study have been published in *Geochimica et Cosmochimica Acta* in 2020.

Goals of this chapter

- Evaluating the germanium isotopic fractionation between metal, silicate and sulfide in primitive ordinary chondrites.
- Characterizing germanium isotopic variations between H, L and L ordinary chondrite groups to constrain their formation.
- Evaluating the correlation between germanium and oxygen isotopes.
- Identifying the causes of oxidation increase through ordinary chondrite sequence.
- Using germanium isotopes as a novel genetic link for OC and IIE meteorite relationship.

II. Article in Geochimica et Cosmochimica Acta

Available online at www.sciencedirect.com

ScienceDirect

Geochimica et Cosmochimica Acta 269 (2020) 270–291

Geochimica et Cosmochimica Acta

www.elsevier.com/locate/gca

Influence of redox processes on the germanium isotopic composition of ordinary chondrites

Guillaume Florin [a,b,*], Béatrice Luais [a], Tracy Rushmer [b], Olivier Alard [b,c]

[a] Centre de Recherches Pétrographiques et Géochimiques, CRPG-CNRS - UMR 7358, Université de Lorraine, 15 Rue Notre Dame des Pauvres, 54500 Vandœuvre-lès-Nancy, France

[b] Department of Earth and Planetary Sciences, Macquarie University, NSW 2109, Australia

[c] Géosciences Montpellier, UMR 5243, CNRS & Université Montpellier, 34095 Montpellier, France

Received 29 May 2019; accepted in revised form 28 October 2019; Available online 6 November 2019

Abstract

Ordinary chondrites (OCs) are classified into three groups, according to their oxidation state, which increases from the H to L to LL groups. This is demonstrated by the decrease in metal content (H = ~8 vol%, L = ~4 vol%, and LL = ~2 vol%), and by a positive correlation between $\Delta^{17}O$ and %Fa through the OC sequence. Compared to other chondrites, OCs exhibit the largest variation in oxidation state, but there is an ongoing debate on the processes that control this variation. To constrain the causes of the variations in the oxidation state with respect to the associated nebular versus parent bodies processes, we investigated the elemental and isotopic variations of germanium (moderately siderophile and volatile) in the bulk sample, as well as in the metal, silicate and sulfide phases, over a range of petrographic types for the H, L, and LL ordinary chondrites.

We found that $\delta^{74/70}Ge_{metal}$ is a proxy for the $\delta^{74/70}Ge_{bulk}$ composition and that each OC group is distinguishable by their $\delta^{74/70}Ge_{metal}$, which increases from -0.51 ± 0.09‰ for H chondrites, -0.31 ± 0.06‰ for L chondrites, and, finally, to -0.26 ± 0.09‰ for LL chondrites (2σ SD). Additionally, the OC sequence exhibited a positive correlation, from H to L to LL, between $\delta^{74/70}Ge_{metal}$ and %Fa, as well as oxygen isotopes ($\delta^{17}O$, $\delta^{18}O$ and $\Delta^{17}O$), that was not a consequence of a "size sorting effect" on chondrules (*i.e.*, chondrule mixing) or metamorphic processes in the parent bodies but, rather, was the result of nebular processes. We propose that the correlation between the $\delta^{74/70}Ge$ values and %Fa, $\Delta^{17}O$, $\delta^{18}O$ can be explained by an increasing proportion of accreted hydrated phyllosilicates, from the H, L to LL groups, with high $\delta^{74/70}Ge$ and $\Delta^{17}O$. We found that 10 to 15% of phyllosilicates, with a composition of [Ge] = 4–7 ppm and $\delta^{74/70}Ge$ = 3–2.5‰, is needed to change the $\delta^{74/70}Ge$ from H to LL, which corresponds to a $\Delta^{17}O \approx 8$–7‰. This value agrees with the $\Delta^{17}O \approx 7$‰ composition of the accreted nebular component reported by Choi et al. (1998). During thermal metamorphism, phyllosilicates destabilize, liberating germanium that will be incorporated in the metal, then leading to its high $\delta^{74/70}Ge$ signature.

High-temperature metamorphism can explain the lack of $\delta^{74/70}Ge_{metal}$ variation with the petrologic type in the OC, even for the type 3 chondrites (T ≈ 675 °C), implying a complete reaction even at low petrologic types. In addition, metal-silicate re-equilibration in response to thermal metamorphism results in a decrease in $\Delta^{74/70}Ge_{metal\text{-}silicate}$ from 0.33‰ to 0.06‰, within the H chondrite group, which is interpreted as the result of $\delta^{74/70}Ge_{silicate}$ variation. The mean positive $\Delta^{74/70}Ge_{metal\text{-}silicate}$ fractionation factor of $+0.22 \pm 0.36$‰ (error propagation on individual error) also displays a remarkable similarity to the direction of isotopic fractionation with other germanium isotopic metal-silicate datasets, such as the magmatic iron meteorites, the Earth silicate reservoirs. We propose that the $\Delta^{74/70}Ge_{metal\text{-}silicate}$ and the negative $\delta^{74/70}Ge$ values of OCs are inherited from metal-silicate melting and partial exchange before planetesimal accretion in a light isotope-enriched gas. Finally, the

* Corresponding author.
E-mail address: guillaume.florin@univ-lorraine.fr (G. Florin).

https://doi.org/10.1016/j.gca.2019.10.038

$\delta^{74/70}Ge_{metal}$-$\Delta^{17}O_{silicate}$ correlation between the IIE iron meteorites and OCs, provides new evidence for the existence of a highly reduced HH group.

Keywords: Germanium isotopes; Ordinary chondrite; Oxidation state; Nebular processes; Thermal metamorphism; HH chondrites; Oxygen isotopes; IIE iron meteorites

1. INTRODUCTION

Ordinary chondrites (OCs) are undifferentiated meteorites that formed in the first 1–3 Myr after the formation of refractory Calcium-Aluminium Inclusions (CAIs) (Kleine et al., 2008; Archer et al., 2019; Hellmann et al., 2019), as well as during a short accretion time interval of less than 0.5 Myr (Monnereau et al., 2013). OCs also postdate magmatic iron meteorite formation. Several studies argue for their formation via the disruption-re-accretion of early-differentiated planetesimals (Elkins-Tanton et al., 2011; Lichtenberg et al., 2018). As a result, OCs should represent a record between the early formed planetesimals and terrestrial planets as we know them today.

Ordinary chondrites are composed of an assemblage of chondrules and matrix, which contain silicates, FeNi alloys, sulfides, and rare CAIs. The OC sequence has been classified into three groups, *i.e.*, H (High metallic Fe content), L (low metallic Fe content) and LL (low total Fe and low metallic Fe content), according to the oxidized iron content relative to the metal iron (Urey and Craig, 1953), oxygen isotopic composition (Clayton et al., 1991), bulk volatile elemental concentration, including water, and chondrule size (Wasson, 1972; Chou and Cohen, 1973; Chou et al., 1973; Kallemeyn et al., 1989; Wasson, 2000; Rubin, 2005). Each chondrite group is thought to originate from at least one parent body and are subdivided into petrologic types, from the least metamorphosed and unequilibrated (group 3) to the most metamorphosed and highly equilibrated (group 6; Van Schmus and Wood, 1967). Studies on OC ages, cooling times, and petrographic types led to the "onion-shell" model in which thermal metamorphism increases with planetesimal depth (Göpel et al., 1994). With increasing petrographic type, the temperature (Tait et al., 2014) and oxidation state increase (Chou and Cohen, 1973; Chou et al., 1973; Rubin, 2005), metallic iron content decreases, and metal becomes more equilibrated with silicate through oxidation reactions (McSween and Labotka, 1993). Moreover, as thermal metamorphism increases, the metal grain-size, as well as the grain circularity, increase, which define additional parameters for characterizing the petrologic types (Guignard and Toplis, 2015).

The percentage of fayalite in olivine (%Fa) is commonly used as a redox proxy (Chou et al., 1973; Rubin, 2005). Clayton et al. (1991) first showed that there was an increase in the oxygen isotopic composition from the H to LL groups, which led McSween and Labotka (1993) and Rubin (2005) to demonstrate that there is a positive correlation between %Fa and the oxygen isotopic composition throughout the OC sequence. This implies that variations in $\delta^{18}O$ and $\Delta^{17}O$ are related to the oxidation state. However, the origin of oxidation processes remains highly controversial. Previous studies have argued that this evolution reflects primitive conditions in the solar nebula recorded by planetesimals through progressive accretion of high $\Delta^{17}O$ nebula water hosted in phyllosilicates (*i.e.*, Rubin, 2005). Thermal metamorphism, induced by heat release from the decay of short-lived radioactive elements (^{26}Al), liberates heavy-O water, which produces both an increase in the oxidation state and oxygen isotopic composition. On the other hand, the oxidation state can also be explained by an increase in the proportion of type II chondrules (oxidized) and the decrease of type I chondrules (reduced) from H to LL. Type I is reduced, O^{16}-rich, and contain metallic Fe, whereas type II is oxidized, ^{16}O-depleted, and Fe is present in an oxidized form (Zanda et al., 2006). Chou and Cohen (1973) and Chou et al. (1973) have shown that OCs groups are also resolvable using the siderophile element concentration, *e.g.*, the germanium content in the metal increases from H to LL with the Ni content, as a proxy of the redox state. They proposed that a significant proportion of Ge condenses in the silicate at its formation, such that Ge is redistributed between the metal and silicate through oxidation-reduction during metamorphic processes on their parent bodies.

Germanium is a moderately siderophile and volatile element ($T_{50\%\ cond} = 883$ K at $pH_2O/pH_2 = 4.2 * 10^{-4}$ atm; Lodders et al., 2009), commonly used with Ir, Au, and Ni to constrain the formation of iron meteorites and metal phases in chondrites (Wasson, 1974). Experimental studies have shown that Ge partitioning between metal and silicate phases is strongly redox-dependent, with D(Ge) metal-silicate values greater than 10^4 under highly reduced conditions (-2.7 log fO_2 relative to the IW buffer; Kegler and Holzheid, 2011). Germanium is also a chalcophile element but the amount of Ge in troilite (FeS) from the OCs represents only 3 to 5% (0.3 to 0.5 ppm) of the total amount of Ge in OCs (Chou and Cohen, 1973; Wai and Wasson, 1979), whereas it is strongly concentrated, *i.e.*, up to several hundred ppm, in terrestrial low-temperature sulfides (Bernstein, 1985).

Germanium has five stable isotopes, *i.e.*, ^{70}Ge, ^{72}Ge, ^{73}Ge, ^{74}Ge, and ^{76}Ge, with the Ge isotopic composition given as a delta notation: $\delta^{74/70}Ge = ((^{74}Ge/^{70}Ge_{Sample}/^{74}Ge/^{70}Ge_{Standard}) - 1) \times 1000$. To date, previous studies have analyzed the germanium isotopic composition of differentiated bodies that experienced metal-silicate segregation to investigate the conditions and processes of planetary differentiation. Magmatic iron meteorites that represent planetesimal cores display positive and heavier Ge isotopic compositions than the Earth's mantle and crust (Luais, 2007; Luais, 2012). The Ge isotopic composition of the

Earth's silicate reservoir is, thus far, homogeneous and has not been significantly modified by complex crust–mantle exchange via fluids in subduction zones (El Korh et al., 2017). The volatile behavior of germanium can also be responsible for large Ge isotopic fractionations that occur in IIE non-magmatic iron meteorites (Luais, 2007), which form due to metal segregation following impact-driven melting at the sub-surface of their parental bodies (Wasson and Wang, 1986; Wasson, 2017). To date, the only constituents that display strong negative $\delta^{74/70}$Ge values are schreibersite (Fe-Ni-P) inclusions in iron meteorites (Rouxel and Luais, 2017) and low-temperature terrestrial Zn-sulfides (Belissont et al., 2014). Metal-silicate segregation, volatility, and phosphide/sulfide exsolution/crystallization are the main processes, currently known, that strongly fractionate germanium and its isotopes.

Germanium isotopes represent potential tools to investigate processes of formation and evolution of ordinary chondrites (1) during condensation of metal-silicate-sulfide from the solar nebula (Sears, 1978; Wai and Wasson, 1979), (2) by inheritance from previously destroyed planetesimals (Lichtenberg et al. (2018)), and (3) metal-silicate equilibrium fractionation on parent bodies following a major impact (Tomkins et al., 2013) or after metamorphism (Humayun and Campbell, 2002; Guignard and Toplis, 2015). In addition, ordinary chondrites provide a suitable environment to explore the relationships between Ge and O isotopes, as well as the redox conditions. The combined use of these data can establish constraints on the environment in which OCs form and the processes that lead to metal-silicate fractionation and equilibration. Germanium isotopic measurements on separated phases from unequilibrated and equilibrated OCs are used to evaluate the effect that metamorphism has on metal-silicate isotope fractionation. Clayton et al. (1991) first proposed the genetic association between ordinary chondrites and IIE iron meteorites based on their oxygen isotopic compositions in silicate clasts. The IIE–OCs relationship has been further constrained with Mo isotopic anomalies (Burkhardt et al., 2011; Budde et al., 2016). Here, based on the Ge isotopic composition in the metal phase, we examine a new genetic link between IIE iron meteorites and H OCs.

2. SAMPLES AND METHODS

2.1. Sample selection

To constrain the metamorphic and shock effects on Ge systematics, sixteen OCs (eight H, six L, and two LL) were selected to represent all petrologic types (Van Schmus and Wood, 1967) and various shock stages as defined by Stöffler et al. (1991). In addition, two samples were specifically selected to assess the effect of shock: Rose City, an impact melt breccia, and Portales Valley, a low shock meteorite with large metal veins as an example of metal migration (Ruzicka et al., 2005). Table 1 summarizes the sample characteristics.

2.2. Analytical procedures

2.2.1. Sample preparation

Approximately 500 mg of initial bulk meteorite material was cleaned with 0.2 M HNO_3 under cold ultrasonic agitation for 5 minutes. The acid was removed, the samples were rinsed with pure water under ultrasonic agitation and then rinsed with acetone to avoid metal oxidation. Afterward, 300 mg of the meteorite sample was gently powdered in an agate mortar for bulk elemental and isotopic measurements.

Metal and sulfide separation. The remaining 200 mg of clean sample was gently crushed in an agate mortar. FeNi

Table 1
The H, L, and LL ordinary chondrites analyzed in this study, with their petrologic types and shock stages. All meteorites are falls.

Samples	Sample N° (Sources)	Petrologic types	Shock stage and references
Sharps (Shs)	USNM 640 (SI)	H3.4	S3 (*1*)
Dhajala (Dhj)	USNM 5832 (SI)	H3.8	S1 (*1*)
St Marguerite (StM)	MNHN 3290 (MNHN-Paris)	H4	S2 (*2*)
Allegan (Alg)	USNM 215 (SI)	H5	S1 (*2*)
Rose city (RC)	USNM 6771 (SI)	H5 IB	S6 (*1*)
Guarena (Gn)	(MNCN)	H6	S1 (*3*)
Kernouvé (Kn)	(SI)	H6	S1 (*3*)
Portales Valley (PV)	USNM 6975 (SI)	H6	S1 (*3*)
Herdjaz (Hdj)	MNHN 2132 (MNHN-Paris)	L3.7	S4 (*2*)
Björbole (Bjb)	USNM 6705 (SI)	L4	S1 (*5*)
Tourine la Grosse (TlG)	MNHN 191 (MNHN-Paris)	L6	S3 (*5*)
Alfianello (Alf)	MNHN 885 (MNHN-Paris)	L6	S5 (*2*)
Vouillé (Vll)	MNHN 148 (MNHN-Paris)	L6	S5 (*4*)
Granes (Grn)	MNHN 2852 (MNHN-Paris)	L6	NA
Parnalle (Pr)	USNM 1613 (SI)	LL3.6	
NWA 118 (N118)	Private collection	LL6	S3 (*7*)

[1]: Stöffler et al. (1991); [2]: Rubin (1994); [3]: Reisener And Goldstein (2003); [4]: Rubin (2003); [5]: Dodd and Jarosewich (1979); [6]: Bennett and McSween (1996); [7]: Grossman and Zipfel (2001).
Abbreviations: MNCN, Museo Nacional de Ciencias Naturales, Madrid; MNHN, Muséum National d'Histoire Naturelle, Paris; SI, Smithsonian; USNM, United States National Museum, Washington; IB, Impact Breccia.

metal was removed from the crushed sample with a hand-magnet. The magnetic fraction was crushed multiple times in an agate mortar, followed by several minutes of ultrasonic agitation in an acetone medium to remove all silicate particles remaining on the metal surface. A Frantz magnetic separator was used to separate the sulfides from the remaining weakly magnetic powder. Between 10 and 40 mg of metal and 10 to 20 mg of sulfide were separated using these procedures.

Silicate separation. The crushed non-magnetic sample fraction that mostly contained impure silicates was gently grounded in an agate mortar to a fine powder. To remove the non-magnetic sulfides and small metal particles stuck on the silicates, two successive cleanings with 6 M HCl and 2 M HNO_3 were performed for 5 minutes under ultrasonic agitation at room temperature. As Ge is highly volatile when associated with HCl at a high temperature ($T > 60$ °C), this protocol was first tested on San Carlos olivine samples to evaluate Ge loss. Uncleaned olivines have $[Ge] = 0.89 \pm 0.02$ ppm and $\delta^{74/70}Ge = 0.70 \pm 0.08$‰ while clean olivines have $[Ge] = 0.90 \pm 0.02$ ppm and $\delta^{74/70}Ge = 0.71 \pm 0.09$‰ (Table 2), which demonstrates that there was no Ge loss nor isotopic fractionation during cold HCl leaching. This step is important because metallic phases are at least one hundred times more concentrated in germanium than silicates or sulfides (Chou and Cohen, 1973). The presence of small metal particles on the silicate surface would have introduced a bias on the elemental and isotopic compositions of Ge in silicates.

Chondrule separation. Separation was only performed on Dhajala (H3.8). A total of 1 g of Dhajala was cleaned and gently crushed in an agate mortar to preserve the chondrules. Unbroken chondrules were separated by hand-picking and sieved into two fractions, *i.e.*, 100–300 µm and > 300 µm, with a recovery of 9.1 and 130.5 mg, respectively.

All fractions were later checked and purified by hand-picking under a binocular microscope, successively cleaned with diluted HNO_3, distilled H_2O, and acetone under cold ultrasonic agitation, and dried under a laminar flow hood.

2.2.2. Sample digestion and chemical purification of germanium

The germanium chemistry analytical procedures for metal, sulfide, and silicate phases follow those described in Luais (2007, 2012, references therein) and Belissont et al. (2014). Samples were dissolved in Teflon beakers on a hotplate in concentrated HF-HNO_3 solutions for the silicate and sulfide fractions while metal phases were dissolved in an HNO_3-only solution. Bulk samples were digested under pressure (25 bar) using Bola Teflon bombs at 150 °C (Luais et al., 2009) for one week in an oven to ensure the dissolution of all phases, including chromite. To ensure that no Ge was lost at high temperatures under pressure, this protocol was tested using a BIR-1 geo-standard. We obtained a $\delta^{74/70}Ge$ of 0.59 ± 0.10‰ for BIR-1 that was digested in the bomb while this was $\delta^{74/70}Ge = 0.59 \pm 0.06$‰ for conventional hotplate BIR-1 dissolution. This demonstrates that there was no isotopic fractionation using this digestion method (Table 2). Germanium purification from silicate and sulfide matrices was completed in two steps using ion exchange resins. First, anionic resin (AG1-X8 resin chloride form, 200–400 mesh, Biorad, Hercules, CA, U.S.A.) allowed us to eliminate most elements (*i.e.*, the alkalis, Mn, Al, Co, Ni, Zn, Ga, and most Fe) using 1 M HF. Germanium (±Fe, Mg) was eluted with 0.2 M HNO_3. Germanium purification from Fe and the remaining matrix was performed solely using cation exchange resin (AG 50W-X8, Biorad, 159 Hercules, CA, U.S.A.) and 0.5 M HNO_3. Germanium isolation from the Fe-Ni matrix of the metal phase was performed only using the cation exchange resin step. These two procedures had a germanium yield of 100% within error (Luais, 2007; Luais, 2012). All acids used for digestion and germanium chemical separation were high-purity grade SeaStar® reagents.

2.2.3. Elemental measurements

Bulk powder samples and metal phase separates from H OCs, and metal from L samples were analyzed for major and trace elemental compositions including Ge at the SARM analytical facility (Service Analytique des Roches

Table 2
The Ge isotopic compositions of standards and geostandards, cleaning tests on San Carlos olivines for silicate purification, and BIR-1 digestion in Bola Teflon bombs at 150 °C and 25 bar. Germanium concentrations were measured using an ICP-MS *X-Series* at CRPG, with a precision of less than 2%. n is the number of replicates.

	Ge ppm	$\delta^{72/70}Ge$‰	± 2σ SD	$\delta^{73/70}Ge$‰	± 2σ SD	$\delta^{74/70}Ge$‰	± 2σ SD	n
In-house standard								
Magura (IAB iron)	427[(1)]	0.42	0.06	0.58	0.11	0.78	0.08	19
Standard solutions								
JMC-Ge		−0.15	0.08	−0.19	0.13	−0.32	0.11	95
Aldrich-Ge		−1.01	0.07	−1.52	0.13	−1.97	0.12	99
Geostandards								
BIR-1								
- Hotplate digestion	1.52[(2)]	0.32	0.04	0.42	0.07	0.59	0.06	7
- Bomb digestion	1.50	0.31	0.05	0.42	0.14	0.59	0.01	3
San Carlos Olivines								
- Un-cleaned	0.89	0.35	0.04	0.48	0.08	0.70	0.08	3
- Cleaned	0.90	0.36	0.03	0.47	0.14	0.71	0.09	3

[(1)] Value from Luais (2007). [(2)] Value from Luais (2012).

et des Minéraux, CRPG-Nancy) using a *ThermoFischer* ICP-MS *X7*. Errors associated with the Ge, Ni and Co measurement were <5% for our sample concentrations. The separated mass of pure sulfides was low (*i.e.*, approximately 10–20 mg) due to their low occurrence in the OCs (~5.7%; Lauretta et al., 1997). Similarly, only 10–40 mg of pure silicate separates were obtained. These available low mass fractions rule out the possibility of analyzing them using routine procedures at the SARM. These fractions were analyzed for their Ge elemental compositions using a *ThermoFischer* ICP-MS *X-Series* at CRPG (Nancy, France) with a 2σ SD of 1.2%.

2.2.4. Ge isotopic measurements

Samples in a 0.5 M HNO_3 solution from the cation exchange step were analyzed for their Ge isotopic compositions using a Neptune*Plus* multiple-collector inductively coupled plasma mass spectrometer (MC-ICP-MS) at CRPG coupled with a hydride generator introduction system (HGIS). The HGIS method involves mixing the sample with a high-reducing solution of $NaBH_4$-NaOH. The reactions between these two solutions convert volatile aqueous species ($GeOH_4$) to gaseous ($GeH_{4\ gas}$) hydride species (Dedina and Tsalev, 1995; Abdul-Majeed and Zimmerman, 2012). As the reducing solution is in excess, the reaction yield is 100%. This technique removes isobaric interferences from elements that do not form hydrides, avoiding Zn, NiO, and FeO interferences, as well as matrix effects. The result is a gain in signal sensitivity of at least a factor of 30, required for routine isotopic measurements of 10–20 ng Ge (exceptionally down to 5 ng) to obtain high precision and a good external reproducibility of less than 0.1‰ (2σ SD) (see Rouxel and Luais, 2017 for more details). Data were acquired in static mode using the ^{68}Zn, ^{69}Ga, ^{70}Ge, ^{71}Ga, ^{72}Ge, ^{73}Ge, and ^{74}Ge isotopes that corresponded to the L3, L2, L1, C, H1, H2, and H3 Faraday cups, respectively. We report an intensity of 1.5–2.5 V on ^{74}Ge for a 10 ppb Ge standard solution. Each measurement was composed of a 320 s data acquisition sequence distributed over 40 cycles. Procedural Ge blanks, including chemistry and MC-ICPMS, were better than 70 pg and negligible as this represents less than 0.1% of the 100 ng of Ge processed for each sample. Sample measurements were bracketed using the NIST3120a Ge standard solution. Results are reported in delta (δ) notation using $^{x}Ge/^{70}Ge$ ratios with respect to the mean ratios of the NIST 3120a standard analyzed just before and after the sample (Luais, 2012):

$$\delta^{x/70}Ge_{NIST3120a} = \delta^{x}Ge/^{70}Ge = \left(\frac{(^{x}Ge/^{70}Ge)_{Sample}}{(^{x}Ge/^{70}Ge)_{NIST3120a}} - 1\right) * 1000 \quad (1)$$

JMC and Aldrich germanium standard solutions were analyzed during the course of the study, yielding $\delta^{74/70}Ge = -0.32 \pm 0.11$‰ (n = 95) and $\delta^{74/70}Ge = -1.97 \pm 0.12$‰ (n = 99) (2σ SD), respectively. The BIR-1 basalt geostandard yielded $\delta^{74/70}Ge = 0.63 \pm 0.17$‰ (n = 10) and the in-house IAB Magura iron meteorite (Luais, 2007) had a $\delta^{74/70}Ge$ value of 0.78 ± 0.08‰ (n = 19). These values agree with the references given in Luais (2012) and Escoube et al. (2012).

3. RESULTS

3.1. Elemental composition

The majority of the bulk H OCs displayed a rather uniform Ge concentration, ranging from 10.3 to 22.2 ppm ($[Ge]_{mean} = 15.8 \pm 0.8$ ppm; see Table 3 and Fig. 1) with no variation among the petrologic types, which is in agreement with $[Ge]_{mean} = 12.7 \pm 1.5$ ppm reported in Fouché and Smales (1967), and similar to the value reported for L OCs in Tandon and Wasson (1968). However, Allegan H5 ([Ge] = 22.2 ppm, [Ni] = 1.52 wt.%) and Guareña ([Ge] = 21.4 ppm, [Ni] = 1.59 wt.%) had slightly higher Ge and Ni contents (see Fig. A2 in the Appendix) compared to the OC mean ($[Ge]_{mean} = 15.8 \pm 0.8$ ppm, $[Ni]_{mean} = 1.28 \pm 0.54$ wt.%) and bulk data reported by Wasson and Kallemeyn (1988). For these samples, this may be due to a sampling bias from either a high taenite zone or, although the main mass may appear to be homogeneous, a small-scale heterogeneous repartition of metal that led to the sampling of a metal-rich zone.

Germanium concentrations in metal ranged from 50 to 83.5 ppm for H chondrites, with a mean of 64.6 ± 17.6 ppm (2σ SD), 104.3 to 157.8 ppm for L chondrites, with a mean of 135.9 ± 53.2 ppm (2σ SD), and 85 to 120 ppm for LL chondrites, with a mean of 102.5 ± 49.5 ppm. These values are within those reported by Chou et al. (1973) and Chou and Cohen (1973), who proposed that a significant amount of Ge in the silicates was redistributed in the metal during metamorphism. Moreover, the increase in the oxidation state from H to L to LL should have decreased the amount of the metal phase, and, consequently, increased the concentration of Ge in the metal. Taken together, all the metal samples define a positive correlation among Ge, Ni, and Co, demonstrating that taenite (Ni-rich) is more concentrated in Ge than kamacite (Ni-poor) (see Figure A in the Appendix).

Germanium concentrations in silicates from the H group ranged from 0.2 (H4 Ste Marguerite) to 2.2 ppm (H3.4 Sharps) (see Table 3 and Fig. 1), identical to the order of magnitude for data reported in Chou et al. (1973). However, we observed a discrepancy for the Allegan Ge concentration between our data, *i.e.*, 0.35 ppm compared with a value of 0.06 ppm reported in Chou et al. (1973). In the L group, Ge concentrations in silicates ranged from 0.05 ppm (L6 Alfianello) to 0.65 ppm (L4 Björbole) (Table 3 and Fig. 1). They are identical to the values reported by Chou and Cohen (1973)

The sulfides from H6 Kernouvé and H4 Ste Marguerite were strongly depleted in Ge, with concentrations of 1.75 and 1.95 ppb (see Table 3 and Fig. 1), respectively. This indicates the strong compatibility of Ge in the Fe-Ni metallic phase.

Table 3
The Ni, Co, and Ge concentrations, as well as the $\delta^{72/70}$Ge, $\delta^{73/70}$Ge, and $\delta^{74/70}$Ge values of the ordinary chondrites relative to NIST 3120a. Reproducibility is given as 2σ SD. N is the number of replicates for $\delta^{72/70}$Ge, $\delta^{73/70}$Ge, and $\delta^{74/70}$Ge. Error of less than 5% for the Ge, Ni, and Co elemental compositions.

Samples	Ni (wt%)	Co (ppm)	Co/Ni	Ge (ppm)	$\delta^{72/70}$Ge ‰	± 2σ SD	$\delta^{73/70}$ Ge ‰	± 2σ SD	$\delta^{74/70}$Ge ‰	± 2σ SD	N
H ordinary chondrites											
Bulk											
Dhajala (H3.8)	1.22	850	0.070	15.2	−0.16	0.06	−0.25	0.12	−0.37	0.15	8
Sharps (H3.4)	1.26	668	0.053	12.1	−0.29	0.06	−0.49	0.15	−0.59	0.04	3
Ste. Marguerite (H4)	0.83	580	0.070	10.3	−0.23	0.06	−0.37	0.11	−0.47	0.09	4
Allegan (H5)	1.52	1448	0.095	22.2	−0.20	0.07	−0.33	0.10	−0.55	0.04	3
Guareña (H6)	1.59	1123	0.071	21.4	−0.23	0.09	−0.38	0.13	−0.51	0.16	11
Kernouvé (H6)	1.27	776	0.061	13.6	−0.29	0.12	−0.45	0.17	−0.56	0.17	10
Mean	*1.28*	*908*	*0.070*	*15.8*	*−0.23*	*0.10*	*−0.38*	*0.17*	*−0.54*[1]	*0.09*	
Metal											
Dhajala (H3.8)	6.79	4746	0.070	57.3	−0.16	0.10	−0.23	0.13	−0.33	0.09	8
Sharps (H3.4)	7.78	4543	0.058	60.3	−0.24	0.02	−0.38	0.04	−0.49	0.04	5
Ste. Marguerite (H4)	9.07	4940	0.054	67.0	−0.23	0.13	−0.36	0.21	−0.52	0.12	8
Allegan (H5)	22.11	2527	0.011	83.5	−0.25	0.11	−0.38	0.17	−0.48	0.12	8
Roses City Veins (H5)	7.14	4200	0.059	63.1	−0.25	0.03	−0.36	0.05	−0.56	0.06	3
Guareña (H6)	9.44	4893	0.052	64.2	−0.19	0.24	−0.31	0.37	−0.52	0.06	4
Kernouvé (H6)	9.24	5280	0.057	67.8	−0.24	0.03	−0.37	0.05	−0.49	0.02	3
Portales Valley V (H6)	9.65	4724	0.049	50.0	−0.19	0.05	−0.34	0.08	−0.43	0.05	3
Portales Valley CC(H6)	7.3	5038	0.069	62.8	−0.26	0.07	−0.40	0.01	−0.55	0.11	3
Portales Valley C (H6)	8.83	4587	0.052	70.5	−0.28	0.03	−0.40	0.05	−0.57	0.12	3
Mean	*9.74*	*4548*	*0.053*	*64.6*	*−0.23*	*0.07*	*−0.35*	*0.1*	*−0.51*[1]	*0.09*	
Silicate											
Dhajala (H3.8)				0.5	−0.26	0.03	−0.39	0.14	−0.50	0.11	3
Sharps (H3.4)				2.2	−0.42	0.00	−0.63	0.01	−0.82	0.01	3
Ste. Marguerite (H4)				0.2	−0.32	0.10	−0.53	0.07	−0.66	0.17	3
Allegan (H5)				0.4	−0.41		−0.67		−0.92		1
Guareña (H6)				0.6	−0.31	0.04	−0.47	0.10	−0.58	0.05	3
Kernouvé (H6)				0.5	−0.27	0.06	−0.42	0.11	−0.55	0.12	3
Mean				*0.7*	*−0.33*	*0.14*	*−0.52*	*0.23*	*−0.67*	*0.33*	
Sulfide [2]											
Ste. Marguerite (H4)				0.002					−1.60	-	1
Kernouvé (H6)				0.002	−0.59	-			−1.56	-	1
Mean				*0.002*					*−1.58*	*0.02*	
Chondrules: Dhajala											
<300 μm fraction					−0.17	0.06	−0.27	0.05	−0.28	0.12	2
>300 μm fraction					−0.21	0.06	−0.32	0.03	−0.38	0.11	3
L ordinary chondrites											
Metal											
Hedjaz (L3.7)	10.06	5766	0.057	104.3	−0.16	0.12	−0.30	0.11	−0.35	0.09	3
Björbole (L4)	18.15	8400	0.046	174.5	−0.16	0.03	−0.24	0.04	−0.32	0.02	3
Alfianello (L6)	11.6	7042	0.061	117.5	−0.11	0.03	−0.19	0.03	−0.28	0.01	2
Granes (L6)	15.76	5242	0.033	120.7	−0.16	0.01	−0.25	0.03	−0.33	0.05	3
Tourine la Grosse (L6)	21.21	5466	0.026	157.8	−0.17	0.07	−0.24	0.07	−0.30	0.09	4
Vouillé (L6)	14.18	6806	0.048	140.4	− 0.11	0.02	−0.20	0.07	−0.28	0.04	3
Mean	*15.2*	*6454*	*0.045*	*135.9*	*−0.15*	*0.05*	*−0.24*	*0.08*	*−0.31*	*0.06*	
Silicate											
Hedjaz (L3.7)				0.23	−0.32	0.02	−0.58	0.41	−0.85	0.22	2
Björbole (L4)				0.65	−0.27	0.05	−0.40	0.12	−0.50	0.09	5
Alfianello (L6)				0.05	−0.57		−0.92		−1.25		1
Granes (L6)				0.18	−0.44	0.21	−0.69	0.07	−0.92	0.25	2
Vouillé (L6)				0.24	−0.22		−0.51		−0.83		1
Mean				*0.27*	*−0.36*	*0.09*	*−0.62*	*0.2*	*−0.87*	*0.18*	
LL ordinary chondrites											
Metal											
Parnalle (LL3.6)				120	−0.18	0.07	−0.31	0.17	−0.29	0.08	3
NWA 118 (LL6)				85	−0.13	0.06	−0.19	0.1	−0.23	0.10	4
Mean				*102.5*	*−0.16*	*0.07*	*−0.25*	*0.2*	*−0.26*	*0.09*	

[1] Dhajala was excluded from the mean due to its unusual Ge isotopic composition, see Section 4.3 for explanations. [2] There is no standard deviation for sulfide because only one measurement was done per sample due to their low concentration.

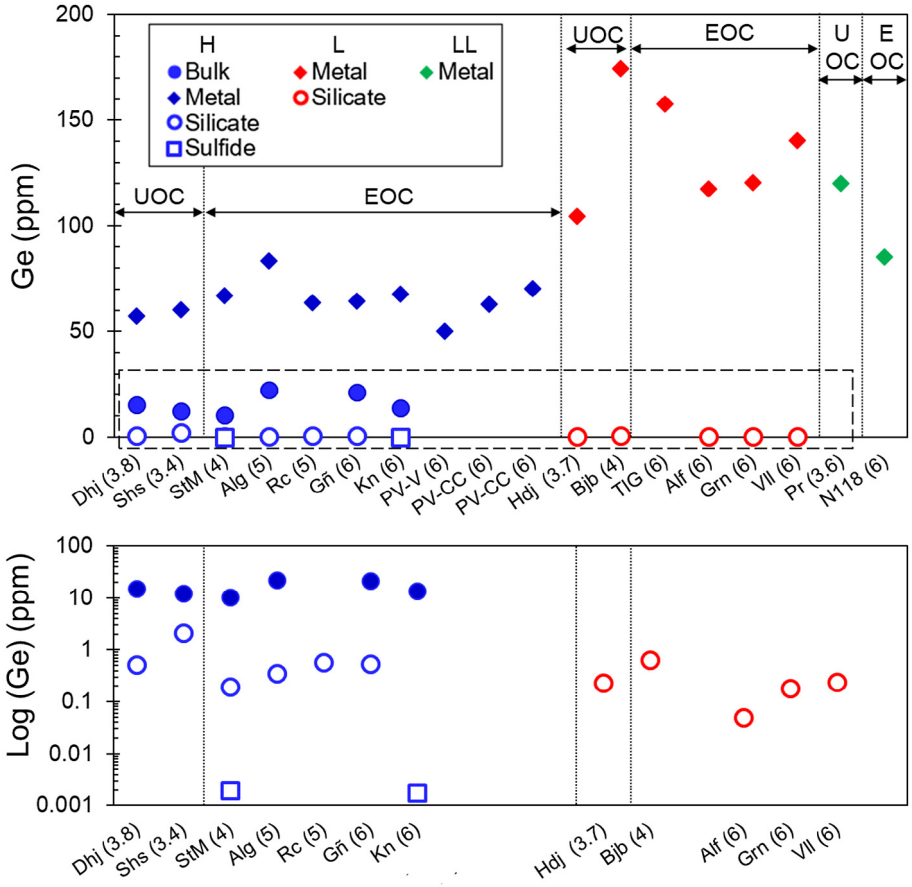

Fig. 1. (A) Elemental compositions of the bulk meteorites (filled circles), metal (diamond), silicate (empty circle), and sulfide (square) from H (in blue), L (in red), and LL (in green) ordinary chondrites. Data shows large variation among all phases. The germanium concentration decreases from the metal (60 to 170 ppm as a function of the chondrite group) to bulk (≈10 to 20 ppm) to silicate (≈0.1 to 1 ppm) to sulfide (≈2 ppb) phases. There is no variation associated with the petrologic type. (B) A detailed view, in log scale, of the low Ge silicates and sulfide phases (dashed rectangle of A). Table 1 lists all abbreviations. (For interpretation of the references to color in this figure legend, the reader is referred to the web version of this article).

3.2. Germanium isotopic data

Germanium isotope measurements were performed on bulk samples, silicates, and sulfides from H group chondrites, whereas we only analyzed L samples for metal and silicate, and LL for metal (Table 3). All samples plot on the mass-dependent fractionation line (see Fig. B in the Appendix).

Bulk Ge isotopic compositions define a narrow range from $\delta^{74/70}Ge = -0.59 \pm 0.04‰$ to $-0.37 \pm 0.15‰$, with a mean of $\delta^{74/70}Ge = -0.54 \pm 0.09‰$. Only Dhajala (with the highest $\delta^{74/70}Ge$ value at $-0.37‰$) deviated by more than 0.1‰ from the mean. Therefore, this sample was not included in the mean (see Section 4.5 for explanation) (Fig. 2A).

The $\delta^{74/70}Ge$ composition for metal from H group samples ranged from $-0.33 \pm 0.12‰$ (Dhajala) to $-0.57 \pm 0.12‰$ (metallic globules from Portales Valley), with a mean of $-0.51 \pm 0.09‰$ (*N.B.* we excluded the Dhajala value due to its unusual Ge isotopic composition, see Section 4.5 for explanation). The $\delta^{74/70}Ge_{metal}$ compositions for L group samples showed small variations from $-0.35 \pm 0.09‰$ (Hedjaz) to $-0.28 \pm 0.01‰$ (Alfianello), with a mean of $\delta^{74/70}Ge = -0.31 \pm 0.06‰$. The LL group yielded a mean value of $\delta^{74/70}Ge = -0.26 \pm 0.09‰$.

Silicates displayed lighter Ge isotopic compositions than bulk samples, with a large range in $\delta^{74/70}Ge$ from $-0.92‰$ for Allegan (H5) to $-0.50 \pm 0.11‰$ for Dhajala (H3), with a mean of $-0.67 \pm 0.33‰$ for the H groups (Fig. 2A) and from -1.25 (Alfianello, L6) to -0.50 ± 0.09 (Björbole, L4) with a mean of -0.87 ± 0.18 for the L group (Fig. 3A).

The sulfides were analyzed in two samples, without replicates due to their low abundance in OCs and Ge concentration (≈ 2 ppb). They were characterized by the lightest isotopic values at $\delta^{74/70}Ge = -1.60‰$ (Ste Marguerite, H4) and $\delta^{74/70}Ge = -1.56‰$ (Kernouvé, H6). We attributed the highest error to these samples based on the standards at ± 0.20‰ (2σ SD) (Fig. 3).

The two chondrule fractions from Dhajala had similar isotopic compositions of $\delta^{74/70}Ge = -0.28 \pm 0.12‰$ for < 300 µm chondrules and $\delta^{74/70}Ge = -0.38 \pm 0.11‰$ for > 300 µm chondrules (Table 3).

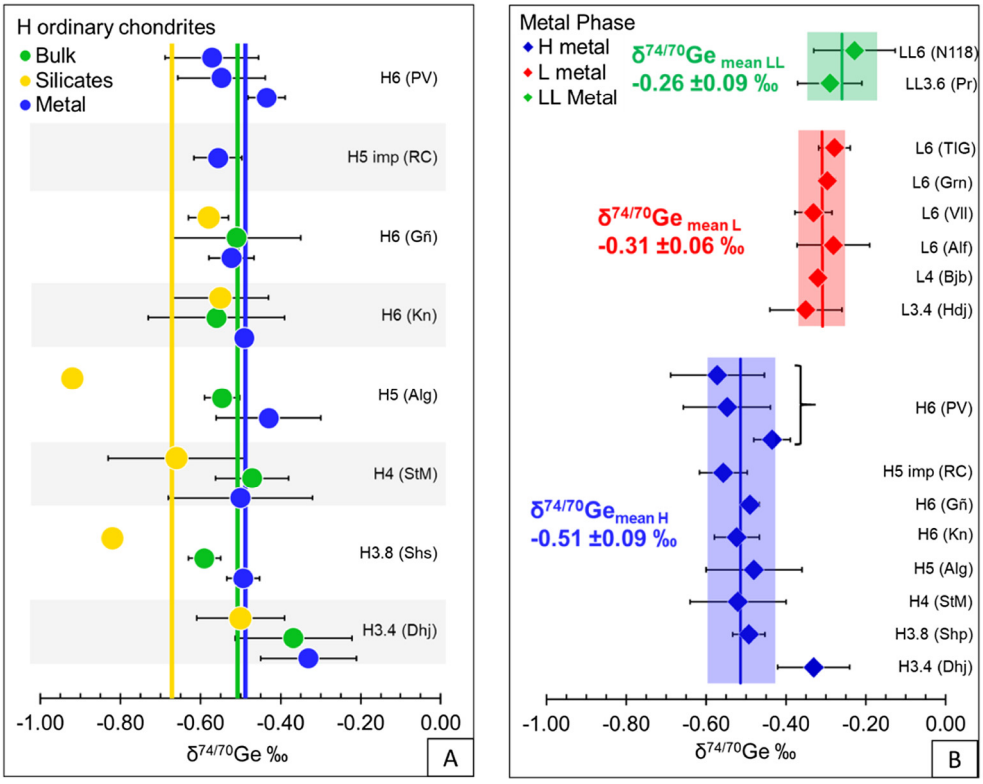

Fig. 2. (A) A detailed view of the $\delta^{74/70}$Ge isotopic compositions among the bulk, metal, and silicate in the H ordinary chondrites. The meteorites are ordered from the least metamorphosed (Dhajala H3.4) to highest (Guareña H6) types. Rose City and Portales Valley are plotted separately due to their specific textures (see text). The $\delta^{74/70}$Ge compositions become lighter from metal, to bulk sample, and, finally, to silicate. Silicates display larger $\delta^{74/70}$Ge variations than the metal and bulk samples. Isotopic fractionation between the phases are: $\Delta^{74/70}Ge_{bulk\text{-}metal} = -0.03 \pm 0.21‰$, $\Delta^{74/70}Ge_{bulk\text{-}silicate} = +0.16 \pm 0.33‰$, $\Delta^{74/70}Ge_{bulk\text{-}sulfide} = +1.06 \pm 0.16‰$, and $\Delta^{74/70}Ge_{metal\text{-}silicate} = +0.22 \pm 0.36‰$. (B) A comparison of the $\delta^{74/70}Ge_{metal}$ values between the H (blue diamonds), L (red diamonds), and LL (green diamond) groups. All meteorites from the H and L and LL groups are plotted, with mean values of $H_{mean} = -0.51 \pm 0.09‰$, $L_{mean} = -0.31 \pm 0.06‰$, and $LL_{mean} = -0.26 \pm 0.09‰$. The value for Dhajala was not included in the mean value for H group due to its off-trend isotopic composition (see Section 4.5 for more details). Identical abbreviations as Fig. 1 and Table 1. (For interpretation of the references to color in this figure legend, the reader is referred to the web version of this article).

3.3. Metal phases: main contributors to Ge isotopic compositions in bulk OCs

The metal phase is at least 60 times more concentrated in Ge than the silicates (Chou et al., 1973) and four orders of magnitudes higher than sulfide (Fig. 3A). The germanium isotope compositions of bulk H chondrites (mean $\delta^{74/70}Ge_{bulk} = -0.54 \pm 0.09‰$) were within error of the metal (mean $\delta^{74/70}Ge_{metal} = -0.51 \pm 0.09‰$), except for Sharps, and higher than the silicate (mean $\delta^{74/70}Ge_{silicate} = -0.67 \pm 0.33‰$). In a $\delta^{74/70}$Ge versus Log(1/Ge) diagram (Fig. 3B), the mixing line defined by the bulk sample, metal, silicate, and sulfide phases (mean $\delta^{74/70}Ge_{sulfide} = -1.56 \pm 0.02‰$), at all metamorphic grades, indicates that the $\delta^{74/70}$Ge measurements of separate phases are consistent with the $\delta^{74/70}$Ge measurements of the bulk chondrite. The Ge isotopic fractionation, *i.e.*, $\Delta^{74/70}Ge_{bulk\text{-}metal} = \delta^{74/70}Ge_{bulk} - \delta^{74/70}Ge_{metal} = -0.03 \pm 0.21‰$, for the H OC is near zero, compared with $\Delta^{74/70}Ge_{bulk\text{-}silicate} = +0.16 \pm 0.33‰$, $\Delta^{74/70}Ge_{bulk\text{-}sulfide} = +1.06 \pm 0.16‰$, and $\Delta^{74/70}Ge_{metal\text{-}silicate} = +0.22 \pm 0.36‰$ (Table 4; Fig. 4A, B). This indicates that the metal phase was the main contributor to the bulk Ge isotopic budget and that the $\delta^{74/70}Ge_{metal}$ values are a proxy for the $\delta^{74/70}Ge_{bulk}$ values.

In addition, we did not observe any correlation between the degree of shock and germanium isotopic composition. For example, Allegan (H5, S1) and Roses city (H5, S6) had identical $\delta^{74/70}Ge_{bulk}$ isotopic compositions (Table 3) composition.

4. DISCUSSION

4.1. Metal-silicate-sulfide fractionation during condensation

During the cooling of a primordial nebular gas, metal (FeNi) and forsterite (Mg_2SiO_4) condense at similar temperatures, *i.e.*, $T_{50\%\ cond} = 1370$ K at 10^{-4} atm (Yoneda and Grossman, 1995). The most abundant gaseous molecular species of germanium are GeS, $GeBr_2$, and GeO (Sears, 1978). As $GeBr_2$ is a highly volatile species of Ge, which condenses at much lower temperatures than GeS and

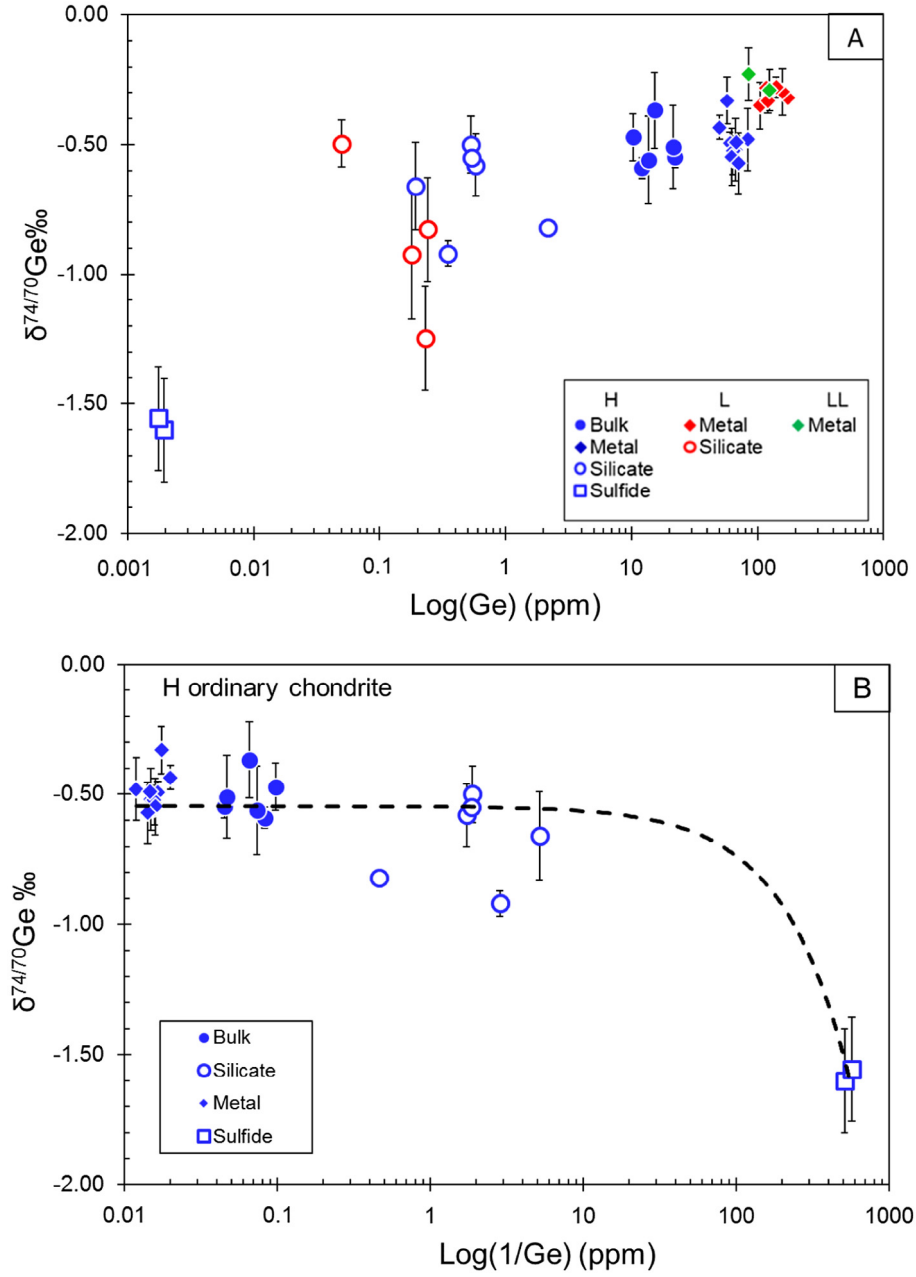

Fig. 3. (A) $\delta^{74/70}$Ge versus Log(Ge) concentration of the bulk and mineral phases of the H, L, and LL ordinary chondrites. (B) Negative correlation between $\delta^{74/70}$Ge and Log(1/[Ge]) for the metal, silicate, bulk sample, and sulfide phases in the H chondrites ($R^2 = 0.85$).

Table 4
The germanium isotopic factor ($\Delta^{74/70}$Ge ‰) among the bulk, metal, silicate, and sulfide of H ordinary chondrites, as well as the Ge elemental fractionation (DGe) between metal and silicate.

Samples	$\Delta^{74/70}Ge_{bulk\text{-}metal}$	$\Delta^{74/70}Ge_{bulk\text{-}silicate}$	$\Delta^{74/70}Ge_{metal\text{-}silicate}$	$\Delta^{74/70}Ge_{bulk\text{-}sulfide}$	$DGe_{metal\text{-}silicate}$
Sharps (H3.4)	−0.10	+0.23	+0.33	-	38
Dhajala (H3.8)	−0.04	+0.13	+0.17	-	123
Ste. Marguerite (H4)	+0.05	+0.19	+0.16	+1.13	395
Allegan (H5)	−0.07	+0.37	+0.49	-	272
Guareña (H6)	+0.01	+0.07	+0.06	-	126
Kernouvé (H6)	−0.07	−0.01	+0.06	+1.00	143
Mean	*−0.03 ± 0.21*	*+0.16 ± 0.33*	*+0.22 ± 0.36*	*+1.06 ± 0.16*	*183*

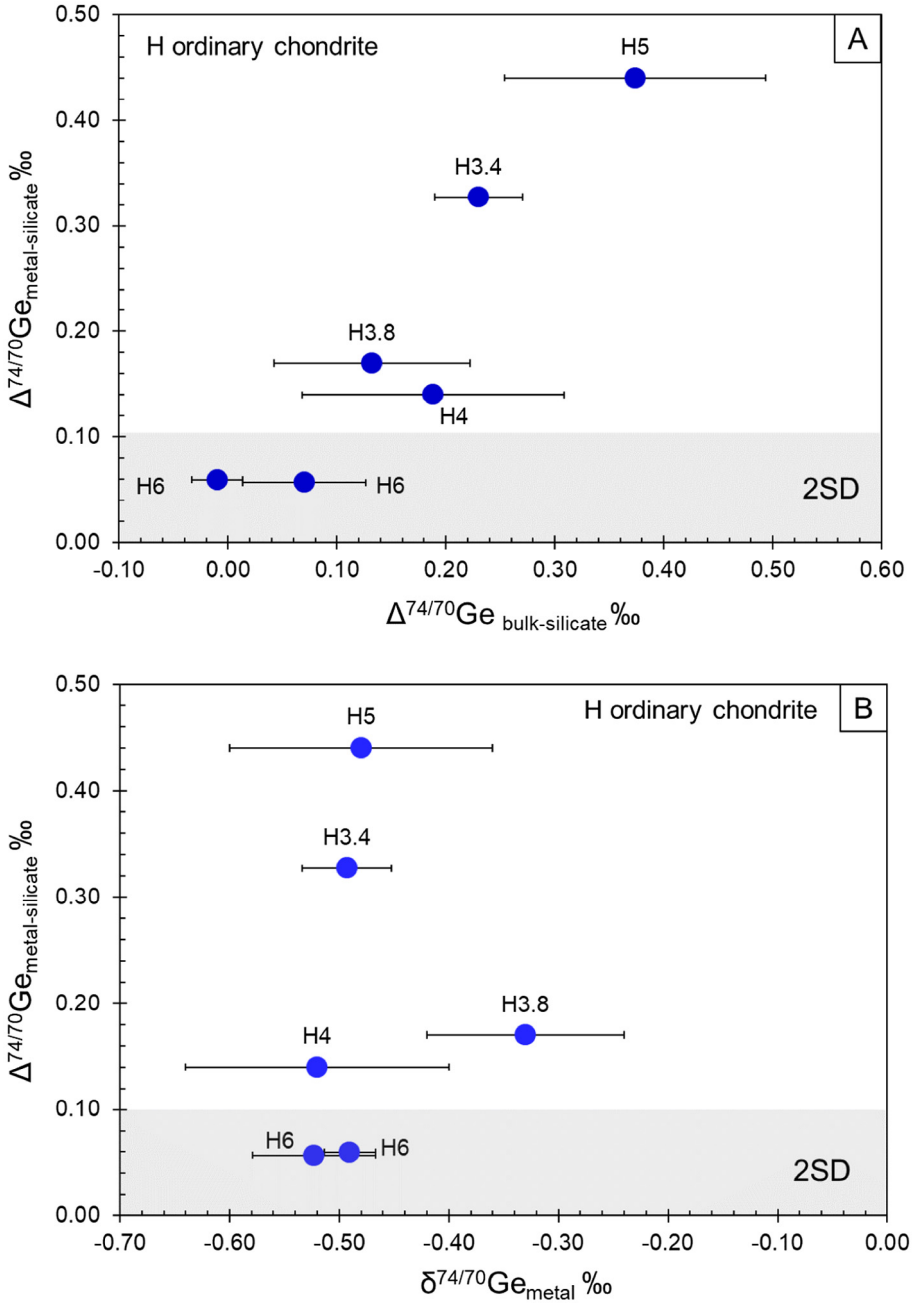

Fig. 4. Variations in the germanium isotopic composition and isotopic fractionation for H ordinary chondrites. (A) Correlation between $\Delta^{74/70}Ge_{metal\text{-}silicate}$ and $\Delta^{74/70}Ge_{bulk\text{-}silicate}$ with a slope of 1.2 ($R^2 = 0.9$). Metal and bulk Ge isotopic compositions are similar within a 2σ SD. (B) $\Delta^{74/70}Ge_{metal\text{-}silicate}$ versus $\delta^{74/70}Ge_{metal}$ shows no isotopic variation for metals among the petrologic groups. Values are from Table 4.

GeO (Sears, 1978; Wai and Wasson, 1979; Wood et al., 2019), here, we only discuss GeS and GeO condensation. Condensation of GeS and GeO via reactions with existing silicates and FeNi alloys occur at $T_{50\%\ cond} = 883$ K (ideal Ge solution; Lodders et al., 2009) or $T_{50\%\ cond} = 825$–830 K (no ideal solution; Wai and Wasson, 1977; Wood et al., 2019) and $pH_2O/pH_2 = 4.2 * 10^{-4}$. Sears (1978) showed that Ge is siderophile during high-temperature condensation and becomes lithophile at low temperatures. Thus, germanium condenses first in the metal based on the following reaction (Sears, 1978; Wai and Wasson 1979):

$$GeS_{(g)} + H_2 = Ge_{(s,metal)} + H_2S_{(g)} \quad (2)$$

Then, at lower temperatures, the remaining Ge is incorporated into the silicate phase according to the following reaction (Wai and Wasson, 1977; Sears, 1978):

$$nGeO_{(g)} + 2Mg_2SiO_{4(s)} + H_2O_{(g)} = 2MgSiO_{3(s)} + Mg_2(nGe, 1-nSi)O_{4(s)} + H_2 \quad (3)$$

On the other hand, sulfide condenses at lower temperatures than metal and silicate ($T_{50\%\ cond} = 691$ K) via reactions between H_2S_{gas} and solid metal based on the following reaction (Lauretta et al., 1997, and references therein):

$$H_2S_{(g)} + Fe_{(s)} = FeS_{(s)} + H_{2(g)} \quad (4)$$

The extent and direction of isotopic fractionation in the solid condensate with respect to the vapor source is difficult to evaluate and depends on whether the system maintains equilibrium, is kinetically controlled, or is in a closed or open system. High-temperature equilibrium processes do not induce significant isotopic fractionation, whereas kinetic condensation can result in isotopic fractionation based on the relative cooling rate of the gas and partial pressure of the relevant elements in the gas (Richter, 2004). Calculations from Richter (2004) demonstrate that condensation in an environment, in which the temperature drop is relatively fast compared to the condensation time, results in $P_i \ll P_{i,sat}$ (where P_i is the partial pressure of a volatile element and $P_{i,sat}$ is its saturation vapor pressure). In this case, kinetic condensation produces a large isotopic fractionation between the source and condensing phase, where the first condensate is enriched in light isotopes. In the condensation sequence, the metal phase that condenses first has the lightest Ge isotopic composition compared with that of the silicate and sulfide. In contrast, we observed higher $\delta^{74/70}Ge_{metal}$ values for the metal than for the silicate and the lowest $\delta^{74/70}Ge_{sulfide}$ values in the H chondrites (Fig. 3A).

We can draw the same conclusion from the sulfide data. Sulfides in equilibrated OCs are depleted in germanium, with a Ge content as low as 2 ppb and light isotopic composition of $\delta^{74/70}Ge = -1.56‰$ (Fig. 3A). As the first Ge condensates are incorporated into the Fe-Ni alloys, the late sulfide condensate result in (i) a low Ge content (as observed here), despite the fact that Ge is a chalcophile element (Chou et al., 1973), and (ii) a heavier Ge isotopic composition for the sulfides as compared with the metal (Davis and Richter, 2014). The lighter $\delta^{74/70}Ge_{sulfide}$ values compared with the $\delta^{74/70}Ge_{metal}$ values, however, rules out condensation from a protoplanetary disk as a viable process for the origin of Ge isotopic fractionation in metal-silicates and sulfides in ordinary chondrites.

4.2. Evidence for metal-silicate-sulfide partial equilibration before OC accretion

Germanium isotopic compositions in metal, silicate, and sulfide phases in all samples of the H chondrites display the following relationship: $\delta^{74/70}Ge_{sulfide} \ll \delta^{74/70}Ge_{silicate} < \delta^{74/70}Ge_{metal}$ (Fig. 3A). This relationship holds even for the most reduced type 3 samples, which are the least affected by thermal metamorphism at $T < 675$ °C (Tait et al., 2014), which is too low to melt metal or silicate. This observation suggests that the positive $\Delta^{74/70}Ge_{metal\text{-}silicate} = +0.22 \pm 0.36‰$ (varying from +0.17 to +0.33‰ in H3) values is due to metal-silicate exchange that occurred before the accretion of H ordinary chondrite parent body. This positive $\Delta^{74/70}Ge_{metal\text{-}silicate}$ also occurs between the Earth silicate reservoir ($\delta^{74/70}Ge = +0.56 \pm 0.16‰$) and magmatic Fe-meteorites ($\delta^{74/70}Ge = +1.41 \pm 0.22‰$) (Luais, 2012), which may represent the core of early formed planetesimals. Therefore, higher $\delta^{74/70}Ge$ values in metal compared to silicate, in both undifferentiated and differentiated bodies, appears to be the result of metal-silicate equilibrium. The larger $\Delta^{74/70}Ge_{metal\text{-}silicate}$ of + 0.85‰ in differentiated bodies reservoirs (*e.g.*, the silicate Earth and Fe- meteorites, Luais, 2012) compared to $\Delta^{74/70}Ge_{metal\text{-}silicate}$ in OCs can reflect additional isotopic fractionation during core-mantle differentiation.

The addition of sulfur in the Fe-Ni system strongly modifies the Ge incorporation into the metal phase. Chabot et al. (2003) and Chabot and Jones (2003) demonstrated that, during fractional crystallization at FeNi-S metallic liquid equilibrium, the $D(Ge)_{solid\ metal/liquid\ metal}$ value increases by several orders of magnitude as S increases in the liquid. Similar low Ge contents have also been observed in S-rich melts during Fe-Ni-S partial melting experiments (Rushmer et al., 2005). Low Ge contents (2 ppb) in sulfide from type 4 and 6 OCs (Fig. 3A) likely result from late-stage fractional crystallization of Fe-Ni-S melts. The strongly negative $\delta^{74/70}Ge_{sulfide}$ value of −1.56‰ appears to be a feature common to sulfides formed by fractional crystallization, such as terrestrial sulfides (Belissont et al., 2014). As we have no isotopic values for the H3 type, it is unclear if sulfide crystallization occurs during nebular processes or on the parent body. However, the discrepancy between temperatures associated with the H4 petrologic type (676–865 °C; Tait et al., 2014) and FeNi-S fusion temperature (963 °C; Mare et al., 2014) suggest that negative Ge isotopic composition of sulfides could have been inherited from processes that occur before parent body accretion, as it has been proposed for metal and silicate phases.

Equilibrium among metal, silicate, and sulfide in ordinary chondrites must then reflect processes before the accretion, such as (1) partial re-equilibration of material produced by disruption of partially differentiated planetesimals, or (2) a heating event in the solar nebula. Bischoff et al. (2018) reported that, in more than 2280 polished OC thin sections, there was a high abundance of brecciated rocks and occurrences of xenolithic fragments (*e.g.*, CI, CM, and Ureilite) in type 3 OCs. This supports the hypothesis that OCs can represent aggregates of early formed achondritic, chondritic, and chondrule materials. Lichtenberg et al. (2018) argued that OC parent bodies can form from early impact on a preheated (*i.e.*, ^{26}Al decay) and partially differentiated planetesimal (Bryson et al., 2019). Thus, the negative $\delta^{74/70}Ge$ values of the bulk sample and all separated OC phases, compared with positive values for magmatic iron meteorites and Earth silicate reservoirs, imply a light isotope-enriched environment for OC formation, *i.e.*, an impact plume environment. Evaporation processes that occur during an impact would likely overprint any $\Delta^{74/70}Ge_{metal\text{-}silicate}$ signature from a previous generation of planetesimals. Metal, metal-silicate, and sulfide would partially re-equilibrate after this event during partial

melting in a gas enriched in light Ge isotopes. This model of metal melting before OC accretion agrees with a recent study of metal formation in L OCs (Okabayashi et al., 2019).

4.3. Post accretional processes

4.3.1. No shock effect on $\delta^{74/70}Ge_{metal}$ and $\delta^{74/70}Ge_{bulk}$ values

As the germanium is a moderately volatile element, evaporation should result in a significant enrichment in heavy isotopes in highly shocked samples. The H chondrite Roses City, an impact melt breccia (S6), shows no deviation in $\delta^{74/70}Ge_{metal}$ from the mean values for H group while Dhajala (S1) is enriched in heavy isotopes compared with other H chondrites. Similarly, for L group samples, there is no $\delta^{74/70}Ge_{metal}$ difference between highly shocked (Alfianello and Vouillé, both S5) and minimally shocked samples (Bjürbole, S1). The lack of a shock effect on the $\delta^{74/70}Ge$ values can be explained by the deep burial of material, which should inhibit light isotope evaporation due to the pressure (*e.g.*, Roses City, H5), or an increase in temperature during a low energetic impact, which may be not sufficient to efficiently evaporate Ge.

4.3.2. Effects of metamorphism

Unequilibrated OCs (type 3) are primitive and may correspond to the outer layer of a layered planetesimal (Trieloff et al., 2003) that experienced low-temperature metamorphic processes (<675 °C; Tait et al., 2014). They represent the most reduced type of each OC group (Rubin, 2005). This implies that metal-silicate exchange is limited compared to other petrologic types and that younger processes may not have overprinted isotopic fractionation, which had been established before planetesimal accretion (Van Schmus and Wood, 1967).

From the H3 to H5 petrologic types, certain variations in the $\Delta^{74/70}Ge_{\text{metal-silicate}}$ values (Fig. 4B) indicate Ge isotopic exchange between metal and silicate during thermal metamorphism. However, the lack of variation in the $\delta^{74/70}Ge_{metal}$ values suggests that metamorphism had no measurable effect on the Ge isotopic composition of the metal phase. Thus, variations in the $\Delta^{74/70}Ge_{\text{metal-silicate}}$ values (Fig. 4B) indicate an increased sensitivity to $\delta^{74/70}Ge_{silicate}$ during metamorphic processes due to the lower Ge content in the silicate compared to the metal. Melting points for the FeNi-S assemblage and silicate are 963 °C and 1050 °C, respectively, at 0.3 kBar (Mare et al., 2014 and references therein). Types 3 to 5 OCs experienced different peak metamorphism temperatures from $T < 675$ °C for H3, 525–727 °C for H4, and 676 °C $< T <$ 865 °C for H5 (Monnereau et al., 2013; Tait et al., 2014). These temperature ranges are likely too low to melt FeNi-S alloy and cause metal-silicate exchange. In contrast, type 6 OCs reached temperatures between 866 °C and 1000 °C (Monnereau et al., 2013; Tait et al., 2014). FeNi-S melting and efficient Ge silicate-metal exchange resulted in an increase in the Ge content for metals from the H3–H5 types ($[Ge]_{mean} = 61.9$ ppm), excluding Allegan (see Section 3.1), to the H6 type ($[Ge]_{mean} =$ 66.0 ppm), which agrees with Ge diffusion from silicate to metal during metamorphism (Chou et al., 1973). Similarly, Ge isotopic exchange between metal and silicate in H6 resulted in a heavier silicate isotopic composition, which approached the isotopic composition of the metal. This led to a similar Ge isotopic composition for the silicate, metal, and bulk in the H6 chondrites within the 2σ error range (Fig. 4).

The global scheme for L chondrites is not as clear as it is for H chondrites. Except for the Bjürbole sample (L4 at −0.5‰), silicates from the L6 chondrites have negative and heterogeneous $\delta^{74/70}Ge$ values that are distinct from the metal phase values (Fig. 3A), which suggest that there was no isotopic re-equilibration, such as that observed in H6 chondrites. The "onion shell" model is less constrained for L chondrites. Göpel et al. (1994) proposed that the L parent body formed from thermal gradient disruption due to impact processes and reassembly. If this had occurred before metal-silicate equilibration, this could have prevented the efficient Ge exchange between the metal and silicate. Finally, the isotopic uniformity of the metal phases from H3 to H6 and L3 to L6 (Fig. 2B) are consistent with closed-system metamorphism within each parent body.

4.4. Links between the redox process and $\delta^{74/70}Ge$ variations throughout the H–L–LL sequence

The main characteristic of ordinary chondrites is their increase in oxidation state through the H, L, and LL sequences, which is inferred from the decrease in metal content and increase in the percentage of fayalite in olivine (Chou et al., 1973). The similar increase in the $\delta^{18}O$ composition and $\Delta^{17}O$ anomalies from the H to LL OCs (Clayton et al. 1991) led Rubin (2005) to identify a correlation between the % Fa in olivine and the $\delta^{18}O$ and $\Delta^{17}O$ values.

The Ge concentration and isotopic composition in metal increases from the H to L to LL groups (Fig. 2B), which discounts the occurrence of any Ge loss and evaporative processes during OC formation. A well-defined positive correlation was identified among the %Fa, Ge concentrations, and $\delta^{74/70}Ge$ in metal for all petrographic types and groups (Fig. 5A and B). At first glance, this suggests that the metal becomes enriched in Ge and the heavy isotopes of Ge with increasing oxidation. However, as the D(Ge) value decreases with an increasing fO_2 (Kegler and Holzheid, 2011), we can expect the metal in the L chondrites to become depleted in Ge compared to the metal in H chondrites, whereas we observe the opposite (Fig. 5). Therefore, oxidation is not the main process that causes an increase in Ge content from H to LL. In the Urey and Craig-type diagram, *i.e.*, $Fe_{\text{metal + sulfide}}$ vs FeO (Krot et al., 2014), variations in reduced Fe and FeO do not follow the reduction-oxidation trend, suggesting that the system has lost some of its iron metal. In this case, the increase in the Ge content for the metal from H to LL, with a broadly constant Ge bulk concentration (Wasson and Kallemeyn, 1988), can be explained by the incorporation of Ge into the remaining metal. However, this process cannot explain the increase in the $\delta^{74/70}Ge$ throughout the OC sequence. In conclusion, the increases in Ge, $\delta^{74/70}Ge$, and %Fa are not related to oxidation conditions in the environ-

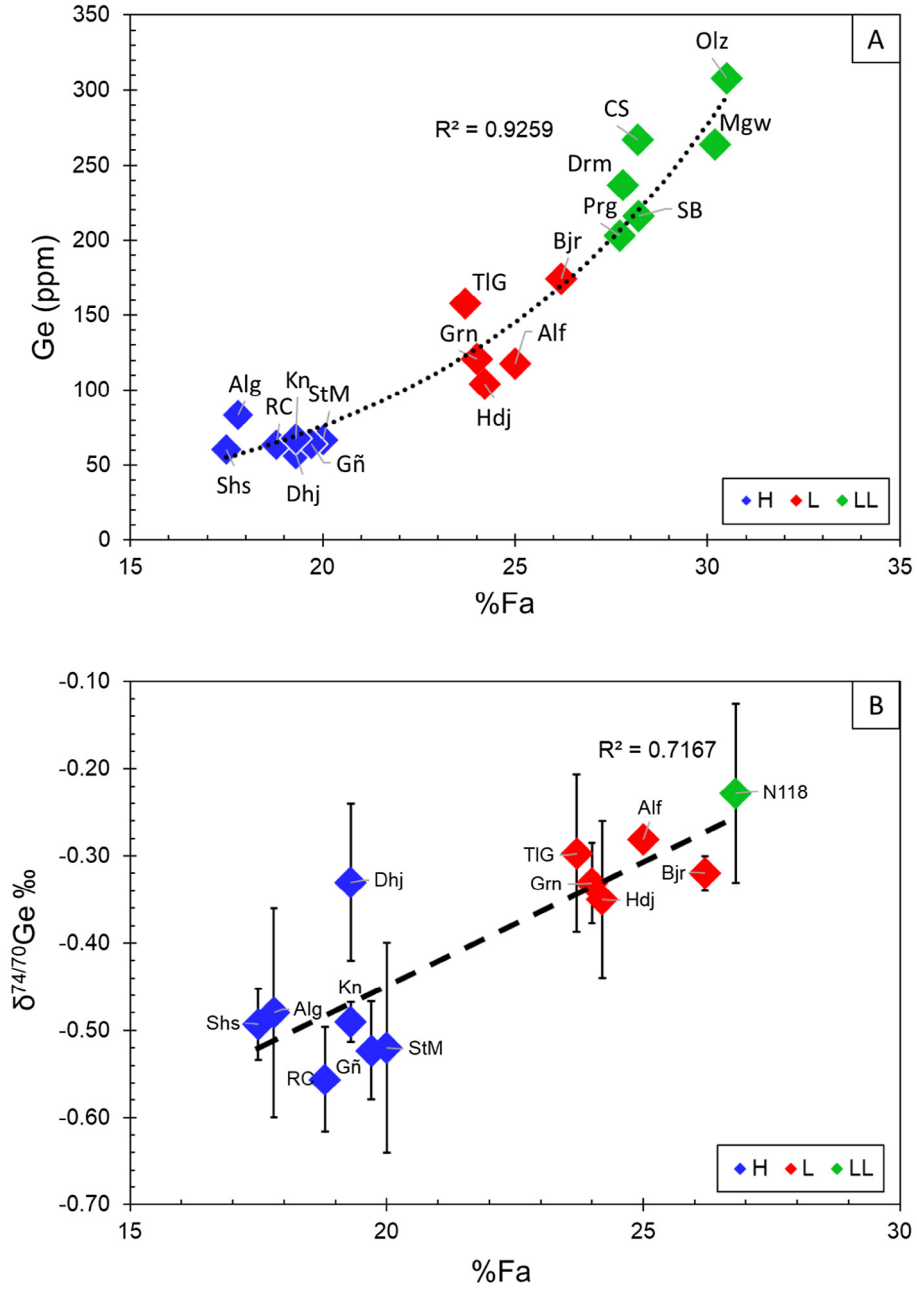

Fig. 5. (A) The Ge elemental composition versus %Fa in olivine for the three OC groups. All data plot near the regression line ($R^2 = 0.92$). (B) $\delta^{74/70}$Ge of the metal phase versus %Fa in olivine for the H, L, and LL groups. Both the H and L groups plot near the regression line, where no clear correlation occurs within the groups. There is no data for %Fa for Parnalle due to its large range in olivine composition (*e.g.*, Rubin, 1990). Ge data for LL for Sako-Banja (SB), Cherokee Spring (CS), Olivenza, (Olz), Paragould (Prg), Dhurmsala (Drm), and Mangwendi (Mgw) are from Chou and Cohen (1973) and %Fa data are from Dodd (1968) and Dunn et al. (2010). See Table 5 for other references and %Fa (For interpretation of the references to color in this figure legend, the reader is referred to the web version of this article).

ment of OC formation, *i.e.*, the fO_2 conditions. One explanation may be the involvement of an oxidizing component.

The $\delta^{74/70}$Ge values and δ^{18}O and Δ^{17}O are also characterized by a positive correlation (Fig. 6) in which these three groups are distinguishable outside of the analytical errors, with the following values for H (mean $\Delta^{17}O = 0.71 \pm 0.12‰$ and $\delta^{74/70}Ge = -0.51 \pm 0.09‰$), L (mean $\Delta^{17}O = 1.02 \pm 0.15‰$ and $\delta^{74/70}Ge = -0.31 \pm 0.06‰$), and LL chondrites (mean $\Delta^{17}O = 1.18 \pm 0.12‰$ and $\delta^{74/70}Ge = -0.26 \pm 0.09‰$). As metamorphism does not modify $\delta^{74/70}$Ge in metal and bulk chondrite, we suggest that Ge isotopic variations among the three groups are the result of accretionary processes. Hence, correlations among [Ge]-$\delta^{74/70}$Ge-%Fa, δ^{18}O, and Δ^{17}O reflect processes that originated in the accretionary disk, which were broadly linked to the redox state. Specifically, chondrule mixing of

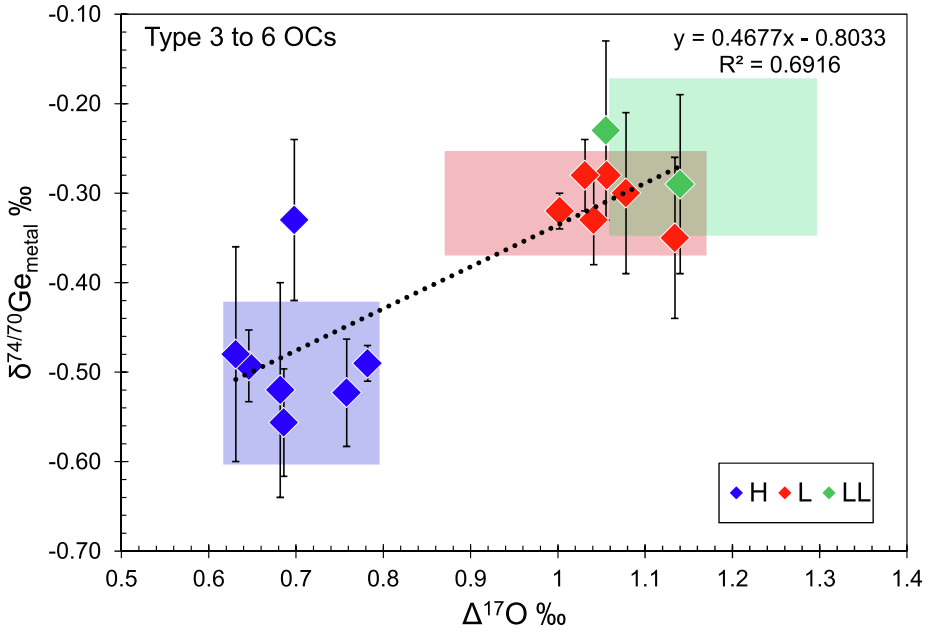

Fig. 6. $\delta^{74/70}$Ge of the metal phase versus Δ^{17}O of the bulk sample for type 3 to 6 ordinary chondrites. Δ^{17}O values are from Clayton et al. (1991), Folco et al., (2004), and the new data from this study. Rectangles in color represent fields of Δ^{17}O variations (1σ SD) calculated from data reported in Clayton et al. (1991) and $\delta^{74/70}$Ge variations (2σ SD). Note that Dhajala value was not included in the H mean because due to its special isotopic composition (see Section 4.5 for more details). The dotted line is a linear regression calculated for all individual values ($R^2 = 0.676$). %Fa, Δ^{17}O data, and references are given in Table 5 (For interpretation of the references to colour in this figure legend, the reader is referred to the web version of this article).

type I-reduced and type II metal-free chondrules (Clayton et al., 1991, Zanda et al., 2006), as well as the incorporation of an oxidizing component during OC accretion (Rubin, 2005) were the two main processes (see discussion below).

4.4.1. Chondrules as carriers of a high $\delta^{74/70}$Ge signature?

Clayton et al. (1991) demonstrated that, in certain ordinary chondrites, small-size chondrules (with diameter $d < 300$ μm) show enrichment in ^{16}O and depletion in ^{17}O compared with larger chondrules ($d > 300$ μm). This difference has been interpreted in terms of the interaction between ^{16}O-poor melted chondrules and ^{16}O-rich gas at their time of formation. Chondrules were then classified into type I chondrules (magnesian), which are small, reduced, metal-rich, and depleted in volatiles, and type II chondrules (ferroan), which are larger, oxidized, metal-free, and volatile-rich (Zanda, 2004; Zanda et al., 2006). Additionally, Zanda et al. (2006) showed that the proportions of the type I chondrule decrease through the OC sequence while type II increases (type I: 45%, 28%, and 22%; type II: 36%, 58%, and 61% in the H, L, and LL groups, respectively). Based on the sizes of type I and II chondrules, their volume in the H, L, and LL OCs, and the oxygen isotopic compositions of large chondrules (heaviest) compared to small chondrules, Clayton et al. (1991) argues that the increase in Δ^{17}O through the H-L-LL sequence can be explained by a "size-sorting process" of chondrules, whereas Zanda et al. (2006) argue for mixing between petrological components of the chondrites. Thus, considering the $\delta^{74/70}$Ge-δ^{18}O-Δ^{17}O correlations (Figs. 6 and 7), we can assess if type II chondrules have a heavier $\delta^{74/70}$Ge composition compared with type I chondrules. An increase in type II can elevate the $\delta^{74/70}$Ge ratio in type II rich-ordinary chondrites.

We used two approaches to test the chondrule mixing hypothesis. First, we calculated the inferred $\delta^{74/70}$Ge composition of type I and type II chondrules, as well as the matrix, to account for variations in $\delta^{74/70}$Ge from H to LL due to mixing between these components (Fig. 7A). This mass balance calculation is based on Zanda et al. (2006), with type I and II chondrules, the matrix proportions in H, L, and LL, and their respective oxygen isotopic compositions (see the caption for Fig. 7 for more details and Table 2 in Zanda et al. 2006). Based on this modeling, we obtained the following theoretical compositions: $\delta^{74/70}Ge_{typeI} = -0.81‰$, $\delta^{74/70}Ge_{typeII} = 2.15‰$, and $\delta^{74/70}Ge_{matrix} = -7.35‰$.

For the second approach, we analyzed the Ge isotopic composition of type I and II chondrules. As it is not possible to distinguish between type I and II chondrules at the macroscopic scale, we used the same protocol as Clayton et al. (1991) on the same meteorite (Dhajala H3.8). We separated two chondrule fractions (*i.e.*, $d < 300$ and $d > 300$ μm) based on the assumption that the smaller fraction should be mainly composed of type I chondrules while the larger fraction contains type II chondrules. Our results on the chondrule fractions show that the $\delta^{74/70}$Ge values of small ($\delta^{74/70}Ge_{d<300\mu m} = -0.28 \pm 0.12‰$) and large chondrules ($\delta^{74/70}Ge_{d>300\mu m} = -0.38 \pm 0.11‰$) (Table 3) are similar within error and are near the Dhajala bulk value ($\delta^{74/70}Ge = -0.37 \pm 015‰$). In the $\delta^{74/70}$Ge-δ^{18}O diagram,

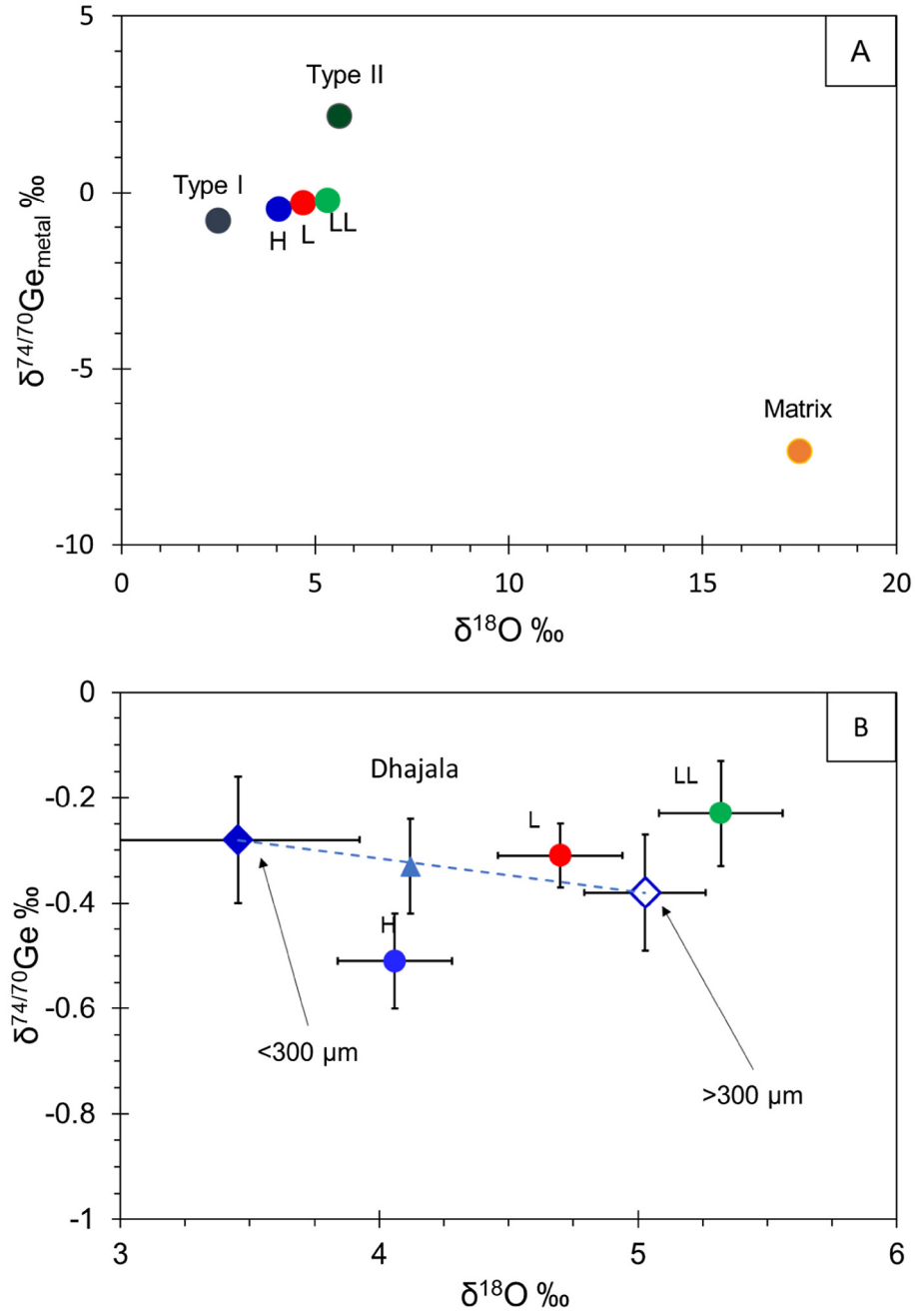

Fig. 7. (A) Germanium isotopic compositions versus oxygen isotopic compositions for the two chondrule fractions from Dhajala (<300 µm are filled blue diamond and >300 µm are empty blue diamond). The x-axis oxygen isotopic compositions for the <300 µm and >300 µm size fraction chondrules are the variations reported in Clayton et al. (1991). Blue, red, and green circles represent averages of the germanium and oxygen isotopic compositions for the H, L, and LL groups, respectively. Oxygen isotopic compositions and references are given in Table 5. (B) Theoretical Type I and II chondrules and matrix germanium isotopic composition based on chondrules and matrix mixing calculations. All data for the chondrules, matrix proportions (type I = 45%, 28 % and 22%; type II = 36%, 58%, and 61%; matrix = 12.4%, 10.2%, and 15.4%, for H, L, and LL, respectively), and their respective oxygen isotopic compositions are from Zanda et al. (2006). The calculated Ge isotopic compositions of $\delta^{74/70}Ge_{type\ I} = -0.81‰$, $\delta^{74/70}Ge_{type\ II} = +2.15‰$, and $\delta^{74/70}Ge_{matrix} = -7.35‰$ do not agree with the measurements of $\delta^{74/70}$Ge in chondrules displayed in Fig. 7A. (For interpretation of the references to color in this figure legend, the reader is referred to the web version of this article.)

Dhajala bulk chondrite plots on the mixing line defined by type I and II Dhajala chondrules, indicating no analytical artefact. However, type I and II chondrule isotopic compositions do not plot on the $\delta^{74/70}$Ge-δ^{18}O OC mixing line (Fig. 7B) and do not agree with the calculated values for type I and II chondrules. This precludes any mixing process between type I and II chondrules that can explain the H, L, and LL correlation.

An *in-situ* ion probe study of oxygen isotopes in individual olivine and pyroxene phases of OC chondrules yielded a more complex picture. Variable $\delta^{18}O$ but similar $\Delta^{17}O$ values have been found in type I and II chondrules from H chondrites, as well as the Semarkona (LL3) chondrite (Kita et al., 2010). In Semarkona, type I and II chondrules both have similar $\Delta^{17}O$ values (+0.5–0.7‰) that are lower than bulk LL chondrites (+1.2‰), indicating that chondrule phenocrysts do not host the $\Delta^{17}O$ anomalies. Thus, the issue is not the dichotomy between the O isotopic compositions of type I and II chondrules but the recognition of a high $\Delta^{17}O$ anomaly. For example, a previous study has found a $\Delta^{17}O$ anomaly in chondrule glass from the LL chondrite, which resulted from aqueous alteration with a high $\Delta^{17}O$ ice component (Kita et al., 2010). Germanium isotopes and detailed studies of O anomalies in chondrules do not favor a mixing model that links phenocrysts in type I and II chondrules with the redox state but mixing with, or incorporation of, a high $\Delta^{17}O$ oxidized component in the chondrules or chondrite matrix is a viable model. The similar Ge isotopic composition between the type I and II chondrules suggests that evidence of an oxidizing component with high $\Delta^{17}O$ must occur in the matrix of ordinary chondrites. A systematic investigation of the Ge isotopic compositions of chondrules and the matrix of the H, L, and LL types is necessary to understand similarities in their composition.

4.4.2. $\delta^{74/70}$Ge- Δ^{17}O-%Fa correlations in OCs and accretion of hydrated phyllosilicate

The main issue with the correlation between Ge elemental/isotopic variations in ordinary chondrites and %Fa in olivine, as well as between $\delta^{18}O$ and the $\Delta^{17}O$, is the origin of oxidation and how it relates to asteroidal processes and/or a nebular origin.

Clayton and Mayeda (1988) first identified the correlations between %Fa in olivine and $\delta^{18}O$ and $\Delta^{17}O$ in Urelites. They interpreted these correlations to be associated with oxidation processes in the nebula. Similarly, Rubin (2005) highlighted the $\Delta^{17}O$-%Fa positive correlation among OC groups, suggesting that the increase in the oxidation state through the OC sequence is related to an increase in the proportion of an accreted oxidizing agent with high $\delta^{17}O$, $\delta^{18}O$, and $\Delta^{17}O$ signatures. Choi et al. (1998) identified such elevated oxygen isotopic signatures in magnetite from unequilibrated LL OCs, which show a large and unusual deviation from the Terrestrial Fractionation Line (TFL; $\Delta^{17}O \approx 5‰$) compared with OCs that have typical values ($\Delta^{17}O \approx 0$ to 2‰). Choi et al. (1998) suggested that high ^{18}O-nebular water ($\delta^{18}O = 21‰$ and $\Delta^{17}O \approx 7‰$) accreted onto the OC parent body and induced low-temperature aqueous alteration. Such asteroidal alteration was responsible for the formation of magnetite via FeNi alloy oxidation (Wasson and Krot, 1994; Krot et al., 1997; Choi et al., 1998), the growth of fayalite rims on pyroxene grains via reactions between oxidized Fe and silica (Wasson and Krot, 1994), and the presence of phyllosilicates in LLs and unequilibrated OCs (Hutchison et al., 1987; Choi et al., 1998).

Attributing the high Ge-$\delta^{74/70}$Ge compositions to the high ^{18}O-nebular component (Figs. 5 and 6) and the main oxidizing agent in the low temperature (T < 500 K) nebula to an H_2O-gaseous component (McSween and Labotka, 1993; Krot et al., 1997) is tempting. However, there is a large debate on the thermodynamic state of H_2O. McSween and Labotka (1993) and Krot et al. (1997) have proposed that ice condensate in the nebula accreted to OC parent bodies, and, then, later heated to form vapor during metamorphism and reacted to form phyllosilicates, such as described in the LL3 unequilibrated chondrites. Wasson and Krot (1994) and Wasson (2000) argued that the low temperatures, *i.e.*, 160 K (or at 182 K; Lodders et al., 2009), required to condensate ice cannot be attained in the nebular locations that form OCs (within 2–3 AU). Instead, they have suggested that H_2O derived from accreted hydrated silicates. Here, the key issue is how germanium can be incorporated into the low-temperature H_2O-oxidizing component. At germanium condensation temperature ($T_{50\%\ cond}$) of 875 K at 10^{-4} atm, Ge may have already condensed, and low-temperature ice condensates likely do not contain much Ge. However, hydrated silicates that form at the end of the condensation sequence but at higher temperatures than ice ($T_{50\%\ cond} < 350$ °C; Grossman and Larimer, 1974) can contain small amounts of Ge. Therefore, one possibility is that dust enrichment in the continuously accreting nebula can yield higher $T_{50\%\ cond}$ (Wasson, 2000; Davis and Richter, 2014). We propose that the last fraction of Ge, likely in the form of $GeBr_2$ (the second Ge most abundant species of Ge specie in the solar nebula, which is highly volatile; Sears, 1978), can condense in phyllosilicates and acquire the high $\delta^{74/70}$Ge values discussed in Section 4.1

We have modelled the mixing between bulk H chondrite and the oxidizing phyllosilicate (Fig. 8) to (1) reproduce the OCs correlation in Fig. 6 and, (2) determine what percentage of accreted phyllosilicate is needed to change the composition from H to LL chondrites in terms of Ge content and $\delta^{74/70}$Ge in phyllosilicate. To constrain the model, we have considered the amount of accreted phyllosilicate, which cannot be higher than the amount of matrix (<15%, Krot et al., 2014), and the Ge content in terrestrial phyllosilicates. This value ranges between 1.1 and 8.5 ppm with means of 3.8 ± 3.2 ppm (2σ SD, calculated from Bernstein, 1985, and references therein). The model shows that at Ge content of 3.8 ± 3.2 ppm and ~10 to 15% of accreted phyllosilicate, a composition from $\delta^{74/70}Ge = +6‰$ to +3.2‰, respectively, is needed to change the isotopic composition from H to LL. By extrapolation of the $\delta^{74/70}$Ge-$\Delta^{17}O$ correlation shown in Fig. 6, we find that the $\delta^{74/70}Ge = 3.2 - 6‰$ in phyllosilicates would correspond to a $\Delta^{17}O \approx +8$ to +15‰. The lower $\Delta^{17}O$ is close to the value of the oxidized nebular component incorporated in OC parent bodies reported by Choi et al. (1998) ($\Delta^{17}O \approx +7‰$), yet a better match is attained for a $\delta^{74/70}Ge = +2.5‰$ ($\Delta^{17}O = +7‰$) in phyllosilicates. This value implies a Ge content of about 4.8–7 ppm for 15% and 10% of phyllosilicate, respectively. So, it seems possible that phyllosilicates could contain between 4 to 7 ppm of Ge with a

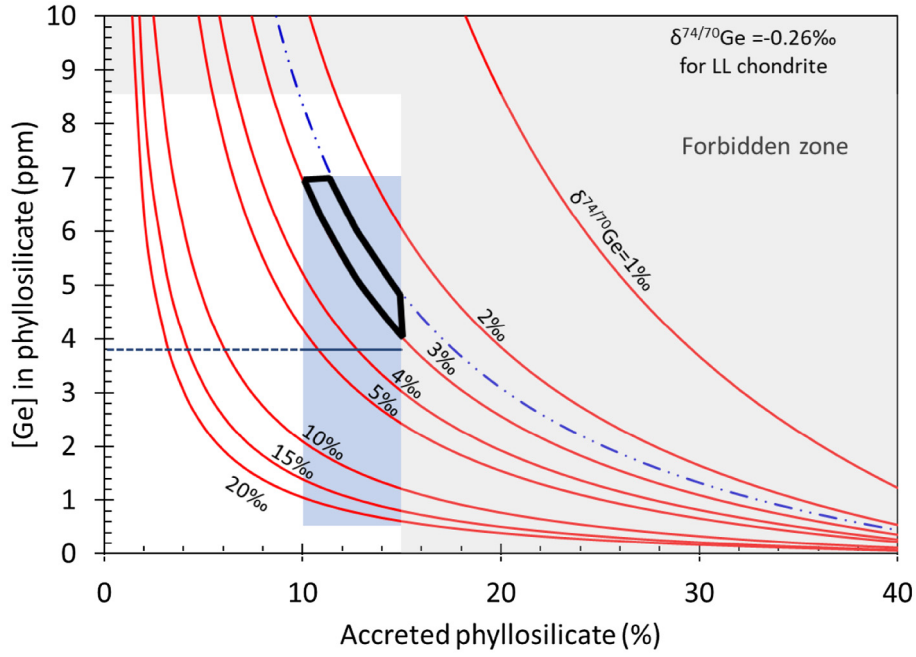

Fig. 8. Modelling of the germanium content (ppm) in phyllosilicate required to change the germanium isotopic composition from an H (−0.51‰) to LL chondrite composition (−0.26‰) as a function of the accreted amount of phyllosilicates and their $\delta^{74/70}Ge_{phyllosilicate}$ composition at 1‰, 2‰, 3‰, 4‰, 5‰, 10‰, 15‰, and 20‰. The blue dashed line corresponds to $\delta^{74/70}Ge_{phyllosilicate} = +2.5‰$, representing the isocurve that matches the $\Delta^{17}O$ of ≈+7‰ reported in Choi et al. (1998) (see text). The horizontal dark blue line is the mean Ge content in terrestrial phyllosilicates (3.8 ppm; Bernstein, 1985, and references therein) and the dark blue zone is the 2σ SD of the mean. The highlighted area in black represents the likely composition of the phyllosilicates (see the text for more details). The forbidden zone can be defined beyond the maximum percentage of matrix in ordinary chondrites (15%; Krot et al., 2014) and maximum phyllosilicates (up to 8.5 ppm; Bernstein, 1985) (For interpretation of the references to color in this figure legend, the reader is referred to the web version of this article).

composition of $\delta^{74/70}Ge \approx +3$ to +2.5‰. It can be noted that a Ge content in phyllosilicates of few ppm is likely from the thermodynamic calculation (Sears, 1978). They predict that a significant proportion of Ge (in the form of $GeBr_2$) would remain in the gas even after troilite condensation and that Ge would become lithophile at the end of the condensation sequence (Sears, 1978).

During planetesimal heating, the dehydration of accreted phyllosilicates triggers a redox reaction on the parent body. The release of ^{18}O-rich and $\delta^{74/70}Ge$-high water (or vapor) oxidizes the Fe-Ni metal as FeO, forming magnetite, which then increases the %Fa in olivine. Germanium released in water is likely incorporated in the metal due to its siderophile behavior. However, the small amount of Ge does not contribute to the significant increase in Ge from the H to L to LL OCs. In contrast, the high $\delta^{74/70}Ge$ composition of the released H_2O component that reacted with the metal should have significantly increased the $\delta^{74/70}Ge_{metal}$ proportional to the amount of accreted oxidizing agent on each OC parent body. As such interaction may occur during metamorphism, a correlation for the $\delta^{74/70}Ge_{metal}$ composition is possible for types 3–6 in a given OC group. However, we propose that the lack of a $\delta^{74/70}Ge_{metal}$ correlation with the petrologic type is imputable to the relatively high temperature of thermal metamorphism, which is even recorded in the earlier stage of pervasive H_2O alteration via magnetite formation in the type 3 chondrite ($T < 675$ °C) (Krot et al. 1997; Choi et al., 1998; Tait et al., 2014). The fractionation of stable isotopes at equilibrium is a function of $1/T^2$, such that an increase in the metamorphic temperature from types 3–6 ($T < 675$ to 975 °C, Tait et al., 2014) does not induce significant variations in the Ge isotopic fractionation between the H_2O-component and metal with the petrologic type. Hence, the observed Ge isotopic fractionation among groups is primarily a function of the amount of nebular hydrated phyllosilicate with a high $\delta^{74/70}Ge$ signature accreted onto the parent body. The heavy O isotopic composition of OCs that partly derive from phyllosilicate destabilization can be considered, along with the previous H_2O gas or ice model for the origin of accreted water.

4.5. Dhajala: a reduced L chondrite

The higher $\delta^{74/70}Ge_{metal}$ composition of Dhajala (H3.8) compared with the other H chondrites, including Sharps (H3.4), which has a similar petrologic type, requires discussion because Dhajala does not fit the correlations shown in Fig. 5B and 6. Dhajala and Sharps have both experienced a low degree of metamorphism. They lie within the oxygen isotope field as H chondrites, but Dhajala (H3.8) has oxygen isotopic anomalies that are slightly higher than Sharps

Table 5
The oxygen isotopic compositions and percentage of fayalite (%Fa) in ordinary chondrites.

Meteorites	%Fa	Ref	$\delta^{18}O$ (‰)	$\delta^{17}O$ (‰)	$\Delta^{17}O$ (‰)	2σ SD	Ref
Ordinary chondrites							
Sharps (H3.4)	17.5	*5*	3.95	2.7	0.646		*1*
Dhajala (H3.8)	19.3	*4*	4.12	2.84	0.698		*1*
Ste Marguerite (H4)	20.0	*9*	3.59	2.54	0.682		*3*
Allegan (H5)	17.8	*4*	3.97	2.68	0.631		*1*
Rose City (H5, IM)	18.8	*4*	3.68	2.6	0.686		*2*
Guareña (H6)	19.7	*4*	4.1	2.89	0.758		*1*
Kernouvé (H6)	19.3	*7*	4.15	2.94	0.782		*1*
Hedjaz (L3.7)	24.2	*4*	4.57	3.51	1.134		*1*
Bjurböle (L4)	26.2	*4*	4.9	3.55	1.002		*1*
Alfianelo (L6)	25.0	*4*	4.69	3.54	1.056		*3*
Granes (L6)	24.0	*9*	4.01	3.17	1.041		*3*
Vouillé (L6)	-		4.67	3.51	1.031		*3*
Tourine la Grosse (L6)	23.7	*6*	4.66	3.55	1.078		*3*
Parnalle (LL3.6)	-	*4*	5.15	3.82	1.140		*1*
NWA 118 (LL6)	26.8	*8*	4.61	3.5	1.055		*3*
Mean H	*18.9*		*4.06*	*2.81*	*0.705*	*0.09*	
Mean L	*24.6*		*4.70*	*3.46*	*1.020*	*0.15*	
Mean LL	-		*5.32*	*3.95*	*1.180*	*0.12*	
IIE Iron meteorites							
Netschaëvo			3.46	2.37	0.57		*10*
Miles			4.75	3.04	0.57		*10*
Weekeroo station			4.11	2.58	0.62		*10*

References: 1: Clayton et al. (1991); 2: Folco et al. (2004); 3: This study; 4: Rubin (1990); 5: Dodd (1968); 6: Dodd & Jarosewich (1979); 7: Reisener et al. (2006); 8: Grossman & Zipfel (2001); 9: Mason (1963); 10: Clayton and Mayeda (1996). Oxygen isotopic measurements of the samples from this study follow techniques from Pack et al. (2016), with errors for $\delta^{18}O$ and $\delta^{17}O$ of 0.15‰ and 0.08‰, respectively. The UWGE garnet standard (Valley et al., 1995; $\delta^{18}O = 5.75‰$) measured during this session gives a value of 5.76 ± 0.16‰ (n=5).

(H3.4) ($\Delta^{17}O_{Dhajala} = 0.698‰$ and $\Delta^{17}O_{Sharps} = 0.646‰$; Clayton et al., 1991). The high Fe_{metal} (15.98 wt.%), and low FeO_{bulk} (10.18 wt.%) contents in Dhajala compared with Sharps ($Fe_{metal} = 12.02$ wt.%, $FeO_{bulk} = 13.64$ wt.%) (Table 5) reflect more reduced conditions for Dhajala than for Sharps. In contrast, the high percentage of fayalite and low carbon content in Dhajala (%Fa = 19.3; C = 0.04 wt. %) indicate more oxidized conditions than for Sharps (%Fa = 17.5 and C = 0.95 wt.% Jarosewich, 1990). In addition, the Dhajala germanium isotopic composition is closer to L type composition than H type (Figs. 2 and 6). Thus, we propose that Dhajala accreted identical proportions of oxidizing component than L chondrites, which led to olivine formation with high %Fa (>20) and an increase in the $\delta^{74/70}Ge_{metal}$ composition that approaches the L Ge isotopic signature. Dhajala then experienced reduction by carbon (McSween and Labotka, 1993) based on the following reaction (Warren and Huber, 2006):

$$C + MgFeSiO_4 = MgSiO_3 + Fe + CO \quad (5)$$

In conclusion, the elevated $\delta^{74/70}Ge_{metal}$ composition in Dhajala with low %Fa is the result of high carbon activity in this meteorite, which did not decrease due to C dissolution in taenite (Romig and Goldstein, 1978) by contrast with Sharps. This implies that Dhajala most likely formed in the L region of the accretionary disk before reduction via carbon. This suggests that the OC accretion environment is heterogeneous and $\delta^{74/70}Ge$ should be considered a tracer of the primary locations that formed undifferentiated meteorites.

4.6. Relationship between the OC redox state and IIE iron meteorites

IIE non-magmatic iron meteorites formed by impact-induced melting and the destruction of a chondritic parent body, followed by metal silicate re-accretion (Wasson and Wang 1986; Luais, 2007; Ruzicka, 2014). This group can be divided into old (Miles, Weekeroo Station) and young groups (Netschaëvo, Watson), which formed from 4.3–4.5 to 3.5–3.8 Ga, respectively (Bogard et al., 2000). They have a complex mineralogy, mainly composed of metal and silicate inclusions. These inclusions represent 5 to 10 vol. % of the IIE meteorites and are composed of silicates (feldspar, pyroxene, and olivine) phosphates, sulfides, and chromite (McDermott et al., 2016). Silicate inclusions can be classified into two categories, chondritic inclusions with relic chondrules and differentiated inclusions (McDermott et al., 2016).

The genetic links between the H OC and IIE iron meteorites were first identified based on the similar elemental and oxygen isotopic compositions of silicate inclusions from IIE iron and silicates from the H OC (Olsen and Jarosewich, 1971; Clayton and Mayeda, 1996). However, based on the (1) concentrations in the refractory and volatile siderophile elements and (2) low $\Delta^{17}O$ values in silicate inclusions in the IIE Netschaevo meteorite, we can infer that the impact, which formed the IIE iron meteorites, occurred on an HH parent body that was more reduced than the H group (McDermott et al., 2016; Wasson, 2017).

To study the genetic link between the IIE irons and OCs, we only must consider meteorite samples from the IIE old

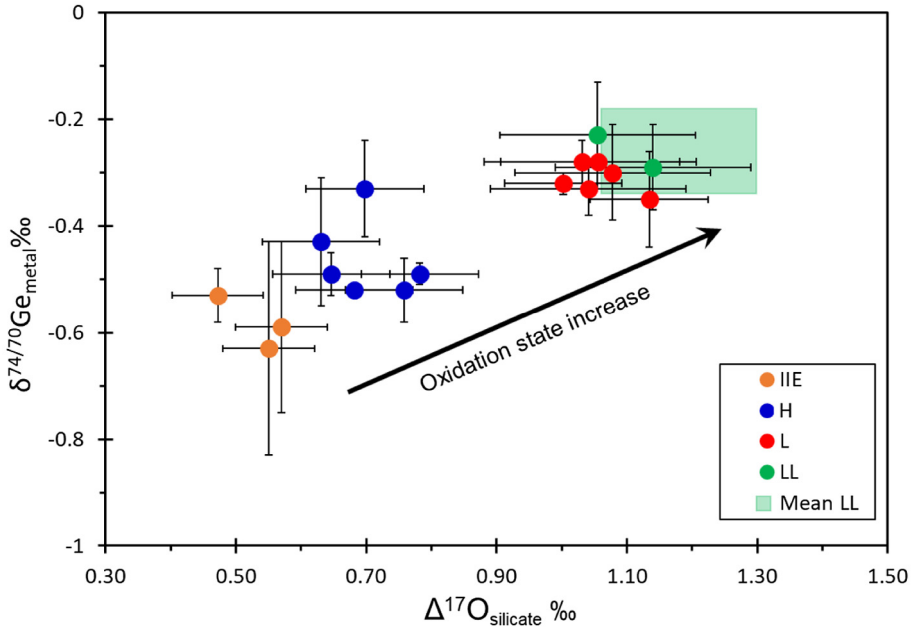

Fig. 9. $\Delta^{17}O$ of silicates (bulk ordinary chondrites and silicate inclusions of IIE iron meteorites) versus $\delta^{74/70}Ge$ of the metal phase in ordinary chondrites and IIE iron meteorites. The positive correlation between the IIE iron meteorites and LL ordinary chondrites demonstrates that the IIE parent body could have formed on a distinct and more reduced parent body than the H ordinary chondrite body, known as the HH parent body. As the $\Delta^{17}O$ of the NWA-118 sample is low compared to other LL chondrites, we also report the mean $\delta^{74/70}Ge$ versus $\Delta^{17}O$ for the LL chondrites (green square). References for the oxygen isotopic compositions are given in Table 5. The Ge isotopic composition of the IIE iron meteorites are from Luais (2007, 2012) (For interpretation of the references to color in this figure legend, the reader is referred to the web version of this article).

group because they display the most pristine $\delta^{74/70}Ge_{metal}$ compositions compared with the young group, which show an increase in $\delta^{74/70}Ge_{metal}$ due to successive impacts (Luais, 2007). Fig. 9 shows the positive correlation among the $\delta^{74/70}Ge$ composition of IIE bulk metal (Luais, 2007; Luais, 2012), OC metal (data from this study), and $\Delta^{17}O$ measured in silicate inclusions from IIE irons and bulk silicates from the H, L, and LL OCs (see Table 5 for oxygen references). IIE iron meteorite values for $\delta^{74/70}Ge_{metal}$ and $\Delta^{17}O_{silicate\ inclusions}$ are lower than those for the H chondrites. As the H chondrites are the less oxidized group, the lower $\delta^{74/70}Ge_{metal}$ and $\Delta^{17}O_{silicate\ inclusion}$ values (Fig. 9) of the IIE old groups compared to the H group, correspond to the isotopic composition of the most reduced HH parent body. Germanium isotopes demonstrate that there is a genetic link between the IIE iron meteorites and HH parent body.

5. SUMMARY

We report the first data set of germanium isotopic compositions for bulk and separated phases from ordinary chondrites. The Germanium isotopic compositions were measured by an MC-ICP-MS coupled to a hydride generator system with a 2σ SD long term reproducibility of 0.1‰. We found that the Ge isotopic composition of ordinary chondrites is mainly driven by the metal phase, which is a good proxy for the OC bulk composition. The $\delta^{74/70}Ge_{metal}$ values significantly increased throughout the OC sequence, such that H, L, and LL groups are distinguishable at −0.51 ± 0.09‰, −0.31 ± 0.09‰, and −0.26 ± 0.09‰, respectively. The implications of the germanium isotopic compositions for the understanding of ordinary chondrite compositions can be summarized as follows.

- The lack of significant $\delta^{74/70}Ge_{metal}$ variation between the unequilibrated and equilibrated OCs within each group implies that $\delta^{74/70}Ge$ variation among groups is inherited from nebular processes rather than parent body processes.
- Metal and silicate are partially equilibrated in a closed system during metamorphism.
- The positive $\Delta^{74/70}Ge_{metal\text{-}silicate}$ signature is remarkably similar to previously reported Ge isotopic fractionations between magmatic iron meteorites and Earth silicates. However, the light $\delta^{74/70}Ge$ composition of both metal and silicate suggests that metal, silicate, and sulfide have interacted before the accretion of ordinary chondrite parent bodies in a gas enriched in light Ge isotopes.
- The two well-defined positive correlations between $\delta^{74/70}Ge_{metal}$ and %Fa, as well as $\Delta^{17}O$, demonstrate that the Ge isotopic composition can be used as a tracer of oxidizing processes during accretion. The similar Ge isotopic compositions of small and large chondrules (from Dhajala) indicate that the size sorting chondrule mechanism cannot account for the $\delta^{74/70}Ge_{metal}$-%Fa and $\Delta^{17}O$ correlations. Therefore, these correlations can be explained by an increase in the amount of accreted high $\Delta^{17}O$ hydrated nebular phyllosilicates with high $\delta^{74/70}Ge$ of about 2.5–3‰, throughout the ordinary chondrite

sequence. We can reconsider the origin of the heavy O isotopic signature in ordinary chondrites to derive from either H_2O (water) or hydrated silicate.
- The $\delta^{74/70}Ge_{metal}$-$\Delta^{17}O_{silicate}$ correlation in the OCs provides evidence for the existence of an HH reduced parent body and its genetic link with the IIE iron meteorites.

Declaration of Competing Interest

The authors declare that they have no known competing financial interests or personal relationships that could have appeared to influence the work reported in this paper.

ACKNOWLEDGMENTS

The authors thank Damien Cividini for his valuable assistance on the Neptune*Plus* MC-ICP-MS and his advice on germanium chemistry, and Delphine Yeghicheyan (SARM "Service d'Analyses des Roches et des Minéraux", CRPG-CNRS, Nancy) for contribution to elemental analyses. The authors also acknowledge Andreas Pack (Göttingen University) for oxygen isotopic measurements. We thank M. Gounelle and the "Comité de gestion" at the "Muséum National d'Histoire Naturelle" (MNHN) of Paris, T. McCoy and J. Hoskin from the Smithsonian Institute, and A. Nieto Codina from the "Museo Nacional de Ciencias Naturales" (MNCN) of Madrid for providing the meteorite samples. Jesse Davenport is thanked for his kind and careful correction of the manuscript. Finally, we thank Fang Huang for editorial handling, and three anonymous reviewers for their thorough and constructive reviews that helped to improve the manuscript. This is CRPG contribution n°2724.

RESEARCH DATA

Research Data associated with this article can be access at http://dx.doi.org/10.17632/wvf8s3mrg3.3.

APPENDIX A. SUPPLEMENTARY MATERIAL

Supplementary data to this article can be found online at https://doi.org/10.1016/j.gca.2019.10.038.

REFERENCES

Abdul-Majeed W. S. and Zimmerman W. B. (2012) Computational modelling of the hydride generation reaction in a tubular reactor and atomization in a quartz cell atomizer. *JASMI* **02**, 126–139.

Archer G. J., Walker R. J., Tino J., Blackburn T., Kruijer T. S. and Hellmann J. L. (2019) Siderophile element constraints on the thermal history of the H chondrite parent body. *Geochim. Cosmochim. Acta* **245**, 556–576.

Belissont R., Boiron M.-C., Luais B. and Cathelineau M. (2014) LA-ICP-MS analyses of minor and trace elements and bulk Ge isotopes in zoned Ge-rich sphalerites from the Noailhac – Saint-Salvy deposit (France): Insights into incorporation mechanisms and ore deposition processes. *Geochim. Cosmochim. Acta* **126**, 518–540.

Bennett M. E. and McSween H. Y. (1996) Shock features in iron-nickel metal and troilite of L-group ordinary chondrites. *Meteorit. Planet. Sci.* **31**, 255–264.

Bernstein L. R. (1985) Germanium geochemistry and mineralogy. *Geochim. Cosmochim. Acta* **49**, 2409–2422.

Bischoff A., Schleiting M., Wieler R. and Patzek M. (2018) Brecciation among 2280 ordinary chondrites – constraints on the evolution of their parent bodies. *Geochim. Cosmochim. Acta* **238**, 516–541.

Bogard D. D., Garrison D. H. and McCoy T. J. (2000) Chronology and petrology of silicates from IIE iron meteorites: evidence of a complex parent body evolution. *Geochim. Cosmochim. Acta* **64**(12), 2133–2154.

Bryson J. F. J., Weiss B. P., Getzin B., Abrahams J. N. H., Nimmo F. and Scholl A. (2019) Paleomagnetic evidence for a partially differentiated ordinary chondrite parent asteroid. *J. Geophys. Res. Planets* **124**(7), 1880–1898.

Budde G., Burkhardt C., Brennecka G. A., Fischer-Gödde M., Kruijer T. S. and Kleine T. (2016) Molybdenum isotopic evidence for the origin of chondrules and a distinct genetic heritage of carbonaceous and non-carbonaceous meteorites. *Earth Planet. Sc. Lett.* **454**, 293–303.

Burkhardt C., Kleine T., Oberli F., Pack A., Bourdon B. and Wieler R. (2011) Molybdenum isotope anomalies in meteorites: constraints on solar nebula evolution and origin of the Earth. *Earth Planet. Sc. Lett.* **312**(3–4), 390–400.

Chabot N. L., Campbell A. J., Jones J. H., Humayun M. and Agee C. B. (2003) An experimental test of Henry's Law in solid metal-liquid metal systems with implications for iron meteorites. *Meteorit. Planet. Sci.* **38**, 181–196.

Chabot N. L. and Jones J. H. (2003) The parameterization of solid metal-liquid metal partitioning of siderophile elements. *Meteorit. Planet. Sci.* **38**, 1425–1436.

Choi B.-G., McKeegan K. D., Krot A. N. and Wasson J. T. (1998) Extreme oxygen-isotope compositions in magnetite from unequilibrated ordinary chondrites. *Nature* **392**, 577–579.

Chou C.-L., Baedecker P. A. and Wasson J. T. (1973) Distribution of Ni, Ga, Ge and Ir between metal and silicate portions of H-group chondrites. *Geochim. Cosmochim. Acta* **37**, 2159–2171.

Chou C.-L. and Cohen A. J. (1973) Gallium and germanium in the metal and silicates of L- and LL-chondrites. *Geochim. Cosmochim. Acta* **37**, 315–327.

Clayton R. N. and Mayeda T. K. (1988) Formation of ureilites by nebular processes. *Geochim. Cosmochim. Acta* **52**, 1313–1318.

Clayton R. N. and Mayeda T. K. (1996) Oxygen isotope studies of achondrites. *Geochim. Cosmochim. Acta* **60**, 1999–2017.

Clayton R. N., Mayeda T. K., Goswami J. N. and Olsen E. J. (1991) Oxygen isotope studies of ordinary chondrites. *Geochim. Cosmochim. Acta* **55**, 2317–2337.

Davis A. M. and Richter F. M. (2014) 1.10 - Condensation and evaporation of solar system materials. In *Treatise on Geochemistry (second ed.)* (eds. H. D. Holland and K. K. Turekian). Elsevier, Oxford, pp. 335–360.

Dedina J. and Tsalev D. L. (1995) *Hydride generation, atomic absorption spectrometry*. Wiley, Chichester (UK).

Dodd R. T. (1968) Recrystallized chondrules in the Sharps (H-3) chondrite. *Geochim. Cosmochim. Acta* **32**, 1111–1120.

Dodd R. T. and Jarosewich E. (1979) Incipient melting in and shock classification of L-group chondrites. *Earth Planet. Sc. Lett.* **44**, 335–340.

Dunn T. L., McCoy T. J., Sunshine J. M. and McSween, Jr, H. Y. (2010) A coordinated spectral, mineralogical, and compositional study of ordinary chondrites. *Icarus* **208**(2), 789–797.

El Korh A., Luais B., Boiron M.-C., Deloule E. and Cividini D. (2017) Investigation of Ge and Ga exchange behaviour and Ge isotopic fractionation during subduction zone metamorphism. *Chem. Geol.* **449**, 165–181.

Elkins-Tanton L. T., Weiss B. P. and Zuber M. T. (2011) Chondrites as samples of differentiated planetesimals. *Earth Planet. Sc. Lett.* **305**, 1–10.

Escoube R., Rouxel O. J., Luais B., Ponzevera E. and Donard O. F. X. (2012) An intercomparison study of the germanium isotope composition of geological reference materials. *Geostand. Geoanal. Res.* **36**, 149–159.

Folco L., Bland P. A., D'Orazio M., Franchi I. A., Kelley S. P. and Rocchi S. (2004) Extensive impact melting on the H-chondrite parent asteroid during the cataclysmic bombardment of the early solar system: evidence from the achondritic meteorite Dar al Gani 89611Associate editor: W.U. Reimold. *Geochim. Cosmochim. Acta* **68**, 2379–2397.

Fouché K. F. and Smales A. A. (1967) The distribution of trace elements in chondritic meteorites. 1. Gallium, Germanium and Indium. *Chem. Geol.* **2**, 5–33.

Göpel C., Manhès G. and Allègre C. J. (1994) U/Pb systematics of phosphates from equilibrated ordinary chondrites. *Earth Planet. Sc. Lett.* **121**, 153–171.

Grossman L. and Larimer J. W. (1974) Early chemical history of the solar system. *Rev. Geophys.* **12**, 71.

Grossman J. N. and Zipfel J. (2001) The meteoritical bulletin, No. 85, 2001 September. *Meteorit. Planet. Sci.* **36**, A293–A322.

Guignard J. and Toplis M. (2015) Textural properties of iron rich phases in H ordinary chondrites and quantitative links to the degree of thermal metamorphism. *Geochim. Cosmochim. Acta* **149**, 46–63.

Hellmann J. L., Kruijer T. S., Van Orman J. A., Metzler K. and Kleine T. (2019) Hf-W chronology of ordinary chondrites. *Geochim. Cosmochim. Acta* **258**, 290–309.

Humayun M. and Campbell A. J. (2002) The duration of ordinary chondrite metamorphism inferred from tungsten microdistribution in metal. *Earth Planet. Sc. Lett.* **198**(1–2), 225–243.

Hutchison R., Alexander C. M. O. and Barber D. J. (1987) The Semarkona meteorite: first recorded occurrence of smectite in an ordinary chondrite, and its implications. *Geochim. Cosmochim. Acta* **51**, 1875–1882.

Jarosewich E. (1990) Chemical analyses of meteorites: A compilation of stony and iron meteorites analyses. *Meteoritics* **25**, 323–337.

Kallemeyn G. W., Rubin A. E., Wang D. and Wasson J. T. (1989) Ordinary chondrites: bulk compositions, classification, lithophile-element fractionations and composition-petrographic type relationships. *Geochim. Cosmochim. Acta* **53**, 2747–2767.

Kegler P. and Holzheid A. (2011) Determination of the formal Ge-oxide species in silicate melts at oxygen fugacities applicable to terrestrial core formation scenarios. *ejm* **23**, 369–378.

Kita N. T., Nagahara H., Tachibana S., Tomomura S., Spicuzza M. J., Fournelle J. H. and Valley J. W. (2010) High precision SIMS oxygen three isotope study of chondrules in LL3 chondrites: role of ambient gas during chondrule formation. *Geochim. Cosmochim. Acta* **74**, 6610–6635.

Kleine T., Touboul M., Van Orman J. A., Bourdon B., Maden C., Mezger K. and Halliday A. N. (2008) Hf–W thermochronometry: closure temperature and constraints on the accretion and cooling history of the H chondrite parent body. *Earth Planet. Sc. Lett.* **270**, 106–118.

Krot A. N., Zolensky M. E., Wasson J. T., Scott E. R. D., Keil K. and Ohsumi K. (1997) Carbide-magnetite assemblages in type-3 ordinary chondrites. *Geochim. Cosmochim. Acta* **61**, 219–237.

Krot A. N., Keil K., Scott E. R. D., Goodrich C. A. and Weisberg M. K. (2014) Classification of meteorites and their genetic relationships. *Meteorites Cosmochem. Process.*, 1–63.

Lauretta D. S., Lodders K., Fegley B. and Kremser D. T. (1997) The origin of sulfide-rimmed metal grains in ordinary chondrites. *Earth Planet. Sc. Lett.* **151**, 289–301.

Lichtenberg T., Golabek G. J., Dullemond C. P., Schönbächler M., Gerya T. V. and Meyer M. R. (2018) Impact splash chondrule formation during planetesimal recycling. *Icarus* **302**, 27–43.

Lodders K., Palme H. and Gail H. (2009) Abundances of the elements in the solar system. In *LandoltBörnstein, New Series*, Vol. VI/4B (ed. J. E. Trümper). Springer-Verlag, Berlin, Heidelberg, New York, pp. 560–630 (Chap. 4.4).

Luais B. (2007) Isotopic fractionation of germanium in iron meteorites: Significance for nebular condensation, core formation and impact processes. *Earth Planet. Sc. Lett.* **262**, 21–36.

Luais B., Carlier L, de Veslud C., Géraud Y. and Gauthier-Lafaye F. (2009) Comparative behavior of Sr, Nd and Hf isotopic systems during fluid-related deformation at middle crust levels. *Geochim. Cosmochim. Acta* **73**, 2961–2977.

Luais B. (2012) Germanium chemistry and MC-ICPMS isotopic measurements of Fe–Ni, Zn alloys and silicate matrices: Insights into deep Earth processes. *Chem. Geol.* **334**, 295–311.

Mare E. R., Tomkins A. G. and Godel B. M. (2014) Restriction of parent body heating by metal-troilite melting: thermal models for the ordinary chondrites. *Meteorit. Planet. Sci.* **49**, 636–651.

Mason B. (1963) Olivine composition in chondrites. *Geochim. Cosmochim. Acta* **27**, 1011–1023.

McDermott K. H., Greenwood R. C., Scott E. R. D., Franchi I. A. and Anand M. (2016) Oxygen isotope and petrological study of silicate inclusions in IIE iron meteorites and their relationship with H chondrites. *Geochim. Cosmochim. Acta* **173**, 97–113.

McSween H. Y. and Labotka T. C. (1993) Oxidation during metamorphism of the ordinary chondrites. *Geochim. Cosmochim. Acta* **57**, 1105–1114.

Monnereau M., Toplis M. J., Baratoux D. and Guignard J. (2013) Thermal history of the H-chondrite parent body: Implications for metamorphic grade and accretionary time-scales. *Geochim. Cosmochim. Acta* **119**, 302–321.

Okabayashi S., Yokoyama T., Nakanishi N. and Iwamori H. (2019) Fractionation of highly siderophile elements in metal grains from unequilibrated ordinary chondrites: implications for the origin of chondritic metals. *Geochim. Cosmochim. Acta* **244**, 197–215.

Olsen E. and Jarosewich E. (1971) Chondrules: first occurrence in an iron meteorite. *Science* **174**, 583–585.

Pack A., Tanaka R., Hering M., Sengupta S., Peters S. and Nakamura E. (2016) The oxygen isotope composition of San Carlos olivine on the VSMOW2-SLAP2 scale. *Rapid Commun. Mass Spectrom.* **30**, 1495–1504.

Reisener R. J. and Goldstein J. I. (2003) Ordinary chondrite metallography: Part 1. Fe-Ni taenite cooling experiments. *Meteorit. Planet. Sci.* **38**, 1669–1678.

Reisener R. J., Goldstein J. I. and Petaev M. I. (2006) Olivine zoning and retrograde olivine-orthopyroxene-metal equilibration in H5 and H6 chondrites. *Meteorit. Planet. Sci.* **41**, 1839–1852.

Richter F. M. (2004) Timescales determining the degree of kinetic isotope fractionation by evaporation and condensation. *Geochim. Cosmochim. Acta* **23**, 4971–4992.

Romig A. D. and Goldstein J. I. (1978) Determination of the Fe-rich portion of the Fe-Ni-C phase diagram. *MTA* **9**, 1599–1609.

Rouxel O. J. and Luais B. (2017) Germanium isotope geochemistry. *Rev. Mineral. Geochem.* **82**, 601–656.

Rubin A. E. (1990) Kamacite and olivine in ordinary chondrites: intergroup and intragroup relationships. *Geochim. Cosmochim. Acta* **54**, 1217–1232.

Rubin A. E. (1994) Metallic copper in ordinary chondrites. *Meteoritics* **29**, 93–98.

Rubin A. E. (2003) Chromite-plagioclase assemblages as a new shock indicator; implications for the shock and thermal histories of ordinary chondrites. *Geochim. Cosmochim. Acta* **67**, 2695–2709.

Rubin A. E. (2005) Relationships among intrinsic properties of ordinary chondrites: oxidation state, bulk chemistry, oxygen-isotopic composition, petrologic type, and chondrule size. *Geochim. Cosmochim. Acta* **69**, 4907–4918.

Rushmer T., Petford N., Humayun M. and Campbell A. J. (2005) Fe-liquid segregation in deforming planetesimals: coupling Core-Forming compositions with transport phenomena. *Earth Planet. Sc. Lett.* **239**, 185–202.

Ruzicka A. (2014) Silicate-bearing iron meteorites and their implications for the evolution of asteroidal parent bodies. *Chem. Erde-Geochm.* **74**, 3–48.

Ruzicka A., Killgore M., Mittlefehldt D. W. and Fries M. D. (2005) Portales Valley: petrology of a metallic-melt meteorite breccia. *Meteorit. Planet. Sci.* **40**, 261–295.

Sears D. W. (1978) Condensation and the composition of iron meteorites. *Earth Planet. Sc. Lett.* **41**, 128–138.

Stöffler D., Keil K. and Edward R. D. S. (1991) Shock metamorphism of ordinary chondrites. *Geochim. Cosmochim. Acta* **55**, 3845–3867.

Tait A. W., Tomkins A. G., Godel B. M., Wilson S. A. and Hasalova P. (2014) Investigation of the H7 ordinary chondrite, Watson 012: Implications for recognition and classification of Type 7 meteorites. *Geochim. Cosmochim. Acta* **134**, 175–196.

Tandon S. N. and Wasson J. T. (1968) Gallium, germanium, indium and iridium variations in a suite of L-group chondrites. *Geochim. Cosmochim. Acta* **32**, 1087–1109.

Tomkins A. G., Weinberg R. F., Schaefer B. F. and Langendam A. (2013) Disequilibrium melting and melt migration driven by impacts: Implications for rapid planetesimal core formation. *Geochim. Cosmochim. Acta* **100**, 41–59.

Trieloff M., Jessberger E. K., Herrwerth I., Hopp J., Fiéni C., Ghélis M., Bourot-Denise M. and Pellas P. (2003) Structure and thermal history of the H-chondrite parent asteroid revealed by thermochronometry. *Nature* **422**, 502–506.

Urey H. C. and Craig H. (1953) The composition of the stone meteorites and the origin of the meteorites. *Geochim. Cosmochim. Acta* **4**, 36–82.

Valley J. W., Kitchen N., Kohn M. J., Niendorf C. R. and Spicuzza M. J. (1995) UWG-2, a garnet standard for oxygen isotope ratios: Strategies for high precision and accuracy with laser heating. *Geochim. Cosmochim. Acta* **59**(24), 5223–5231.

Van Schmus W. R. and Wood J. A. (1967) A chemical-petrologic classification for the chondritic meteorites. *Geochim. Cosmochim. Acta* **31**, 747–765.

Wai C. M. and Wasson J. T. (1977) Nebular condensation of moderately volatile elements and their abundances in ordinary chondrites. *Earth Planet. Sc. Lett.* **36**, 1–13.

Wai C. M. and Wasson J. T. (1979) Nebular condensation of Ga, Ge and Sb and the chemical classification of iron meteorites. *Nature* **282**, 790.

Warren P. H. and Huber H. (2006) Ureilite petrogenesis: A limited role for smelting during anatexis and catastrophic disruption. *Meteorit. Planet. Sci.* **41**, 835–849.

Wasson J. T. (2017) Formation of non-magmatic iron-meteorite group IIE. *Geochim. Cosmochim. Acta* **197**, 396–416.

Wasson J. T. (1972) Formation of ordinary chondrites. *Rev. Geophys.* **10**(3), 711–759.

Wasson J. T. (1974) *Meteorites: Classification and Properties*. Springer-Verlag, Berlin, Heidelberg.

Wasson J. T. (2000) Oxygen-isotopic evolution of the solar nebula. *Rev. Geophys.* **38**, 491–512.

Wasson J. T. and Kallemeyn G. W. (1988) Compositions of chondrites. *Philos. Trans. Roy. Soc. Math. Phys. Eng. Sci.* **325**, 535–544.

Wasson J. T. and Krot A. N. (1994) Fayalite-silica association in unequilibrated ordinary chondrites: evidence for aqueous alteration on a parent body. *Earth Planet. Sc. Lett.* **122**, 403–416.

Wasson J. T. and Wang J. (1986) A nonmagmatic origin of group-IIE iron meteorites. *Geochim. Cosmochim. Acta* **50**, 725–732.

Wood B. J., Smythe D. J. and Harrison T. (2019) The condensation temperatures of the elements: a reappraisal. *Am. Mineral.* **104** (6), 844–856.

Yoneda S. and Grossman L. (1995) Condensation of CaO-MgO-Al_2O_3-SiO_2 liquids from cosmic gases. *Geochim. Cosmochim. Acta* **59**, 3413–3444.

Zanda B. (2004) Chondrules. *Earth Planet. Sc. Lett.* **224**, 1–17.

Zanda B., Hewins R., Bourot-Denise M., Bland P. and Albarede F. (2006) Formation of solar nebula reservoirs by mixing chondritic components. *Earth Planet. Sc. Lett.* **248**, 650–660.

Associate editor: Fang Huang

Chapter 6

Conclusions, ongoing project and perspectives

Table of contents

I. Conclusions

My PhD studies were focused on metal formation and evolution in two primitive chondrites groups: the Carbonaceous Bencubbinite chondrites (CB) and the ordinary chondrites. The main objectives of that PhD were to (1) constrain metal grain condensation at intermediate temperature (chapter 3); (2) investigate the effects of heating events on the metal phase and to bring constrains on the metal precursor (chapter 4); (3) constrain oxidation effects on the metal phase (chapter 4 and 5); (4) enhance our understanding of the genetic links between ordinary chondrite groups (chapter 5). To answer these questions, we have chosen to study the moderately volatile and refractory elements, as well as the germanium isotopes of these two meteorite groups. Thus, I have performed (1) in–situ elemental measurements on metal phases in CB and H ordinary chondrites at Macquarie University (Sydney–Australia); (2) germanium isotopic measurements on metal from CB and ordinary chondrites, as well as on bulk, sulfide, and silicate phases from all ordinary chondrite groups at the CRPG–Nancy (France).

In the chapter 3, we present our first study focused on the characterisation of the metal phase condensation at intermediate temperature (~850 K). We have investigated the Ge isotopic composition ($\delta^{74/70}$Ge) in metal grains from the two CB chondrite groups, CB_a and CB_b. In the first part of the chapter, we have shown that the CB_a and the CB_b groups have two distinct germanium isotopic compositions, $\delta^{74/70}Ge_{mean}$ = 0.97 ± 0.2‰ and $\delta^{74/70}$Ge = -0.65 ± 0.1‰, respectively. We suggest that the two distinct $\delta^{74/70}$Ge signatures reflect two distinct cooling dynamics. Previous studies demonstrated that the two groups are closely related (e.g. Weisberg et al., 2001, Campbell et al., 2002) and possibly formed by condensation after impact (Weyrauch et al., 2019). If the two groups formed at two different cooling rates, the distinct isotopic compositions agree with their condensation in a thermally zoned plume. Therefore, the CB_a can be formed in the inner part of the plume where the temperature is stable and the CB_b in the outer part of the plume where the temperature drops quickly (Fig. 6.1 A). In the second part of that study, we show a decrease of the $\delta^{74/70}$Ge from the core of CB_a metallic grains to their edges (e.g. $\delta^{74/70}$Ge = 1.03 ± 0.19‰; 0.71 ± 0.22‰; 0.65 ± 0.20‰, respectively). These zonations highlight that important effect of evaporation / re–condensation happened during the formation of metal grains (Fig. 6.1 B). It also demonstrates the suitability of germanium isotopes for recording the late stages of metal condensation, contrary to Fe, Ni that have a higher temperature of condensation.

The centre of the chapter 4 was the formation of metal by heating event in the solar nebula. Whereas previous studies focused on the highly siderophile and refractory elements, we have combined the use of moderately volatile elements (e.g. Ga, Ge) to refractory elements to study metal phase formation. We have shown that the Ge/Ir ratio is a tracer of metal melting when metal contains carbon. We also highlight a large grain to grain variation in refractory elements

in primitive H ordinary chondrites and a correlation of these variations with the Ge/Ir ratio. We conclude that this is the result of metal partial melting before accretion in presence of ~5.2% of carbon in the metal (Fig. 6.1 C). An issue is the large variations of W, Mo and Ga between metal grains, which disagree with the metal melting model. Yet, in agreement with the positive $\Delta^{74/70}Ge_{metal-silicate}$ (Chapter 5), we suggest that it results from metal-silicate interaction and local variations (from grain to grain) in oxidation state between chondrite particle before accretion (Fig. 6.1 D). The results imply that the precursors of OC were not highly oxidized, but that an oxidizing component occurred within metal and silicate precursors. Thus, the various oxidation states can have been triggered by heterogeneous repartition of this oxidizing component in chondrite precursors (Fig. 6.1 D). This hypothesis provides a good explanation for the large variability of iron content in olivine of unequilibrated ordinary chondrites (Fig. 6.1 E). Finally, we have shown that the metal in H ordinary chondrites has been homogenised in a closed system during metamorphism. Consequently, the formation of large metallic veins as in the H6 Portales Valley, can result from melting of the metal present within the parent body.

The chapter 5 explores the germanium isotopic differences through the OC sequence. The major conclusion is that the three groups are distinguishable by their germanium isotopic compositions, which increase from H to L and to LL groups ($\delta^{74/70}Ge_{metal} = -0.51 \pm 0.09‰$; $-0.31 \pm 0.06‰$; $-0.26 \pm 0.09‰$, respectively; Fig. 6.1 F). These $\delta^{74/70}Ge$ variations in the metal and in the bulk from one group to another are correlated with the increase of $\delta^{18}O$, $\Delta^{17}O$ and %Fa (Fig. 6.1 F). We suggest that these correlations are the result of the accretion of an oxidizing agent with a high $\delta^{74/70}Ge$, $\delta^{18}O$, and $\Delta^{17}O$ (Fig. 6.1 G). During metamorphism, germanium and oxygen isotopes will be released by the oxidizing component. The produced fluid has triggered metal oxidation and the incorporation of heavy germanium isotopes in metal. The $\delta^{74/70}Ge$ of the metal consequently increases while the oxidized metal produces iron oxide with high oxygen isotopic composition (Fig. 6.1 H, Choi et al., 1998). The presence of a significant amount of Ge in the oxidizing component implies that it cannot be pure ice or water, and is more likely a hydrated silicate, such as phyllosilicate. This model shows that the oxidation is not only linked to ice or water accretion, but also that hydrated minerals can be carriers of the oxidant fluid. Moreover, we have emphasized that the combined use of $\delta^{74/70}Ge$ in the metal and $\Delta^{17}O$ in the silicate have a high potential to highlight genetic links between meteorites.

During this PhD, we have combined the use of refractory, moderately volatile and siderophile elements with the isotopic composition of the germanium in metal phase. With these new results, we have brought additional constrains to the formation and evolution of the metal phase from condensation to nebular processes and to parent body processes. Our major conclusions are as follow:

1) The $\delta^{74/70}Ge$ can trace the dynamics of condensation even after Fe-Ni condensation. An enrichment in light isotopes compared to the source reservoir is an indication for high

cooling rate, while a heavier composition is likely the result of a quick evaporation followed by slow cooling.

2) At odds with previous studies, we demonstrate that the metal precursor in ordinary chondrites was not particularly oxidized, and that the variation in redox state within chondrite precursors can be very local during heating event in the solar nebula. Consequently, it is very important to consider the grain to grain redox variations to understand the formation of such objects. It implies that some volatile elements may not require a large global enrichment to be highly concentrated in chondrules, for example.
3) The difference between the three ordinary chondrites groups is, at least, partly established during a melting event in the solar nebula. Also, the variable proportion of reducing component in a carbon form in their environments must have played a role in metal composition. This local variation in oxidation state can, for example, account for the large range of Fe content in silicate minerals of very primitive ordinary chondrites (type petrologic <3.4). Finally, a second oxidation step occurred on the parent body. This is, at least, partly the result of the accretion of hydrated phyllosilicates and is responsible for the increase of $\delta^{74/70}$Ge and Δ^{17}O through the OCs sequence.
4) The combined use of siderophile and lithophile elements, allows to highlight complex genetic links between meteorite groups.

We can conclude that the use of germanium isotopes as well as other moderately siderophile elements is of primary importance to understand the processes that lead to the formation of pristine metal, and thus to the planet formations.

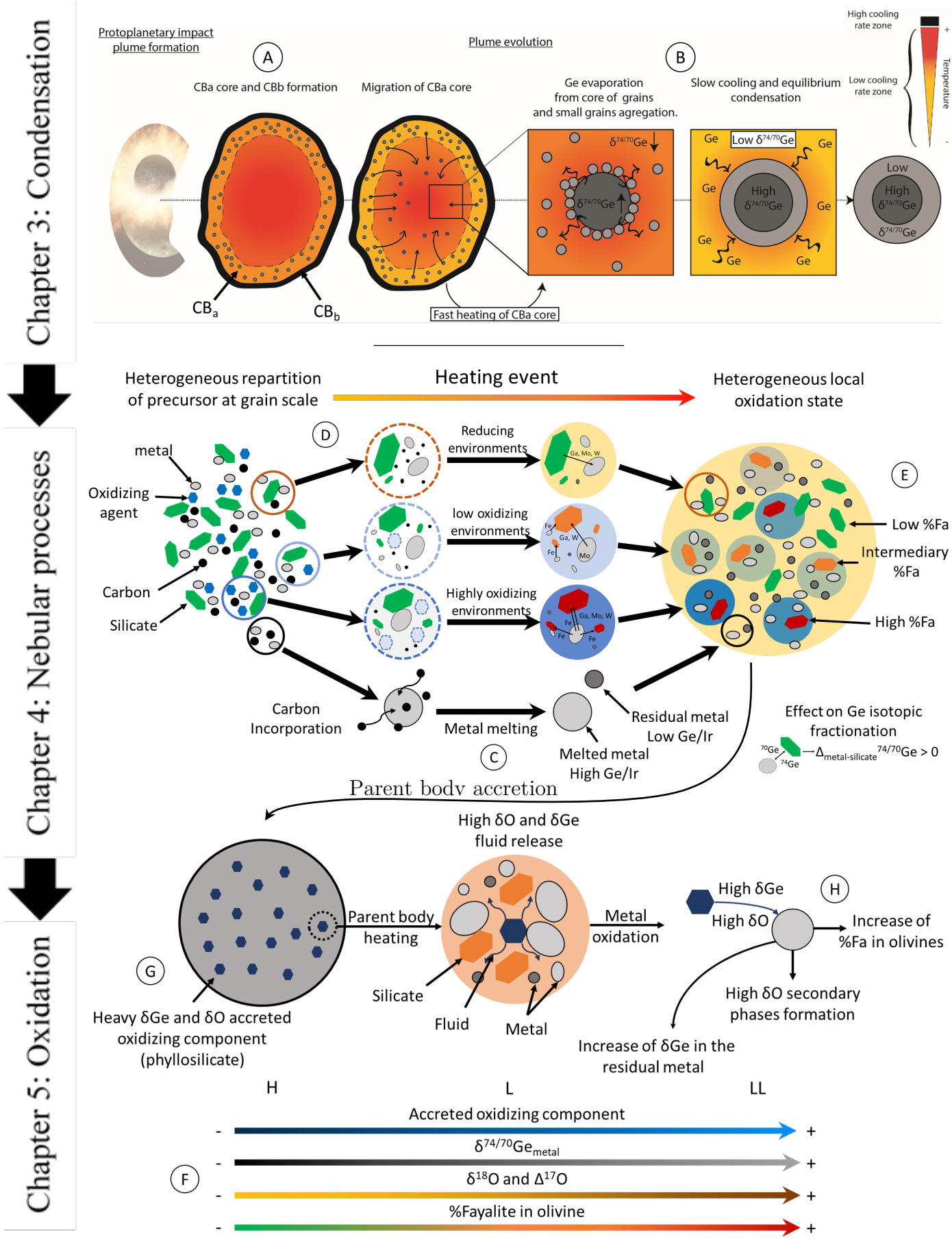

Figure 6.1: Schematic representation of the thesis conclusions

II. Ongoing project: Migration of the metal in parent bodies and core formation

1 Introduction

The question of the formation of a metallic core by metal migration inside of a large asteroid or a protoplanet is of a main importance to understand planet formation in the Solar System. Through a series of twelve scientific communications (*The chemical classification of iron meteorites*) between 1967 and 1998, Wasson and collaborators classified the iron meteorites in function of their chemical composition. They divided iron meteorites into two groups, the magmatic group and the non–magmatic group in function of their Ge, Ir, Ni but also Au and Ga content. These groups have been confirmed by their germanium isotope compositions (Luais, 2007, 2012). Wasson and collaborators suggest that magmatic iron meteorites were the core of partly differentiated protoplanets. More recently, Goldstein et al. (2009) summarized chemical data for magmatic iron meteorites, and proposed, on the basis of their Ir, Ni and Ge contents, that the chemical variations in each magmatic group is the result of fractional crystallisation on more than 50 distinct bodies.

However, the mechanism of parent body differentiation, and the processes of metal–silicate segregation within a parent body are not well understood. Regardless of the numerical simulations, it is difficult to reproduce the complex mineral assemblages of the known planetary mantles, cores or their chemistry (e.g. Šrámek et al. 2010, 2012). In addition, it is commonly assumed that the first large objects in the Solar System were formed by the accretion of primitive particles and then differentiated to form larger bodies with a metallic core surrounded by silicate. However, it has been demonstrated that the majority of the magmatic iron meteorites has been formed before the formation of the primitive chondrites (Qin et al. 2008). This observation is at the odds of the previous hypotheses and rules out the possibility for "primitive" chondrites (e.g. ordinary or carbonaceous chondrites) to be the precursors of iron meteorites.

Regarding the capacity of germanium to differentiate the distinct iron meteorites groups, as well as the germanium isotopic composition of magmatic iron meteorites, we decided to run experiments of germanium isotopic fractionation between melted and unmelted metal. This work is currently an ongoing project at Macquarie University (Sydney–Australia). In the following part we describe the analytical procedures and give first results.

2 Experimental procedures

Tracking the evolution of the germanium isotopic composition also implies to perform in–situ elemental measurements to be able to quantify the degree of melting as well as the elemental fractionation between the two phases. Thus, this project is divided into three major parts: (1) Producing experimental samples by melting metal using the piston cylinder apparatus; (2) Analysing the elemental composition of the two phases by LA–ICP–MS; (3) Measuring the germanium isotopic composition of the melted and the unmelted metal phase.

The first part is the centre of the project and consists of melting experiments under 1GPa to simulate the effect of the pressure on a 30 to 100 km diameter body. This is divided into two experimental series, time-series experiments that aim to image the effect of equilibration on the germanium isotopic composition of the melted and unmelted phase for a given percentage of melting. The second series is a temperature-series experiments that aim to image the effect on the germanium isotopic composition of the melted and unmelted phase for an increase in the percentage of melting at a given time. The goal is to explore both, the effect of a very short melting event like impacts and very long heating events like radiogenic decay (e.g. ^{26}Al, ^{60}Fe). To perform the project, we have used an iron meteorite with 1) homogeneous texture with only one metallic phase, e.g. hexaedrites with Ni $< 6.5\%$ and composed only of kamacite, 2) well-characterised elemental compositions, with a sufficient germanium content to be easily measured, and 3) known germanium isotopic composition. Another constraint is the percentage of sulfide of sample that needs to be low because the germanium is highly incompatible with a FeNi-$S_{\text{-rich}}$ fluid. The presence of S can add a level of complexity and highly modify the germanium isotopic composition and thus induces bias. Therefore, we have chosen the well-characterised and mostly homogeneous Coahuila meteorite from the IIA group of the magmatic iron classification, with Ge content of 178 ppm (Wasson, 1969), and $\delta^{74/70}$Ge of 1.42 ± 0.06‰ (Luais, 2007, 2012).

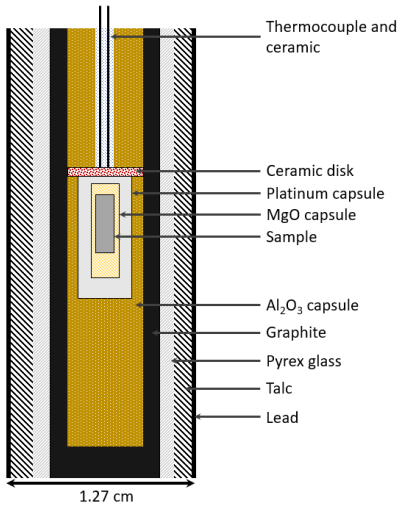

Figure 6.2: Schematic representation of an assemblage for piston cylinder experiments at 1 GPa. (Herpfer and Larimer, 1993; Righter et al., 2005, 2010)

The issue with a FeNi alloy that contain no sulfide is the high melting temperature around 1540°C that constrains the capsules because of the needed high temperature for partial

melting. Additionally, the presence of carbon in the FeNi system highly modifies the elemental behaviour during melting, which also rules out the use of inner carbon capsule. Hence, the sample is encapsulated in a MgO capsule and then in a platinum capsule. This assemblage is encapsulated in a larger capsule composed of Al_2O_3 / pyrex glass / talc / lead (Figure 6.2).

No data exists for pure FeNi melting at 1 GPa, so we have incrementally searched for the solidus temperature. Time-series and temperature-series steps will be defined according to that temperature. Until now, two experiments have been made. For the first one, the target temperature was 1520 °C for 30 minutes and 1GPa, but the temperature was too low to melt the sample. For the second experiment, the target temperature was 1560 °C. However, the thermocouple broke during the experimentation and the capsule as well as the sample melted, meaning that the temperature increased over the melting temperature of the platinum capsule (~1768 °C at 1 atm).

Once we have the successful experimental samples and can show appropriate degrees of partial melting, the samples would be cut in half. The first part will be analysed for elemental concentration with the LA–ICP–MS. From the second part, the melted and the unmelted phases will be separated using a MicroMill device for Ge isotopic measurements by MC–ICP–MS at the CRPG–Nancy (France). From these experiments we are expecting Ge isotopic fractionation that could help to make the link between primitive metal and the iron meteorites, as well as to explain the elemental and isotopic differences between iron meteorite groups.

III. Perspectives on Ordinary Chondrites

Within the ordinary chondrite groups, some major areas of uncertainty remain. For example, it has been demonstrated that the percentage of metal decreases from the H to the L and to the LL group (Urey and Craig, 1953). At first glance, this increase is correlated with an increase of the oxidation state and can be attributed to the incorporation of Fe in silicates. Yet first studies on ordinary chondrites demonstrate a decrease of the iron content in the bulk from H to L, to LL, implying a loss of iron between the three groups (Urey and Craig, 1953). This iron loss is not explained at the moment and is usually attributed to the composition of ordinary chondrites precursors or to iron volatilisation.

Secondly, many different types of chondrules exist in ordinary chondrites (Scott and Krot 2014). They reflect multiple conditions of cooling rates, environments of formation as well as precursor compositions (Jones 2012). The presence of all these different types of chondrules cannot be the result of a single event such as precursor melting as suggested for the metal in chapter 4. It implies that OCs environment experienced chondrule mixing during their accretion. One possibility is that chondrules have been carried from various regions of the disk to the OCs formation environments, or that the environment of OCs formation was sufficiently heterogeneous in terms of temperature and composition to allow the creation of the various types of chondrules in the OCs region. More research is needed in this direction. Recent studies on oxygen isotopic compositions Kita et al. (2008, 2010) try to explain the formation of chondrules in pristine chondrites. They suggest that a component with a high oxygen anomaly drag chondrule isotopic composition in OCs chondrites to very high oxygen composition. Once again, the large variability of chondrule compositions makes difficult to constrain their formation.

Ordinary chondrite groups represent the largest group of meteorites in museum collections. One of the major issues concerns the pristine OCs meteorites that were analysed these last decades. The large majority of the data have been mostly acquired on one L and one LL, Bishunpur (L3.15) and Semarkona (LL3.0), respectively. The petrological and chemical characteristics of the silicates and the metal in these meteorites are well known by detailed studies on these two chondrites. However, the trichotomy between H, L and LL remain highly difficult to deconvolute. One of the main issues is the lack of highly detailed studies of very primitive H samples so they can be compared to the primitive L and LLs. A possible way to bring some additional information about OCs formation is to fully characterise a very pristine H chondrite to compare it to the primitive Bishunpur and Semarkona chondrites. This work on a recently acquired very primitive H chondrite will be undertaken after this PhD.

As ordinary chondrites are the major primitive representant of the inner Solar System that originate in the asteroid belt, this will help to explain the chemical spatial evolution of the inner

Solar System. Also, it will lead to understand the reasons for the lack of planet in the area of the asteroid belt, and to highlight potential chemical or physical gradients in the inner Solar System.

In a broader context, the recent discovery of protoplanetary disk in others planetary system needs to be taken into account for the future studies of the Solar System formation. Indeed, if the different concentric disks (figure 6.3) that are observed in such structures are the result of different gas proportion or gas composition, it may help to constrain the thermodynamic parameters (pressure, temperature, etc.) as well as the chemistry of the early stage evolution of the Solar System. For example, the very controversial early formation of Jupiter would not be needed if the concentric disks in young protoplanetary disks were the result of pressure bumps (Braser and Mojzes, 2020). Thus, a model that would be able to unify the evolution of the primitive chondrites to the astronomical observations of young protoplanetary disks will be able to validate or deny the recent theory of non-carbonaceous / carbonaceous dichotomy. And thus, it will be of great interest to explain the formation of the Solar System.

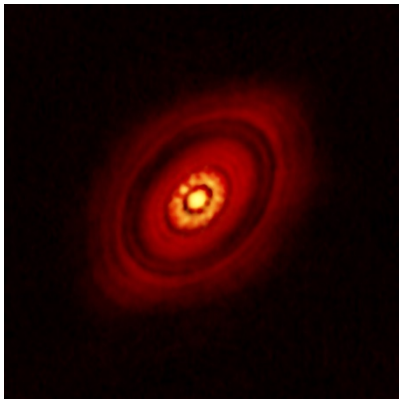

Figure 6.3: Image of a protoplanetary disk compute from data obtain with the ALMA telescope, the diameter is about 200 astronomical units. After Carrasco-González et al. (2016).

References

Alard O., Griffin W. L., Lorand J. P., Jackson S. E., and O'Reilly S. Y. 2000. Non-chondritic distribution of the highly siderophile elements in mantle sulphides. Nature 407:891–894.

Albarède F., and Beard B. 2004. Analytical Methods for Non-Traditional Isotopes. Reviews in Mineralogy and Geochemistry 55:113–152.

Alexander C. M. O., Barber D. J., and Hutchison R. 1989. The microstructure of Semarkona and Bishunpur. Geochimica et Cosmochimica Acta 53:3045–3057.

Anders E., and Grevesse N. 1989. Abundances of the elements: Meteoritic and solar. Geochimica et Cosmochimica Acta 53:197–214.

Baker J., Bizzarro M., Wittig N., Connelly J., and Haack H. 2005. Early planetesimal melting from an age of 4.5662 Gyr for differentiated meteorites. Nature 436:1127–1131.

Bearman R. J., and Jolly D. L. 1981. Mass dependence of the self diffusion coefficients in two equimolar binary liquid Lennard-Jones systems determined through molecular dynamics simulation. Molecular Physics 44:665–675.

Belissont R., Boiron M.-C., Luais B., and Cathelineau M. 2014. LA-ICP-MS analyses of minor and trace elements and bulk Ge isotopes in zoned Ge-rich sphalerites from the Noailhac – Saint-Salvy deposit (France): Insights into incorporation mechanisms and ore deposition processes. Geochimica et Cosmochimica Acta 126:518–540.

Belissont R. 2016. Germanium and related elements in sulphide minerals: crystal chemistry, incorporation and isotope fractionation.

Benedix G. K., Mccoy T. J., Keil K., and Love S. G. 2000. A petrologic study of the IAB iron meteorites: Constraints on the formation of the IAB-Winonaite parent body. Meteoritics & Planetary Science 35:1127–1141.

Bonnet, J., Cauzid, J., Testemale, D., Kieffer, I., Proux, O., Lecomte, A., & Bailly, L. (2017). Characterization of germanium speciation in sphalerite (ZnS) from Central and Eastern Tennessee, USA, by X-ray absorption spectroscopy. *Minerals*, *7*(5), 79.

Bouvier A., Brennecka G., and Wadhwa M. 2011. Absolute chronology of the first solids in the Solar System. p. 9054.

Brasser R., and Mojzsis S. J. 2020. The partitioning of the inner and outer Solar System by a structured protoplanetary disk. Nature Astronomy.

Brearley A. J. 1990. Carbon-rich aggregates in type 3 ordinary chondrites: Characterization, origins, and thermal history. Geochimica et Cosmochimica Acta 54:831–850.

Brezina A. 1904. The Arrangement of Collections of Meteorites. Proceedings of the American Philosophical Society 43:211–247.

Campbell A. J., and Humayun M. 1999. Microanalysis of Platinum Group Elements in Iron Meteorites Using Laser Ablation ICP-MS. In Microanalysis of Platinum Group Elements in Iron Meteorites Using Laser Ablation ICP-MS. Houston. p. 1974.

Campbell A. J., Humayun M., and Weisberg M. K. 2002. Siderophile element constraints on the formation of metal in the metal-rich chondrites Bencubbin, Weatherford, and Gujba. Geochimica et Cosmochimica Acta 66:647–660.

Campbell A. J., and Humayun M. 2003. Formation of metal in Grosvenor Mountains 95551 and comparison to ordinary chondrites. Geochimica et Cosmochimica Acta 67:2481–2495.

Campbell A. J., Humayun M., and Weisberg M. K. 2005a. Compositions of unzoned and zoned metal in the CB b chondrites Hammadah al Hamra 237 and Queen Alexandra Range 94627. Meteoritics & Planetary Science 40:1131–1148.

Campbell A. J., Zanda B., Perron C., Meibom A., and Petaev M. I. 2005b. Origin and Thermal History of Fe-Ni Metal in Primitive Chondrites. 26.

Cartier C., and Wood B. J. 2019. The Role of Reducing Conditions in Building Mercury. Elements 15:39–45.

Carrasco-González C. et al. 2016. The vla view of the hl tau disk: disk mass, grain evolution, and early planet formation. The Astrophysical Journal 821:L16.

Cavell R. G., Barnes E. M., Arboleda P. H., Cavell P. A., Feng R., Gordon R. A., and Webb M. A. 2004. An X-ray and electron microprobe study of Fe, Ni, Ga, and Ge distribution and local structure in a section of the Canyon Diablo iron meteorite. American Mineralogist 89:519–526.

Chabot N. L., and Jones J. H. 2003. The parameterization of solid metal-liquid metal partitioning of siderophile elements. Meteoritics & Planetary Science 38:1425–1436.

Chabot N. L., Wollack E. A., McDonough W. F., Ash R. D., and Saslow S. A. 2017. Experimental determination of partitioning in the Fe-Ni system for applications to modeling meteoritic metals. Meteoritics & Planetary Science 52:1133–1145.

Chabot N. L., and Haack H. 2006. Evolution of Asteroidal Cores. 26.

Choi B.-G., Ouyang X., and Wasson J. T. 1995. Classification and origin of IAB and IIICD iron meteorites. Geochimica et Cosmochimica Acta 59:593–612.

Choi B.-G., McKeegan K. D., Krot A. N., and Wasson J. T. 1998. Extreme oxygen-isotope compositions in magnetite from unequilibrated ordinary chondrites. Nature 392:577–579.

Chou C.-L., and Cohen A. J. 1973. Gallium and germanium in the metal and silicates of L- and LL-chondrites. Geochimica et Cosmochimica Acta 37:315–327.

Chou C.-L., Baedecker P. A., and Wasson J. T. 1973. Distribution of Ni, Ga, Ge and Ir between metal and silicate portions of H-group chondrites. Geochimica et Cosmochimica Acta 37:2159–2171.

Clarke R. S., and Scott E. R. D. 1980. Tetrataenite—ordered FeNi, a new mineral in meteorites. American Mineralogist 65:624–630.

Clayton R. N., Grossman L., and Mayeda T. K. 1973. A Component of Primitive Nuclear Composition in Carbonaceous Meteorites. Science 182:485–488.

Clayton R. N., and Mayeda T. K. 1996. Oxygen isotope studies of achondrites. Geochimica et Cosmochimica Acta 60:1999–2017.

Dasch E. J. 1996. Macmillan encyclopedia of earth sciences, Macmillan Library Reference.

Davis A. M., and Richter F. M. 2014. Condensation and Evaporation of Solar System Materials. In Treatise on Geochemistry. Elsevier. pp. 335–360

Davison T. M., O'Brien D. P., Ciesla F. J., and Collins G. S. 2013. The early impact histories of meteorite parent bodies. Meteoritics & Planetary Science 48:1894–1918.

DeCarlo E. Heinen., Zeitlin Harry., and Fernando Quintus. 1981. Simultaneous separation of trace levels of germanium, antimony, arsenic, and selenium from an acid matrix by adsorbing colloid flotation. Analytical Chemistry 53:1104–1107.

Desch S. J., Kalyaan A., and Alexander C. M. O. 2018. The Effect of Jupiter's Formation on the Distribution of Refractory Elements and Inclusions in Meteorites. The Astrophysical Journal Supplement Series 238:11.

Dodd R. T. 1981. Meteorites: A petrologic-chemical synthesis, CUP Archive.

El Korh A., Luais B., Boiron M.-C., Deloule E., and Cividini D. 2017. Investigation of Ge and Ga exchange behaviour and Ge isotopic fractionation during subduction zone metamorphism. Chemical Geology 449:165–181.

Elkins-Tanton L. T., Weiss B. P., and Zuber M. T. 2011. Chondrites as samples of differentiated planetesimals. Earth and Planetary Science Letters 305:1–10.

Elkins-Tanton L. T. 2017. The Taxonomy of Planetesimals: Consequences for Planets. Planetesimals: Early Differentiation and Consequences for Planets.

Escoube R., Rouxel O. J., Luais B., Ponzevera E., and Donard O. F. X. 2012a. An Intercomparison Study of the Germanium Isotope Composition of Geological Reference Materials. Geostandards and Geoanalytical Research 36:149–159.

Escoube R., Rouxel O. J., Luais B., Ponzevera E., and Donard O. F. X. 2012b. An Intercomparison Study of the Germanium Isotope Composition of Geological Reference Materials. Geostandards and Geoanalytical Research 36:149–159.

Farrington O. Cummings. 1907. Analyses of iron meteorites compiled and classified. Geological series 8:59–110.

Fedkin A. V., Grossman L., Humayun M., Simon S. B., and Campbell A. J. 2015. Condensates from vapor made by impacts between metal-, silicate-rich bodies: Comparison with metal and chondrules in CB chondrites. Geochimica et Cosmochimica Acta 164:236–261.

Fegley B., and Palme H. 1985. Evidence for oxidizing conditions in the solar nebula from Mo and W depletions in refractory inclusions in carbonaceous chondrites. Earth and Planetary Science Letters 72:311–326.

Fehr M. A., Rehkämper M., and Halliday A. N. 2004. Application of MC-ICPMS to the precise determination of tellurium isotope compositions in chondrites, iron meteorites and sulfides. International Journal of Mass Spectrometry 232:83–94.

Florin G., Luais B., Rushmer T., and Alard O. 2020. Influence of redox processes on the germanium isotopic composition of ordinary chondrites. Geochimica et Cosmochimica Acta 269:270–291.

Goldstein J. I., Scott E. R. D., and Chabot N. L. 2009. Iron meteorites: Crystallization, thermal history, parent bodies, and origin. Geochemistry 69:293–325.

Göpel C., Manhès G., and Allègre C. J. 1994. U/Pb systematics of phosphates from equilibrated ordinary chondrites. Earth and Planetary Science Letters 121:153–171.

Grady M. M. 2009. Astronomy by microscope. Astronomy & Geophysics 50:4–21.

Grossman L., and Larimer J. W. 1974. Early chemical history of the Solar System. Reviews of Geophysics 12:71.

Grossman L., and Olsen E. 1974. Origin of the high-temperature fraction of C2 chondrites. Geochimica et Cosmochimica Acta 38:173–187.

Guignard J., and Toplis M. J. 2015. Textural properties of iron-rich phases in H ordinary chondrites and quantitative links to the degree of thermal metamorphism. Geochimica et Cosmochimica Acta 149:46–63.

Haack H., and McCoy T. 2004. Iron and stony-iron meteorites. Treatise on Geochemistry, Meteorites, Comets and Planets, vol. 1.

Herpfer M. A., and Larimer J. W. 1993. Core Formation: an Experimental Study of Metallic Melt-Silicate Segregation. Meteoritics 28.

Hewins R. H., Yu Y., Zanda B., and Bourot-Denise M. 1997. Do nebular fractionations, evaporative losses, or both, influence chondrule compositions? Antarctic Meteorite Research 10:275–298.

Hirata T. 1997. Isotopic variations of germanium in iron and stony iron meteorites. Geochimica et Cosmochimica Acta 61:4439–4448.

Hirth J. P., and Pound G. M. 1963. Condensation and evaporation; nucleation and growth kinetics, New York: Macmillan.

Horan M. F., Alexander C. M. O., and Walker R. J. 2009. Highly siderophile element evidence for early Solar System processes in components from ordinary chondrites. Geochimica et Cosmochimica Acta 73:6984–6997.

Humayun M., and Clayton R. N. 1995. Potassium isotope cosmochemistry: Genetic implications of volatile element depletion. Geochimica et Cosmochimica Acta 59:2131–2148.

Huss G. R., Rubin A. E., and Grossman J. N. 2006. Thermal Metamorphism in Chondrites. Meteorites and the Early Solar System II 567–586.

Jarosewich E. 1990. Chemical analyses of meteorites: A compilation of stony and iron meteorite analyses. Meteoritics 25:323–337.

Johnson C. M., Beard B. L., and Albarède F. 2004. Overview and General Concepts. Reviews in Mineralogy & Geochemistry 55:1–24.

Jones R. H. 2012. Petrographic constraints on the diversity of chondrule reservoirs in the protoplanetary disk. Meteoritics & Planetary Science 47:1176–1190.

Kallemeyn G. W., and Wasson J. T. 1981. The compositional classification of chondrites—I. The carbonaceous chondrite groups. Geochimica et Cosmochimica Acta 45:1217–1230.

Kallemeyn G. W., Rubin A. E., Wang D., and Wasson J. T. 1989. Ordinary chondrites: Bulk compositions, classification, lithophile-element fractionations and composition-petrographic type relationships. Geochimica et Cosmochimica Acta 53:2747–2767.

Kallemeyn G. W., Rubin A. E., and Wasson J. T. 1991. The compositional classification of chondrites: V. The Karoonda (CK) group of carbonaceous chondrites. Geochimica et Cosmochimica Acta 55:881–892.

Kallemeyn G. W., Rubin A. E., and Wasson J. T. 1994. The compositional classification of chondrites: VI. The CR carbonaceous chondrite group. Geochimica et Cosmochimica Acta 58:2873–2888.

Kallemeyn G. W., Rubin A. E., and Wasson J. T. 2001. Compositional Studies of Bencubbin Dark Silicate Host and an OC Clast: Relationships to Other Meteorites and Implications for Their Origin. p. 2070

Kelly W. R., and Larimer J. W. 1977. Chemical fractionations in meteorites—VIII. Iron meteorites and the cosmochemical history of the metal phase. Geochimica et Cosmochimica Acta 41:93–111.

Kita N. T., Ushikubo T., Kimura M., Nyquist L. E., and Valley J. W. 2008. Heterogeneous oxygen isotope ratios of olivine in chondrules from Y-793408 (H3. 2) chondrite. Meteoritics and Planetary Science Supplement 43.

Kita N. T., Nagahara H., Tachibana S., Tomomura S., Spicuzza M. J., Fournelle J. H., and Valley J. W. 2010. High precision SIMS oxygen three isotope study of chondrules in LL3 chondrites: Role of ambient gas during chondrule formation. Geochimica et Cosmochimica Acta 74:6610–6635.

Kleine T., Mezger K., Palme H., Scherer E., and Münker C. 2005. Early core formation in asteroids and late accretion of chondrite parent bodies: Evidence from 182Hf-182W in CAIs, metal-rich chondrites, and iron meteorites. Geochimica et Cosmochimica Acta 69:5805–5818.

Kleine T., Touboul M., Van Orman J. A., Bourdon B., Maden C., Mezger K., and Halliday A. N. 2008. Hf–W thermochronometry: Closure temperature and constraints on the accretion and cooling history of the H chondrite parent body. Earth and Planetary Science Letters 270:106–118.

Koblitz J. 2010. MetBase®, ver. 7.3, Meteorite Data Retrieval Software., Ritterhude, Germany.

Kong P., and Ebihara M. 1996. Metal phases of L chondrites: Their formation and evolution in the nebula and in the parent body. Geochimica et Cosmochimica Acta 60:2667–2680.

Korkisch J. 1989. Handbook of Ion Exchange Resins: Their Application to Inorganic Analytical Chemistry Volume VI, Boca Raton / London / Tokyo: CRC Press.

Krot A. N., Amelin Y., Cassen P., and Meibom A. 2005. Young chondrules in CB chondrites from a giant impact in the early Solar System. Nature 436:989–992.

Krot A. N., Keil K., Scott E. R. D., Goodrich C. A., and Weisberg M. K. 2014. Classification of Meteorites and Their Genetic Relationships. In Treatise on Geochemistry. Elsevier. pp. 1–63.

Kruijer T. S., Burkhardt C., Budde G., and Kleine T. 2017. Age of Jupiter inferred from the distinct genetics and formation times of meteorites. Proceedings of the National Academy of Sciences 114:6712–6716.

Lodders K. 2003. Solar System Abundances and Condensation Temperatures of the Elements. The Astrophysical Journal 591:1220–1247.

Lodders K., Palme H., and Gail H.-P. 2009. 4.4 Abundances of the elements in the Solar System. In Solar System, edited by Trümper J. E. Berlin, Heidelberg: Springer Berlin Heidelberg. pp. 712–770.

Lovering J. F., Nichiporuk W., Chodos A., and Brown H. 1957. The distribution of gallium, germanium, cobalt, chromium, and copper in iron and stony-iron meteorites in relation to nickel content and structure. Geochimica et Cosmochimica Acta 11:263–278.

Luais B. 2007. Isotopic fractionation of germanium in iron meteorites: Significance for nebular condensation, core formation and impact processes. Earth and Planetary Science Letters 262:21–36.

Luais B., Toplis M. J., Tissandier L., and Roskosz M. 2009. Metal-Silicate Segregation and Fractionation of Ge Isotopes: Comparison of Experimental Data and Meteorite. In 72nd Annual Meteoritical Society Meeting. p. 5326.

Luais B. 2012. Germanium chemistry and MC-ICPMS isotopic measurements of Fe–Ni, Zn alloys and silicate matrices: Insights into deep Earth processes. Chemical Geology 334:295–311.

Luais B., Ali F., and Wasson J. T. 2014. Low Germanium Isotopic Composition of IIG Iron Meteorites: Relationship with IIAB Irons and Influence of Sulfur and Phosphorus. p. 5417.

Marty B., Kelley S., and Turner G. 2010. Chronology and shock history of the Bencubbin meteorite: A nitrogen, noble gas, and Ar–Ar investigation of silicates, metal and fluid inclusions. Geochimica et Cosmochimica Acta 74:6636–6653.

Mason B. 1963. Olivine composition in chondrites. Geochimica et Cosmochimica Acta 27:1011–1023.

May T. W., and Wiedmeyer R. H. 1998. A table of polyatomic interferences in ICP-MS. Atomic Spectroscopy 19:6.

McFadden W. H. 1973. Techniques of combined gas chromatography/mass spectrometry.

Meibom A. et al. 2005. Shock melts in QUE 94411, Hammadah al Hamra 237, and Bencubbin: Remains of the missing matrix? Meteoritics & Planetary Science 40:1377–1391.

Minster J.-F., and Allègre C. J. 1979. 87Rb87Sr chronology of H chondrites: Constraint and speculations on the early evolution of their parent body. Earth and Planetary Science Letters 42:333–347.

Monnereau M., Toplis M. J., Baratoux D., and Guignard J. 2013. Thermal history of the H-chondrite parent body: Implications for metamorphic grade and accretionary time-scales. Geochimica et Cosmochimica Acta 119:302–321.

Morbidelli A., Bitsch B., Crida A., Gounelle M., Guillot T., Jacobson S., Johansen A., Lambrechts M., and Lega E. 2016. Fossilized condensation lines in the Solar System protoplanetary disk. Icarus 267:368–376.

Mostefaoui S., Perron C., Zinner E., and Sagon G. 2000. Metal-associated carbon in primitive chondrites: structure, isotopic composition, and origin. Geochimica et Cosmochimica Acta 64:1945–1964.

Néri A., Guignard J., Monnereau M., Toplis M. J., and Quitté G. 2019. Metal segregation in planetesimals: Constraints from experimentally determined interfacial energies. Earth and Planetary Science Letters 518:40–52.

Newsom H. E., and Drake M. J. 1979. The origin of metal clasts in the Bencubbin meteoritic breccia. Geochimica et Cosmochimica Acta 43:689–707.

Okabayashi S., Yokoyama T., Nakanishi N., and Iwamori H. 2019. Fractionation of highly siderophile elements in metal grains from unequilibrated ordinary chondrites: Implications for the origin of chondritic metals. Geochimica et Cosmochimica Acta 244:197–215.

Paterson R. 1970. An introduction to ion exchange, Heyden in cooperation with Sadtler Research Laboratories Philadelphia.

Peters D. G., Hayes J. M., and Hieftje G. M. 1974. Chemical separations and measurements: theory and practice of analytical chemistry, WB Saunders Company.

Prior G. T. 1916. On the genetic relationship and clasaification of Meteorites1. Mineralogical Magazine and Journal of the Mineralogical Society 18:26–44.

Prior G. T. 1920. The classification of Meteorites1. Mineralogical Magazine and Journal of the Mineralogical Society 19:51–63.

Qin L., Dauphas N., Wadhwa M., Masarik J., and Janney P. E. 2008. Rapid accretion and differentiation of iron meteorite parent bodies inferred from 182Hf–182W chronometry and thermal modeling. Earth and Planetary Science Letters 273:94–104.

Rambaldi E. R. 1977. The content of Sb, Ge and refractory siderophile elements in metals of L-group chondrites. Earth and Planetary Science Letters 33:407–419.

Richter F. M. 2004. Timescales determining the degree of kinetic isotope fractionation by evaporation and condensation. Geochimica et Cosmochimica Acta 68:4971–4992.

Richter F. M., Huss G. R., and Mendybaev R. A. 2014. Iron and nickel isotopic fractionation across metal grains from three CBb. 2.

Righter K., Campbell A. J., and Humayun M. 2005. Diffusion of trace elements in FeNi metal: Application to zoned metal grains in chondrites. Geochimica et Cosmochimica Acta 69:3145–3158.

Righter K., Pando K. M., Danielson L., and Lee C.-T. 2010. Partitioning of Mo, P and other siderophile elements (Cu, Ga, Sn, Ni, Co, Cr, Mn, V, and W) between metal and silicate melt as a function of temperature and silicate melt composition. Earth and Planetary Science Letters 291:1–9.

Romig A. D., and Goldstein J. I. 1980. Determination of the Fe-Ni and Fe-Ni-P phase diagrams at low temperatures (700 to 300 °C). Metallurgical Transactions A 11:1151–1159.

Rose G. 1864. Beschreibung und Eintheilung der Meteoriten auf Grund der Sammlung im mineralogischen Museum zu Berlin, Gedruckt in der Druckerei der Königlichen Akademie der Wissenshaften, in Commission bei F. Dümmler's Verlags-Buchhandlung Harrwitz und Gossmann.

Rouxel O., Galy A., and Elderfield H. 2006. Germanium isotopic variations in igneous rocks and marine sediments. Geochimica et Cosmochimica Acta 70:3387–3400.

Rouxel O. J., and Luais B. 2017. Germanium Isotope Geochemistry. Reviews in Mineralogy and Geochemistry 82:601–656.

Rubin A. E. 1990. Kamacite and olivine in ordinary chondrites: Intergroup and intragroup relationships. Geochimica et Cosmochimica Acta 54:1217–1232.

Rubin A. E. 2003. Chromite-plagioclase assemblages as a new shock indicator; implications for the shock and thermal histories of ordinary chondrites. Geochimica et Cosmochimica Acta 67:2695–2709.

Rushmer T., Minarik W. G., and Taylor G. J. 2000. Physical Processes of Core Formation. Origin of the Earth and Moon 227–243.

Rushmer T., and Petford N. 2011. Microsegregation rates of liquid Fe-Ni-S metal in natural silicate-metal systems: A combined experimental and numerical study. Geochemistry, Geophysics, Geosystems 12:1–17.

Schauble E. A. 2004. Applying Stable Isotope Fractionation Theory to New Systems. Reviews in Mineralogy and Geochemistry 55:65–111.

Schönbächler M. 2016. Ion Exchange Chromatography. In Encyclopedia of Geochemistry: A Comprehensive Reference Source on the Chemistry of the Earth, edited by White W. M. Cham: Springer International Publishing. pp. 1–6.

Scott E. R. D., and Wasson J. T. 1975. Classification and properties of iron meteorites. Reviews of Geophysics 13:527.

Scott E. R. D., and Krot A. N. 2014. Chondrites and Their Components. In Treatise on Geochemistry. Elsevier. pp. 65–137.

Scott E. R. D., Krot T. V., Goldstein J. I., and Wakita S. 2014. Thermal and impact history of the H chondrite parent asteroid during metamorphism: Constraints from metallic Fe–Ni. Geochimica et Cosmochimica Acta 136:13–37.

Šrámek O., Ricard Y., and Dubuffet F. 2010. A multiphase model of core formation. Geophysical Journal International 181:198–220.

Šrámek O., Milelli L., Ricard Y., and Labrosse S. 2012. Thermal evolution and differentiation of planetesimals and planetary embryos. Icarus 217:339–354.

Steiger R. H., and Jäger E. 1977. Subcommission on geochronology: Convention on the use of decay constants in geo- and cosmochronology. Earth and Planetary Science Letters 36:359–362.

Stöffler D., Keil K., and Edward R.D S. 1991. Shock metamorphism of ordinary chondrites. Geochimica et Cosmochimica Acta 55:3845–3867.

Tait A. W., Tomkins A. G., Godel B. M., Wilson S. A., and Hasalova P. 2014. Investigation of the H7 ordinary chondrite, Watson 012: Implications for recognition and classification of Type 7 meteorites. Geochimica et Cosmochimica Acta 134:175–196.

Thiemens M. H., and Heidenreich J. E. 1983. The Mass-Independent Fractionation of Oxygen: A Novel Isotope Effect and Its Possible Cosmochemical Implications. Science 219:1073–1075.

Tomkins A. G., Weinberg R. F., Schaefer B. F., and Langendam A. 2013. Disequilibrium melting and melt migration driven by impacts: Implications for rapid planetesimal core formation. Geochimica et Cosmochimica Acta 100:41–59.

Trieloff M., Jessberger E. K., Herrwerth I., Hopp J., Fiéni C., Ghélis M., Bourot-Denise M., and Pellas P. 2003. Structure and thermal history of the H-chondrite parent asteroid revealed by thermochronometry. Nature 422:502–506.

Trinquier A., Birck J., and Allegre C. J. 2007. Widespread 54 Cr Heterogeneity in the Inner Solar System. The Astrophysical Journal 655:1179–1185.

Trinquier A., Birck J.-L., Allègre C. J., Göpel C., and Ulfbeck D. 2008. 53Mn–53Cr systematics of the early Solar System revisited. Geochimica et Cosmochimica Acta 72:5146–5163.

Tschermak H. : G., ed. 1883. Die mikroskopische Beschaffenheit der Meteoriten erläutert durch photographische Abbildungen, Stuttgart, Germany: Schweizerbart Science Publishers.

Urey H. C., and Craig H. 1953. The composition of the stone meteorites and the origin of the meteorites. Geochimica et Cosmochimica Acta 4:36–82.

Van Schmus W. R., and Wood J. A. 1967. A chemical-petrologic classification for the chondritic meteorites. Geochimica et Cosmochimica Acta 31:747–765.

Wai C. M., and Wasson J. T. 1979. Nebular condensation of Ga, Ge and Sb and the chemical classification of iron meteorites. Nature 282:790.

Walter M., Newsom H., Ertel W., and Holzheid A. 2000. Siderophile elements in the Earth and Moon: metal/silicate partitioning and implications for core formation. Origin of the Earth and Moon 265–289.

Warren P. H., and Kallemeyn G. W. 1989. Allan Hills 84025: the second brachinite, far more differentiated than Brachina, and an ultramafic achondritic clast from L chondrite Yamato 75097. LPSC 19:475–486.

Warren P. H. 2011. Stable-isotopic anomalies and the accretionary assemblage of the Earth and Mars: A subordinate role for carbonaceous chondrites. Earth and Planetary Science Letters 311:93–100.

Wasson J. T. 1969. The chemical classification of iron meteorites: III. Hexahedrites and other irons with germanium concentrations between 80 and 200 ppm. 33:859–876.

Wasson J. T. 1985. Meteorites: Their record of early solar-system history. New York, W. H. Freeman and Co., 1985, 274 p.

Wasson J. T., and Kallemeyn G. W. 2002. the IAB iron-meteorite complex: A group, five subgroups, numerous grouplets, closely related, mainly formed by crystal segregation in rapidly cooling melts. Geochimica et Cosmochimica Acta 66:2445–2473.

Wasson J. T. 2017. Formation of non-magmatic iron-meteorite group IIE. Geochimica et Cosmochimica Acta 197:396–416.

Weisberg M. K., Prinz M., Clayton R. N., Mayeda T. K., Sugiura N., Zashu S., and Ebihara M. 2001. A new metal-rich chondrite grouplet. Meteoritics & Planetary Science 36:401–418.

Weyrauch M., Zipfel J., and Weyer S. 2019. Origin of metal from CB chondrites in an impact plume – A combined study of Fe and Ni isotope composition and trace element abundances. Geochimica et Cosmochimica Acta 246:123–137.

Wiederhold J. G. 2015. Metal stable isotope signatures as tracers in environmental geochemistry. Environmental science & technology 49:2606–2624.

Wombacher F., Rehkämper M., Mezger K., Bischoff A., and Münker C. 2008. Cadmium stable isotope cosmochemistry. Geochimica et Cosmochimica Acta 72:646–667.

Wood B. J., Smythe D. J., and Harrison T. 2019. The condensation temperatures of the elements: A reappraisal. American Mineralogist 104:844–856.

Résumé

La formation et l'évolution de la phase métal dans les corps primitifs et les planétésimaux sont d'une importance majeure pour comprendre les premières étapes de l'évolution du Système Solaire primitif. Malgré de nombreuses études sur le métal des chondrites, les conditions de condensation à température intermédiaire, et les processus de chauffe et d'oxydation qui l'affectent dans le disque d'accrétion et dans les planétésimaux sont toujours mal compris. En utilisant une approche combinée des **mesures in situ des éléments fortement sidérophiles** (HSE) **et modérément sidérophiles** (MSE) et volatils (e.g. germanium), ainsi que de la **composition isotopique du germanium** du bulk et des phases séparées des chondrites, cette thèse vise à apporter des contraintes supplémentaires quant à : (1) la formation du métal via condensation et la fusion de précurseurs métalliques dans les **chondrites carbonées de type CB (Bencubbinites)**, (2) l'évolution du métal avec le métamorphisme enregistrée dans la séquence H, L et LL des chondrites ordinaires. Le fractionnement isotopique du germanium permet de distinguer les deux groupes de chondrites carbonées CB et de tracer différentes étapes de condensation à l'équilibre et cinétique, et d'évaporation. Ces processus ne peuvent être enregistrés par les éléments majeurs et réfractaires (Fe, Ni) dont la température de condensation est plus élevée que celle du germanium. Dans le métal des chondrites ordinaires primitives (type H), les larges variations en éléments sidérophiles, ainsi que les valeurs positives du $\Delta^{74/70}Ge_{metal\text{-}silicate}$, suggèrent des variations locales de l'état d'oxydation et des échanges métal-silicate, lors du métamorphisme sur les corps parents. Un des résultats majeurs est l'augmentation corrélée des valeurs $\delta^{74/70}Ge$ et des anomalies isotopiques de l'oxygène $\Delta^{17}O$ et %Fa dans la séquence H, L à LL des chondrites ordinaires. Ces observations sont interprétées et modélisés par l'accrétion graduelle d'un composant oxydant avec une composition élevée en $\delta^{74/70}Ge$ et $\Delta^{17}O$ des groupes H, à L et LL durant la formation des chondrites ordinaires. Ce composant à la fois riche en eau et en Ge pourrait être identifiée comme un phyllosilicate. Les conclusions de cette thèse soulignent le fort potentiel des isotopes du germanium pour enregistrer les processus de formation et d'évolution de la phase métal.

Mots-clés : Chondrites, Isotopes du Germanium, Eléments sidérophiles, Fe-Ni métal, Oxydation, Condensation

Abstract

The **formation and subsequent chemical evolution of FeNi metal phases** is critical for understanding the development of the early Solar System. Despite numerous studies on metal phases in chondrites, the effect of metal condensation at moderate temperatures, as well as of metal heating and oxidation in nebular and protoplanetary environment, is still under debate. By using a combined approach of **germanium isotopic quantification** and **siderophile in–situ measurements** in bulk and separated phases of Bencubbinites carbonaceous chondrites (CB) and ordinary chondrites, this thesis aims to provide new constraints on: (1) the formation of metal via condensation and metallic precursors melting and (2) the processes that can account for the elemental and isotopic difference between the H, L and LL chondrites and metal evolution with metamorphism. The results show that the two groups of CB are distinguishable using $\boldsymbol{\delta^{74/70}Ge_{bulk}}$, providing insights into kinetic and equilibrium condensation processes. Variations in $\delta^{74/70}Ge$ during metal condensation are shown to be the result of evaporation / recondensation processes that are not recorded by major or refractory elements. A large variation in siderophile element content in the metal of H primitive ordinary chondrites has been identified, as well as a positive $\Delta^{74/70}Ge_{metal\text{–}silicates}$. This suggests local oxidation state variation and metal–silicate interactions during heating event(s) in the disk. The thesis also highlights that the H, L and LL groups are resolvable with $\delta^{74/70}Ge$ of bulk and metal. These variations are positively correlated with $\Delta^{17}O$ and %Fa across the ordinary chondrites sequence and suggests the accretion of an increasing proportion of oxidising components with a high $\delta^{74/70}Ge$ and $\Delta^{17}O$ composition from H to L to LL groups. Because the oxidising component contains Ge it suggests that it cannot be ice or water but more likely a silicate phase. These conclusions highlight the high potential of germanium isotopes to record processes leading to metal formation and evolution.

Key-words: Chondrites, Germanium Isotopes, Siderophile Elements, Fe-Ni metal, Oxidation, Condensation